

University of Nottingham
UK | CHINA | MALAYSIA

Investigating Bering Sea oceanographic response to the Milankovitch orbital cycle climatic shift during the middle Pleistocene.

Savannah Worne

BSc (Hons)

Thesis submitted to the University of Nottingham
for the degree of Doctor of Philosophy

July 2019

Acknowledgements

Firstly, I would like to thank George Swann, Sev Kender, Zuzia Stroynowski and Sarah Metcalfe for their incredible supervisory support and continued guidance through countless emails, meetings and paper drafts over the last 4 years, which ultimately shaped both this thesis and the scientific professional that I have become today. In particular, I would like to thank George for encouraging me to apply for this PhD and providing emotional support on a day-to-day basis through the highs and lows that come with academia. I would also like to extend my gratitude to Teresa Needham for her unparalleled problem-solving skills and patience in managing me through my lab work which enabled a far smoother data collection process, both during my undergraduate and through this PhD.

I must also give thanks to the International Ocean Drilling Program (IODP) for providing samples for this research, as well as the Expedition 323 staff and crew of the JOIDES Resolution, and the curators at the Kochi Core Centre, without whom this project would not have come to fruition. Furthermore, I would like to recognise the Natural Environment Research Council (NERC) who through the Envision DTP funded my research and training, supported by CASE funding from the British Geological Survey (BGS) and grants provided by the NERC Isotope Geosciences Facilities Steering Committee (NIGFSC). I am grateful to Christina Ravelo, Dyke Andreasen and Colin Carney from the Ravelo laboratory, as well as Christopher Kendrick and Jack Lacey from the NERC Isotope Geosciences Facility, for support with instrumentation and sample preparation. In particular, I would like to thank Melanie Leng for her comments

in both my first and second year annual reviews, and continued support through the paper submission process.

On a more personal level, I would like to mention my parents (Carol and Andrew), my grandparents (Rita, Brian and Joyce) and my brother (Jake), without whom it would not have been possible for me to complete my University education. Ultimately, this PhD is a testament to their support at every stage of my academic and personal life, and for that I am eternally appreciative. I also owe an enormous thanks my partner Patrick Bointon, who has kept me sane through the rollercoaster of emotions that encompass the PhD experience, putting his own troubles aside to provide a loving environment in which I was able to de-stress. Similarly, I extend a huge thanks to Rhona Savin and my office-mates – Chloe, Catherine, Simon and Phil – who were a constant source of emotional comfort as well as filling my University experience with fun and laughter.

Table of Contents

Acknowledgements ii
List of Figures ix
List of Tables xvii
Abstract 1
Chapter 1: Introduction 2
1.1 Extended Abstract 2
1.2 Modern Oceanography 6
1.2.1 Oceanography of the North Pacific 6
1.2.2 Geographical setting of the Bering Sea 10
1.2.3 Oceanographic setting of the Bering Sea 11
1.2.4 Sea Ice in the Bering Sea 13
1.2.5 Productivity and Nutrient Cycling in the Bering Sea 15
1.3 Quaternary palaeoceanography and the Bering Sea 16
1.3.1 The Pliocene-Pleistocene Transition and the early Pleistocene (~2.7 – 1.2 Ma) 17
1.3.2 Mid-Pleistocene Transition (MPT) (~1.2-0.6 Ma) 19
1.3.3 What caused the MPT? 21
1.4 Research Questions 24
1.4.1 Did sea ice-driven NPIW expansion cause suppressed glacial upwelling of CO_2 rich deep waters, contributing to global cooling in the Pleistocene and the MPT? 25
1.4.2 What role did sea ice dynamics play in controlling nutrient upwelling at Milankovitch and suborbital periodicities, as well as on increasing the duration of glacials via the sea ice switch (SIS) hypothesis? 27
1.4.3 How did the Bering Sea green belt biological pump respond to MPT changes in sea ice and nutrient upwelling strength, and what impact did this have on regional ocean-atmosphere CO_2 exchange? 30
1.5 Materials and Methods 31

1.5.1 Site U1343: site location and core description 32
1.5.2 Benthic foraminiferal $\delta^{18}O$ 34
1.5.3 Age Model 35
1.6 A note on the papers 38
Chapter 2: Coupled climate and subarctic Pacific nutrient upwelling over the last 850,000 years 40
2.1 Introduction 41
2.2 Materials and Methods 44
2.2.1 Core Materials 44
2.2.2 Foraminiferal isotopes 44
2.2.3 Age Model, Sedimentation Rates and Opal MAR calculations 45
2.2.4 Bulk Sedimentary $\delta^{15}N$ 47
2.2.5 Oceanographic indicies 47
2.3 Results 50
2.3.1 $\Delta\delta^{18}O_{849-U1343}$: NPIW formation 50
2.3.2 $\delta^{15}N$ and Opal MAR 52
2.3.3 Glacial-interglacial variability in the upwelling index 55
2.4 Discussion 57
2.5 Conclusion 63
2.6 Supplementary information 65
Chapter 3: Reduced high latitude upwelling in the subarctic Pacific during the MPT, modulated by sea level and sea ice 71
3.1 Introduction 73
3.2 Methods 76
3.2.1 Core materials 76
3.2.2 Updated Site U1343 Age Model (1.01 – 1.20 Ma) 77
3.2.3 Bulk sedimentary $\delta^{15}N$ 78
3.2.4 Upwelling index 78
3.3 Results 80

3.3.1 $\delta^{15}N_{U1343}$ and the upwelling index 80
3.3.2 Cyclicity analysis 81
3.4 Discussion 85
3.4.1 Nutrient upwelling and glacial-interglacial climate 85
3.4.2 Orbital forcing and sea ice control on nutrient upwelling 88
3.4.3 Pre-MPT 89
3.4.4 Upwelling and NPIW expansion: the MPT 93
3.4.5 Post-MPT 95
3.5 Conclusion 96
3.6 Supplementary information 98
Chapter 4: Sea Ice in the Bering Sea during the Mid Pleistocene Transition 101
4.1 Introduction 103
4.1.1 The Bering Sea and the MPT 104
4.2 Methods 107
4.2.1 Core materials, age model and sedimentation rates 107
4.2.2 Diatom assemblages 109
4.2.3 Diatom concentration and accumulation rates 111
4.3 Results and Discussion 111
4.3.1 Diatom ecologies and environmental inference 111
4.3.2 General trends in diatom abundances 114
4.3.3 Pre-MPT: MIS 36-25 (~1.2 – 0.96 Ma) 118
4.3.4 Interim Period: MIS 30-27 (~1.05 – 0.98 Ma) 120
4.3.5 Build up to MPT conditions: MIS 27-25 (~0.98-0.94 Ma) 121
4.3.6 The MPT and the 900 kyr event: MIS 24-22 (~0.94 – 0.87 Ma) 123
4.3.7 Post-MPT: MIS 21-15 (~0.85 – 0.6 Ma) 126
4.4 Wider impact: Assessing MPT Hypotheses 128
4.4.1 Intensified Walker circulation in the early Pleistocene 128

4.4.2 NPIW expansion and reduced CO_2 ventilation 129
4.4.3 Sea Ice Switch Hypothesis 130
4.5 Conclusion 132
4.6 Supporting information 134
Chapter 5: Increased efficiency of the subarctic Pacific biological pump during the Mid Pleistocene Transition 137
5.1 Introduction 138
5.1.1 Paleoceanography of the Bering Sea 141
5.1.2 Diatom silicon isotopes 143
5.2 Methods 144
5.2.1 $\delta^{30}Si_{diatom}$ 144
5.2.2 Diatom assemblage counts 147
5.2.3 Silicic acid utilisation 147
5.2.4 Silicic acid supply 149
5.3 Results 150
5.3.1 Diatom assemblages 150
5.3.2 $\delta^{30}Si_{diatom}$ 152
5.3.3 $\delta^{30}Si_{diatom}$:$\delta^{15}N_{bulk}$ (Si:N) 154
5.3.4 Silicic acid utilisation 155
5.3.5 Silicic acid supply 156
5.4 Discussion 158
5.4.1 Silicic acid utilisation – selecting ε and $\delta^{30}Si(OH)_4$ 158
5.4.2 Seasonal investigation of $\delta^{30}Si_{diatom}$ using assemblage results 160
5.4.3 Palaeoceanographic significance – the biological pump 161
5.4.4 Wider implications 166
5.5 Conclusion 168
5.6 Supplementary information 170
Chapter 6: Synthesis 173

6.1 Summary of thesis and advances to Bering Sea palaeoceanography 173

6.2 Global significance and Future directions 177

6.3 Conclusion 182

Chapter 7: References 185

Chapter 8: Appendix 206

8.1 Appendix 1: Closure of the Bering Strait caused Mid-Pleistocene Transition cooling 206

8.2 Data tables 217

List of Figures

Figure 1.1 The circulation patterns of the subarctic North Pacific, showing the interaction of the Western Subarctic Gyre, the Subarctic Current, the North Pacific Current and the Alaskan Gyre (Takeda, 2011). Figure also displays the west wind drift which separates the two southern boundary currents of the Subarctic North Pacific. The red box highlights the Bering Sea, the region of this study which is depicted in detail in Figure 1.3.....7

Figure 1.2 Cross sectional water properties across the North Pacific. [A] Salinity and temperature distribution while [B] shows the oxygen concentrations across transect P13, taken from the eWOCE Gallery (Schlitzer, 2013). Figures shows that surface waters freshen and cool with latitude, with NPIW from ~300-1000 m depth exhibiting low salinity and temperature concentrations in the subarctic Pacific Ocean. Higher oxygen concentrations at intermediate water depth are found 20-40°N, where newly formed oxygen-rich low salinity OSMW leaves the Okhotsk Sea to enter the mixed water region. Similarly, input of OSMW allows fresher water conditions to extend further south from the subarctic Pacific region at intermediate depth. 9

Figure 1.3 The geographical location and oceanography of the Bering Sea with the white area representing the continental shelf region to the north and the blue represents the Aleutian basin. Yellow dots indicate drill sites that were cored during IODP Expedition 323 in 2009, with Site U1343 (this study) marked by a yellow star. Surface water circulation is marked by red arrows, which flow in from the Alaskan Stream and through various straits and passes in the Aleutian island arc. Surface water circulates in an anti-clockwise gyre, where turbulence and eddies in the shelf adjacent Bering Slope Current (BSC) causes a high productivity region known as the green belt, represented by the green patterned shape (Springer et al., 1996). Deep water circulation is marked by blue arrows, entering from the lower subarctic Pacific Ocean through the deep western Kamchatka Strait.....10

Figure 1.4 Cross sections of the Aleutian passes and volumes of transport through which Alaskan Stream water exchanges with the Bering basin (Stabeno et al., 1999; Takahashi et al., 2011 12

Figure 1.5 Vertical temperature profile (A) and oxygen concentrations (B) across the latitudes of the Bering Sea, with red dots showing the IODP Expedition 323 drill sites (Takahashi et al., 2011) 14

Figure 1.6 Map showing the drill site locations for ODP Leg 145, including Site 882 (Maslin et al. 1995). 16

Figure 1.7 Opal wt% and MAR record from ODP Site 882, showing the "opal crash" at ~2.7 Ma, following the onset of northern hemispheric glaciation (Haug et al., 1995). 17

Figure 1.8 LRO4 Global stack of benthic foraminiferal $\delta^{18}O$ records, which shows the MPT shift from 40 kyr to 100 kyr glacial-interglacial cycles from ~1.2-0.8 Ma (Lisiecki & Raymo, 2005) 19

Figure 1.9 The sea ice switch mechanism as depicted by Gildor and Tziperman (2001), which demonstrates the land versus sea ice hysteresis model where the sea ice maxima occurs after deglaciation of land ice begins. 21

Figure 1.10 Spliced composite records used to create a composite core depth for Site U1343, based on ship-board measurements of a) magnetic susceptibility, b) GRA bulk density, c) NGR and d) colour reflectance b*. Figure taken from (Takahashi et al., 2011b).....34

Figure 2.1 Benthic foraminiferal $\delta^{18}O$ results from U1343. A) Raw $\delta^{18}O$ values are categorised by species/genus and plotted against *E. batialis* (black) to which species-specific offsets are applied (Kender et al., 2018). b) Raw $\delta^{18}O$ data (red dots) are plotted against $\delta^{18}O_{U1343}$ (black line) which has been tuned to *E. batialis*. c) Comparison of $\delta^{18}O_{U1343}$ from this study (black line) against previous data from IODP Site U1343 (Asahi et al., 2016) (blue dots), which were combined in d) to create the updated age model for IODP Site U1343 (orange dots), and has been smoothed using linear interpolation to a 2 kyr resolution (black line). 46

Figure 2.2 Geochemical proxy results from IODP Site U1343 from MIS 2 to 20. a) Benthic foraminiferal $\delta^{18}O$ results from IODP Site U1343 compared to those from the shallower IODP Site U1342 and deep Pacific ODP Site 849. The data from Site U1342 has been recalculated here to match benthic foraminiferal offset for *E. batialis*, used for Site U1343 (Kender et al., 2018). b) The offset in $\delta^{18}O$ between IODP Site U1343 and ODP Site 849 ($\Delta\delta^{18}O_{849\text{-}U1343}$). c) Bulk $\delta^{15}N$ data from IODP Site U1343 compared with deep North Pacific ODP Site 1012 (a site of complete nutrient utilisation) together with bulk $\delta^{15}N$ records from ODP Site 882 and MD2416 in the subarctic North Pacific Ocean. d) The $\delta^{15}N$ offset between IODP Site U1343 and ODP Site 1012 ($\Delta\delta^{15}N_{U1343\text{-}1012}$) which constrains changes in source water $\delta^{15}N$ to reflect changes in Bering Sea nutrient utilisation. e) Opal mass accumulation rate (MAR) from IODP Site U1343 [adapted from Kim et al. (2014), see Methods]. f) The opal (%) and Ba/Al productivity records from ODP Site 882 (Jaccard et al., 2010). Blue bars represent periods of Bering Strait closure (>50 m sea level drop) (Elderfield et al., 2012) with vertical dashed lines indicating deglaciations. 52

Figure 2.3 Comparison of the upwelling indexes against other global and regional paleoenvironmental records. a) Composite LR04 benthic foraminiferal $\delta^{18}O$ stack (Lisiecki & Raymo, 2005) over the last 850 kyr. b) The upwelling index for Site U1343 (red) and Site 882 (grey), which show suppressed rates of upwelling during glacial periods following Bering Strait closure (blue bars). The upwelling index shows strong correlation with the composite EPICA Dome

C Ice Core atmospheric CO_2 record over the last 800 kyr (c) (Lüthi et al., 2008), changes in relative sea level (m) (d) (Elderfield et al., 2012), where the blue lines at -50 m represent modern Bering Strait depth, and global temperature records (temperature deviation from present day) (e) (Jouzel et al., 2007; Snyder 2016). Vertical dashed lines indicate deglaciations. 56

Figure 2.4 Schematic models representing glacial, deglacial and interglacial regimes of biogeochemical cycling in the Bering Sea. a) A low upwelling index indicates reduced upwelling caused by an expansion of NPIW which forms in glacials following the closure of the Bering Strait, leading to an isolated pool of nutrients in the photic zone. This results in reduced primary productivity (opal MAR) but higher rates of nutrient utilisation due to the reduced supply of deep water nutrients into the photic zone. b) A high upwelling index indicates ample nutrient supply from resumed NPDW upwelling which occurs during deglaciation, leading to a high productivity/low nutrient utilisation state. c) An intermediate upwelling index results indicates upwelling typical of an interglacial, similar to the modern regime. 60

Figure 2.5 Benthic foraminiferal comparison of $\delta^{13}C$ and $\delta^{18}O$. a) $\delta^{13}C$ data categorised by species/genus. The poor relationship for $\delta^{13}C$ against both raw $\delta^{18}O$ (b) and $\delta^{18}O_{U1343}$ adjusted to *E. batialis* (c) suggests that diagenetic alteration of foraminiferal shells cannot explain the glacial-interglacial variability in the $\delta^{18}O$..... 65

Figure 2.6 Bulk $\delta^{15}N$ and Biogenic Opal data for IODP Site U1343. a) Bulk $\delta^{15}N$ data (red dots) from this study and previously published lower resolution data (Kim et al., 2017b), smoothed using a linearly interpolation to create a 2 kyr resolution dataset (black line). b) C/N ratios, which are low and show a lack of covariation to $\delta^{15}N$, suggesting that terrestrial input of nitrogen was low and did not drive the $\delta^{15}N$ record. c) New sedimentation rates calculated for IODP Site U1343 using the updated age model presented in this study, which were then applied to d) the biogenic opal record (Kim et al. 2014) to calculate e) the opal mass accumulation rate (MAR) data. 66

Figure 2.7 Assessing the relative contribution of $\delta^{15}N_{1012}$ to $\Delta\delta^{15}N_{U1343\text{-}1012}$. Results demonstrate that there is no significant difference between the upwelling index record calculated using $\Delta\delta^{15}N_{U1343\text{-}1012}$ compared to $\delta^{15}N_{U1343}$ (where the latter does not subtract the ODP 1012 record) ($t = -1.93$, $p = 0.05$). 67

Figure 2.8 %TOC vs %TN cross plots for IODP Site U1343 from this study and previously published lower resolution data (Kim et al., 2017b). a) Shows the cross plot for the whole dataset, with an intercept of 0.0193, suggesting minimal influence of inorganic nitrogen. Similarity between b) glacial intercept of 0.0181 and c) interglacial intercept of 0.0192, suggests that variable contribution of terrestrial/inorganic nitrogen does not drive the bulk $\delta^{15}N$ record presented here. 68

Figure 3.1 Geochemical proxy results from IODP Site U1343 from MIS 2 to 36. a) Benthic foraminiferal $\delta^{18}O$ results from IODP Site U1343 compared to those from the shallower IODP Site U1342 and the LR04 global benthic $\delta^{18}O$ stack (Lisiecki & Raymo, 2005), where blue bars represent glacial periods as identified in the LR04 record. The data from Site U1342 has been recalculated here to match benthic foraminiferal offset for *E. batialis*, used for Site U1343 (Kender et al., 2018). b) Solar insolation received at 55°N. c) Relative sea level changes estimated by Elderfield et al. (2012), where the dashed line represents 50 m lower sea level than present, at which point the Bering Straight was likely closed. d) Bulk $\delta^{15}N$ data from IODP Site U1343 compared with deep North Pacific ODP Site 1012 (a site of complete nutrient utilisation) (black) together with bulk $\delta^{15}N$ records from ODP Site 882 (green) and MD2416 (navy blue) in the subarctic North Pacific Ocean. e) Opal mass accumulation rate (MAR) from IODP Site U1343 [adapted from Kim et al. (2014), using the new age model]. 82

Figure 3.2 REDFIT spectral analysis, setting the oversample and segment size to 1, was run to fit the upwelling index time series dataset to a first-order red-noise model between 0 – 1.2 Ma (Hammer et al., 2001) (a). Similar analysis of pre-MPT data (0.866 – 1.2 Ma) (b) and post-MPT results (0 – 0.866 Ma) (c) are also presented, where the vertical dashed lines represent the key periodicities of the Milankovitch orbital forcings. Confidence bands at 99 (red), 95 and 90% (green) are also displayed. 84

Figure 3.3 Upwelling index results between 0 – 1.2 Ma (red) are compared to proxy derived pCO_2 estimates (black) from the Vostok ice core between 0 – 0.8 Ma (Lüthi et al., 2008), and from boron isotope measurements between ~1.07 – 1.2 Ma (Chalk et al., 2017) (a). Low resolution boron isotope-derived pCO_2 estimates from Hönisch et al. (2009) are also displayed as blue squares (a). b) Wavelet analysis of the upwelling index from 0 – 1.2 Ma, where red/warmer values indicate higher spectral power than blue/colder colours (temperature gradient). Dashed lines represent the periodicities of the Milankovitch orbital cycles, and the solid black line represents the cone of influence, above which results are considered significant. The coloured bars (yellow, grey and white) above panel (b) represent the evolution of sea ice and variable response to orbital and millennial scale forcings (see Figure 3.4). 86

Figure 3.4 a) Comparison of upwelling index results (red) with global climate records including the LR04 benthic stack (Lisiecki & Raymo, 2005) (black), which represents a combined signal of global ice volume and temperature change. b) Relative sea level estimations of Elderfield et al., (2012) are also shown, and exhibits strong similarity to the upwelling index during and after the MPT. c) ΔSST temperature record from the tropical Pacific, which represents the East-West temperature gradient which drives Walker circulation strength, and shows an increase during the early Pleistocene, in line with increased abundance of pack ice associated diatoms at Site U1343 (Stroynowski et al., 2017) (d). Following wavelet analysis results (Figure 3.3) the control of sea ice on NPDW upwelling can be categorised into three states, described at

the bottom of the figure and delineated with dashed lines (marked by white, yellow and grey coloured bars). 90

Figure 3.5 Comparison of upwelling index results (red) from 0 – 1.2 Ma with modelled atmospheric CO_2 concentrations (black) (Chalk et al., 2017)..... 98

Figure 3.6 Wavelet analysis of the upwelling index from 0 – 1.2 Ma calculated at a larger timestep of 6 kyr, where red/warmer values indicate higher spectral power than blue/colder colours (temperature gradient). Dashed lines represent the periodicities of the Milankovitch orbital cycles, and the solid black line represents the cone of influence, above which results are considered significant. 99

Figure 4.1 Published data from the subarctic Pacific Ocean between 0.6- 1.2 Ma which aid interpretation of diatom assemblage results presented here. A) Age model from Site U1343 between 0.6 – 1.2 Ma (red) compared to the global benthic LR04 stack (black). Blue shaded bars represent glacial periods identified in the LR04 stack, and labelled as the respective marine isotope stages (MIS) at the top of the figure. B) Solar insolation received at for 58°N. C) SST temperature from ODP Site 882 in the western subarctic Pacific Ocean (Martinez-Garcia et al., 2010). D) Relative sea level estimated using $\delta^{18}O$ data (Elderfield et al., 2012), where the blue line represents -50 m the modern depth of the Bering Strait, and values below the line are likely periods of Bering Strait closure (Kender et al., 2018; Chapter 3). E) Upwelling index results from Chapter 3, where higher values reflect increased strength of NPDW upwelling and lower values reflect suppressed nutrient upwelling. F) Opal mass accumulation results (MAR) from Kim et al. (2014) reflects siliceous productivity, where higher values are indicative of periods with higher total primary productivity. 109

Figure 4.2 Relative diatom abundance assemblage results from Site U1343 between 0.6 – 1.2 Ma, with species grouped by ecological tolerances or genus (see Section 4.3.1). a) Species associated with pack ice cover at Site U1343 (navy) shows similarity to global benthic LR04 stack (grey), particularly after the 900 kyr event (see Section 4.3.7). Blue bars represent glacial periods identified in the LR04 global stack and labelled by their respective glacial MIS numbers (Lisiecki & Raymo, 2005). Other sea ice associated species plotted include epontic diatoms (ICE) (b) and marginal sea ice (MARG) (c) also show increased abundance through the MPT. d) Benthic species show increased abundance in glacial periods when Site U1343 becomes more coastal while the abundance of *N. seminae* (e) is considered to be representative of Alaskan Stream water influence via the BSC which shows higher abundance during periods of higher sea level/lower sea ice. f) *Chaetoceros* RVS are indicative of high nutrient availability from deep water upwelling during spring sea ice melt (Stroynowski et al., 2017; Sancetta 1982). *Rhizosolenia* spp. (g) and *Actinocyclus* spp. (h) are summer/pelagic species, where both species are indicative of periods with strong water column stratification, while *P. sulcata/M. sol* (i) which dwells on the eastern Bering shelf can provide insight into Bering gyre strength. 116

Figure 4.3 Diatom accumulation rates (DAR) (fainter, thicker lines) have been smoothed using a 2-point spline (darker, thinner lines), allowing investigation into variation in absolute abundance of diatom productivity, with glacial periosd depicted by the blue bars. a) Non-Sea Ice DAR (black) shows similar trends to the upwelling index results (Chapter 3), where higher Non-Sea Ice DAR occurs during periods of increased nutrient upwelling (red). Increased absolute abundance of *Chaetoceros* RVS (b) and All Sea Ice DAR (c) occur during the 900 kyr event. In particular, increased abundance of PACK DAR (d) and ICE DAR (e) contribute to the increase in All Sea Ice DAR during MIS 22. Increased absolute abundance of ICE and MARG DAR (f) also cause higher All Sea Ice DAR during MIS 25 when productivity is high (Figure 4.1). 119

Figure 4.4 Principal Component Analysis (PCA) results confirm that sea ice explains 50% of variability in the diatom percentage data, where the volume of sea ice increases from pelagic open water conditions to thick pack ice environments (blue arrow). "All Sea Ice" group in the bottom left corner is a sum of the PACK, MARG and ICE groups. 134

Figure 4.5 Relative abundance of other diatom species including marginal ice species *P. glacialis* (a), *S. turris* which is indicative of the strength of current speeds through the Aleutian island arc (b), *S. trifultus* which thrives in colder waters (c) and summer blooming species *Coscinodiscus* spp. (d).....135

Figure 4.6 Total DAR (black) is compared to the upwelling index (red; Chapter 3) and shows similar trends with higher total DAR during periods of higher nutrient upwelling, with exception during the 900 kyr event (MIS 23-24) during which there is high Total DAR, despite low nutrient upwelling (a). Total DAR also shows strong similarity to opal MAR (Kim et al., 2014) with high Total DAR during periods of higher productivity (b). 136

Figure 5.1 Geochemical proxy results from Site U1343 including the high resolution age model between 0.6 – 1.2 Ma (Chapter 3) (red) which is tuned to the LR04 global benthic stack (Lisiecki & Raymo, 2005) (black) (a). b) New $\delta^{30}Si_{diatom}$ results from Site U1343, measured on a larger >38 μm fraction ($\delta^{30}Si_{large}$; orange) and a smaller 20-38 μm fraction ($\delta^{30}Si_{small}$; blue). c) Bulk sedimentary $\delta^{15}N$ results from Chapter 3 (purple), where the fainter, thicker line is the raw data and is overlaid by darker, thinner low resolution line, where the data points (circles) align with those on which $\delta^{30}Si$ was measured. d) Si:N ratios for both the large (orange) and small (blue) fractions, calculated using the $\delta^{30}Si_{diatom}$ (a) and $\delta^{15}N_{bulk}$ (c) data. Opal mass accumulation rate (MAR) data from Kim et al. (2014) (e; green), and upwelling index results (f; red) from Chapter 3 are also plotted, where interpolated data points (circles) align with those on which $\delta^{30}Si$ was measured. 146

Figure 5.2 Silicic acid utilisation (a) and supply (relative to 0.605 Ma) (b) rates calculated on the larger >38 μm (orange) and smaller 20-38 μm (blue) fractions, with the black lines representing 100% utilisation (a) and supply at 0.605 Ma (b), respectively. c-i) Relative abundance of key diatom species (>~5-10%

abundance) counted on the cleaned samples in both the large fraction ($species_{large}$; orange) and smaller fracter ($species_{small}$; blue) overlay the diatom assemblage results from the raw sediment (grey; Chapter 4). 153

Figure 5.3 Investigation into the impact of selecting different diatom fractionation factors (ε) and $\delta^{30}Si(OH)_4$ values when calculating silicic acid utilisation. a) ε values weighted using the relative abundance of key species in each size fraction (*T. antarctica* RVS (black and purple lines) and *Chaetoceros* RVS (blue and green lines)) compared to the standard ε value of -1.1 (black line). The rate of silicic acid utilisation is then calculated for each size fraction and using each weighted ε values, an $\delta^{30}Si(OH)_4$ value of 1.23 (b) and 1.63 (c), where the black lines represents 100% silicic acid utilisation. 157

Figure 5.4 Box models representing the differing biogeochemical states at Site U1343 through the Pleistocene. a) Modern and Pre-MPT conditions are characterised by HNLC conditions which are iron limited, causing an inefficiency biological pump which leaks CO_2 to the atmosphere. b) During the 900 kyr event, increased shelf-derived iron supply from expanded sea ice increases the efficiency of the biological pump, with the green belt becoming nitrate-limited due to suppressed NPDW upwelling. c) After the MPT, deglacial periods exhibit resumed deep water upwelling, however enhanced productivity due to remnant iron in the photic zone stimulates the biological pump, causing a smaller net release of CO_2 to the atmosphere. 163

Figure 5.5 Relative abundance of other low abundance diatom species, in the >38 μm (orange) and 20-38 μm (blue) fractions.....170

Figure 5.6 The offset between $\delta^{30}Si_{large}$ and $\delta^{30}Si_{small}$ (a) are compared to the offset between $species_{large}$ and $species_{small}$ (b-m) to ensure that the difference in assemblage composition between each fraction is not the primary cause of the isotopic differences between the two size fractions.....171

Figure 5.7 Relative biovolumes of each species (%biovolume) in the >38 μm (orange) and 20-38 μm (blue) fractions. Given that some species are considerably larger than others, the contribution of each species to the $\delta^{30}Si_{diatom}$ can be estimated using mean biovolume measurements of each species/genus (LeBlanc et al., 2012).....172

Figure 6.1 New age model (a) and upwelling index (c) results from Site U1343 (red) between 0 - 1.2 Ma. Age model was defined through selecting new tie points (b) to the LR04 global benthic stack (Lisiecki & Raymo, 2005) (a; black) during periods of rapid isotope change. New upwelling index (c; red) results show tight correlation with global pCO_2 from ice core records of the last 0.8 Ma (Lüthi et al., 2008) (c; black, 0 – 0.8 Ma) and boron-isotope derived estimates from Chalk et al., 2017 (c;black ~1.1 – 1.2 Ma) and Hönisch et al., (2009) (c;blue squares). Blue bars represent glacial periods, labelled at the top of the

figure by the marine isotope stages (MIS) defined by the LR04 benthic stack. 176

Figure 6.2 Key findings from 0.6 - 1.2 Ma. The new age model for Site U1343 (A) informs upwelling index results (B) which show suppressed nutrient upwelling during the 900 kyr event, coincident with increased abundance of pack ice associated diatoms (C). Simultaneously reduced $\delta^{30}Si_{diatom}$ (D) and Si:N (Chapter 5) are interpreted as a shift to nitrate-limited conditions (supported by diatom resting spore formation), with suppressed NPDW upwelling but increased sea ice formation causes iron to be left unutilised in the green belt region. Blue bars represent glacial periods, labelled by the marine isotope stages (MIS) defined by the LR04 benthic stack (Lisiecki & Raymo, 2005), where the darker band around MIS 22–24 represents the 900 kyr event. 178

List of Tables

Table 1.1 Details of previously published data from Site U1343 and new data presented in this thesis. 32

Table 1.2 The mean and standard deviations of the offsets in $\delta^{18}O$ between various species and *Elphidium batialis* from Site U1343. Offsets were calculated by Kender et al. (2018) and Asahi et al. (2016) in samples where both species were measured, apart from species marked with * where offsets were calculated to the smoothing spline. 36

Table 1.3 Age model error at the midpoint depth between tie points, estimated using the mean sedimentation (sed.) rate and ± 1 standard deviation (σ).....37

Table 1.4 Details of the papers resulting from the work presented in this thesis. 38

Table 2.1 Benthic foraminiferal $\delta^{18}O$ offsets applied to species/genus, from *Elphidium batialis* (Kender et al., 2018). The total number of samples for each group is also noted. 69

Table 2.2 New age-depth tie points for Site U1343, building upon work of Asahi et al., (2016). Age model constructed by tuning to LR04 global benthic stack (Lisiecki & Raymo, 2005) (see Methods).....70

Table 3.1 New age-depth tie points for Site U1343, building on Worne et al. (2019). 99

Table 8.1 New benthic foraminiferal $\delta^{18}O$ data presented in Chapters 2 and 3. 217

Table 8.2 Benthic foraminiferal $\delta^{18}O$ from Asahi et al. (2016), Kender et al. (2018) and new data presented in this thesis, combined to form the new updated high resolution age model for Site U1343 between 0 and 1.2 Ma (Chapter 2-3). 229

Table 8.3 New bulk sedimentary $\delta^{15}N$ presented in this thesis (Chapter 2-3) 295

Table 8.4 Bulk sedimentary $\delta^{15}N$ data for Site U1343 from Kim et al. (2017), Kender et al. (2017) and newly presented data in this thesis (Chapter 2-3), which combine to create a high resolution record between 0 – 1.2 Ma. 303

Table 8.5 Upwelling index result calculated using bulk sedimentary $\delta^{15}N$ (Table 8.3) and opal MAR (Kim et al., 2014), presented in Chapter 2-3. 318

Table 8.6 Diatom assemblage results, classified here by ecological groupings (Stroynowski et al., 2017). For detailed results (e.g. species data) please contact the authors. 324

Table 8.7 $\delta^{30}Si_{diatom}$ data measured on a cleaned sample, sieved at >38 μm ($\delta^{30}Si_{large}$). The rate of silicic acid utilisation ($Utilisation_{large}$) and supply ($Supply_{large}$) are discussed and presented in Chapter 5 340

Table 8.8 $\delta^{30}Si_{diatom}$ data measured on a cleaned sample, sieved at 20-38 μm ($\delta^{30}Si_{small}$). The rate of silicic acid utilisation ($Utilisation_{small}$) and supply ($Supply_{small}$) are discussed and presented in Chapter 5.....342

Abstract

The transition of Earth's glacial-interglacial cycles from 41 kyr to 100 kyr periodicity during the middle Pleistocene (the Mid-Pleistocene Transition (MPT); ~1.2 – 0.6 Ma) marks one of the largest climate events of the Cenozoic, but the causes of this cooling transition remain unclear, as the emergence of the 100 kyr Milankovitch orbital 'eccentricity' in climate records occurred without a long term change in external orbital forcing. Hypotheses for this transition have so far remained largely untested due to a lack of detailed, high resolution climate proxy information from critical regions on the planet. Major hypotheses infer changes to North American Ice Sheet dynamics, an early expansion of subpolar sea ice, and decreasing atmospheric CO_2. Using sediment geochemistry and palaeontological proxies, this thesis assesses how the variability in sea ice, nutrient upwelling and primary productivity in the Northern Bering Sea impacted regional and global climate through the MPT, via their impact on North Pacific Intermediate Water expansion, regional carbon cycling and the subpolar biological pump.

Through calculation of a semi-quantitative nutrient upwelling index (based on nitrogen isotopes and opal accumulation), key findings of this thesis indicate that sea ice played a dominant role on orbital scale variability in nutrient upwelling at the Bering slope, following global changes in atmospheric pCO_2, continental ice sheet accumulation and sea level fluctuations. This is supported by fossil diatom assemblages which distinguish how sea ice dynamics evolved through the MPT, including high resolution variability in response to atmospheric teleconnections in the early Pleistocene. Principally, results support the notion that enhanced glacial formation of NPIW since the 900 kyr

event (0.9 Ma) acted to cause region-wide suppression of deep water CO_2 ventilation in the subarctic Pacific Ocean. Preliminary assessment of diatom silicon isotopes also suggests that sea ice delivery of iron, in combination with changes to nutrient cycling, may have additionally contributed to lowering glacial pCO_2 which promoted increased duration of post-MPT glacials. Overall, this thesis calls for increased attention to subarctic Pacific palaeoceanography in Quaternary climate studies.

Chapter 1: Introduction

1.1 Extended Abstract

During the Pleistocene epoch (~2.60 - 0.01 Ma), large continental ice sheets became established in the Northern Hemisphere and the global climate oscillated between cold (glacial) and warmer (interglacial) conditions (Lisiecki & Raymo, 2005). Glacial-interglacial pacing is primarily driven by variable inputs of solar radiation, regulated by the three Milankovitch cycles, eccentricity (100 kyr), obliquity (41 kyr) and precession (23 kyr), which characterise the Earth's orbit and determine the quantity and distribution of the energy the Earth receives (Hagelberg et al., 1994). Understanding how the internal climate system then responds to orbital forcing to determine the nature of each Milankovitch cycle has been a long term goal of the palaeoclimate community, particularly prior to the last glacial-interglacial transition which has been studied more extensively than the rest of the Quaternary period. Although the identification of age uncertainties is still considered a significant difficulty through initiatives such as the International Ocean Discovery Program (IODP) and International Continental Scientific Drilling Program (ICDP), there has

been an increasing body of palaeoclimate investigation which has contributed to developing our understanding of the global climate through the Quaternary (Crucifix, 2009).

A notable feature of the Quaternary is a global cooling trend between 1.2 - 0.6 Ma known as the Mid-Pleistocene Transition (MPT) in which there is a shift from obliquity-dominant 41 kyr Milankovitch cycles to lower frequency eccentricity-dominant 100 kyr glacial-interglacial cycles (Clark et al., 2006), centring on a stepwise increase in continental ice volume during the 900 kyr event (~0.9 Ma). However, with no significant long term change in the external orbital forcing, there must have been an internal forcing which caused this system response.

Hypotheses for the MPT which invoke high latitude oceanographic changes remain largely untested due to a lack of high resolution palaeoenvironmental data from globally important locations such as the Bering Sea. This marginal sea is located in the subarctic Pacific Ocean (Figure 1.1), where seasonal sea ice has formed since the onset of Northern Hemispheric Glaciation (NHG; ~2.7 Ma), with perennial or near-perennial sea ice during MPT glacials after the 900 kyr event (Teraishi et al., 2016; Stroynowski et al., 2017). The Bering slope, in the north of the Bering Sea, is a particularly important region for investigating high latitude ventilation of CO_2-rich deep water to the atmosphere, as nutrient rich North Pacific Deep Water (NPDW) upwells along the continental shelf (Tsunogai et al., 1979; Reed et al., 1993; Kender et al., 2018). Previous studies suggest that during glacials, low sea levels, closure of the Bering Strait and increased sea ice growth caused the formation and expansion of North Pacific Intermediate Water (NPIW) sourced

from the northern Bering Sea (Knudson & Ravelo, 2015b; Kender et al., 2018). Expansion of this water mass to greater depths and lower latitudes is suggested to have suppressed upwelling of NPDW at the Bering shelf, as well as propagating across the subarctic Pacific Ocean, causing region-wide reduction in vertical mixing and isolation of CO_2 in the deep ocean. Overall, Bering Sea MPT increases in sea ice and a reduction in upwelling of NPDW (increased NPIW formation) could have significantly altered atmospheric moisture availability, surface albedo, photic zone pCO_2 and the efficiency of the biological pump on a regional scale, hence altering net ocean-atmosphere CO_2 exchanges as well as the global climate. Therefore, understanding the impact of glacially expanded sea ice on ocean-atmosphere CO_2 exchange in this region, through both limiting deep water ventilation and altering sequestration via the biological pump, is essential in constraining regional and global MPT dynamics.

Through this thesis, a long term and robust high resolution age model is presented, which supports key proxies to constrain the palaeoceanographic condition in the Bering Sea over the MPT. This includes a benthic foraminiferal $\delta^{18}O$ record (0 – 1.2 Ma) (Chapter 2-3), bulk sedimentary $\delta^{15}N$ (0 – 1.2 Ma) (Chapter 2-3), a sea ice reconstruction using fossil diatom assemblages through the middle Pleistocene (0.6 – 1.2 Ma) (Chapter 4), and diatom-bound $\delta^{30}Si$ (0.6 – 1.2 Ma) (Chapter 5) from Site U1343 on the Bering shelf slope. In addition to a novel calculation of a semi-quantitative upwelling index (Chapter 2-3), an assessment of the variability of sea ice, nutrient upwelling and primary productivity in the northern Bering Sea, and their impact on NPIW expansion, regional carbon cycling and the biological pump is made.

Overall, results support sea ice as a dominant control on glacial-interglacial variability in NPDW upwelling at the Bering slope through glacial formation of NPIW (via brine rejection on the shelf) in the northern Bering Sea during the Pleistocene. Glacial sea ice and NPIW expansion, and hence nutrient upwelling strength (low upwelling during glacials), are shown to follow global changes in orbital cyclicity, in line with global atmospheric pCO_2, continental ice sheet accumulation and changes in sea level. Findings also support a secondary control on sea ice through atmospheric teleconnection with the tropical Pacific Ocean following intensification of the Walker circulation in the early Pleistocene, where intermediate/marginal sea ice conditions at the Bering slope exhibit increased sensitivity to the associated changes in the East Asian Winter Monsoon (EAWM) at suborbital periodicity. The result of increased glacial sea ice and NPIW expansion through the MPT is suppressed deep water ventilation of CO_2 across the subarctic Pacific region, particularly during/after the 900 kyr event when the Bering Strait was closed (sea level drop >50 m), coincident with significantly increased abundance of pack ice associated diatoms. Using geochemical proxies for silica and nitrate utilisation, evidence suggests that the Bering Sea became nitrate-limited during the 900 kyr event (supported by dominance of diatom resting spores), where sea-ice derived iron was likely left unutilised at the Bering slope and propagated to the lower subarctic Pacific Ocean in NPIW after closure of the Bering Strait. This would have caused an increase in the efficiency of the biological pump and enhanced CO_2 drawdown across the subarctic Pacific region. Combined, the influence of reduced subarctic Pacific deep water CO_2 ventilation (due to sea ice and NPIW expansion) and increased CO_2 sequestration following iron fertilisation from the

Bering Sea (due to reduced nutrient upwelling and increased sea ice formation) acted to lower global pCO_2 during the 900 kyr event, contributing to rapid ice sheet accumulation and longer glacial periods. Diatom assemblage evidence demonstrating sustained increases in sea ice after the 900 kyr event, further suggests that continued formation of NPIW during post-MPT glacials, when the Bering Strait was closed, was the ultimate control on deep water upwelling and hence reduced subarctic Pacific Ocean CO_2 outgassing, after the MPT.

1.2 Modern Oceanography

In order to interpret palaeoceanographic signals from sedimentological proxies, a broad understanding of the oceanographic regime is of critical importance. Here, a description of the modern oceanography and geography of the Bering Sea is made to provide context for the palaeoceanographic interpretations made throughout this thesis.

1.2.1 Oceanography of the North Pacific

Surface water circulation in the North Pacific Ocean follows a series of gyres, the largest of which is the North Pacific subtropical gyre. As water circulates westward along the equator and northward it forms the North Pacific Current (Figure 1.1) which is the northern boundary of the gyre (Trujillo & Thurman, 2011). In this current water cools as it flows eastward and approaches the North American coastline before bifurcating with most of the flow turning southward to form the cool-water California Current, the eastern boundary of the subtropical gyre which drives a region of upwelling as it re-joins equatorial flow, known as the Eastern Tropical North Pacific (ETNP). The remainder of the North Pacific Current turns northward into the Gulf of Alaska, forming a subarctic gyre known as the Alaska gyre (Sverdrup & Armbrust, 2009). The

northern boundary of this gyre forms the relatively warm Alaskan Stream, which feeds into the Bering Sea gyre through inflows between the Aleutian Island arc (Stabeno et al., 1999).

Fed by the outflow of the Bering Sea, a smaller subarctic gyre known as the Western Subarctic Gyre is bounded by the Aleutian Islands and Russian coastline and is connected to the broader Subarctic Gyre via the Oyashio current. The Subarctic Gyre is bounded to the south by the North Pacific Current in the winter and the Subarctic Current in the summer (Figure 1.1), where seasonal interaction between these currents facilitates gyre-gyre interaction (PICES, 2005).

North Pacific Intermediate Water (NPIW) is the densest and deepest ventilated water mass in the North Pacific Ocean, and is found between ~300-1000 m depth, representing a salinity minimum through most of the North Pacific Subtropical Gyre (Yasuda, 2004; Fujii et al., 2013). NPIW is thought to originate from Okhotsk Sea Mode Water (OSMW) from the Sea of Okhotsk, a

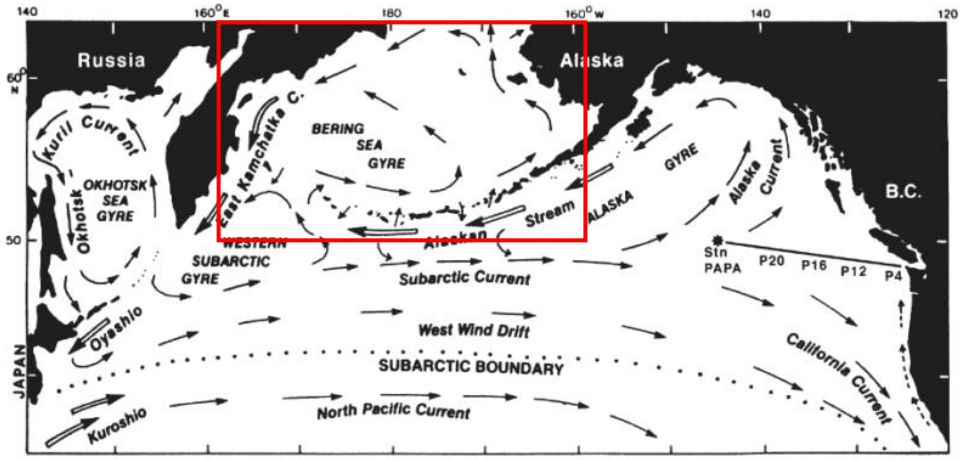


Figure 1.1 The circulation patterns of the subarctic North Pacific, showing the interaction of the Western Subarctic Gyre, the Subarctic Current, the North Pacific Current and the Alaskan Gyre (Takeda, 2011). Figure also displays the west wind drift which separates the two southern boundary currents of the Subarctic North Pacific. The red box highlights the Bering Sea, the region of this study which is depicted in detail in Figure 1.3.

marginal sea of the North Pacific which lies to the south of the Russian Kamchatka peninsula (Yasuda, 2004). OSMW is characteristically cold with low-salinity, as it is formed by waters which were excluded during sea ice formation on the Okhotsk shelf, in a process termed brine rejection. OSMW travels southward and feeds into the Oyashio Current (Figure 1.1), where it mixes with older, warmer and more saline NPIW to form new NPIW which flows into the North Pacific Subtropical Gyre (Yasuda, 2004; Fujii et al., 2013). Through this chain of flow new low salinity NPIW is formed and transported around the North Pacific Ocean.

Deep water circulation in the North Pacific Ocean occurs between ~2,000 - 4,000 m depth and contains nearly homogenous water characteristics (Figure 1.2) (Schlitzer, 2013). It originates from very old, fairly well mixed bottom waters from the southern hemisphere, where North Pacific Deep Water (NPDW) flows north before bifurcating in the western equatorial Pacific Ocean, with some flow continuing north, as the remainder flows eastward to the south of Hawaii. Silica concentrations of NPDW indicate there are two separate, anti-cyclonic deep water circulations in the North Pacific, one to the north and one to the south of the Hawaiian Islands (Talley, 2000). Southward flowing NPDW is separated from colder and fresher Antarctic Bottom Water (Knauss, 1962) by a "benthic front" in the southern and western North Pacific which can extend as far north as ~20°N (Chung, 1975).

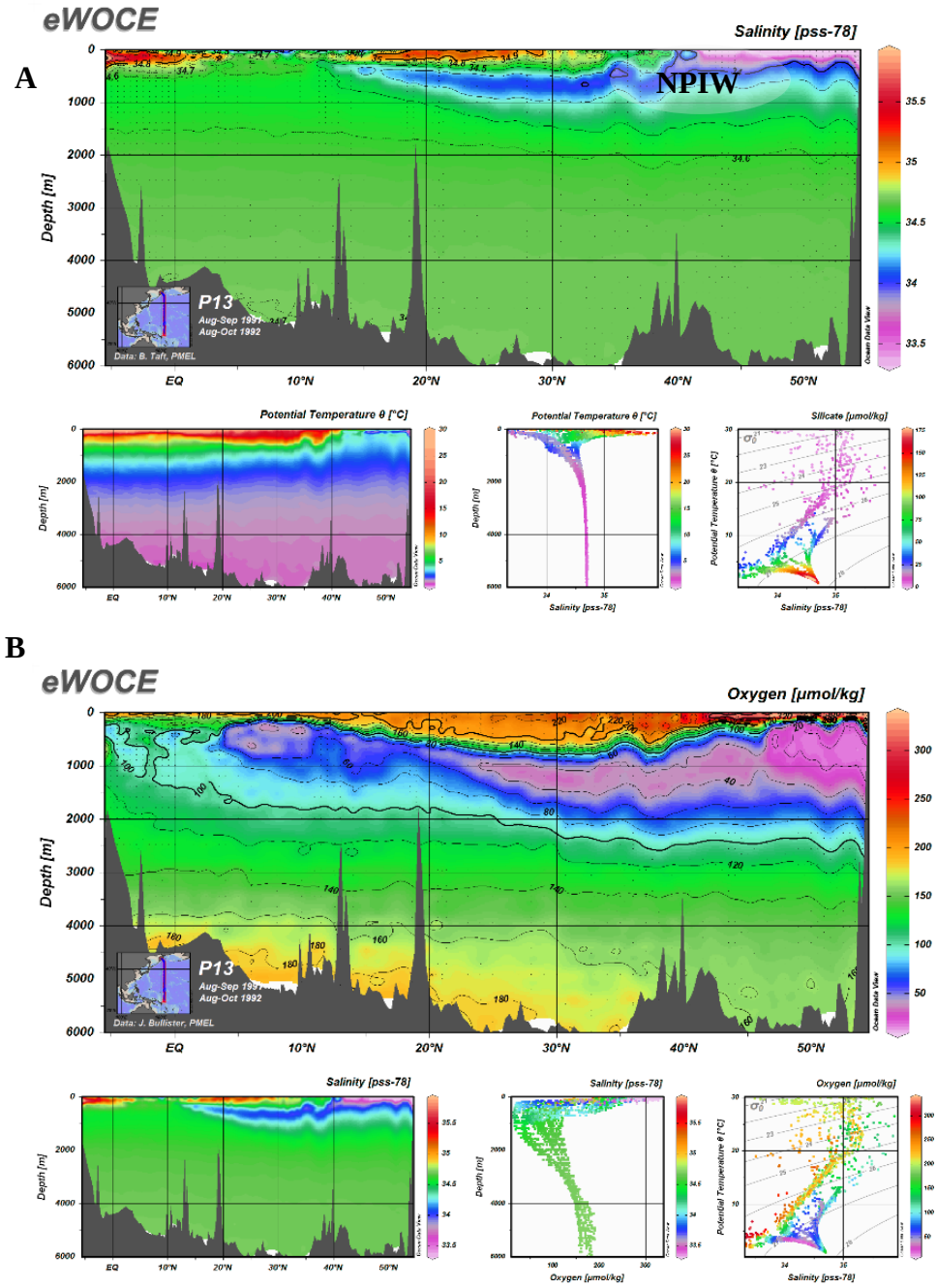


Figure 1.2 Cross sectional water properties across the North Pacific. [A] Salinity and temperature distribution while [B] shows the oxygen concentrations across transect P13, taken from the eWOCE Gallery (Schlitzer, 2013). Figures shows that surface waters freshen and cool with latitude, with NPIW from ~300-1000 m depth exhibiting low salinity and temperature concentrations in the subarctic Pacific Ocean. Higher oxygen concentrations at intermediate water depth are found 20-40°N, where newly formed oxygen-rich low salinity OSMW leaves the Okhotsk Sea to enter the mixed water region. Similarly, input of OSMW allows fresher water conditions to extend further south from the subarctic Pacific region at intermediate depth.

1.2.2 Geographical setting of the Bering Sea

The Bering Sea is situated in the subarctic Pacific Ocean, bounded to the west by Russia, the east by Alaska, and the south by the Aleutian Island arc (Figure 1.3). It is composed of a broad continental shelf with a maximum depth of ~200 m to the north and east and the deep Aleutian basin to the south extending to ~3, 500 m depth, separated by a steep continental slope (Stabeno et al., 1999). At the north of this marginal sea, the Bering Strait permits a small northward flow at ~50 m depth to the Arctic Ocean, providing an important link between

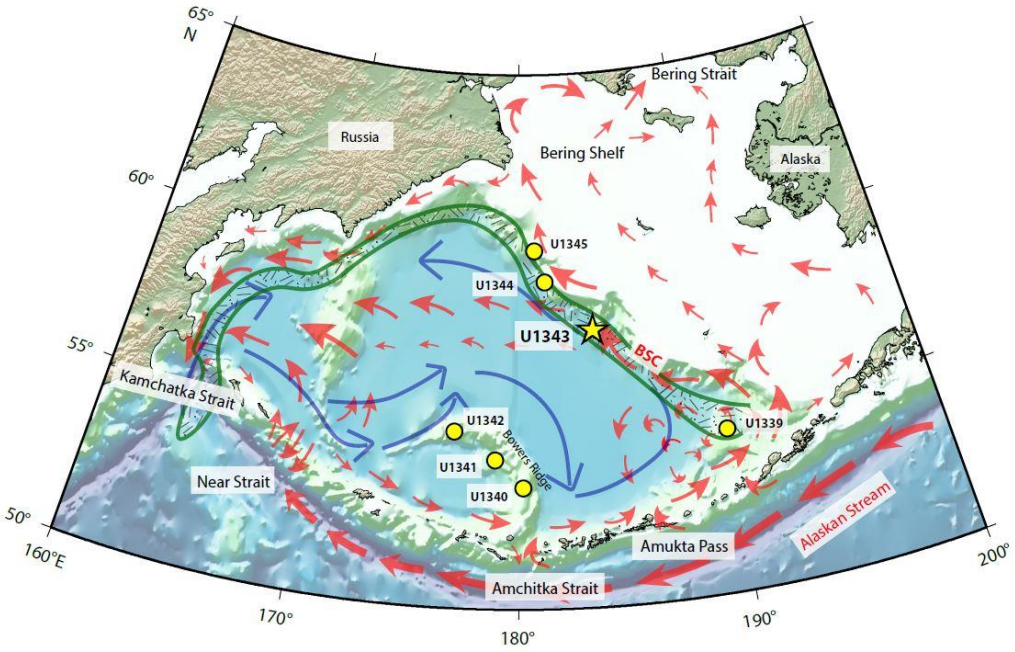


Figure 1.3 The geographical location and oceanography of the Bering Sea with the white area representing the continental shelf region to the north and the blue represents the Aleutian basin. Yellow dots indicate drill sites that were cored during IODP Expedition 323 in 2009, with Site U1343 (this study) marked by a yellow star. Surface water circulation is marked by red arrows, which flow in from the Alaskan Stream and through various straits and passes in the Aleutian island arc. Surface water circulates in an anti-clockwise gyre, where turbulence and eddies in the shelf adjacent Bering Slope Current (BSC) causes a high productivity region known as the green belt, represented by the green patterned shape (Springer et al., 1996). Deep water circulation is marked by blue arrows, entering from the lower subarctic Pacific Ocean through the deep western Kamchatka Strait.

the Pacific and Atlantic Oceans. Variable sea level through the Quaternary would have caused enhancement or closure of this gateway, impacting on both regional and global ocean circulation, nutrient, temperature and salinity distributions (Takahashi et al. 2011). In the southern and western Bering Sea, the Bowers Ridge (Figure 1.3), which extends north from the Aleutian Island Arc, and the Shirshov Ridge which extends south from Kamchatka, funnel water outflow through the Kamchatka Strait, the deepest pass in the Aleutian island arc (Figure 1.4).

1.2.3 Oceanographic setting of the Bering Sea

Surface water circulation in the Bering Sea basin is fed predominantly by Alaskan Stream water which is the northern boundary of the Subarctic Pacific gyre (Figure 1.3). This relatively warm flow enters the basin through various passes between the Aleutian Islands, most notably through the Amukta, Amchitka and Near Straits (Stabeno et al., 1999; Wehrmann et al., 2011). Once inside the basin, water flows eastward in the Aleutian North Slope Current (ANSC) which forms the southern boundary of the Bering Sea gyre. At 167°W, the ANSC turns north-westward and forms the wider shelf-adjacent Bering Slope Current (BSC) (Ladd, 2014). Stronger BSC currents are mostly associated with eddies and instabilities causing upwelling along the shelf break, in turn fueling the high productivity region adjacent to the shelf break, known as the "green belt" (see Section 1.2.5) (Springer et al., 1996; Stabeno et al., 1999). As the BSC continues west, it combines with northward flowing water from Near Strait around 175°E to form the Kamchatka current, the western boundary of the Bering Sea gyre. As this water flows south, the current strength and depth increases along the Russian coast, reaching depths of >1, 500 m at its outflow

through the Kamchatka Strait, where it re-joins the North Pacific Ocean (Stabeno et al., 1999).

Shelf-slope exchange of water is an important process which facilitates northward transport of water through the Bering Strait, linking the subarctic Pacific and the Arctic Ocean. An estimated transport of 0.5 x 10^6 m^3/s of slope waters flows onto the shelf, primarily from regions near the Unimak Plateau and the areas west of the Pribilof islands where the shelf break narrows, as well as episodic events driven by eddy-topography interactions and instabilities in the BSC (Stabeno et al., 1999). Currents on the shelf are of particular significance as they provide nutrients which allow high biological productivity in the Bering Strait and Arctic Ocean (Stabeno et al., 1999). Tidal Currents can also contribute to the physical oceanography of the shelf waters and the BSC, where the kinetic energy plays critical roles in the mechanisms such as shelf water mixing and cross-shelf flux of salt, nutrients, and heat, which maintain high productivity (Stabeno et al., 1999).

Deep ocean currents in the Bering Sea are comparatively understudied, although it is thought that the only significant flow below 1, 500 m depth occurs

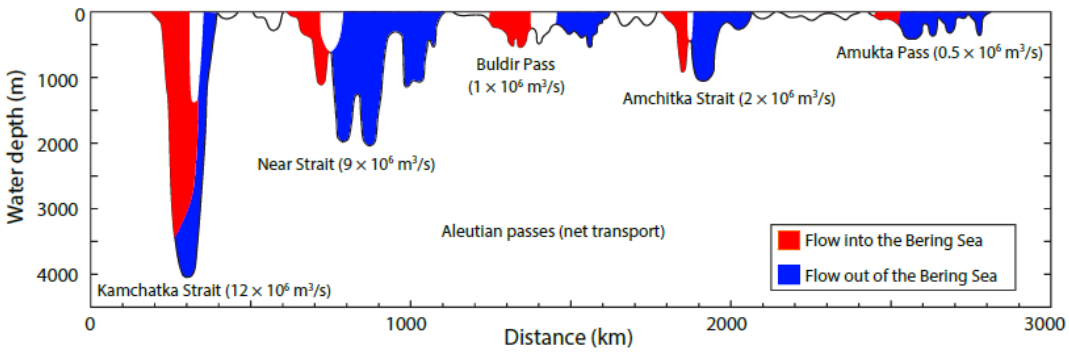


Figure 1.4 Cross sections of the Aleutian passes and volumes of transport through which Alaskan Stream water exchanges with the Bering basin (Stabeno et al., 1999; Takahashi et al., 2011

in the Kamchatka Strait, where inflow of NPDW occurs below 2, 000 m (Reed et al., 1993; Stabeno et al., 1999) (Figure 1.4). This inflow is characteristically more saline, but freshens as it mixes with deep Bering Sea basin water north of the Aleutian Islands. Following entry, this deep water flows northward and eastward and is characterised by warmer temperatures, lower salinity, lower density and lower rates of oxygenation in comparison with open waters in the adjacent North Pacific (Stabeno et al., 1999). There are also very high concentrations of silica (as well as other macronutrients) in deep basin waters (>225 μM l^{-1}) (Tsunogai et al., 1979; Reed et al., 1993), which increase with proximity to the continental slope (Stabeno et al., 1999). Silica measurements from the Kamchatka Strait indicate that there is some return flow of upper deep water above 3, 000m depth on the western side of the strait (Reed et al., 1993; Stabeno et al., 1999), although more data is needed to better understand the sources, flow and variability in deep ocean currents both spatially and temporally (Stabeno et al., 1999).

1.2.4 Sea Ice in the Bering Sea

Sea ice is an important component of the Bering Sea marine environment, showing high sensitivity to changes in winter insolation, wind velocities and the position of pressure systems, resulting in great variability in extent, timing and duration (Hunt & Stabeno, 2002; Kim et al., 2011). Sea ice formation is dependent on the position and interaction of the Siberian High and the Aleutian Low; while the location and intensity of the Aleutian Low are significant in driving the storminess of winter conditions (Rodionov et al., 2007), the Siberian High is more dominant in controlling the East Asian Winter Monsoon (EAWM) which impacts atmospheric moisture content (Gong & Ho, 2002). Advection of

cold air masses and greatest ice production occurs when the Aleutian Low is strong, which, when coupled with strong winds and intense turbulence on shallow open water, causes sea ice formation in polynyas on the leeward side of islands and coasts (Stabeno et al., 1999; Aiello & Ravelo, 2012; Riethdorf et al., 2016). A small portion (<~3%) is also formed in the Arctic Ocean and advected southward through the Bering Strait (Alexander & Niebauer, 1981). Prominent sea ice formation begins in November and is present for almost half the year, being blown southward by prevailing north-easterly winds to reach its maximum extent in March/April, where relatively warmer BSC waters cause melting near the shelf edge (Stabeno et al., 1999). Ice melt in the spring/summer plays an important role in productivity (see Section 1.2.5) through impacting water temperature, stratification and light limitation, as well as the prevalence of these characteristics for the remainder of the year (Hunt & Stabeno, 2002; Kim et al., 2011).

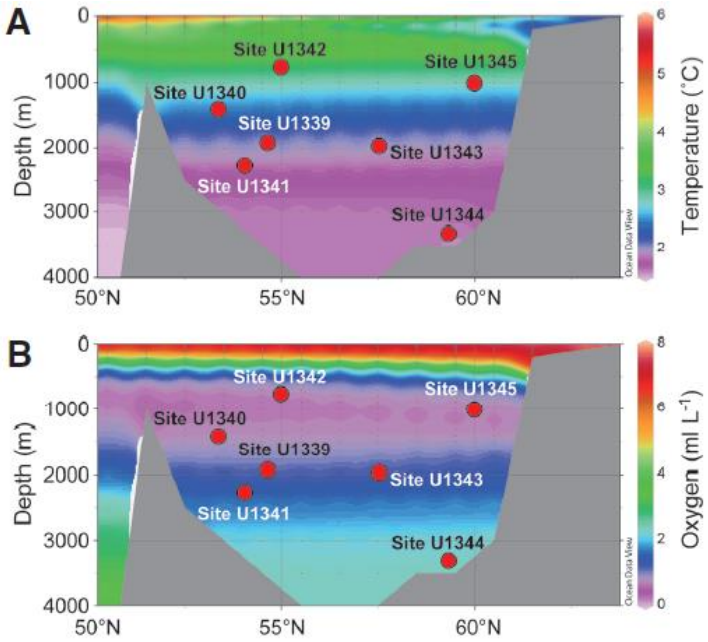


Figure 1.5 Vertical temperature profile (A) and oxygen concentrations (B) across the latitudes of the Bering Sea, with red dots showing the IODP Expedition 323 drill sites (Takahashi et al., 2011)

1.2.5 Productivity and Nutrient Cycling in the Bering Sea

Waters originating from the North Pacific Ocean generally have a high nutrient concentration and low oxygen concentrations (<2 ml L^{-1}) in intermediate and deep water masses (Takahashi et al. 2011) (Figure 1.2, Figure 1.5). Inflow of these waters into the Bering Sea causes the open basin to be defined as a high-nutrient low chlorophyll (HNLC) environment (Wehrmann et al., 2011), where primary production is limited by extremely low (<0.1 nmol L^{-1}) dissolved iron (Buck & Bruland, 2007).

Despite this, seasonally high green belt productivity is fuelled by the upwelling and vertical mixing of nitrate- and silica-rich NPDW, driven by eddies and instabilities in the shelf-adjacent BSC. Estimates of annual primary productivity in the green belt are >175 g C m^2 y^{-1} (Hansell et al., 1993; Springer et al., 1996; Sambrotto et al., 2008), dominated by diatoms. Sea ice melting in the spring/summer stimulates diatom growth due to the surge of melt-water which contains shelf-derived iron and increases water column stability, allowing diatoms to utilise a larger proportion of macronutrients in the photic zone for longer period of time (Aguilar-Islas et al., 2008). Production of coccolithophores and planktonic foraminifera also increase in late summer/early autumn (Takahashi et al., 2002; Riethdorf et al., 2016), although this growth is limited due to nutrient drawdown in the spring/summer-autumn diatom bloom (Buck & Bruland, 2007). The overall success of productivity in this region is therefore highly influenced by the strength of NPDW upwelling which depends on the variability in the flow and turbulence of the BSC (Kim et al., 2011), although tidal mixing and lateral supply of shelf waters from the north are also an important source of iron to the green belt (Buck & Bruland, 2007; Takahashi

et al., 2011a; Wehrmann et al., 2011). Remaining nutrients left unutilised after upwelling at the shelf edge are transported via northward flowing currents to form an important nutrient supply for the Arctic Ocean (Takahashi et al. 2011). Photic zone nutrient concentrations are then replenished from upwelling NPDW during the winter months when productivity is restricted by sea ice and light limitation (Stabeno et al., 2002).

1.3 Quaternary palaeoceanography and the Bering Sea

Given that there is no significant deep water formation in the modern subarctic Pacific region, the high latitude North Atlantic and Southern Oceans have often been considered the most significant regions for driving glacial-interglacial climate change (Sigman et al., 2010; Jaccard & Galbraith, 2018; Farmer et al., 2019). Studies from the subarctic Pacific Ocean have also been mostly restricted to research of the last glacial cycle, based on cores taken from ODP Leg 145 in 1993, particularly from ODP Site 882 (50722°N, 167736°E, water depth 3244 m) (Maslin et al., 1995), and from the nearby marginal Sea of Okhotsk (Figure 1.6). Even recent studies which demonstrate that the subarctic Pacific region

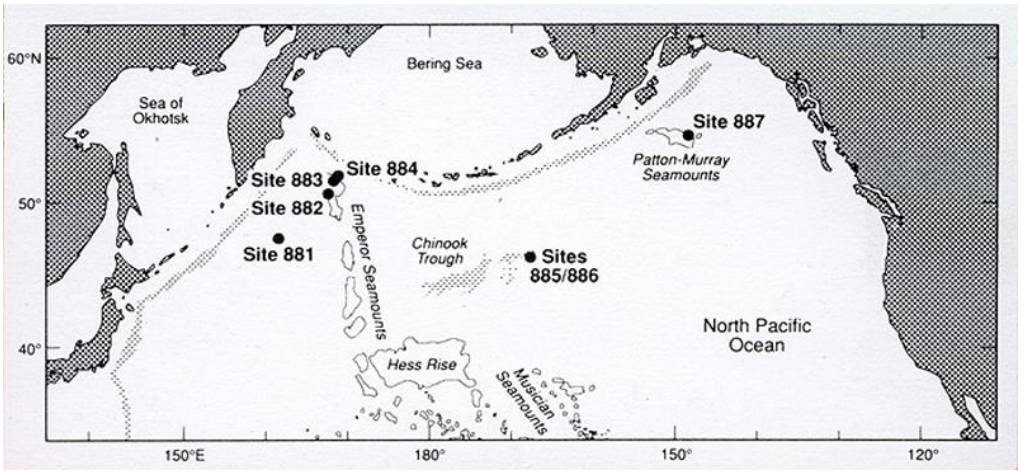


Figure 1.6 Map showing the drill site locations for ODP Leg 145, including Site 882 (Maslin et al. 1995).

played an important role in deglacial deep ocean CO_2 ventilation, are limited to the last glacial cycle (Rae et al., 2014; Gray et al., 2018). However, materials collected during IODP Expedition 323 to the Bering Sea in 2009 have facilitated high resolution and longer term investigation into Plio-Pleistocene dynamics of the subarctic Pacific region (Takahashi et al., 2011a). An additional IODP Expedition (341) to the Gulf of Alaska was also made in 2013, from which similar studies of Pleistocene climate in the eastern subarctic Pacific region are emerging (Jaeger et al., 2013). Here, a brief review of the current understanding of Bering Sea palaeoceanography is made, particularly following IODP Expedition 323 and with respect to Plio-Pleistocene and MPT dynamics.

1.3.1 The Pliocene-Pleistocene Transition and the early Pleistocene (~2.7 – 1.2 Ma)

The onset of Northern Hemispheric Glaciation (NHG), which began as early as 3.6 - 2.7 Ma (Mudelsee & Raymo, 2005), saw a decrease in sedimentation rate and a "crash" in opal mass accumulation rate (MAR) at ~2.7 Ma at ODP Site 882, suggesting that there was a significant decrease in siliceous productivity in

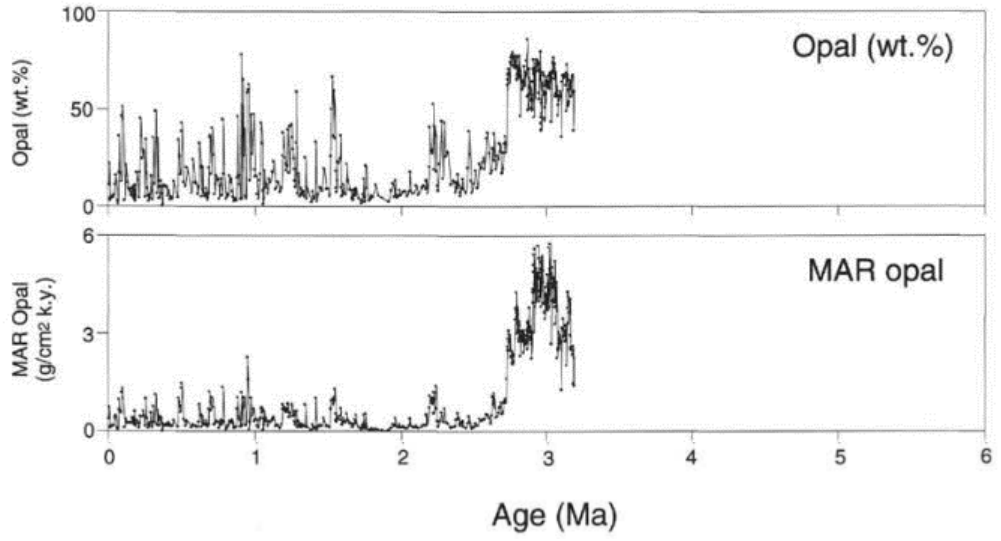


Figure 1.7 Opal wt% and MAR record from ODP Site 882, showing the "opal crash" at ~2.7 Ma, following the onset of northern hemispheric glaciation (Haug et al., 1995).

the subarctic Pacific Ocean (Figure 1.7) (Maslin et al., 1995, 1996; Haug et al., 1999, 2005; Swann, 2010). It is thought that gradual cooling through this period and formation of a permanent halocline caused upper ocean stratification and reduced vertical mixing, which isolated existing nutrients in the euphotic zone without resupply, causing lower productivity (Maslin et al., 1995; Haug et al., 2005; Iwasaki et al., 2016).

Given that sea ice formation on the Okhotsk shelf is a dominant mechanism in supplying iron to intermediate waters which propagate southward into the subarctic Pacific Ocean (Nishioka et al., 2007; Takeda, 2011), similarly strong stratification in this lower latitude marginal sea after onset of NHG also likely reduced iron supply to the already HNLC environment of the subarctic Pacific region (Iwasaki et al., 2016). Although additional iron input through aeolian dust deposition as a result of colder more arid conditions is observed at ODP Site 882, this is assumed to have been too insignificant to relieve productivity limitation following NHG (Bailey et al., 2011; Iwasaki et al., 2016). Overall, this period of relatively stable but colder climate remained until ~1.2 Ma (Chen et al., 2014b), during which time climate varied as a result of obliquity-dominated 41 kyr glacial-interglacial cycles.

In the Bering Sea, the presence of tropical/sub-tropical radiolarian species prior to 2.7 Ma indicates that waters were relatively warm as a result of unimpeded water mass exchange between the subarctic and tropical Pacific Ocean (Chen et al., 2014b). After 2.7 Ma, the onset of NHG marked the expansion of sea ice into the open Bering Sea (Aiello & Ravelo, 2012; Stroynowski et al., 2015), with gradual cooling and water column stratification (Tanaka & Takahashi, 2005; Caissie et al., 2010; Aiello & Ravelo, 2012;

Stroynowski et al., 2015), similar to at Site 882 . However, unlike the observed opal crash in the lower subarctic Pacific Ocean at 2.7 Ma, increased biogenic opal MAR in the southern Bering Sea instead suggests there was higher productivity in this region (Iwasaki et al., 2016; Kim et al., 2016), driven either by an increase in iron delivery to the region (Bailey et al., 2011; Iwasaki et al., 2016) or a leakage of nutrients from the North Pacific into the Bering Sea via the Kamchatka Strait (März et al., 2013; Swann et al., 2016). Further study from more northerly locations proximal to regions of upwelling and sea ice-derived iron supply near the Bering shelf, are needed to constrain these hypotheses on a regional scale during the Pleistocene.

1.3.2 Mid-Pleistocene Transition (MPT) (~1.2-0.6 Ma)

The Mid-Pleistocene Transition (MPT) represents a cooling of global climate, as a result of the changing dominance of Milankovitch orbital cycles on climate variability from obliquity-dominated 41 kyr, to eccentricity-dominated 100 kyr glacial-interglacial cycles (Lisiecki & Raymo, 2005) (Figure 1.8). However, a lack of significant change in external orbital forcing suggests that there must have been an additional internal forcing to cause the observed response in the Earth's climate system (Clark et al., 2006; McClymont et al., 2013).

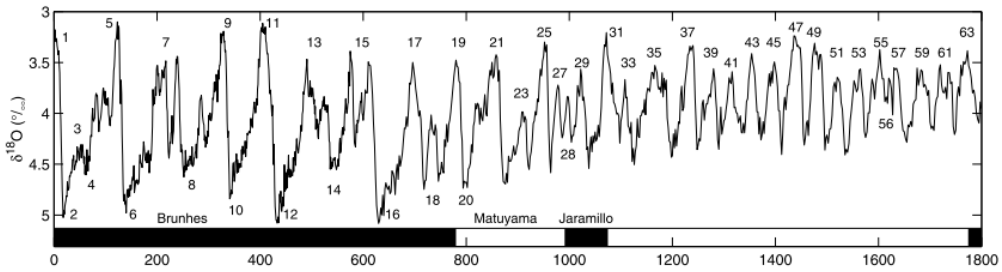


Figure 1.8 LRO4 Global stack of benthic foraminiferal $\delta^{18}O$ records, which shows the MPT shift from 40 kyr to 100 kyr glacial-interglacial cycles from ~1.2-0.8 Ma (Lisiecki & Raymo, 2005)

Onset of the MPT saw many global climate changes (McClymont et al., 2013 and references therein) including a decrease in sea surface and deep ocean temperatures (Marlow et al., 2000; McClymont et al., 2008; Sosdian & Rosenthal, 2009; Rodríguez-Sanz et al., 2012) as well as an changes to African and Asian aridity and monsoon intensity (Heslop et al., 2002; Sun et al., 2006). Notably, a long term increase in average ice volume was observed in both hemispheres, centring on a step change at ~0.9 Ma, termed the "900 kyr event", after which 100 kyr orbital cycles stabilised and became prominent in the proxy record (Lisiecki & Raymo, 2005), resulting in less frequent but more extreme glacials with colder sea surface temperatures and larger ice volume (Lisiecki & Raymo, 2005; Clark et al., 2006; Elderfield et al., 2012).

With regards to the Bering Sea, variable sea level through the Quaternary caused perturbations to the oceanographic regime through enhancement and/or closure of the Bering Strait gateway, as well as impacting surface water inflow into the Bering basin through the Aleutian island passes (Figure 1.3), impacting both regional and global ocean circulation, nutrient, temperature and salinity distributions (Takahashi et al., 2011a; Stroynowski et al., 2017; Kender et al., 2018). Simultaneous with global cooling, changes to poleward heat and moisture delivery following an alteration to the East Asian Winter Monsoon (EAWM) in the early Pleistocene (McClymont et al., 2013; Stroynowski et al., 2017) is suggested to have caused lower surface water temperatures and increased atmospheric moisture which promoted glacial sea ice formation and shoaled the eastern Aleutian passes, reducing Alaskan Stream inflow (Teraishi et al., 2016; Stroynowski et al., 2017). The resultant reduction in Bering Sea gyre energy from less inflow also acted to weaken the BSC,

causing reduced upwelling of nutrient rich NPDW leading to low glacial diatom productivity in the green belt, through the MPT (Kim et al., 2014; Kender et al., 2018).

1.3.3 What caused the MPT?

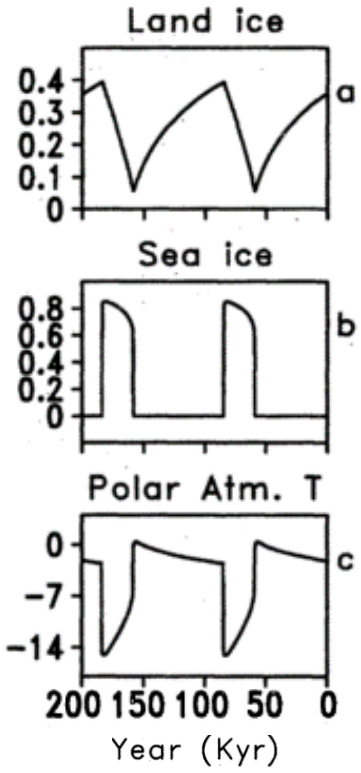


Figure 1.9 The sea ice switch mechanism as depicted by Gildor and Tziperman (2001), which demonstrates the land versus sea ice hysteresis model where the sea ice maxima occurs after deglaciation of land ice begins.

The cause of the MPT is a highly debated topic, with several opposing hypotheses which primarily invoke changes in ice sheet and/or ocean-atmosphere dynamics, which influence the distribution and balance of the Earth's energy budget (Chalk et al., 2017). The MPT can be viewed as a two-step process: firstly, a gradual cooling from ~1.2 Ma, followed by a second step-change at the 900 kyr event, after which 100 kyr glacial cycles became prominent in the proxy record (Lisiecki & Raymo, 2005; McClymont & Rosell-Melé, 2005; Clark et al., 2006). Proposed mechanisms for the initial cooling from ~1.2 Ma include a geological mechanism termed the regolith hypothesis, which describes how the continual erosion of Precambrian crystalline shield bedrock during early Pleistocene glacials facilitated increased ice sheet accumulation and caused a change in ice sheet re—sponse to orbital forcing, causing the MPT (Clark & Pollard, 1998); larger post-MPT ice sheets are proposed to have resulted from reduced underlying sediment, where ice sheets

which form on harder bedrock are thicker and follow 100 kyr cyclicity with abrupt terminations (Clark & Pollard, 1998; Clark et al., 2006). Alternatively, poleward heat transport and thermohaline circulation have also been considered important drivers of MPT climate pacing (Imbrie et al., 1993). For example long term tropical deep-ocean cooling and a resultant intensification of the Walker circulation is proposed to have increased moisture delivery and reduced heat transport to the northern high latitudes, forming an important precursor for ice sheet development during the MPT (McClymont & Rosell-Melé, 2005). In line with this, the "sea ice switch" (SIS) hypothesis suggests the relationship between oceanic sea ice expansion and continental ice sheet dynamics in the Northern Hemisphere was also a key driver of the MPT (Gildor & Tziperman, 2001; Tziperman & Gildor, 2003). Firstly, as a result of deep-ocean cooling and changes in ocean vertical mixing, high latitude sea ice and ice sheet volumes increased during the MPT. Secondly, as a result of this sea ice expansion, reduced moisture supply over the North American continent would have slowed the growth of the NAIS forming a land versus sea ice hysteresis model. In this case, ice sheet decline during glacial terminations would have occurred before the maximum sea ice extent (Figure 1.9), acting to increase the duration of the glacial. The resulting reduction in ice albedo as ice sheets declined would have caused atmospheric warming and a subsequent rapid retreat of sea ice. Support for this mechanism is found in Bering Sea records, where a significant southward expansion of sea ice occurred from 1.2 Ma (Ikenoue et al., 2015; Stroynowski et al., 2015, 2017; Teraishi et al., 2016). Furthermore, lipid biomarker evidence confirms that sea ice volumes increased significantly through the MPT and supports the notion that sea ice maxima occurred during

the late-glacial/deglacial in the Bering Sea during the MPT (Detlef et al., 2018), consistent with the sea ice switch model (Gildor & Tziperman, 2001). However, these conclusions are tentative as the age models and datasets do not have sufficient resolution to determine the exact nature and timing of sea ice expansion on millennial timescales, and whether sea ice maxima occurred during peak glacial conditions or the early deglacial (Detlef et al., 2018).

Other proposals for the MPT invoke a threshold response to lowered atmospheric pCO_2, which facilitated the development of large continental ice sheets and caused an altered climatic response to insolation forcing (Berger et al., 1999; Hönisch et al., 2009; Chalk et al., 2017). Potential mechanisms for reduced glacial CO_2 during the MPT can be categorised as either those which caused increased CO_2 sequestration, or those which reduced CO_2 ventilation from the ocean through isolation of deep waters. Enhanced glacial carbon sequestration is proposed to have occurred as a result of the increased efficiency of the biological pump in the Southern Ocean, causing a larger proportion of CO_2 to be sequestered by primary producers in surface waters and exported to the deep ocean during glacials, following dust fertilisation which results from larger ice sheets (Chalk et al., 2017), however evidence for this has not been found to be globally synchronous (Diester-Haass et al., 2018).

Alternatively, several other proposals suggest increased glacial sea ice was an important mechanism for suppressing CO_2 ventilation from deep waters in high latitudes oceans during the MPT, either through enhancing water column stratification (Lear et al., 2016) or through the expansion of glacial North Pacific Intermediate Water (NPIW) (Kender et al., 2018). In the latter, a boundary condition change is also invoked, where closure of the Bering Strait is proposed

to have occurred for the first time during the 900 kyr event, causing more significant NPIW formation (to at least ~ 2, 000 m water depth) which suppressed deep water CO_2 ventilation across the subarctic Pacific Ocean and facilitated rapid ice accumulation and longer glacial periods (Kender et al., 2018). This is consistent with some of the first MPT studies which interpreted the increase in benthic foraminiferal $\delta^{18}O$ during the 900 kyr event as a rapid accumulation of Northern Hemispheric ice volume (Mudelsee & Schulz, 1997).

An abrupt increase in Antarctic ice volume during the 900 kyr event has also been suggested to have triggered a change in ocean-atmospheric processes, leading to longer glacial periods and the subsequent dominance of 100 kyr glacial cycles (DeConto et al., 2007; Elderfield et al., 2012). This is supported by evidence for a simultaneous "exceptional weakening" of the thermohaline circulation, as North Atlantic ice sheets reached a critical size/stability threshold during the 900 kyr event (Pena & Goldstein, 2014); weakened thermohaline circulation is proposed to have increased atmospheric CO_2 sequestration and caused further cooling through isolating Antarctic deep waters, which in turn, lowered atmospheric temperatures and facilitated Antarctic ice sheet expansion.

1.4 Research Questions

Although it is beyond the scope of this thesis to assess all MPT hypotheses, multiproxy investigations in the Bering Sea are critical for assessing some of the key mechanisms which modulate high latitude ocean-atmosphere dynamics over this interval. In particular, Bering Sea sea ice plays a key role on regional air-sea CO_2 exchange through actively restricting CO_2 outgassing (Loose et al., 2011) and causing NPIW expansion which modulates glacial NPDW upwelling in the subarctic Pacific Ocean (Kender et al., 2018). Sea ice also determines

biological CO_2 pump efficiency through controlling green belt primary productivity (Kim et al., 2014; Detlef et al., 2018). Furthermore, Northern hemispheric sea ice (including that of the Bering Sea) potentially modulated land ice dynamics through its impact on surface albedo and regional moisture availability (Gildor & Tziperman, 2001; Tziperman & Gildor, 2003). Therefore, understanding the nature and timing of increased MPT sea ice in the Bering Sea and its impact on regional oceanography is essential in constraining global dynamics through the Pleistocene. This PhD will therefore aim to address the following three research questions.

1.4.1 Did sea ice-driven NPIW expansion cause suppressed glacial upwelling of CO_2 rich deep waters, contributing to global cooling in the Pleistocene and the MPT?

It is known that NPIW expanded to greater depths (~1,750 - 2,100 m) and lower latitudes during the last glacial (Behl & Kennett, 1996; Rella et al., 2012; Max et al., 2014). The cause of this expansion is, however, still debated. Some proxy data from the Sea of Okhotsk suggest this lower latitude marginal sea remained the primary source of NPIW formation during the last glacial and deglacial period (Max et al., 2014), while other studies suggest that expansion of NPIW can be explained by a shift in source region from the Sea of Okhotsk to the Bering Sea, with NPIW forming in the Bering Sea during glacial periods when the Bering Strait closed due to low sea level (Ohkushi et al., 2003b; Itaki et al., 2009; Horikawa et al., 2010; Rella et al., 2012; Ikenoue et al., 2016).

Recent studies using materials from IODP Expedition 323 at Site U1342 (818m water depth) (Figure 1.3) reconstructed the ventilation history of the Bering Sea over the last 1.2 Ma. Knudson and Ravelo (2015a) proposed that

NPIW formation had originated in the Bering Sea during glacials throughout the Pleistocene; as in the modern Sea of Okhotsk, the proposed mechanism for this draws on brine rejection during sea ice formation, where dense waters excluded during sea ice formation are formed on the northern continental shelf, flow southward and sink at the shelf edge to form NPIW. Further investigation at the more northerly Site U1343 (1, 950 m water depth) at the Bering slope, confirmed that formation of glacial NPIW occurred in the northern Bering Sea during the 900 kyr event to at least ~2, 000 m, following what is thought to be the first closure of the Bering Strait after sea level decline >50 m (Kender et al., 2018) (see Section 8.1). This glacial NPIW, which formed in the Bering Sea, is suggested to have propagated across the subarctic North Pacific, causing region-wide reduction in vertical mixing/NPDW upwelling and isolation of CO_2 in the deep ocean, thereby contributing to longer glacial periods (Kender et al., 2018).

However, this study and it's interpretation covers only a short time interval through the 900 kyr event and draws on low resolution $\delta^{15}N_{bulk}$ data from 0 – 0.6 Ma to assess this mechanism through the late Pleistocene (Kim et al., 2017). A higher resolution investigation of post-MPT ventilation and upwelling at similarly deep locations from 0 – 1.2 Ma is required to assess the validity of this hypothesis as a mechanism for suppressed nutrient upwelling throughout the Pleistocene and causing longer glacial periods after the MPT. Supported by the construction of a high resolution benthic foraminiferal $\delta^{18}O$ age model, the existing $\delta^{15}N_{bulk}$ record at Site U1343 is extended to create a high resolution record covering cover the last 0.85 Ma. Through combining this new nitrate utilisation record ($\delta^{15}N_{bulk}$) with primary productivity data (opal mass accumulation record (MAR) (Kim et al., 2014), **Chapter 2** presents a new semi-

quantitative upwelling index, which characterises glacial-interglacial variability in NPDW nutrient upwelling at the green belt over the last 0.85 Ma. Through comparison with a $\delta^{18}O$-derived assessment of NPIW expansion, the upwelling index record is used to assess the continued influence of NPIW expansion to 2,000 m through the mid-late Pleistocene. Correlation with the atmospheric pCO_2 record and an upwelling index record calculated at ODP Site 882, aids an appraisal of the role of NPIW expansion on regional ocean-atmosphere CO_2 exchange. Additionally, extension of the $\delta^{15}N_{bulk}$ record back to 1.2 Ma in **Chapter 3** (culminating in a high resolution nutrient utilisation record which covers the entire Pleistocene epoch), facilitates an assessment of long term variability in nutrient upwelling (and the control of sea ice and NPIW) at the green belt, to evaluate whether the 900 kyr event represents a tipping point for NPIW formation and hence its significance as a driver of the MPT.

1.4.2 What role did sea ice dynamics play in controlling nutrient upwelling at Milankovitch and suborbital periodicities, as well as on increasing the duration of glacials via the sea ice switch (SIS) hypothesis?

Although the majority of studies on the MPT are focussed on the role of high latitude oceanographic changes, McClymont & Rosell-Melé (2005) suggest that deep-ocean cooling in the eastern equatorial Pacific during the early Pleistocene caused an intensification of East-West sea surface temperature (SST) gradient and strengthened the Walker circulation between ~1.2 and 0.9 Ma, leading to more La Niña-like conditions which exhibit increased moisture delivery and reduced heat transport to the Northern high latitudes. These atmospheric teleconnections are suggested to have propagated to the Bering Sea via changes in the EAWM and zonal pressure gradients which determine the strength and

location of key atmospheric systems, notably the Aleutian Low (Stroynowski et al., 2017). Today, La Niña conditions in the Bering Sea are characterised by cooling and increased storminess as a result of a more westerly Aleutian Low, which promote sea ice formation in the region (McClymont & Rosell-Melé, 2005; Rodionov et al., 2005, 2007; Stroynowski et al., 2017). In combination with an increased moisture delivery to higher latitudes following a reduction in the strength of the EAWM, intensified Walker circulation may have been key to increased sea ice formation in the build up to the 900 kyr event, supported by a correlation between the low resolution record of pack ice diatom abundance in the northern Bering Sea and proxy records for the EAWM (Li & Wang, 2013; Stroynowski et al., 2017). Increased sea ice formation will in turn have impacted both productivity and ocean-atmosphere CO_2 exchange through controlling the intensity of spring and summer diatom blooms, as well as enhancing NPIW formation via brine rejection in the northern Bering Sea (Springer et al., 1996; Knudson & Ravelo, 2015b)

Aligning with this mechanism, the SIS hypothesis describes how expansion of subpolar sea ice during glacials during the MPT could have caused a subsequent reduction in moisture supply over the North American continent, modulating the decline of the NAIS (Gildor & Tziperman, 2001) (see Figure 1.9). Longer glacial periods then result from a reduction in ice albedo which would have caused atmospheric warming, followed by a subsequent retreat of sea ice later during the deglaciation phase. Reduced extent of sea ice during interglacials enhances regional moisture supply allowing regrowth of the NAIS once again. This mechanism is suggested to explain the 'sawtooth' shape of the glacial-interglacial cycles following the MPT as larger ice volumes and

variation in surface albedo would lead to more rapid deglaciation (Tziperman & Gildor, 2003).

This thesis aims to use the new high-resolution age model at Site U1343 presented in **Chapter 2 – 3**, to conduct spectral analysis of the long term upwelling index from 0 – 1.2 Ma. Given that NPDW upwelling is thought to be primarily modulated by sea ice variability (Kender et al., 2018), wavelet transform and spectral analysis results presented in **Chapter 3** are interpreted to assess the variable controls of sea ice and NPIW formation on nutrient upwelling through the Pleistocene. An investigation into the role of intensified Walker circulation as a mechanism for sea ice formation during the early Pleistocene is also made, where expanding sea ice during this period would exhibit variable sensitivity to suborbital forcing as a result of changes in atmospheric pressure systems, moisture delivery and monsoon intensity (Sun et al., 2019).

Following this, **Chapter 4** builds on previous very low resolution sea ice reconstructions at Site U1343 (Teraishi et al., 2016; Detlef et al., 2018), through a new fossil diatom assemblage record. Following the methodology of Stroynowski et al. (2017), which groups key taxa by their ecological niches, for example those associated with pack ice, marginal sea ice, benthic/neritic and open ocean conditions, the extent and seasonality of MPT sea ice variability is evaluated on glacial-interglacial timescales between 0.6 and 1.2 Ma (Stroynowski et al., 2017). Through comparison with the upwelling index record presented in **Chapter 3**, this new sea ice reconstruction characterises the nature, timing and seasonality of sea ice expansion during the early and middle Pleistocene, aiding evaluation of the hypotheses for early Pleistocene

intensification for the Walker circulation and NPIW expansion/Bering Strait closure as a tipping point during the 900 kyr event (McClymont & Rosell-Melé, 2005; Kender et al., 2018). Furthermore, through comparison with lipid biomarker results from Site U1343 (Detlef et al., 2018), the validity of the SIS mechanism as a key driver of glacial-interglacial structure during and after the MPT is assessed.

1.4.3 How did the Bering Sea green belt biological pump respond to MPT changes in sea ice and nutrient upwelling strength, and what impact did this have on regional ocean-atmosphere CO_2 exchange?

Bering Slope nutrient supply is maintained by turbulent eddies in the BSC which cause upwelling of higher nutrient NPDW. Despite high nutrient availability, modern day green belt nutrient utilisation is iron limited (Takeda, 2011), leading to the region acting as a net source of CO_2 to the atmosphere due to the inefficient biological pump, where nutrients are left unutilised in the photic zone. Previous studies in the green belt suggest that post-MPT productivity was markedly lower in glacials, while macronutrient utilisation was higher (Kender et al., 2018). Although this has been previously interpreted to suggest that the supply of nutrients from upwelling was reduced, little consideration has been given to secondary nutrient sources, including the potential increase in iron delivery to the green belt following sea ice expansion (Aguilar-Islas et al., 2008). Furthermore, modern day nutrients which are not utilised at the green belt are transported northward through the Bering Strait and form an important source for Arctic Ocean productivity (Clement et al., 2005). However, during glacial periods when the Bering Strait was closed, this northward flow would have been restricted/prevented. If NPDW upwelling was

suppressed as suggested by geochemical evidence, the fate of shelf-derived nutrients and the impact of altered nutrient cycling during the MPT on glacial-interglacial efficiency of the biological pump is unknown.

Through measuring the $\delta^{30}Si$ of diatoms as a proxy for silicic acid utilisation and supply, in combination with $\delta^{15}N_{bulk}$ (**Chapter 3**) as a proxy for nitrate utilisation, **Chapter 5** aims to assess the impact of suppressed deep water upwelling and sea ice expansion during the MPT on macronutrient and iron availability. Through evaluating changes to nutrient cycling, in combination with the diatom assemblage based sea ice reconstruction (**Chapter 4 - 5**) and previously published opal MAR records (Kim et al., 2014), an evaluation of the efficiency of the biological pump during the MPT is made, with a focus on what role this played in regional ocean-atmosphere CO_2 dynamics, particularly during the 900 kyr event step-change.

1.5 Materials and Methods

This thesis presents a number of new geochemical and palaeontological datasets which are used to build upon the existing body of work completed at Site U1343 to investigate palaeoceanographic change through the Pleistocene. Here a description of the site location and core stratigraphy is given, as well as preliminary work undertaken to confirm the validity of the standard methods used to create the age model, which underpins the findings of this research. Notable studies at Site U1343 which have informed/been utilised during the methodological development for this thesis are detailed in Table 1.1.

Table 1.1 Details of previously published data from Site U1343 and new data presented in this thesis.

Component	Previously published	Newly presented in this thesis
Benthic foraminiferal oxygen isotopes ($\delta^{18}O$) (Table 8.1, Table 8.2)	From 0 – 0.85: 489 data points (Asahi et al., 2016). From 0.85 – 1.02 Ma: 823 data points (Kender et al., 2018); Appendix 1. From 1.02 – 1.2 Ma: 134 data points (Asahi et al., 2016).	From 0 – 0.85 Ma: 222 new data points; Chapter 2. From 1.02 – 1.2 Ma: 52 new data points; Chapter 3.
Age model (Table 2.2, **Table 3.1**)	Previous age depth tie points for Site U1343 age model not used here (Asahi et al., 2016; Kender et al., 2018).	From 0 – 0.85 Ma: 21 new age-depth tie points; Chapter 2. From 0.85 – 1.2 Ma: 9 new age-depth tie points; Chapter 3.
Nitrogen isotopes ($\delta^{15}N_{bulk}$) (Table 8.3, Table 8.4)	From 0 – 0.6 Ma: 97 data points (Kim et al., 2017). From 0.85 – 1.02 Ma: 213 data points (Kender et al., 2018); Appendix 1.	From 0 – 0.85 Ma: 269 new data points; Chapter 2. From 1.02 – 1.2 Ma: 44 new data points; Chapter 3.
Upwelling index (Table 8.5)	Opal MAR data previously published for Site U1343 (Kim et al., 2014).	Novel calculation presented in this thesis. From 0 – 0.85 Ma; Chapter 2 From 0.85 – 1.2 Ma; Chapter 3
Spectral analysis		From 0 – 1.2 Ma – the first upwelling index spectral analysis ever carried out; Chapter 3.
Diatom assemblages (Table 8.6)	Previously published diatom assemblage data from Site U1343 is not used here (Teraishi et al., 2016).	From 0.6 – 1.2 Ma: 183 new data points; Chapter 4.
Diatom silica isotopes ($\delta^{30}Si_{diatom}$) (Table 8.7)	Previously published $\delta^{30}Si_{diatom}$ data from Site U1343 is not used here (Kim & Khim, 2017).	From 0.6 – 1.2 Ma: 60 new data points; Chapter 5.

1.5.1 Site U1343: site location and core description

This study uses marine sediments from IODP Site U1343, collected in the Bering Sea IODP Expedition 323 in 2009. This cruise facilitated the first high

resolution, multi-proxy research of this subarctic marginal sea, as previous efforts produced poorly recovered sediments. Site U1343 (54°33.4'N, 176°49.0'E, water depth 1, 950 m) is situated on a topographic high adjacent to the northern continental shelf (Figure 1.3), proximal to the modern winter sea ice edge and at a depth just below the oxygen minimum zone (Figure 1.5), making it a suitable location to study past changes in both sea ice extent and mid- to deep-water mass characteristics (Takahashi et al. 2011). This site also lies in the high productivity green belt region (Springer et al., 1996), fuelled by upwelling of nutrient rich NPDW and driven by turbulent eddies and instabilities in the BSC which flows westward along the continental shelf (Figure 1.3).

The composite core used in this study is composed of three cores (U1343 A, U1343C and U1343E), each drilled using an advanced piston corer system. A composite core depth was achieved through splicing the three cores together, using the stratigraphic correlation of magnetic susceptibility, gamma ray attenuation (GRA) bulk density, natural gamma radiation (NGR), and color reflectance parameter b* data (Figure 1.10). Sediments were uniform throughout the core, composed of diatom and clay-rich silt with minor contributions from sand, ash, foraminifera, calcareous nannofossils and sponge spicules (Takahashi et al., 2011b). Ship-board XRD analysis indicates that there was no down-core silica diagenesis, with little impact from bioturbation.

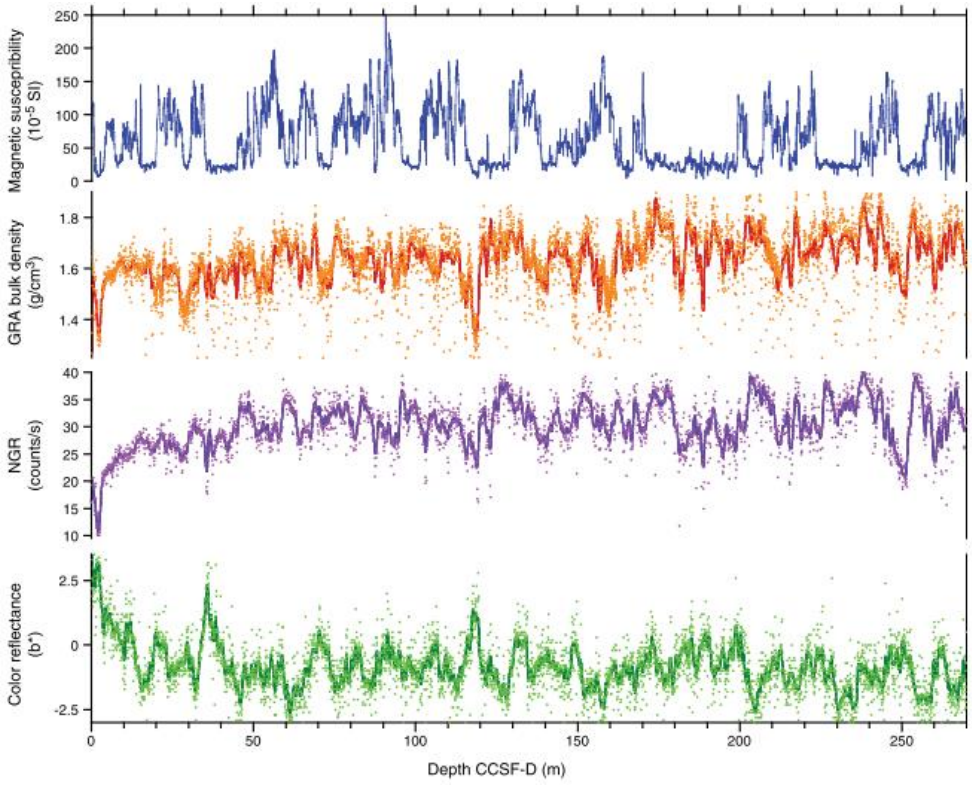


Figure 1.10 Spliced composite records used to create a composite core depth for Site U1343, based on ship-board measurements of a) magnetic susceptibility, b) GRA bulk density, c) NGR and d) colour reflectance b*. Figure taken from (Takahashi et al., 2011b).

1.5.2 Benthic foraminiferal $\delta^{18}O$

To consutrct a high resolution age model, benthic foraminiferal isotope data presented in this thesis were combined with previously published data from Site U1343 (Asahi et al., 2016; Kender et al., 2018) (Table 1.1) to create a total of 1825 $\delta^{18}O_{U1343}$ data points with an average time step of 0.65 kyr between 0 and 1.2 Ma. 388 samples were picked for benthic foraminifera, of which 114 were barren. Monospecific foraminiferal samples from the remaining 274 sediment samples were crushed and ~100 μg of foraminiferal calcite was measured for $\delta^{18}O$ using an IsoPrime© mass spectrometer with a Multicarb device at the British Geological Survey. The stable isotope data were calibrated to the VPDB

scale through the international NBS standards, with a precision of <0.05‰ based on duplicates.

As one species was not present throughout the whole core, $\delta^{18}O_{U1343}$ data were comprised of measurements on ten different species (*Cassidulina parkerianus, Cassidulina teretis, Elphidium batialis, Globobulimina auriculata, Globobulimina pacifica, Islandiella norcrossi, Nonionella labradorica, Uvigerina bifurcata, Uvigerina senticosa* and *Valvulineria spp.*) which were tuned to the $\delta^{18}O$ values for the most commonly occurring species, *E. batialis*. Species-specific offsets were calculated by Asahi et al. (2016) and Kender et al. (2018) through calculating the mean $\delta^{18}O$ offset of each species to the *E. batialis* in the same sample, or where this was not possible through comparison to the smoothed record (Kender et al., 2018). The error on these values can be defined by the standard deviation (Table 1.2). Through this thesis, the offsets defined and selected by Kender et al. (2018) are applied, where the offset for each species calculated using the larger dataset was chosen, with similar offset values produced by both studies.

1.5.3 Age Model

Through Chapter 2 and 3, I construct a high resolution age model, using the composite benthic foraminiferal $\delta^{18}O$ dataset. Through applying 30 age-depth tie points based on major deglacials, a good match to the global composite LR04 stack is achieved (r^2 = 0.61), with a consistent offset of ~0.5‰. Using this correlative method, it is assumed that there is a constant linear sedimentation between tie points (see Section 2.2.3 and Section 3.2.2). Therefore, although at deglacials the error in the age model is likely to be no greater than ± 4 kyr (Lisiecki & Raymo, 2009), there will be an increasing error between tie points.

Using the mean sedimentation rate (28.5 m/kyr) and the standard deviation (± 9.9 m/kyr) for the 0 – 1.2 Ma record, the age model error at the midpoint between tie points is estimated at an average of ±8.1 kyr (Table 1.3). Therefore, low age model error which is relatively consistent through time, provides confidence in the validity of the age model on orbital and millennial timesacles through the study interval.

Table 1.2 The mean and standard deviations of the offsets in $\delta^{18}O$ between various species and *Elphidium batialis* from Site U1343. Offsets were calculated by Kender et al. (2018) and Asahi et al. (2016) in samples where both species were measured, apart from species marked with * where offsets were calculated to the smoothing spline.

Species	$\delta^{18}O$ offset to *E. batialis*	σ (Kender et al., 2018)
Cassidulina spp. *	0.56	± 0.09
Globobulimina spp.	0.85	± 0.22
*Islandiella norcrossi**	0.48	± 0.08
Lenticulina spp.*	-0.02	± 0.15
Nonionella labradorica	0.65	± 0.27
Uvigerina spp.	0.87	± 0.20
Valvulineria spp.*	0.25	± 0.12

Table 1.3 Age model error at the midpoint depth between tie points, estimated using the mean sedimentation (sed.) rate and ± 1 standard deviation (σ).

Midpoint Age using linear sed. rate (kyr)	Midpoint Age using mean sed. rate (kyr)	Midpoint Age using mean sed. rate + 1σ (kyr)	Midpoint Age using mean sed. rate - 1σ (kyr)	Average age model error at midpoint (± kyr)
33.76	33.44	27.41	45.94	9.27
94.40	96.87	86.65	118.06	15.70
156.44	151.28	146.14	161.93	7.90
200.26	202.02	196.70	213.05	8.17
230.82	234.84	230.75	243.30	6.27
261.27	261.55	256.63	271.73	7.55
307.55	309.33	301.73	325.08	11.68
365.65	367.31	358.99	384.57	12.79
410.28	404.57	402.40	409.08	3.34
452.66	442.91	438.11	452.85	7.37
496.86	507.48	500.61	521.72	10.56
529.05	525.07	521.89	531.66	4.89
562.90	562.20	557.84	571.26	6.71
600.93	601.14	595.79	612.22	8.22
631.21	623.46	622.92	624.57	0.82
670.53	657.76	653.43	666.73	6.65
712.94	707.36	705.47	711.30	2.92
739.74	731.66	730.15	734.79	2.32
772.19	774.67	769.23	785.96	8.37
801.81	800.36	797.87	805.51	3.82
839.41	845.09	836.75	862.38	12.81
891.70	885.19	880.21	895.51	7.65
938.24	945.23	938.04	960.14	11.05
971.25	980.05	974.60	991.33	8.36
993.24	994.79	991.87	1000.85	4.49
1017.29	1020.83	1016.21	1030.40	7.09
1047.27	1055.90	1049.61	1068.94	9.67
1093.98	1102.02	1091.91	1122.97	15.53
1157.73	1156.77	1148.55	1173.82	12.64
Average:				8.09

1.6 A note on the papers

The papers presented in the following chapters of this thesis are at various stages in the publication process, and have multiple authorships associated with each paper. In Table 1.4 below, I have detailed my contribution towards each paper as well as the state of their publication.

I have also included a publication which has stemmed from my PhD research, but which is not appropriate for inclusion within the main thesis. This article, published in Nature Geoscience by Kender et al., (2018), is directly related to Chapters 2 and 3 of this thesis and formed the pilot work which led to my PhD proposal. I am named as the third author on this paper due to my contribution towards the written text in previous drafts which discussed the reliability of bulk $\delta^{15}N$ datasets in the Bering Sea, and due to my involvement in group discussions which aided the interpretation of results/analysis.

Table 1.4 Details of the papers resulting from the work presented in this thesis.

Title	Chapter	Contribution
Worne, S., Kender, S., Swann, G. E. A., Leng, M. J. and Ravelo, A. C. (2019). Coupled climate and subarctic Pacific nutrient upwelling over the last 850,000 years. *Earth and Planetary Science*, 522, 87-97	2	Lead role in the acquisition, analysis, design and interpretation of age model and $\delta^{15}N$ data and results, as well as primary responsibility for drafting and revising the manuscript
Worne, S., Kender, S., Swann, G. E. A., Leng, M. J. and Ravelo, A. C. (in prep).	3	Lead role in the acquisition, analysis and interpretation of age model and $\delta^{15}N$ data and results, as well as

Reduced high latitude upwelling in the subarctic Pacific during the MPT, modulated by sea level and sea ice. *Paleoceanography*.		primary responsibility for drafting and revising the manuscript
Worne, S., Stroynowski, Z., Swann, G. E. A. and Kender, S. (in prep). Sea Ice in the Bering Sea during the Mid Pleistocene Transition. *Paleoceanography*.	4	Lead role in the acquisition, analysis and interpretation of diatom assemblage data and results, as well as primary responsibility for drafting and revising the manuscript
Worne, S., Swann, G. E. A., Kender, S. and Leng, M. J. (in prep). Increased efficiency of the subarctic Pacific biological pump during the Mid Pleistocene Transition. *Paleoceanography*.	5	Lead role in the acquisition, analysis and interpretation of diatom assemblage data and results, as well as primary responsibility for drafting and revising the manuscript
Kender, S., Ravelo, A. C., **Worne, S.,** Swann, G. E. A., Leng, M. J., Asahi, H., et al. (2018). Closure of the Bering Strait caused Mid-Pleistocene Transition cooling. *Nature Communications*, 9 (5386).	Appendix 8.1	Key role in discussions which aided interpretation of $\delta^{15}N$ results as well as contribution towards drafting of manuscript

Chapter 2: Coupled climate and subarctic Pacific nutrient upwelling over the last 850,000 years

Savannah Worne[1]*, Sev Kender[2,3], George E. A. Swann[1], Melanie J. Leng[3,4], and Ana Christina Ravelo[5]

[1]Centre for Environmental Geochemistry, School of Geography, University of Nottingham, Nottingham, NG7 2RD, UK

[2]Camborne School of Mines, University of Exeter, Penryn Campus, Penryn, Cornwall, TR10 9FE, UK

[3]British Geological Survey, Keyworth, Nottingham, NG12 5GG, UK

[4]Centre for Environmental Geochemistry, School of Biosciences, University of Nottingham, Sutton Bonington Campus, Loughborough, NE12 5RD, UK

[5]University of California, Santa Cruz, CA 95064, USA

*Corresponding author. Email: savannah.worne@nottingham.ac.uk

Accepted for publication in Earth and Planetary Science Letters (20/06/19).

Abstract

High latitude deep water upwelling has the potential to control global climate over glacial timescales through the biological pump and ocean-atmosphere CO_2 exchange. However, there is currently a lack of continuous long nutrient upwelling records with which to assess this mechanism. Here we present geochemical proxy records for nutrient upwelling and glacial North Pacific Intermediate Water (NPIW) formation in the Bering Sea over the past 850 kyr, which demonstrates that glacial periods were characterised by reduced nutrient

upwelling, when global atmospheric CO_2 and temperature were also lowered. We suggest that glacial expansion of sea ice in the Bering Sea, and the simultaneous expansion of low nutrient NPIW, inhibited vertical mixing and nutrient supply across the subarctic Pacific Ocean. Our findings lend support to the suggestion that high latitude sea ice and the resultant intermediate water formation, modulated deep water upwelling and ocean-atmosphere CO_2 exchange on glacial-interglacial timescales.

2.1 Introduction

Recent studies have shown a sharp increase in both surface ocean subarctic Pacific productivity and CO_2 ventilation during the last deglaciation (Galbraith et al., 2007; Gray et al., 2018), and suggested that the equivalent of ~30 ppm atmospheric CO_2 was released into the atmosphere due to increased overturning (Rae et al., 2014). This was proposed to coincide with a collapse of glacial North Pacific Intermediate Water (NPIW), allowing overturning to bring nutrient and CO_2-rich deep water to the surface (Gray et al., 2018). Although a pervasive link between subarctic Pacific export productivity and Pleistocene glacial-interglacial cycles has been demonstrated (Jaccard et al., 2005, 2010), it is not yet known if this was primarily controlled by changes in iron supply (Galbraith et al., 2008; Praetorius et al., 2015), water column stratification and/or light limitation (Jaccard et al., 2010; Lam et al., 2013) and/or the extent of NPIW (Knudson & Ravelo, 2015b; Li et al., 2017) and nutrient upwelling (Gray et al., 2018). If the upwelling of nutrient and CO_2-rich water was the predominant control on subarctic Pacific productivity variations (Kender et al., 2018), this would imply the region has been an active source of pCO_2 throughout the Pleistocene and not just the last deglacial, because they are coupled with ice

core temperature records (Jaccard et al., 2005, 2010). One way to test for NPIW and its effect on upwelling nutrients is from the Bering Sea, which today contains an active upwelling zone.

Surface waters in the Bering Sea are fed by the subarctic Pacific Alaskan Stream, which enters through passes and straits in the Aleutian arc and circulates northward around the basin, forming the shelf-adjacent Bering Slope Current (BSC) (Stabeno et al., 1999) (Figure 1.3-1.4). Turbulent eddies in the BSC extend below the surface waters at ~300 m water depth, causing upwelling of North Pacific Deep Water (NPDW), which contains some of the highest nutrient concentrations in the marine system (Stabeno et al., 1999). This seasonally raises photic zone CO_2 and fuels a high productivity region at the Bering shelf break, known as the "green belt" (Springer et al., 1996) (Figure 1.3). Due to its terminal position in the ocean conveyor and deep bathymetric eddies, any glacial reduction in NPDW upwelling across the subarctic Pacific should also be apparent as reduced nutrient availability in the green belt.

Modern North Pacific Intermediate Water (NPIW) is sourced from the Okhotsk Sea and is widely distributed across the North Pacific ocean at a water depth between ~300 – 800 m characterized by salinity minima with density centred at 26.8 $\sigma\ \theta$ (Talley, 1993; Yasuda, 1997). During the last glacial maximum, intensified NPIW expanded down to 2000 m (Matsumoto et al., 2002a), with previous studies suggesting that the Bering Sea was a key source of glacial NPIW (Ohkushi et al., 2003a; Horikawa et al., 2010) as a result of enhanced brine rejection on the Beringian shelf, following increased sea ice growth since ~900 kyr (Knudson & Ravelo, 2015a; Jang et al., 2017; Kender et

al., 2018). Given its density, the formation of glacial NPIW from the Bering Sea has the potential to suppress upwelling by preventing eddies in the BSC from reaching NPDW. Expansion of this low nutrient glacial NPIW from the Bering Sea would crucially act to enhance stratification across the subarctic region – not just the smaller Bering Sea – causing region-wide impact on vertical mixing, nutrient supply and the biological pump.

Here, we present a new high resolution long sedimentary nitrogen isotope record ($\delta^{15}N$), in combination with previously published lower resolution results (Kim et al., 2017), from IODP Site U1343 in the Bering Sea green belt (Figure 1.3) to assess variation in nitrate utilisation between Marine Isotope Stages (MIS) 1 and 21, where we assume that the sedimentary bulk $\delta^{15}N$ is a representation of total macronutrient utilisation. To account for changes in export production, we normalise the opal mass accumulation rate (MAR) and produce the first high latitude record of nutrient delivery from deep to surface water (termed the "upwelling index"; see Methods). By semi-quantitatively assessing the offset between the opal MAR and $\delta^{15}N$ in this way, we constrain the impact of local growth rate and iron supply, to reveal long-term variability in macronutrient supply from deep water upwelling. We also present a new high-resolution multi-species benthic foraminiferal oxygen isotope record for an improved age model and produce the first assessment of the influence of NPIW at 2 km water depth in the Bering Sea. From this, we discuss the extent to which oceanographic changes in Bering Sea upwelling and NPIW production may have contributed towards NPDW upwelling and glacial-interglacial pCO_2 changes in the subarctic Pacific over the last 850 kyr.

2.2 Materials and Methods

2.2.1 Core Materials

IODP Site U1343 (54°33.4'N, 176°49.0'E, water depth 1950 m) is situated on a topographic high in the Bering Sea green belt adjacent to the northern continental shelf, proximal to the modern winter sea ice edge and at a depth just below the oxygen minimum zone (Figure 1.5). Marine sediments are composed primarily of fine clays and biogenic material, and are characteristically distinct from shelf-transported materials (Aiello & Ravelo, 2012).

2.2.2 Foraminiferal isotopes

Foraminiferal preservation is notably good at this site given the shallow North Pacific-wide lysocline which limits carbonate preservation at other Bering Sea sites (Takahashi et al., 2011a), providing an excellent opportunity to create a robust high resolution $\delta^{18}O_{U1343}$ age model (Asahi et al., 2016; Kender et al., 2018). In the absence of a single species consistently occurring in all samples, 262 samples of ~100 µg of foraminiferal calcite were measured for $\delta^{18}O$ using ten different species of benthic foraminifera (*Cassidulina parkerianus, Cassidulina teretis, Elphidium batialis, Globobulimina auriculata, Globobulimina pacifica, Islandiella norcrossi, Nonionella labradorica, Uvigerina bifurcata, Uvigerina senticosa* and *Valvulineria spp.*) at an average sampling resolution of 0.84 m from 2 – 222 m CCSF-A. Measurements were made using an IsoPrime© mass spectrometer with a Multicarb device at the British Geological Survey, where the analytical precision of duplicates was <0.05‰. The stable isotope data were calibrated to the VPDB scale through the international NBS standards. Species-specific offsets from Kender et al. (2018) were applied to fit the data to the most commonly occurring species, *E. batialis*,

and are presented in Figure 2.1 and Table 2.1. Given that benthic foraminiferal $\delta^{13}C$ is sensitive to diagenetic alteration, as calcite dissolution, re-precipitation and overgrowth can alter the isotopic composition of their tests (Cook et al., 2016), poor linear regressions between foraminiferal $\delta^{13}C$ and both raw $\delta^{18}O$ ($R^2 = 0.09$, $p < 0.001$) and $\delta^{18}O$ adjusted to *E. batialis* ($R^2 = 0.00$, $p > 0.05$) confirms that diagenetic alteration of foraminiferal shells cannot explain the glacial-interglacial variability in the $\delta^{18}O$ (Figure 2.5).

2.2.3 Age Model, Sedimentation Rates and Opal MAR calculations

Benthic foraminiferal isotope data presented here were combined with previously published data from Site U1343 (Asahi et al., 2016) to create a total of 751 $\delta^{18}O_{U1343}$ data points with an average time step of 1.1 kyr at an average resolution of 0.30 m from 0 – 222 m CCSF-A. The age model was defined by correlating to the LR04 global composite stack (Lisiecki & Raymo, 2005), and constructed by selecting 17 age-depth tie points during periods of rapid isotopic change primarily at deglacial intervals (Table 2.2). Although there is a possible time lag, where Pacific benthic $\delta^{18}O$ records may lag the Atlantic Ocean (Lisiecki & Raymo, 2005; Asahi et al., 2016), the high sample resolution and strong correlation between $\delta^{18}O_{U1343}$ and LR04 ($r = 0.82$, $p = <0.001$) suggests that these are within the expected uncertainty of the age model.

The high sedimentation rate at IODP Site U1343 and a lack of hiatuses in core material provides confidence in the continuity of its record (Asahi et al., 2016). Based on the new composite age model, sedimentation rates were calculated between each age-depth tie point. The average sedimentation rate was 29.15 cm kyr^{-1}, with higher rates during interglacials and a notable

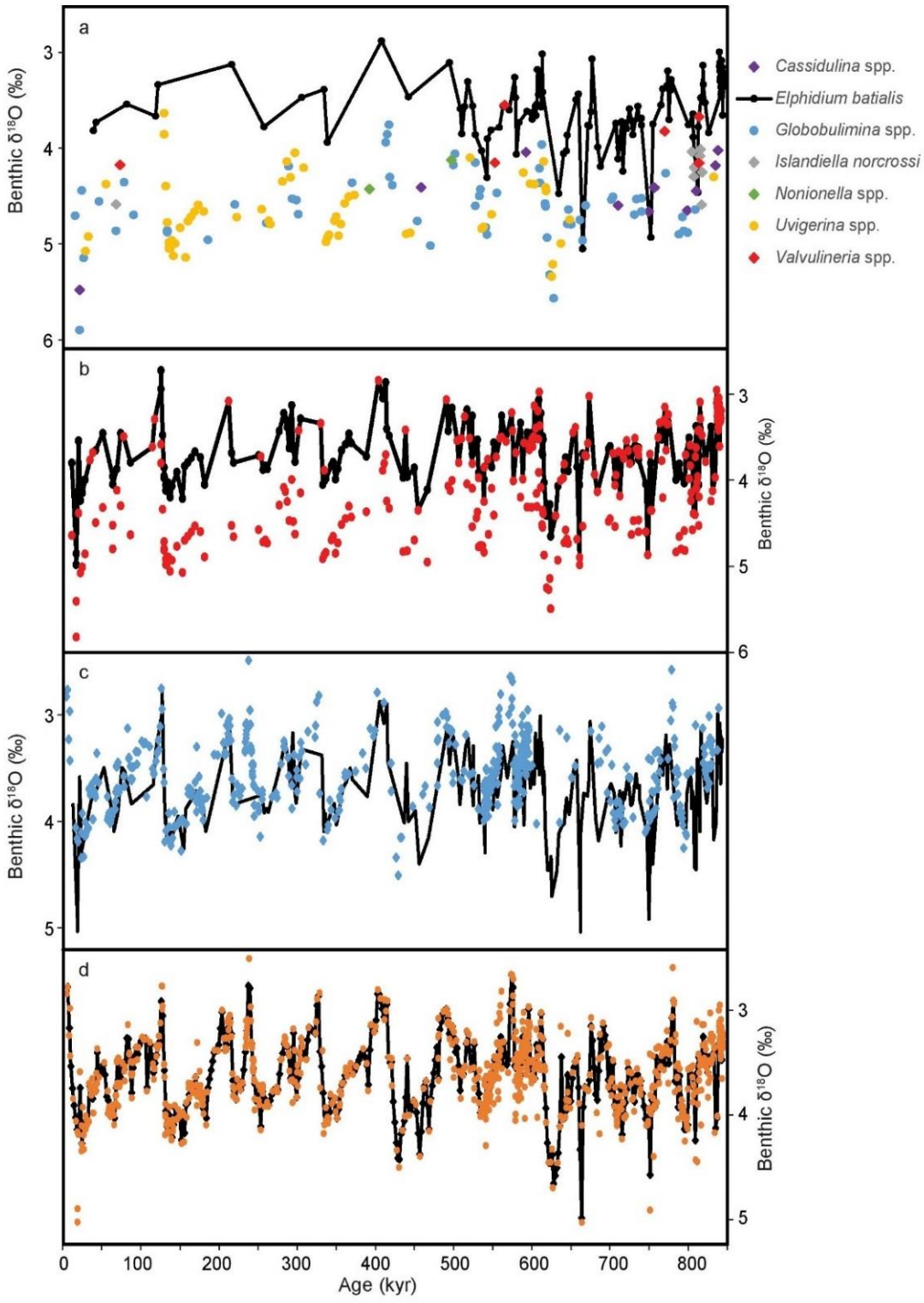


Figure 2.1 Benthic foraminiferal $\delta^{18}O$ results from U1343. A) Raw $\delta^{18}O$ values are categorised by species/genus and plotted against *E. batialis* (black) to which species-specific offsets are applied (Kender et al., 2018). b) Raw $\delta^{18}O$ data (red dots) are plotted against $\delta^{18}O_{U1343}$ (black line) which has been tuned to *E. batialis*. c) Comparison of $\delta^{18}O_{U1343}$ from this study (black line) against previous data from IODP Site U1343 (Asahi et al., 2016) (blue dots), which were combined in d) to create the updated age model for IODP Site U1343 (orange dots), and has been smoothed using linear interpolation to a 2 kyr resolution (black line).

sedimentation rate crash at ~630 kyr (likely due to low biogenic opal; Figure 2.6). These new sedimentation rates were applied to existing opal data (Kim et al., 2014) to calculate an opal MAR record using linear interpolation of the ship dry bulk density data and a ten-point smoothing average.

2.2.4 Bulk Sedimentary $\delta^{15}N$

Bulk samples at an average resolution of 0.81 m CCSF-A, totalling 276 samples between 0 – 222 m CCSF-A were analysed for $\delta^{15}N$ with 500 mg of raw material run on a Carlo Erba 1108 elemental analyzer, interfaced to a Thermo Finnigan Delta Plus XP IRMS at the University of California, Santa Cruz, with a precision of 0.15‰ based on both sediment standards and replicates. Results, relative to atmospheric nitrogen (AIR), were combined with previously published data from Site U1343 (Kim et al., 2017), to produce a composite record of 373 data points ($\delta^{15}N_{U1343}$), with an average resolution of 0.60 m between 0 and 222 m CCSF-A; average resolution of 2.3 kyr on the new age model (Figure 2.6).

2.2.5 Oceanographic indicies

2.2.5.1 $\Delta\delta^{18}O_{849-U1343}$

To assess regional variation and discrepancies between Site U1343 and the deep North Pacific Ocean, a Pacific end-member record from ODP Site 849 (Mix et al., 1995) (0°11'N, 110°31'W; 3851 m water depth) was used to remove high frequency and glacial-interglacial variability. A consistent offset of ~0.5 ‰ was found between $\delta^{18}O_{U1343}$ and $\delta^{18}O_{849}$, and so this was added to $\delta^{18}O_{U1343}$ first, to ensure offset values reflected only differences in $\delta^{18}O$ amplitude. After being linearly interpolated at an interval of 2 kyr (Figure 2.1), a three-point smoothing

spline was applied to the $\delta^{18}O_{U1343}$, and was subtracted from the similarly processed $\delta^{18}O_{849}$ record ($\Delta\delta^{18}O_{849\text{-}U1343}$), following a similar methodology to Knudson & Ravelo (2015a). Lower $\delta^{18}O_{U1343}$ become more similar to those of shallower water Bering Sea Site U1342 at ~800 m water depth (Figure 1.3, Figure 2.2a), which is suggested to be influenced by NPIW (Knudson & Ravelo, 2015b). Therefore, where $\Delta\delta^{18}O_{849\text{-}U1343}$ is approximately 0, Site U1343 is assumed to reflect the same water mass as the deep North Pacific Ocean, which upwells along the Bering Sea shelf edge today (Stabeno et al., 1999). Whereas more positive $\Delta\delta^{18}O_{849\text{-}U1343}$ values occur when $\delta^{18}O_{U1343}$ is lower than $\delta^{18}O_{849}$, suggesting a colder and/or more saline intermediate water mass is present at Site U1343, similar to the NPIW signature at Site U1342.

2.2.5.2 Upwelling Index

To account for the changes in the isotope values of deep North Pacific source water ($\delta^{15}N_{source}$) and gain insights into regional nitrate utilisation, we follow previous work (Galbraith et al., 2008; Knudson & Ravelo, 2015a) by subtracting the record of ODP Site 1012 in the eastern tropical North Pacific (Liu et al., 2005) (32°17'N, 118°24'W; 1172 m water depth) which is influenced by waters from the Eastern Tropical North Pacific denitrification zone, and is thought to be a site of near complete nitrate utilisation throughout the Pleistocene (Galbraith et al., 2008). $\delta^{15}N_{1012}$ was linearly interpolated at a time interval of 2 kyr (the average resolution of $\delta^{15}N_{1012}$) and subtracted from the similarly interpolated $\delta^{15}N_{U1343}$, to produce a record driven by nutrient utilisation for Site U1343 ($\Delta\delta^{15}N_{U1343\text{-}1012}$) (Figure 2.7).

Given that high $\Delta\delta^{15}N_{U1343\text{-}1012}$ values can either reflect higher export production (more rapid removal of nitrate from the euphotic zone) or a slower nutrient resupply (slower replenishment of the surface nitrate pool), and as diatoms are the dominant contributors to export production, the opal MAR can be used to constrain the impact of variable productivity on $\Delta\delta^{15}N_{U1343\text{-}1012}$. Comparison of the opal MAR with the opal (%) confirms that the MAR record is not an artefact of the age model and calculated sedimentation rates (Figure 2.6). The opal MAR record was also linearly interpolated at an interval of 2 kyr and then normalised so that all values ranged between 0 and 1. Then the similarly normalised $\Delta\delta^{15}N_{U1343\text{-}1012}$ was subtracted to create a semi-quantitative proxy termed the 'upwelling index', with low (higher) values indicating decreased (increased) upwelling nutrient supply on the Bering shelf slope (Figure 2.3b, Equation 2.1)

$$Upwelling\ Index = Normalised\ Opal\ MAR - Normalised\ \Delta\delta^{15}N_{U1343-1012}$$

Equation 2.1

In doing this we assume that the rate of export production is a reflection on total primary productivity, and that the majority of macronutrient delivery to the photic zone at IODP Site U1343 was from upwelling of NPDW and that rates of nutrient utilisation were controlled by both nutrient upwelling and delivery of iron (Fe) to the photic zone (predominantly derived from sea ice and shelf-derived material (Aguilar-Islas et al., 2008)). During times of low Fe input and incomplete nutrient utilisation, when increased upwelling will decrease nutrient utilisation (as the nutrient pool is larger) while productivity will show a smaller

increase (from the small amount of upwelled Fe which will be scaled proportionally with macronutrient increase), causing the upwelling index to increase at a lower rate than for times of higher Fe delivery. The result of the upwelling index can be classified by three potential states which reflect interglacial, glacial and deglacial changes in biogeochemical cycling (Figure 2.4).

2.3 Results

2.3.1 $\Delta\delta^{18}O_{849-U1343}$: NPIW formation

Over the last 850 kyr benthic foraminiferal $\delta^{18}O_{U1343}$ varied between +2.47 and +5.02 ‰ (mean = +3.58 ‰), with an amplitude of change similar to LR04 and ODP Site 849 in the eastern equatorial Pacific (range from +3.08 to +5.10 ‰; mean = +4.12 ‰; Figure 2.2a, Figure 2.3a). The highest $\Delta\delta^{18}O_{849\text{-}U1343}$ values occur during glacial maxima of MIS 4, 6, 8, 12, 16 and 20 (Figure 2.2b). As the two $\delta^{18}O$ records are used to create the age models, with rapid deglacial changes in $\delta^{18}O$ as the tie points, rapid $\Delta\delta^{18}O_{849\text{-}U1343}$ shifts at deglacials may be artificially amplified. However, $\Delta\delta^{18}O_{849\text{-}U1343}$ values are significantly higher in glacial periods (mean = 0.05) than interglacial periods (mean = 0.00; $p < 0.05$), with values gradually increasing as glacial periods developed and became more intense, suggesting an increasing influence of glacial NPIW in the Bering Sea slope region. During deglacial periods NPIW collapses, and the $\Delta\delta^{18}O_{849\text{-}U1343}$ becomes more negative during interglacials, as $\delta^{18}O_{U1343}$ is more similar to the deep water record from the eastern equatorial Pacific Site 849, suggesting NPDW influence at the 2 km water depth at Bering Sea slope Site U1343.

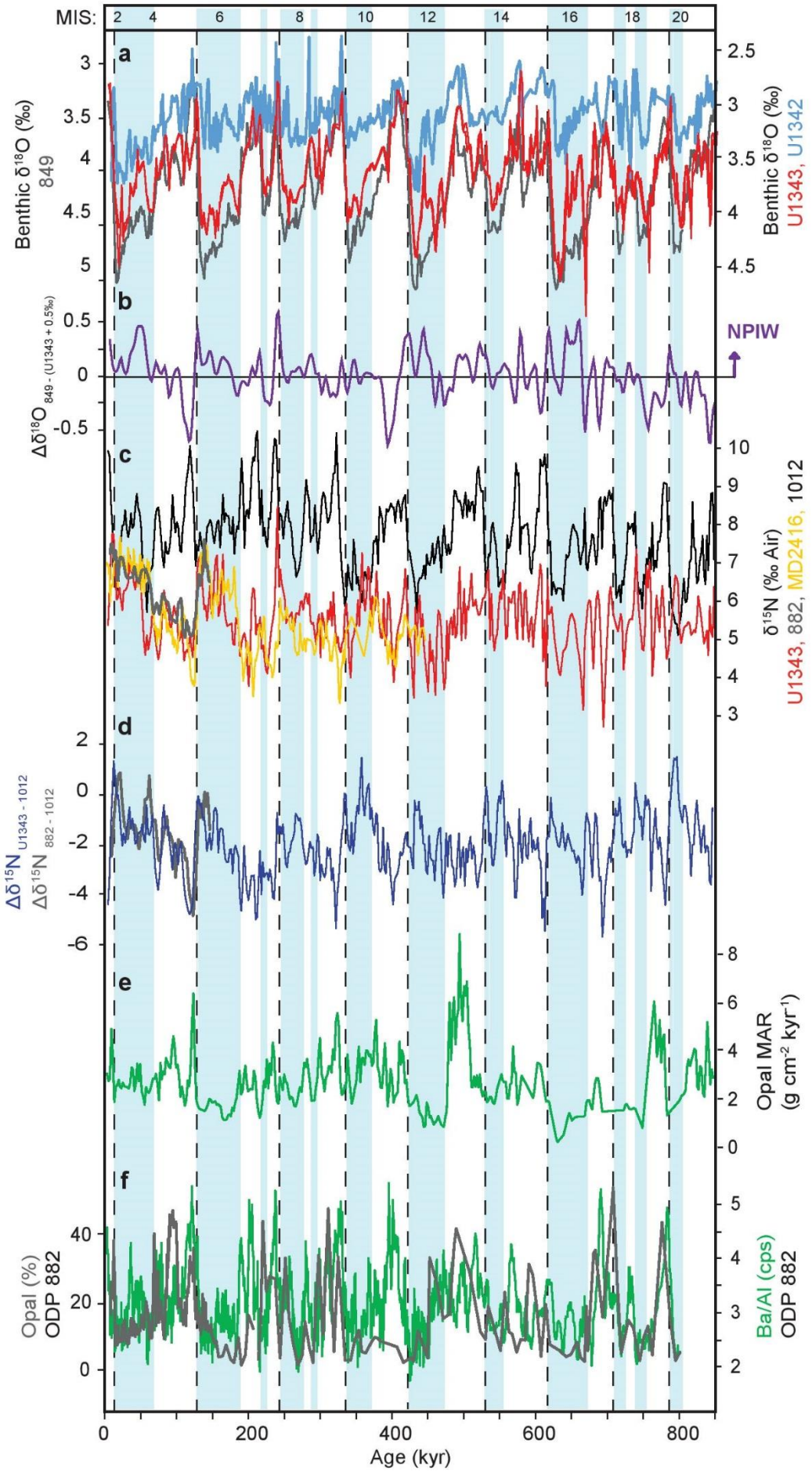

MIS:
2
4
6
8
10
12
14
16
18
20
a
Benthic δ18O (‰)
849
Benthic δ18O (‰)
U1343, U1342
b
Δδ18O 849 - (U1343 + 0.5‰)
NPIW
c
δ15N (‰ Air)
U1343, 882, MD2416, 1012
d
Δδ15N U1343 - 1012
Δδ15N 882 - 1012
e
Opal MAR
(g cm-2 kyr-1)
f
Opal (%)
ODP 882
Ba/Al (cps)
ODP 882
Age (kyr)

Figure 2.2 Geochemical proxy results from IODP Site U1343 from MIS 2 to 20. a) Benthic foraminiferal $\delta^{18}O$ results from IODP Site U1343 compared to those from the shallower IODP Site U1342 and deep Pacific ODP Site 849. The data from Site U1342 has been recalculated here to match benthic foraminiferal offset for *E. batialis*, used for Site U1343 (Kender et al., 2018). b) The offset in $\delta^{18}O$ between IODP Site U1343 and ODP Site 849 ($\Delta\delta^{18}O_{849\text{-}U1343}$). c) Bulk $\delta^{15}N$ data from IODP Site U1343 compared with deep North Pacific ODP Site 1012 (a site of complete nutrient utilisation) together with bulk $\delta^{15}N$ records from ODP Site 882 and MD2416 in the subarctic North Pacific Ocean. d) The $\delta^{15}N$ offset between IODP Site U1343 and ODP Site 1012 ($\Delta\delta^{15}N_{U1343\text{-}1012}$) which constrains changes in source water $\delta^{15}N$ to reflect changes in Bering Sea nutrient utilisation. e) Opal mass accumulation rate (MAR) from IODP Site U1343 [adapted from Kim et al. (2014), see Methods]. f) The opal (%) and Ba/Al productivity records from ODP Site 882 (Jaccard et al., 2010). Blue bars represent periods of Bering Strait closure (>50 m sea level drop) (Elderfield et al., 2012) with vertical dashed lines indicating deglaciations.

2.3.2 $\delta^{15}N$ and Opal MAR

Today Bering Sea green belt primary productivity is dominated by diatoms which primarily bloom in spring/summer following seasonal sea ice melt, which provides a source of dissolved iron and promotes water column stability, allowing diatoms to remain in the photic zone and utilise available nutrients (Aguilar-Islas et al., 2008). Estimates of annual primary productivity in the green belt are >170 g C m^{-2} yr^{-1} (Sambrotto et al., 2008) with blooms sustained by tidal mixing and lateral supply of iron rich waters from the shelf (Aguilar-Islas et al., 2008). Conditions, however, are reversed during winter months (November to April) when sea ice expansion and associated reductions in light availability reduces primary productivity, leading to incomplete nutrient utilisation and the emergence of high-nutrient low chlorophyll (HNLC) conditions similar to the lower subarctic Pacific and central Bering Sea (Galbraith et al., 2008; Sambrotto et al., 2008; Knudson & Ravelo, 2015a). With diatoms as the primary contributors to biogenic material within the IODP Site U1343 sediment record (Teraishi et al., 2016), the opal mass accumulation

(MAR) record, recalculated using sedimentation rates from our new age model, is thought to approximate changes in primary productivity (Kim et al., 2014), where productivity was significantly higher in interglacials (mean = 3.30 g cm^{-2} kyr^{-1}) than in glacials (mean = 2.66 g cm^{-2} kyr^{-1}; $p < 0.001$; Figure 2.2e) (Kim et al., 2014). Although the phytoplankton community structure will likely have varied in response to changing seasonality, diatoms have remained the dominant contributors to export production in the Bering Sea (Takahashi et al., 2011a). As changes in the composition of the phytoplankton community will be minor in comparison to glacial-interglacial variation in export production, we assume these changes are unlikely to have impacted our geochemical signals on millennial timescales. Furthermore, silica supply is not considered a limiting nutrient in the Bering Sea (Tsunogai et al., 1979), and hence the opal MAR likely reflects first order changes in productivity (Kim et al., 2014).

Changes in $\delta^{15}N_{U1343}$ are assumed to primarily reflect temporal variations in nitrate utilisation which is influenced by the amount of productivity and nutrient availability, which is in turn dependent on the rate of upwelling of macronutrient rich NPDW, driven by eddies in the BSC along the shelf break. Terrestrial input with low $\delta^{15}N$ is not considered to have driven the record due to the lack of covariation of $\delta^{15}N$ and sedimentary C/N ratio (Figure 2.6), and the broad similarity with ODP Site 882 and MD2416 in the North Pacific which are far from land (Figure 2.2c) (Galbraith et al., 2008; Jaccard et al., 2010). Similarly, variable inorganic contribution is not considered to bias the bulk $\delta^{15}N$ record, as the intercepts on %TOC vs. %TN do not vary significantly between glacial and interglacials (Figure 2.8). In addition, diatom-bound $\delta^{15}N$ records from the Bering Sea and subarctic Pacific show similar

trends to their bulk $\delta^{15}N$ counterparts (Brunelle et al., 2007; Galbraith et al., 2008; Studer et al., 2012), indicating bulk sediment nitrogen is a good proxy for nutrient utilisation in surface water. $\delta^{15}N_{U1343}$ values range from +2.72 to +8.89 ‰ (mean = +5.59 ‰) with peak values occurring in glacials, particularly during MIS 2 at ~14 kyr and MIS 8 at ~245 kyr (Figure 2.2c).

Prior to ~ MIS 13, there appears to be less distinctive glacial-interglacial variability in $\delta^{15}N_{U1343}$, which could reflect sedimentary preservation, however diagenetic alteration of nitrogen is considered less of an influence in this high sedimentation rate setting (Brunelle et al., 2007; Robinson et al., 2012). Alternatively, the greater glacial-interglacial variability in nutrient utilisation over the last ~600 kyr may be expected, given that 100 kyr cycles in the late Quaternary are characterised by colder and more severe glacial periods, and warmer interglacial periods, than the preceding 41 kyr cycles (McClymont et al., 2013).

Low $\delta^{15}N_{U1343}$ excursions (< 4.5‰) may be a result of inorganic or terrestrial input, as the modern deep ocean average $\delta^{15}N$ is ~4.5‰ (Sigman et al., 2009). However, the $\delta^{15}N$ record is not a direct recorder of deep ocean $\delta^{15}N$ and more likely reflects surface water $\delta^{15}N$, which will be a combination of the deep water signal, as well as surface water processes such as productivity. Confidence in the fidelity of low $\delta^{15}N_{U1343}$ values (<5.0‰) is provided by other subarctic Pacific records from open ocean sites great distances from the continent, such as from Site MD2416 (Galbraith et al., 2008), Site 882 (Jaccard et al., 2010) (Figure 2.2c) and Site 887 (Studer et al., 2012). Furthermore, diatom-bound $\delta^{15}N$ results also show values less than 5‰ in the subarctic

(Brunelle et al., 2007; Studer et al., 2012). Although nitrate uptake can only account for increases in $\delta^{15}N_{U1343}$, terrestrial/inorganic nitrogen input is unlikely to impose a first-order control on the glacial-interglacial variability at U1343.

2.3.3 Glacial-interglacial variability in the upwelling index

The upwelling index is highly correlated with the LR04 deep ocean $\delta^{18}O$ record ($r = -0.72$, $p < 0.001$) – a combination of global ice volume and deep ocean temperature – with a significantly lower upwelling index in glacials (mean = -0.40) than in interglacials (mean = -0.10; $p < 0.001$) (Figure 2.3). Minimal upwelling index values during glacial maxima (due to increased rates of nitrate utilisation ($\delta^{15}N_{U1343}$) despite lowered primary productivity (opal MAR)), suggest there was a smaller pool of nutrients in the photic zone, concomitant with expanded NPIW (Figure 2.2). We propose that presence of glacial NPIW was a pivotal mechanism in reducing nutrient supply from deep water upwelling (see Discussion). A rapid deglaciation phase occurred at all major glacial terminations (dashed lines in Figure 2.3) when nutrient upwelling peaked, indicating ample nutrient supply from resumed NPDW upwelling and the establishment of a high productivity/low nitrate utilisation state.

Although upwelling is also correlated with relative sea level (Elderfield et al., 2012) ($r = -0.55$, $p < 0.001$) and Antarctic air temperature (Jouzel et al., 2007) ($r = 0.56$, $p < 0.001$) (Figure 2.3), the high correlation with global surface ocean temperature (Snyder, 2016) ($r = 0.60$, $p < 0.001$) and ice core atmospheric CO_2 records over the last 800 kyr are of particular interest ($r = 0.60$, $p < 0.001$) (Lüthi et al., 2008). These tight correlations are despite the limitations to our productivity and nutrient utilisation proxies and possible inter-site age model

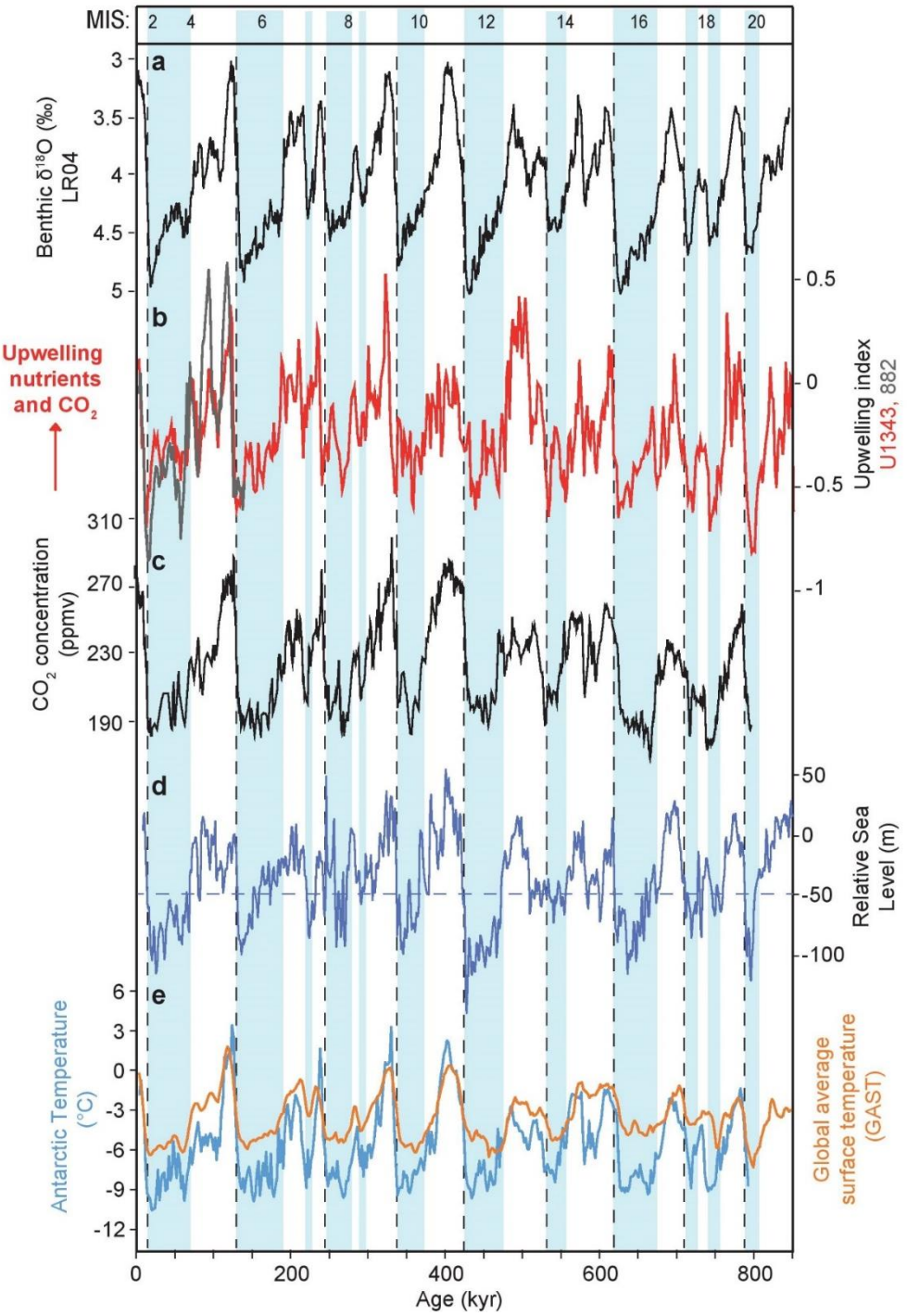


Figure 2.3 Comparison of the upwelling indexes against other global and regional paleoenvironmental records. a) Composite LR04 benthic foraminiferal $\delta^{18}O$ stack (Lisiecki & Raymo, 2005) over the last 850 kyr. b) The upwelling index for Site U1343 (red) and Site 882 (grey), which show suppressed rates of upwelling during glacial periods following Bering Strait closure (blue bars). The upwelling index shows strong correlation with the composite EPICA Dome C Ice Core atmospheric CO_2 record over the last 800 kyr (c) (Lüthi et al., 2008), changes in relative sea level (m) (d) (Elderfield et al., 2012), where the blue lines at -50 m represent modern Bering Strait depth, and global temperature records (temperature deviation from present day) (e) (Jouzel et al., 2007; Snyder 2016). Vertical dashed lines indicate deglaciations.

discrepancies, therefore suggesting a common link between upwelling, atmospheric temperature and CO_2. Although correlation does not imply causation, the consistency in the relationship between the upwelling index and the ice-core derived CO_2 provides support for a shared underlying mechanism. Exceptions to this correlation between the upwelling index and CO_2 occurs during MIS 13, when the upwelling index was high but pCO_2 was lower than subsequent interglacials, and MIS 11, when the upwelling index was lower than might be expected given the higher pCO_2 for this interglacial (Figure 2.3). While the former discrepancy may be a result of the MAR calculations, where sedimentation is relatively high during MIS 13, this also correspond with the Mid-Brunhes Transition (MBT) where interglacial conditions became warmer (Jouzel et al., 2007). A productivity peak at MIS 13 in response to increased sea ice melt may explain the high upwelling index result at this time. Alternatively, notably warm conditions during "super interglacial" MIS 11 (Melles et al., 2012) likely caused earlier and rapid sea ice melt, which would have reduced iron availability to the green belt, reducing the duration of the spring bloom and limiting summer productivity (Aguilar-Islas et al., 2008). After post-MBT warming, from MIS 11 onward, the relationship between upwelling index and Antarctic CO_2 is particularly strong ($r = 0.70$, $p < 0.001$).

2.4 Discussion

Changes in nutrient upwelling are likely to have been controlled by a combination of sea level change, sea ice presence and NPIW extent (Kender et al., 2018). Geochemical and biological proxy evidence indicate that an expansion of sea ice occurred during glacials throughout the last 850 kyr (Teraishi et al., 2016; Stroynowski et al., 2017; Detlef et al., 2018), causing

lower rates of primary productivity (Kim et al., 2014) and actively restricting air-sea gas exchange. Coincident with glacials and maximal sea ice extent, our $\Delta\delta^{18}O_{849\text{-}U1343}$ results provide evidence for intermediate water presence to at least 2 km water depth, supporting data from IODP Site U1342 which indicates NPIW presence to at least 800 m water depth (Knudson & Ravelo, 2015b) (Figure 2.2a-b). Brine rejection on the Bering Sea shelf during enhanced sea ice formation in glacials is the proposed mechanism for formation of a more saline water body, which would sink to intermediate depths at the shelf slope and propagate southward as NPIW (Knudson & Ravelo, 2015b), as observed for NPIW in the modern Okhotsk Sea.

Although direct sea ice reconstructions from the Bering Sea are of lower resolution, they broadly support NPIW expansion, as glacial periods during this time interval were characterised by extended thick pack ice which peaked during the mid-to-late glacials, when we see the largest offsets in $\Delta\delta^{18}O_{849\text{-}U1343}$ (Stroynowski et al., 2017; Detlef et al., 2018). Changes in sea-ice would have been in combination with sea level falls of ~50-150 m during glacials (Elderfield et al., 2012) (Figure 2.3d), causing closure of the Bering Strait (modern depth of ~50 m) and retention of both cold/fresh surface waters and denser modified shelf-water (following brine rejection) within the Bering Sea, as the northward flow into the Arctic Ocean was prevented (Knudson & Ravelo, 2015b; Kender et al., 2018). The resultant expanded NPIW at the shelf edge likely prevented eddies in the BSC from reaching NPDW, isolating nutrients in the photic zone without significant resupply (low upwelling index) and causing the observed high rates of nitrate utilisation but low productivity, whilst also trapping CO_2 in deep waters during glacials over the last 850 kyr (Figure 2.4b).

In addition to sea ice and NPIW expansion during glacials triggering a reduction in productivity and nutrient upwelling, lowered sea level would have hindered Alaskan Stream water from flowing into the basin by shoaling the passes along the eastern Aleutian arc (Figure 1.3) Although we cannot quantify this effect, it would have caused some degree of decrease in surface water flow around the Bering Sea basin. This is important because the strength of BSC flow controls eddy field fluctuation, where increased flow maintains higher primary productivity by promoting vertical nutrient supply, and vice versa (Mizobata & Saitoh, 2004). There is evidence for glacial reductions in the inflow of the Alaskan Stream from reduced proportions of the diatom species *Neodenticula seminae* near the inflow sites at the Aleutian arc in the southern Bering Sea, as well as at the slope (Teraishi et al., 2016; Stroynowski et al., 2017). The resultant decrease in BSC flow in glacials would have therefore reduced large eddy formation, further lowering NPDW upwelling of nutrients, productivity and photic zone CO_2 (Mizobata & Saitoh, 2004). Simultaneously, sea ice expansion over a shallowed Beringian shelf during glacials may have increased the mobilisation of sediments and transport of shelf-derived iron to the slope (Aguilar-Islas et al., 2008). Reduced vertical macronutrient supply but sustained iron supply from sea ice, which is a key source of bioavailable iron in the green belt today (Aguilar-Islas et al., 2008), could help to explain the co-occurrence of low productivity and high nutrient utilisation in glacials (Figure 2.2, Figure 2.4b). Overall, our results support previous proposals that enhanced sea ice and NPIW formation during periods of low glacial sea level were a key mechanism for controlling deep water upwelling and green belt nutrient supply over the last 850 kyr (Kender et al., 2018). Reduced upwelling of nutrient-rich NPDW due

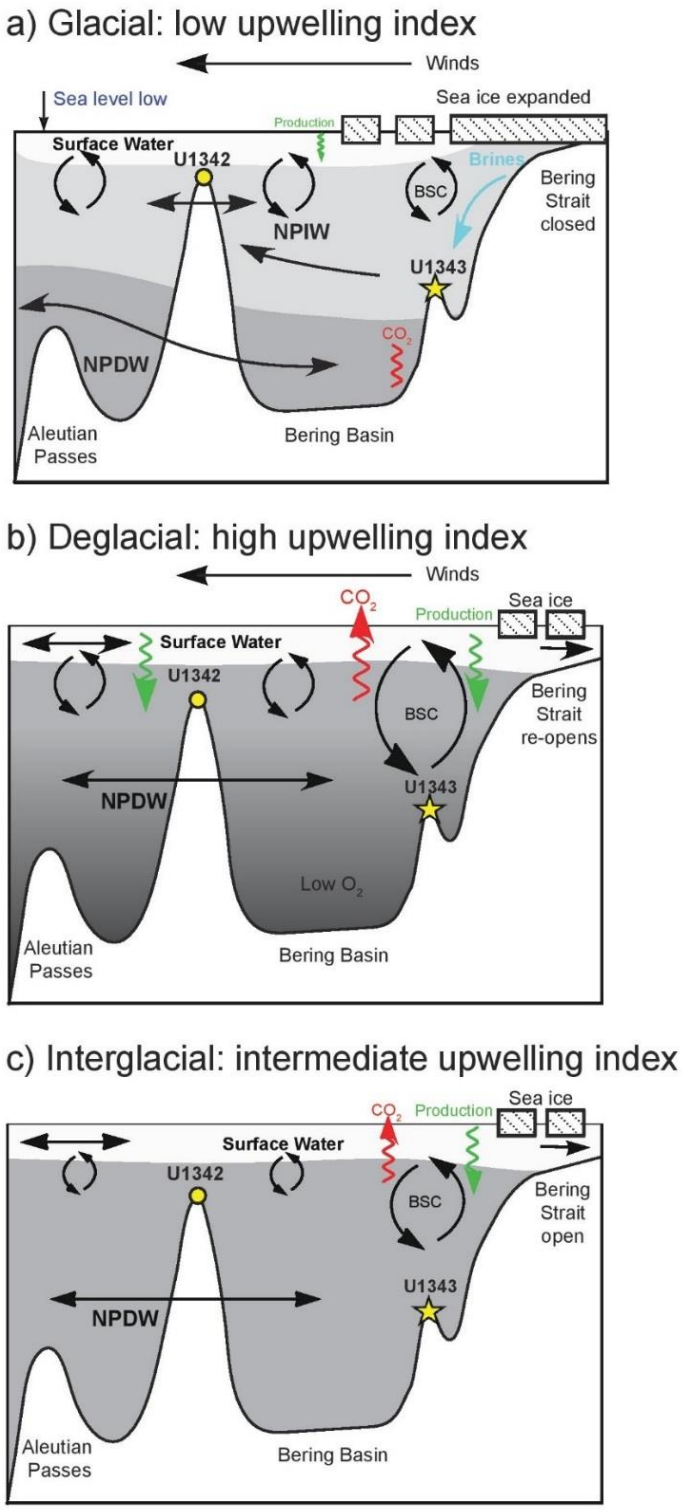


Figure 2.4 Schematic models representing glacial, deglacial and interglacial regimes of biogeochemical cycling in the Bering Sea. a) A low upwelling index indicates reduced upwelling caused by an expansion of NPIW which forms in glacials following the closure of the Bering Strait, leading to an isolated pool of nutrients in the photic zone. This results in reduced primary productivity (opal MAR) but higher rates of nutrient utilisation due to the reduced supply of deep water nutrients into the photic zone. b) A high upwelling index indicates ample nutrient supply from resumed NPDW upwelling which occurs during deglaciation, leading to a high productivity/low nutrient utilisation state. c) An intermediate upwelling index results indicates upwelling typical of an interglacial, similar to the modern regime.

to NPIW presence and lowered BSC strength and physical overturning in glacials could then have caused the green belt region to act as a larger net carbon sink.

During deglaciation, conditions would have reversed with the break up and retreat of sea ice (Kim et al., 2014; Stroynowski et al., 2017) and sea level rise, causing re-strengthening of the BSC and both local and regional collapse of NPIW (Figure 2.4b). Coupled with high shelf-derived iron from deglacial flooding of the Beringian shelf and potentially increased deglacial Yukon River flow (VanLaningham et al., 2009), this rapid restoration of regional upwelling nutrients explains the observed productivity peaks during deglaciations (Kim et al., 2014) from at least MIS 20-21 onwards. Modelling has shown that late in the last deglacial, wind strength across the Bering Sea and subarctic remained greatly increased due to the remanence of large North America ice sheets (Gray et al., 2018). This would have aided eddy formation in the Bering Sea and upwelling of NPDW across the subarctic region through promoting vertical mixing. Once ice sheets had declined and sea ice diminished, seasonally variable upwelling and vertical mixing across the subarctic Pacific would have become re-established in interglacials, similar to modern conditions (Figure 2.4c).

We have demonstrated for the first time that the glacial reductions in Bering Sea slope primary productivity were driven at least in part by reduced upwelling of nutrients (Figure 2.3b) and propose that this was largely controlled by sea ice and expanded low- nutrient NPIW (Figure 2.2b). Whilst we do not suggest that this mechanism solely explains the observed proxy evidence from

across the North West Pacific Ocean during the Pleistocene, similar productivity and nutrient utilisation $\delta^{15}N$ records are seen at ODP Site 882 and MD2416 (Figure 2.2) (Galbraith et al., 2008; Jaccard et al., 2010), whilst an upwelling index derived for ODP Site 882, using a $\Delta\delta^{15}N_{882\text{-}1012}$ record for regional nutrient utilisation and opal (%) as a productivity record (Jaccard et al., 2010) (Figure 2.2), shows remarkably similar trends to the Bering Sea upwelling index. Although the upwelling index for Site 882 only covers a short time period, the high correlation between the upwelling index for Sites U1343 and 882 ($r = 0.77$, $p < 0.001$) provides support for a common controlling mechanism of NPIW between the Bering Sea and wider subarctic Pacific region.

I propose that reduced upwelling of nutrients in the subarctic Pacific Ocean, as recorded at ODP Site 882 and MD2416, was the cause of reduced glacial export production, forced by the expansion of low nutrient NPIW, similar to the Bering Sea slope (at U1343). The formation of dense NPIW in the Bering Sea likely propagated south through the deep western Kamchatka Strait (Figure 1.3), although this does not discount additional contributions of NPIW from the Okhotsk Sea (Max et al., 2014). This mechanism was proposed for the last glacial cycle in the subarctic Pacific Ocean, where model and proxy evidence from the Bering and Okhotsk Seas indicated that enhanced NPIW during Heinrich Stadial 1 increased intermediate-to-deep ocean stratification, isolating abyssal carbon in NPDW (Gong et al., 2019). Furthermore, the disappearance of NPIW during the latter part of last deglaciation allowed renewed upwelling of deeper water rich in nutrients and is considered responsible for increases in surface water proxies for CO_2 (Gray et al., 2018). Our new data support glacial NPIW production as the underlying mechanism

driving the strength of nutrient upwelling both along the Bering Sea slope and across the open subarctic Pacific Ocean over the past 850 kyr.

Changes in the Southern Ocean are considered to be a dominant component in driving glacial-interglacial changes in pCO_2 (Jaccard et al., 2013; Gottschalk et al., 2016). For example, glacial reduction of atmospheric pCO_2 has been linked to an increased rate of biological sequestration in the Southern Ocean and/or reduced supply of nutrients and CO_2 upwelled from the deep ocean as a result of intermediate water formation and expanded sea ice cover (Sigman et al., 2010). Although net CO_2 flux in the Southern Ocean is regarded as the largest single control on glacial-interglacial variability in pCO_2 (Sigman et al., 2010), we demonstrate here that similar processes occurred in the subarctic Pacific region. With modelling studies suggesting that ~30 ppm atmospheric CO_2 was released into the atmosphere due to increased overturning in the subarctic region at the last deglaciation (Rae et al., 2014), we surmise that similar magnitude ocean-atmospheric CO_2 fluxes may have occurred over the last 850 kyr in response to changes in deep water nutrient upwelling across the Bering Sea and subarctic Pacific Ocean. This aids ongoing efforts to fully explaining observed trends in atmospheric pCO_2 over this interval (Rae et al., 2014; Gray et al., 2018).

2.5 Conclusion

Overall, we constructed a new high resolution benthic oxygen isotope stratigraphy for IODP Site U1343, to aid the development of a new nutrient upwelling index which uses $\delta^{15}N_{bulk}$ and opal MAR to assess glacial-interglacial variability in the supply of nutrients from NPDW upwelled at the Bering shelf

edge. We find a tight correlation between the upwelling index results and global temperature, sea level and atmospheric pCO_2, as well as the upwelling index calculated for the short term record at ODP Site 882 in the western subarctic Pacific Ocean. We posit that increased sea ice volumes in the Bering Sea and the resultant expansion of NPIW caused suppression of both nutrient and CO_2 upwelling during periods of Bering Strait closure, both in the Bering Sea and across the subarctic Pacific Ocean region.

Results here suggest that the regional significance of sea ice and deep water ventilation in the subarctic Pacific Ocean has been generally underestimated when modelling Quaternary climate change, where glacial NPIW growth and propagation from the Bering Sea influences both local and, importantly, regional upwelling of NPDW and export production. The strong correlation between high latitude upwelling and glacial cycles in atmospheric CO_2 (Figure 2.3b-c), and the bipolar nature of Quaternary glaciations, also supports suggestions that sea ice was a primary control on the past global climate state (Sigman et al., 2010). Overall, improved understanding of this mechanistic relationship between the Bering Sea and the subarctic Pacific will aid future efforts to constrain the role of glacial-interglacial oceanographic variability in global climate, in complement to Southern Ocean-driven dynamics.

2.6 Supplementary information

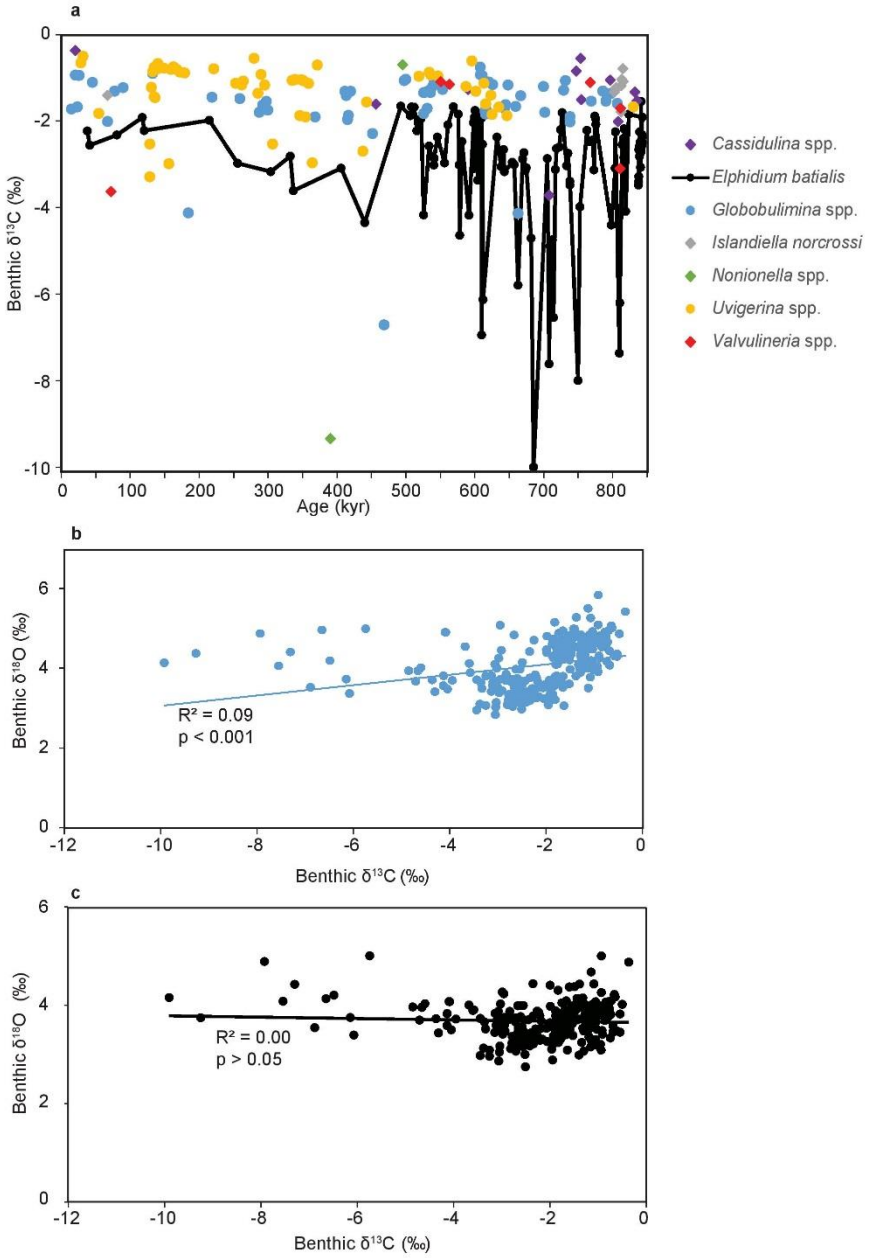


Figure 2.5 Benthic foraminiferal comparison of $\delta^{13}C$ and $\delta^{18}O$. a) $\delta^{13}C$ data categorised by species/genus. The poor relationship for $\delta^{13}C$ against both raw $\delta^{18}O$ (b) and $\delta^{18}O_{U1343}$ adjusted to *E. batialis* (c) suggests that diagenetic alteration of foraminiferal shells cannot explain the glacial-interglacial variability in the $\delta^{18}O$.

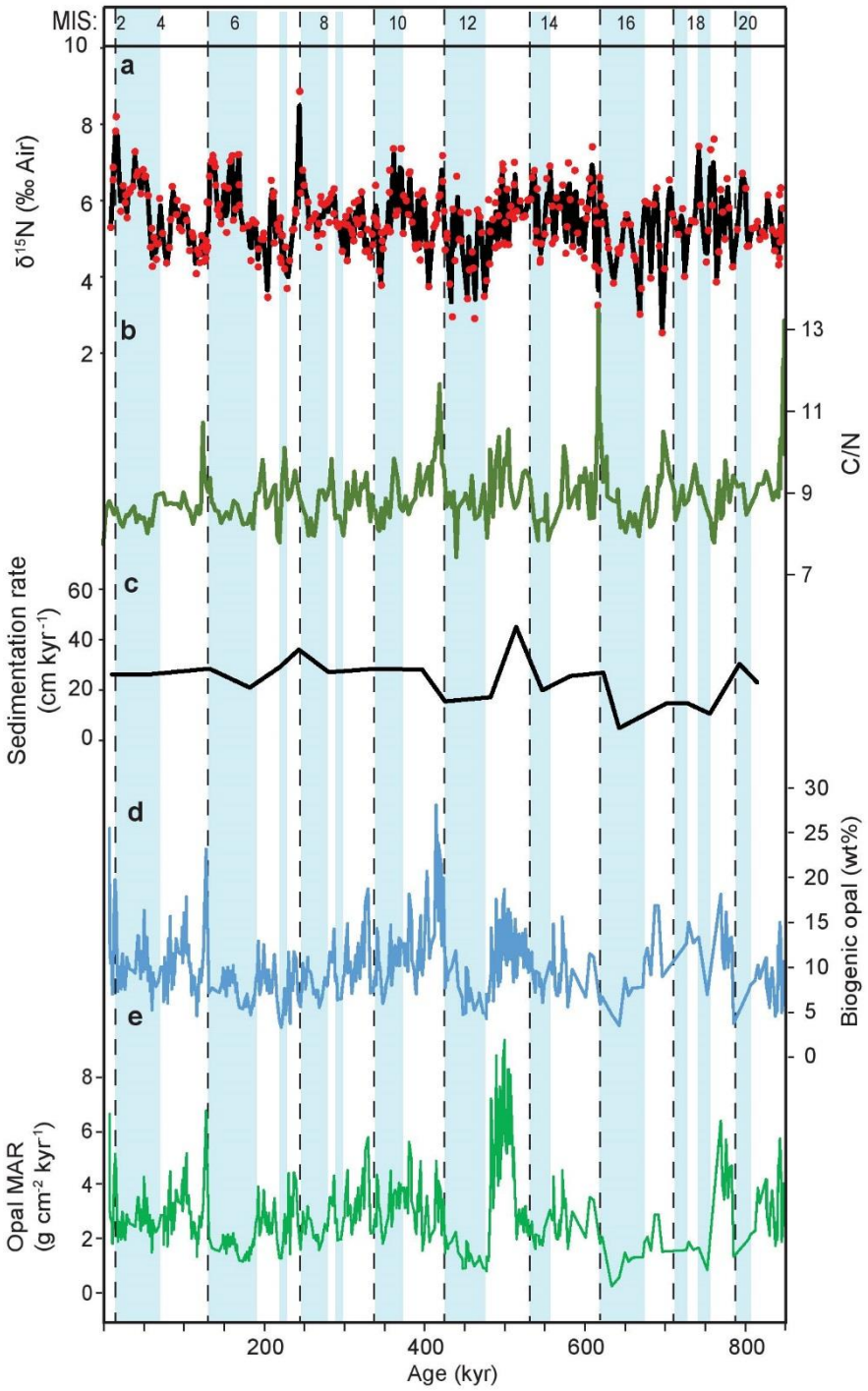


Figure 2.6 Bulk $\delta^{15}N$ and Biogenic Opal data for IODP Site U1343. a) Bulk $\delta^{15}N$ data (red dots) from this study and previously published lower resolution data (Kim et al., 2017b), smoothed using a linearly interpolation to create a 2 kyr resolution dataset (black line). b) C/N ratios, which are low and show a lack of covariation to $\delta^{15}N$, suggesting that terrestrial input of nitrogen was low and did not drive the $\delta^{15}N$ record. c) New sedimentation rates calculated for IODP Site U1343 using the updated age model presented in this study, which were then applied to d) the biogenic opal record (Kim et al. 2014) to calculate e) the opal mass accumulation rate (MAR) data.

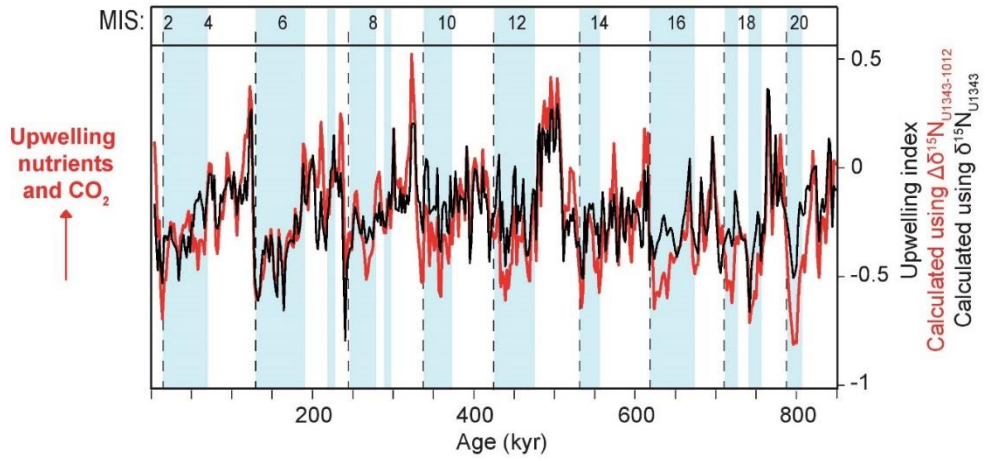


Figure 2.7 Assessing the relative contribution of $\delta^{15}N_{1012}$ to $\Delta\delta^{15}N_{U1343\text{-}1012}$. Results demonstrate that there is no significant difference between the upwelling index record calculated using $\Delta\delta^{15}N_{U1343\text{-}1012}$ compared to $\delta^{15}N_{U1343}$ (where the latter does not subtract the ODP 1012 record) ($t = -1.93$, $p = 0.05$).

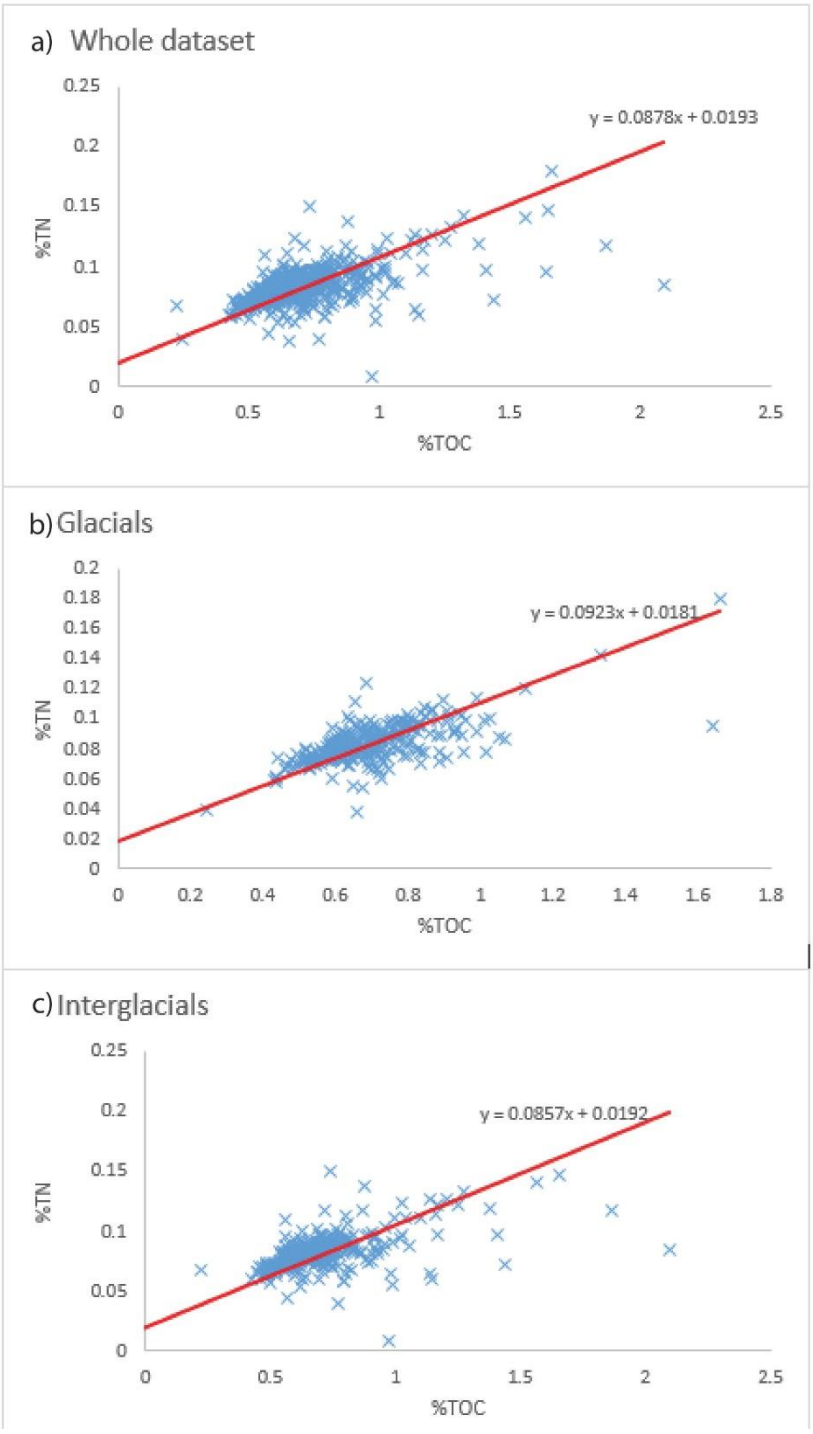


Figure 2.8 %TOC vs %TN cross plots for IODP Site U1343 from this study and previously published lower resolution data (Kim et al., 2017b). a) Shows the cross plot for the whole dataset, with an intercept of 0.0193, suggesting minimal influence of inorganic nitrogen. Similarity between b) glacial intercept of 0.0181 and c) interglacial intercept of 0.0192, suggests that variable contribution of terrestrial/inorganic nitrogen does not drive the bulk $\delta^{15}N$ record presented here.

Table 2.1 Benthic foraminiferal $\delta^{18}O$ offsets applied to species/genus, from *Elphidium batialis* (Kender et al., 2018). The total number of samples for each group is also noted.

Species	**Offset from *Elphidium batialis* (‰)**	**Number of samples**
Elphidium batialis	0	117
***Valvulineria* spp.**	+ 0.25	6
Islandiella norcrossi	+ 0.48	9
***Cassidulina* spp.**	+ 0.56	11
***Nonionella* spp.**	+ 0.65	2
***Globobulimina* spp.**	+ 0.85	61
***Uvigerina* spp.**	+ 0.87	56

Table 2.2 New age-depth tie points for Site U1343, building upon work of Asahi et al., (2016). Age model constructed by tuning to LR04 global benthic stack (Lisiecki & Raymo, 2005) (see Methods).

Depth (CCSF – A) (m)	Age (kyr)
0.96	10.15
14.23	57.38
36.72	131.41
48.03	181.46
59.73	219.06
68.72	242.57
79.52	279.96
96.24	335.14
114.56	396.17
119.35	424.39
129.90	480.93
145.02	512.78
152.01	545.32
161.63	580.48
173.39	621.39
174.57	641.03
184.09	700.03
188.27	725.84
191.58	753.63
203.57	790.75
209.04	812.86

Chapter 3: Reduced high latitude upwelling in the subarctic Pacific during the MPT, modulated by sea level and sea ice

Savannah Worne[1]*, Sev Kender[2,3], George E. A. Swann[1], Melanie J. Leng[3,4], and Ana Christina Ravelo[5]

[1]Centre for Environmental Geochemistry, School of Geography, University of Nottingham, Nottingham, NG7 2RD, UK

[2]Camborne School of Mines, University of Exeter, Penryn Campus, Penryn, Cornwall, TR10 9FE, UK

[3]British Geological Survey, Keyworth, Nottingham, NG12 5GG, UK

[4]Centre for Environmental Geochemistry, School of Biosciences, University of Nottingham, Sutton Bonington Campus, Loughborough, NE12 5RD, UK

[5]University of California, Santa Cruz, CA 95064, USA

*Corresponding author. Email: savannah.worne@nottingham.ac.uk

Abstract

An enigmatic global cooling and shift in glacial-interglacial cyclicity occurred between 0.6 and 1.2 Ma, known as the Mid-Pleistocene Transition (MPT). During this period, reduced high latitude upwelling and ocean-atmospheric CO_2 fluxes, particularly in the Southern Ocean, are considered a potential mechanism for the change in climatic response to orbital forcing. However, growing evidence from the Bering Sea suggests that the subarctic Pacific Ocean

may also play a key role in glacial-interglacial CO_2 dynamics. Although sea ice is considered the ultimate control on late Quaternary Bering Sea nutrient upwelling, there are so far no continuous high latitude upwelling records over the MPT with which to test this hypothesis. Using nitrogen isotopes and opal mass accumulation rates (MAR) from 0–1.2 Ma, I calculate a high resolution nutrient upwelling index to determine long term variability in deep water nutrient upwelling in the Bering Sea and assess the role of sea ice, sea level and NPIW in controlling upwelling.

In addition to strong obliquity forcing, time series analysis shows varying contributions of precession and suborbital periodicities on nutrient upwelling. Higher frequency cyclicity suggests a seasonal influence on sea ice-controlled nutrient upwelling, forced by changes in lower latitude Pacific climate (increased Walker circulation and a weakening of the East Asian winter monsoon) that expanded sea ice before the MPT. I find that upwelling nutrients broadly follow the global benthic $\delta^{18}O$ stack (LR04), lending support to the hypothesis that high latitude upwelling could have modulated atmospheric CO_2 and global climate changes through the MPT. During the 900 kyr event, suppressed nutrient upwelling due to significant sea ice volume was coincident with the greatest sea level decline and closure of the Bering Strait. The resultant expansion of North Pacific Intermediate Water (NPIW) likely contributed to low atmospheric pCO_2 in post-MPT glacials. I also find higher frequency fluctuations in upwelling which are proposed to result from atmospheric teleconnections to lower latitude Pacific Ocean processes linked to the increase in Walker circulation (McClymont & Rosell-Melé, 2005; Stroynowski et al., 2017).

3.1 Introduction

The Mid-Pleistocene Transition (MPT) occurred between ~1.2 - 0.6 Ma during which glacial-interglacial cycles in global climate increased from a 41 kyr to a longer quasi-100 kyr periodicity (McClymont et al., 2013). The MPT centres on a step-wise increase in benthic foraminiferal $\delta^{18}O$ at the "900 kyr event" (~ 0.9 Ma) which is characterised thereafter by a dramatic increase in continental ice sheet volume and a rapid decline in global sea level (~50 – 150 m) during post-MPT glacial periods where 100 kyr cyclicity emerges (Lisiecki & Raymo, 2005; Elderfield et al., 2012). One mechanism for MPT climate evolution includes changing land ice-sheet dynamics (Clark & Pollard, 1998; Raymo et al., 2006; Crowley & Hyde, 2008), either controlled by basal erosion or continental ice-sheet instability (Clark et al., 2006) following expansion of the Antarctic ice sheet (Clark et al., 2006; Pollard & DeConto, 2009), triggering increased fluctuations in sea level (Elderfield et al., 2012) and thermohaline circulation (Schmieder et al., 2000; Sexton & Barker, 2012). Alternatively, the MPT may represent a tipping point in a long-term decrease in atmospheric pCO_2 (Raymo, 1997) and/or a shift in ocean-atmosphere CO_2 exchange (Pena & Goldstein, 2014) particularly from high latitude oceans, as a result of increased stratification and/or increased efficiency of the biological pump following altered nutrient/dust supply (Martínez-Garcia et al., 2011; Chalk et al., 2017; Kender et al., 2018). This is supported by evidence for expansion of polar/sub-polar water masses in the Pacific, Atlantic and Southern Oceans (McClymont et al., 2008; Martinez-Garcia et al., 2010; Rodríguez-Sanz et al., 2012) during the MPT. Others have suggested that a shift in the relationship between sea ice and land ice formation (the "sea ice switch") following deep ocean cooling

could also have been key (Gildor & Tziperman, 2001). In this case, expanded glacial sea ice limited moisture availability for land ice growth, forming a land versus sea ice hysteresis model. At a critical threshold, deglaciation of continental ice sheets is triggered prior to the sea ice maxima, instigating longer glacials with rapid deglacial phases which characterise the saw-tooth shape of post-MPT glacial cycles (Tziperman & Gildor, 2003).

Many of these hypotheses remain largely untested due to a lack of high resolution and long term palaeoenvironmental data. For example, the longest continuous observational record for atmospheric pCO_2 is limited to the last 0.8 Ma (Lüthi et al., 2008). An additional study by Chalk et al., (2017) uses boron isotopes ($\delta^{11}B$) to infer pre-MPT pCO_2 concentrations, however this is limited to a short time window between 1.08 and 1.25 Ma and does not include samples over the 900 kyr event. Although there is increasing evidence for changing ocean/atmosphere interaction in the high latitudes and sensitivity to atmospheric teleconnection with lower latitudes during the MPT, linked with ice-sheet expansion (Marlow et al., 2000; Heslop et al., 2002; Liu & Herbert, 2004; McClymont & Rosell-Melé, 2005; McClymont et al., 2008; Sexton & Barker, 2012) it is not clear whether these feedbacks were sufficient to control climate change and cause increased ice volumes and/or decreased atmospheric pCO_2 through the mid-late Pleistocene, or simply modulated the pace of climatic response to orbital variability.

Modelling and observational evidence is also heavily biased towards the Southern Ocean, which is known to be a critical region for the growth of land and sea ice, deep water formation and the upwelling of nutrient- and CO_2-rich waters, fuelling an efficient but variable biological pump that has dominated

atmospheric pCO_2 variability over Quaternary glacial-interglacial cycles (Billups et al., 2018). Another key, but comparatively understudied location, is the high latitude subarctic Pacific Ocean and the Bering Sea, which is adjacent to the North American Ice Sheets (NAIS) and has been influenced by sea ice since the onset of Northern Hemispheric glaciation (~2.7 Ma) (Teraishi et al., 2016; Stroynowski et al., 2017). Furthermore, the Bering Sea is of palaeoceanographic importance, as North Pacific Deep Water (NPDW) upwells at the Bering shelf; previous research from the Bering slope has shown a strong link between NPDW upwelling at the shelf edge and global atmospheric pCO_2 in the mid-late Pleistocene (post-MPT), with expanded sea ice suggested to modulate deep water upwelling and ocean-atmosphere CO_2 exchange across the wider subarctic Pacific region (Kender et al., 2018; Worne et al., 2019). This process may have been driven via the influence of sea ice on the formation of dense and nutrient poor North Pacific Intermediate Water (NPIW), which expanded during glacial periods and prevented vertical mixing and the upwelling of NPDW to the photic zone (Kender et al., 2018; Worne et al., 2019). The closure of the Bering Strait, following a sea level drop of >50 m during the 900 kyr event, is considered a critical threshold at which point Bering Shelf-formed NPIW was forced to flow southward into the lower subarctic, causing region-wide isolation of CO_2 in deep waters (Kender et al., 2018).

However, the short temporal resolution of existing MPT records and the lack of similar datasets from the early Pleistocene limit the assessment of long term and high resolution investigation of the relationship between global climate, atmospheric pCO_2 and subarctic nutrient upwelling, prior to significant glacial sea level decline at 0.9 Ma. Therefore, the first continuous, high resolution

nutrient upwelling index (Worne et al., 2019) from the Bering Sea slope (Site U1343, 1,950 m water depth) which extends from 1.2 Ma to present is presented here, in order to assess the evolution of Bering Sea nutrient upwelling with respect to sea ice and sea level (NPIW) through the early Pleistocene, and to determine the long term significance of these changes for the wider subarctic Pacific Ocean. In this paper a continuous nutrient upwelling record for the Bering Sea is provided by combining records of opal accumulation and bulk sedimentary $\delta^{15}N$, as proxies for productivity and nutrient utilisation, respectively. From this, changes in nutrient upwelling are used to constrain the role of sea ice, subarctic Pacific oceanography and atmospheric teleconnections (with the lower latitude Pacific Ocean) on glacial-interglacial climate dynamics through the Pleistocene.

3.2 Methods

3.2.1 Core materials

Core materials from IODP Site U1343 (57°33.39′N, 175°48.95′W, water depth 1,950 m) were collected during IODP Expedition 323. Situated on a topographic high adjacent to the northern continental shelf, and proximal to the modern winter sea ice edge, IODP Site U1343 sits in the green belt region and is directly influenced by the BSC and high eddy activity, causing high rates of nutrient upwelling and primary productivity (Figure 1.3). Marine sediments are composed primarily of fine clays and biogenic material, and are characteristically distinct from shelf-transported materials (Aiello & Ravelo, 2012).

3.2.2 Updated Site U1343 Age Model (1.01 – 1.20 Ma)

Good preservation of benthic foraminifera at Site U1343 has allowed construction of a high resolution $\delta^{18}O_{U1343}$ age model from 0 - 1.02 Ma (Asahi et al., 2016; Kender et al., 2018; Worne et al., 2019). Here an additional 48 new data points from 284.06 – 338.32 m CCSF-A extend the high resolution age model back to 1.2 Ma. Following previous studies at this site, ~100 μg of foraminiferal calcite from ten different species were measured for $\delta^{18}O$, applying species-specific offsets to fit the data to the most commonly occurring species, *E. batialis*. $\delta^{18}O$ measurements were made using an IsoPrime© mass spectrometer with a Multicarb device at the British Geological Survey, with a precision of <0.05‰ based on duplicates. The stable isotope data were calibrated to the VPDB scale through the international NBS standards.

Benthic foraminiferal isotope data presented here were combined with previously published data from Site U1343 (Asahi et al., 2016; Kender et al., 2018; Worne et al., 2019) to create a total of 1825 $\delta^{18}O_{U1343}$ data points with an average time step of 0.65 kyr (Figure 3.1). Using 30 age-depth tie points at periods of rapid isotopic change (e.g. deglacials), the age model was defined by correlating to the LR04 global composite stack (Lisiecki & Raymo, 2005) (Table 1.3). Poor linear regressions between foraminiferal $\delta^{13}C$ and both raw $\delta^{18}O$ ($R^2 = 0.00$) and $\delta^{18}O$ adjusted to E. batialis ($R^2 = 0.19$) suggests that diagenetic alteration of foraminiferal shells does not explain the glacial-

interglacial variability in the benthic foraminiferal $\delta^{18}O$ isotope data at IODP Site U1343 (Asahi et al., 2016; Kender et al., 2018; Worne et al., 2019).

3.2.3 Bulk sedimentary $\delta^{15}N$

Bulk sedimentary $\delta^{15}N$ was measured using 500 mg of raw material on a Carlo Erba 1108 elemental analyzer, interfaced to a Thermo Finnigan Delta Plus XP IRMS at the University of California, Santa Cruz, with a precision of 0.15‰ based on both sediment standards and replicates. At Site U1343 ($\delta^{15}N_{U1343}$), the 63 data points measured on samples taken between 1.02 - 1.2 Ma presented here (relative to atmospheric nitrogen (AIR)), were combined with previously published data from 0 – 1.02 Ma (Kim et al., 2017; Kender et al., 2018; Worne et al., 2019) to produce a composite record of 623 data points, with an average resolution of 1.9 kyr on the updated age model (Figure 3.1).

3.2.4 Upwelling index

The bulk $\delta^{15}N_{U1343}$ record in the Bering Sea has been suggested to be influenced by a denitrification signal which propagates from the Eastern Tropical North Pacific (ETNP) (Brunelle et al., 2007). Therefore, I follow previous work (Galbraith et al., 2008; Knudson & Ravelo, 2015a; Worne et al., 2019) which uses linear interpolation to subtract the North Pacific Ocean $\delta^{15}N$ records from ODP Site 1012 ($\delta^{15}N_{1012}$), thought to be a site of near complete nutrient utilisation as well as being influenced by waters from the ETNP denitrification zone (Liu et al., 2005; Galbraith et al., 2008). By constraining for background changes in source water $\delta^{15}N$, the resultant isotope record ($\delta^{15}N_{U1343\text{-}1012}$) reflects only changes in nutrient utilisation at the Bering slope (Worne et al., 2019).

As nutrient utilisation is a product of both the total nutrient supply and biogenic productivity, the opal MAR records from Site U1343 (Figure 3.1) (Kim et al., 2014) can be used to further constrain the changes in local nutrient utilisation, following the methodology of Worne et al. (2019) . Assuming that the upwelling of NPDW was the dominant supply of macronutrients to surface waters at Site U1343, the rates of nutrient utilisation are controlled by both upwelling strength and the delivery of iron (Fe) from sea ice entrained sources (in addition to contributions from deep water). Given that the green belt is iron limited, under a constant rate of nutrient upwelling, Fe supply will increase both productivity and nutrient utilisation and will therefore not change the upwelling index significantly (Worne et al., 2019). Therefore, the resultant "upwelling index", is a semi-quantitative measure of nutrient supply, where low (high) values suggest a decrease (increase) in NPDW upwelling strength at the Bering slope.

Applying this calculation to the linearly interpolated $\delta^{15}N_{U1343}$ data presented here from 0.85 – 1.2 Ma, the upwelling index results are extended to cover the last 1.2 Ma , on which REDIFT and time series analysis by means of a continuous wavelet transform are performed using PAST (Hammer et al., 2001) (with a time step of 2 kyr), to identify the significant periodicities and the role of orbital forcing on nutrient upwelling (Figure 3.2, Figure 3.3). Given that the MPT is characterised by a step-wise change in the dominant periodicity, the record was also split into two time intervals, pre MPT (0.866 – 1.2 Ma) and post MPT (0 – 0.866 Ma), on which spectral analysis was performed, to assess the different orbital frequencies impacting nutrient upwelling in each discrete period (Figure 3.2).

3.3 Results

3.3.1 $\delta^{15}N_{U1343}$ and the upwelling index

Pre-MPT $\delta^{15}N_{U1343}$ results (1.02 – 1.2 Ma) show a higher mean (6.56) than during the 900 kyr event (~0.85 - 0.95 Ma; mean = 6.03) or post-MPT (0 – 0.85 Ma; mean = 5.58) (Figure 3.1). This is consistent with higher opal MAR during this period, where increased productivity caused a larger proportion of the nutrient pool to be used. With the exception of MIS 31/32 boundary (~1.06 Ma) when nutrient utilisation is notably low, there is also glacial-interglacial variability in the $\delta^{15}N_{U1343}$ with glacials exhibiting significantly lower nutrient utilisation (mean = 5.73) than interglacial periods (mean = 5.90, $p < 0.05$), reflecting higher productivity during warmer periods (Figure 3.1). Low $\delta^{15}N_{U1343}$ excursions may be a result of inorganic or terrestrial input, however, given that $\delta^{15}N$ reflects a combination of both surface water $\delta^{15}N$ processes and the deep water signal, low C/N ratios during these intervals and a lack of glacial-interglacial covariation between $\delta^{15}N_{U1343}$ and C/N, suggests inorganic nitrogen input does not control $\delta^{15}N_{U1343}$ (Kim et al., 2017; Worne et al., 2019). Furthermore, low $\delta^{15}N$ values measured at other open ocean subarctic North Pacific sites, e.g. Site MD2416, ODP Site 882 and ODP Site 887, together with diatom-bound $\delta^{15}N$ values less than 5‰ at Site U1343 (Kim & Khim, 2016), also provides confidence that nutrient utilisation changes rather than terrestrial/inorganic nitrogen input, is the most significant control on Quaternary glacial-interglacial $\delta^{15}N_{U1343}$ variability.

From MIS 33, the upwelling index shows a gradual increase, reaching a peak in early glacial MIS 30 (~1.05 Ma), where productivity is high and nutrient utilisation is minimal (Figure 3.1, Figure 3.3). Between MIS 30 and MIS 28

(~1.05 – 0.98 Ma), results show a sharp and continued decrease in nutrient upwelling as colder MPT conditions develop, with interglacial upwelling remaining low during MIS 29 (~1.02 Ma). Despite a recovery in nutrient upwelling strength through MIS 27 – 25 (~0.97 – 0.93 Ma), particularly in interglacials where both productivity (opal MAR) and the rate of nutrient utilisation ($\delta^{15}N_{U1343}$) are notably high, a rapid decline in the upwelling index occurs during MIS 24 (~0.91 Ma) where productivity is minimal (Figure 3.1, Figure 3.3) During the 900 kyr event, there is a continued minima in the upwelling index results, particularly through MIS 23 and early MIS 22 (~ 0.86 – 0.91), coincident with sustained sea level drop >50 m water depth (Figure 3.1, Figure 3.3). At the end of glacial MIS 22 there is a gradual increase in upwelling strength, reflecting recovering productivity until the deglacial peak. From ~0.85 Ma onwards, nutrient upwelling exhibits strong glacial-interglacial variability, with low (high) upwelling during glacials (interglacials)(Worne et al., 2019).

3.3.2 Cyclicity analysis

Spectral analysis of the whole 1.2 Ma record identified all three orbital forcing bands, where the eccentricity and precession periodicities (100 kyr and 23kyr, respectively) were the most dominant with a confidence interval of 99%, while the obliquity forcing (41 kyr) was distinguished with 95% confidence (Figure 3.2). Spectral analysis of pre-MPT (0.87 – 1.2 Ma) and post-MPT (0 – 0.86 Ma) sections were also completed, to assess the changing role of solar forcing on nutrient upwelling in each time period. Post-MPT results showed the same results as those for the whole record, with the 100 kyr being the most dominant frequency. This is consistent with other global proxy records which identify an

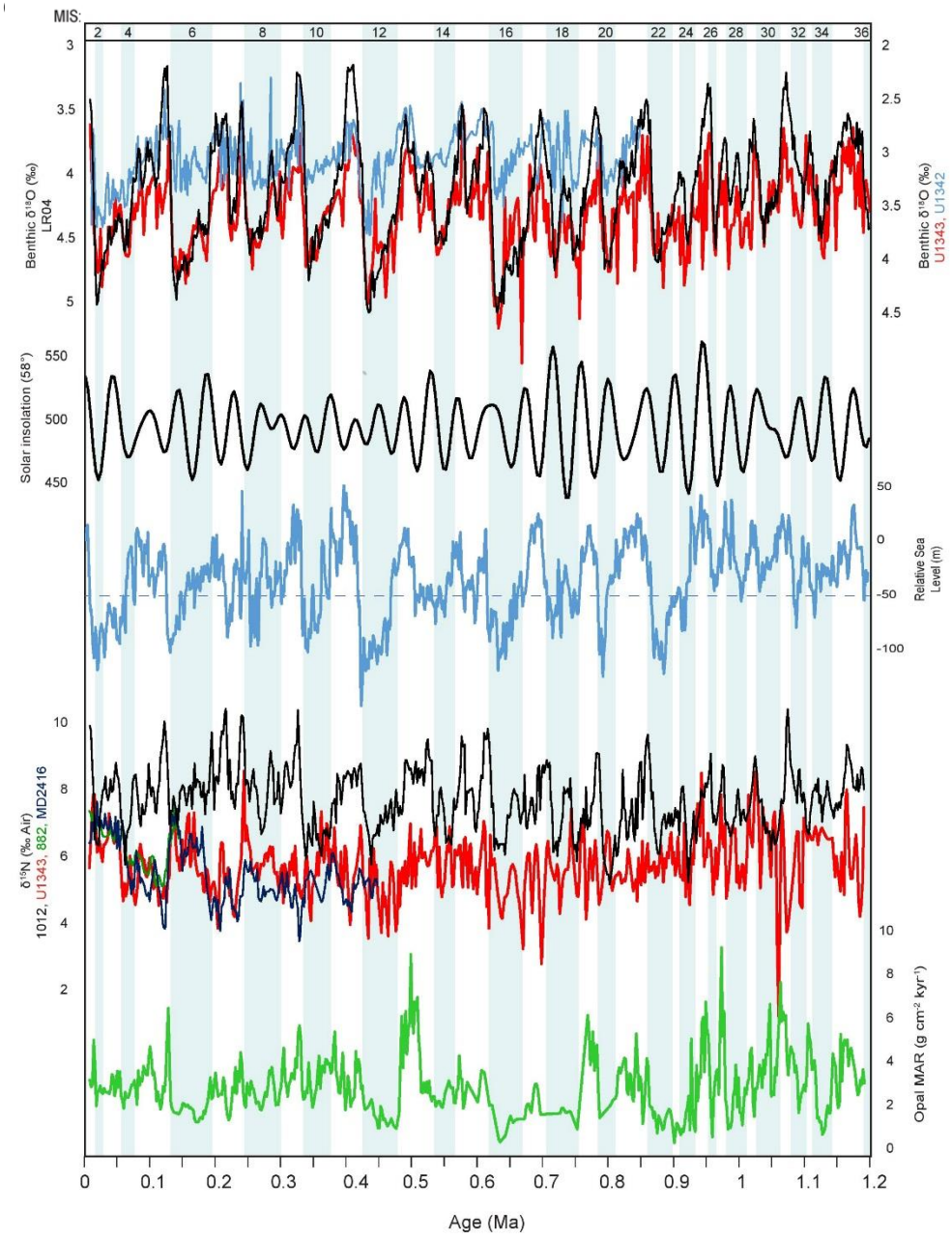


Figure 3.1 Geochemical proxy results from IODP Site U1343 from MIS 2 to 36. a) Benthic foraminiferal $\delta^{18}O$ results from IODP Site U1343 compared to those from the shallower IODP Site U1342 and the LR04 global benthic $\delta^{18}O$ stack (Lisiecki & Raymo, 2005), where blue bars represent glacial periods as identified in the LR04 record. The data from Site U1342 has been recalculated here to match benthic foraminiferal offset for *E. batialis*, used for Site U1343 (Kender et al., 2018). b) Solar insolation received at 55°N. c) Relative sea level changes estimated by Elderfield et al. (2012), where the dashed line represents 50 m lower sea level than present, at which point the Bering Straight was likely closed. d) Bulk $\delta^{15}N$ data from IODP Site U1343 compared with deep North Pacific ODP Site 1012 (a site of complete nutrient utilisation) (black) together with bulk $\delta^{15}N$ records from ODP Site 882 (green) and MD2416 (navy blue) in the subarctic North Pacific Ocean. e) Opal mass accumulation rate (MAR) from IODP Site U1343 [adapted from Kim et al. (2014), using the new age model].

mid-late Pleistocene (Clark et al., 2006). However, pre-MPT results show that the most dominant periodicity in nutrient upwelling was ~12 kyr, with a confidence interval of 99%.

Given that the MPT represents a non-stationary shift in periodicity, continuous wavelet transform analysis of the upwelling index was completed to assess the changing role of insolation forcing through time (Figure 3.3). Results indicate a significant periodicity reflecting the obliquity forcing band of ~41 kyr through almost the entire record, except during the 900 kyr event. I acknowledge that through tuning the age model with the LR04 benthic stack (Lisiecki & Raymo, 2005), glacial-interglacial variability is somewhat imposed upon the upwelling index, however use of a limited number of deglacial tie points and the high resolution of the record (2 kyr) suggests consistent identification of this periodicity is likely a real signal. Between MIS 30 and MIS 34 (~1.14 – 1.04 Ma), the upwelling index also appears to respond to the precession forcing of ~23 kyr. However, this is replaced by a suborbital frequency of ~12 kyr between MIS 28 – 24 (~ 0.9 – 1 Ma), when interglacial nutrient upwelling partially recovers to higher values. Although neither the obliquity nor precession forcing bands are identified in the pre-MPT spectral period, this is likely a result of the averaging the spectral power across the 0.87 – 1.2 Ma period which shows high variability; therefore discussion of the continuous wavelet analysis results are prioritised.

Also coincident with the development of suborbital periodicity, a ~123 kyr cycle emerges around ~ 1.1 Ma, which then extends through the MPT up until at least ~0.4 Ma. Although it falls outside of the cone of influence and hence cannot be deemed significant, it is possible that this longer cyclicity

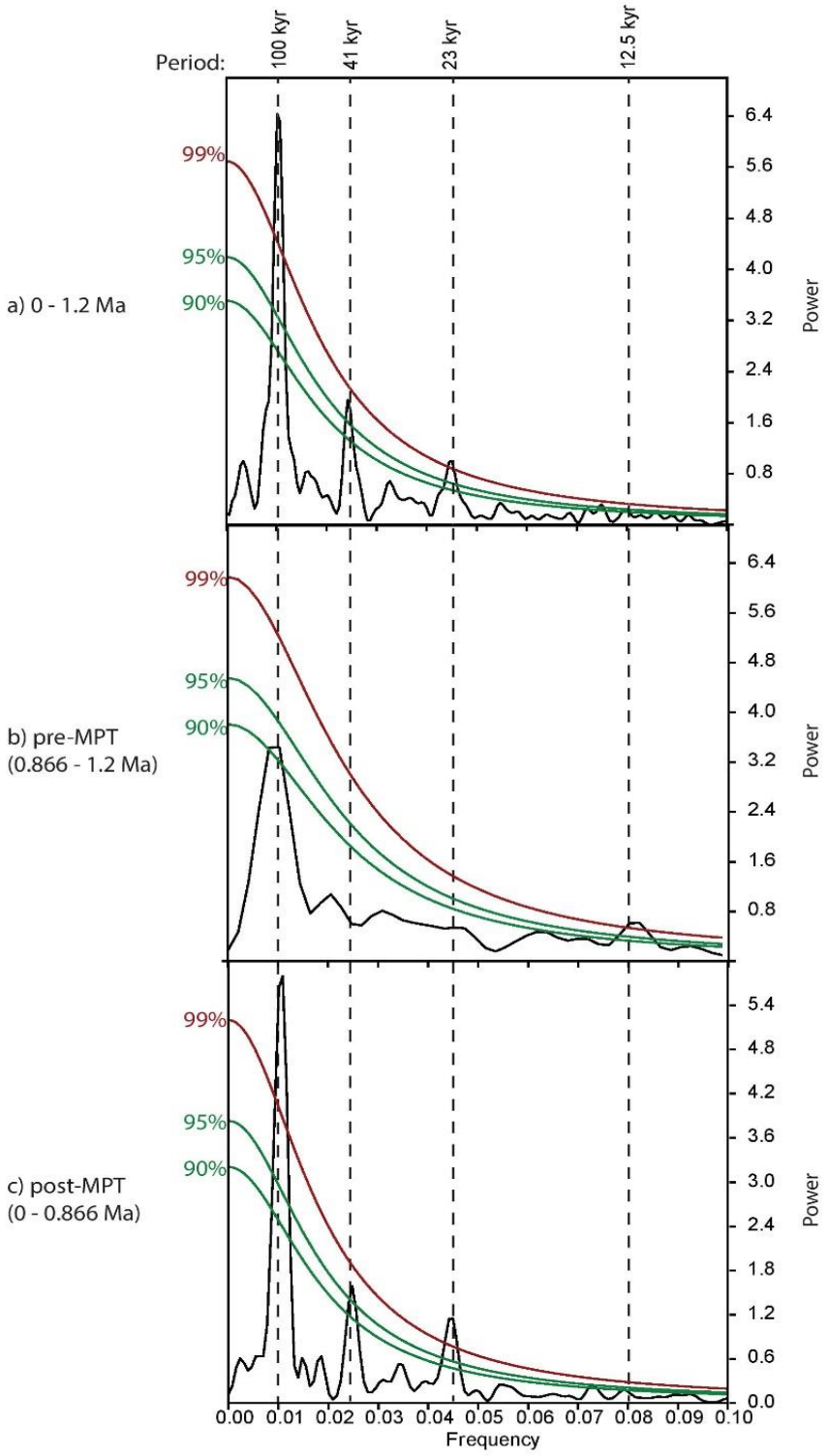


Figure 3.2 REDFIT spectral analysis, setting the oversample and segment size to 1, was run to fit the upwelling index time series dataset to a first-order red-noise model between 0 – 1.2 Ma (Hammer et al., 2001) (a). Similar analysis of pre-MPT data (0.866 – 1.2 Ma) (b) and post-MPT results (0 – 0.866 Ma) (c) are also presented, where the vertical dashed lines represent the key periodicities of the Milankovitch orbital forcings. Confidence bands at 99 (red), 95 and 90% (green) are also displayed.

the upwelling index and the LR04 benthic stack (Figure 3.4). This is supported by significance of the 100 kyr periodicity in the spectral analysis of the post-MPT section (0 - 0.87 Ma). During the 900 kyr event, a ~50 kyr periodicity is the most significant cyclicity, and most likely reflects a harmonic of the longer ~100 kyr eccentricity cycle. After the MPT step-change, the 23 kyr precession and 41kyr obliquity forcings again become significant, as in the early Pleistocene, persisting until ~0.4 Ma. The millennial scale periodicity (~12 kyr) which disappeared through the mid-Pleistocene then re-emerges after ~0.4 Ma, until present.

To confirm that the higher frequency periodicity of 12 kyr identified in the wavelet analysis is robust, the same analysis was completed on a recalculated upwelling index with a time-step of 6 kyr (Supplementary Figure 3.6). This larger time-step was selected as it exceeds the mean + 2σ of the resolution of both the $\delta^{15}N_{U1343}$ (mean + 2σ = 4.8 kyr) and opal MAR (mean + 2σ = 5.4 kyr) datasets. As this time-step was larger, it is perhaps unsurprising that the 12 kyr signal in the early and late Pleistocene is lost, where only two data point would contribute to a 12 kyr cycle. Instead, an unusual ~16 kyr cyclicity is significantly identified throughout the study interval.

3.4 Discussion

3.4.1 Nutrient upwelling and glacial-interglacial climate

The upwelling index from 0 – 0.85 Ma has been previously shown to correlate with a number of proxy and modelled climate records (Worne et al., 2019), including the LR04 deep ocean $\delta^{18}O$ record (reflecting a combination of global ice volume and deep ocean temperature) (Lisiecki & Raymo, 2005), relative sea

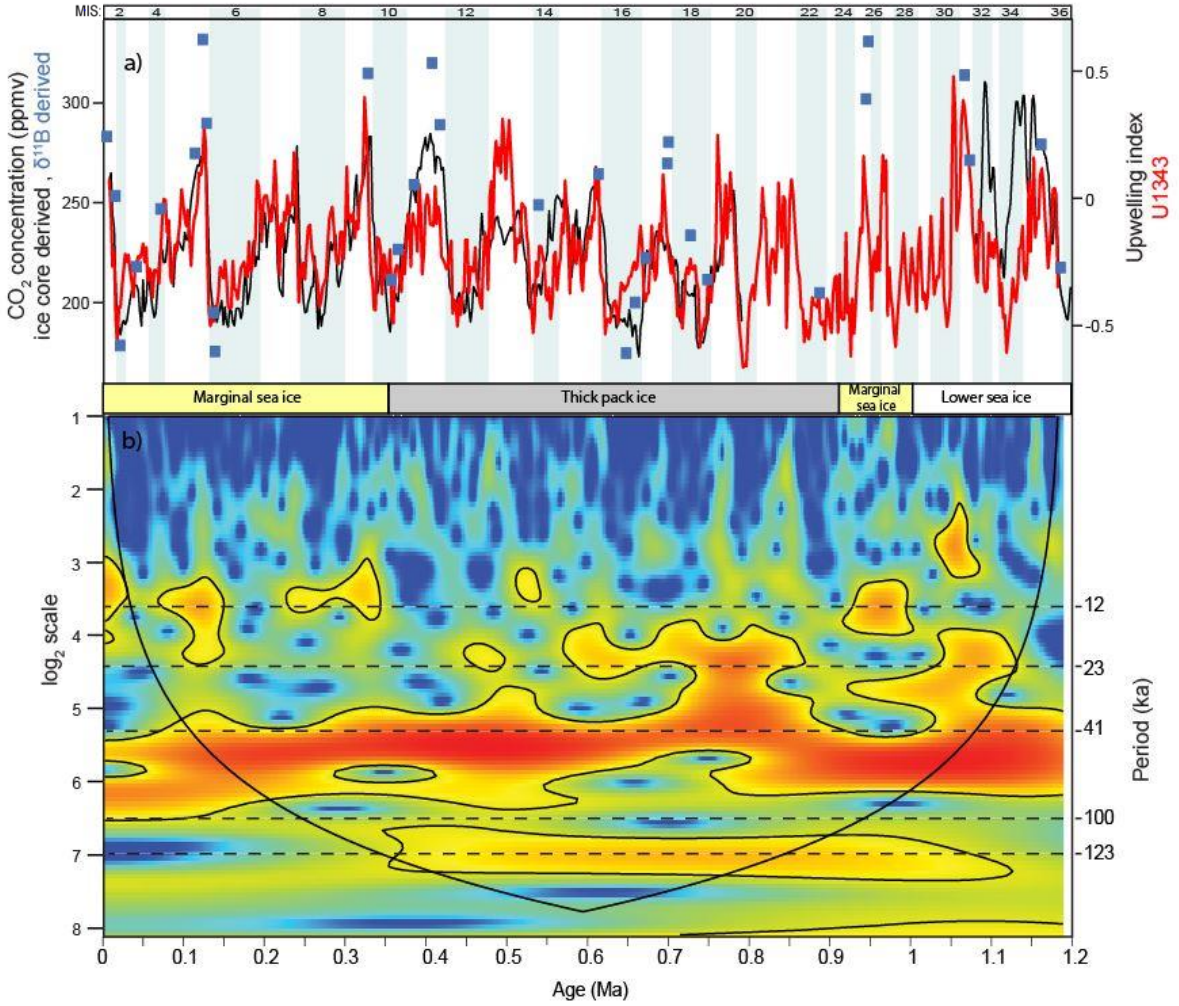


Figure 3.3 Upwelling index results between 0 – 1.2 Ma (red) are compared to proxy derived pCO_2 estimates (black) from the Vostok ice core between 0 – 0.8 Ma (Lüthi et al., 2008), and from boron isotope measurements between ~1.07 – 1.2 Ma (Chalk et al., 2017) (a). Low resolution boron isotope-derived pCO_2 estimates from Hönisch et al. (2009) are also displayed as blue squares (a). b) Wavelet analysis of the upwelling index from 0 – 1.2 Ma, where red/warmer values indicate higher spectral power than blue/colder colours (temperature gradient). Dashed lines represent the periodicities of the Milankovitch orbital cycles, and the solid black line represents the cone of influence, above which results are considered significant. The coloured bars (yellow, grey and white) above panel (b) represent the evolution of sea ice and variable response to orbital and millennial scale forcings (see Figure 3.4).

level changes (Elderfield et al., 2012), global surface ocean temperatures (Snyder, 2016) and Antarctic air temperatures (Jouzel et al., 2007). In particular, a strong correlation with global pCO_2 (Lüthi et al., 2008), was suggested to indicate a common underlying mechanism between NPDW upwelling in the Bering Sea and global climate changes (Worne et al., 2019).

Over the longer 0 - 1.2 Ma interval presented here, there is a strong correlation between the upwelling index and relative sea level (r = - 0.47) and surface air temperatures (r = 0.58), although the tightest correlation occurs with the LR04 stack (r = - 0.65). Although the age model for the upwelling index was tuned to the LR04 stack, the high resolution of the dataset (2 kyr) and the limited number of tie points used (30), suggests that there is a likely relationship between global ice volume, deep ocean temperature and Bering Sea nutrient upwelling. While there is no continuous pCO_2 proxy record through the MPT, $\delta^{11}B$ inferred pCO_2 reconstruction from ODP Site 990 in the Caribbean Sea between ~1.1 - 1.2 Ma (Chalk et al., 2017) and sporadic measurements from ODP Site 668B in the eastern equatorial Atlantic across the Plio-Pleistocene (Hönisch et al., 2009), consistently follows the upwelling index results during the early Pleistocene (Figure 3.3) with higher nutrient upwelling and pCO_2 occurring during warmer interglacial periods. Despite an offset between pCO_2 and nutrient upwelling minima, the increase in pCO_2 from late MIS 34 is consistent with increasing nutrient upwelling.

Further support for the tight correlation between nutrient upwelling in the Bering Sea and global pCO_2 prior to the MPT is found in the predicted pCO_2 record from the CYCLOPS carbon cycle model (Chalk et al., 2017) (Figure 3.5). Comparison with the upwelling index record presented here, demonstrates glacial-interglacial consistency over the last 1.2 Ma (Figure 3.3, Figure 3.5), where the magnitudes of change in nutrient upwelling appear to scale consistently with changes in pCO_2. The only sustained discrepancy between the two datasets appears during the 900 kyr event, when nutrient upwelling remains lower than predicted pCO_2, particularly during late MIS 22 (Figure 3.5).

3.4.2 Orbital forcing and sea ice control on nutrient upwelling

Glacial-interglacial variability in the upwelling index is thought to be largely controlled by sea ice (Worne et al., 2019), where it plays an active role in controlling total annual primary production (opal MAR) through stabilising the water column and supplying micronutrients which facilitate a spring melt associated bloom (Aguilar-Islas et al., 2008; Kanematsu et al., 2013), brine rejection and formation of intermediate water (Knudson & Ravelo, 2015b). The size of the subsequent summer/autumn bloom is highly dependent on the degree of post-melt stratification and the availability of remaining nutrients after drawdown in the spring (Hansell et al., 1989). Sea ice also influences the rate of nutrient utilisation ($\delta^{15}N$), as the strength of deep water upwelling and the availability of nutrients will be at least in part dependent on the presence of NPIW formed during brine rejection on the continental shelf (Kender et al., 2018; Worne et al., 2019).

Wavelet analysis revealed that 41 kyr obliquity insolation forcing is consistently a significant driver of the nutrient upwelling index for the entire 1.2 Ma record, consistent with the correlation between Bering Sea upwelling and global climate (LR04 benthic stack) (Figure 3.3, Figure 3.4). As obliquity controls global latitudinal heat gradients and the amount of insolation received annually by the Earth, it is considered the dominant influence on northern high latitude climate (Raymo & Nisancioglu, 2003). Latitudinal heat gradients also drive variability in atmospheric circulation, which in turn propagate through atmospheric pressure systems. In the Bering Sea, this may manifest through the location and intensity of the Aleutian Low, which plays a key control on winter conditions. Advection of cold air masses, increased storm frequency and

greatest sea ice production is associated with a strong/displaced Aleutian Low and a weakened East Asian winter monsoon (EAWM) (Rodionov et al., 2007). Therefore, the obliquity forcing band can influence upwelling strength through varying these systems which drive wind-driven eddy formation in the BSC, Bering gyre strength and sea ice growth/extension (through poleward moisture and heat delivery as well as storm frequency).

On the other hand, precession-driven variability with a cyclicity of 23 kyr determines the strength of the summer/autumn insolation and seasonal contrast, and would play an important role in determining the timing and rapidity of sea ice melt, as well as summer/autumn stratification of the photic zone (Stabeno et al., 1999). Therefore, the identification of precession insolation forcing on the upwelling index through various sections of the record (Figure 3.2, Figure 3.3), likely reflects the crucial and changing role of timing/duration of sea ice melting on primary productivity and nutrient utilisation.

3.4.3 Pre-MPT

Consistency in the magnitude and timing of glacial-interglacial variability in the upwelling index and pCO_2 reconstruction in the late Pleistocene suggests a common mechanism, identified as sea-ice driven glacial NPIW expansion by previous studies (Kender et al., 2018; Worne et al., 2019). Key to this is the severe drop in sea level during glacial periods after the 900 kyr event, which probably caused closure of the Bering Strait (Kender et al., 2018). However, higher glacial sea levels in the early Pleistocene coincide with the identification of precession and suborbital forcing band in the continuous wavelet analysis of the upwelling index, suggesting that variability in nutrient utilisation and productivity may have been controlled by additional or alternative mechanisms

related to seasonal insolation. During this period (0.92 – 1.2 Ma), amplification of the Walker circulation is considered an important precursor to the MPT

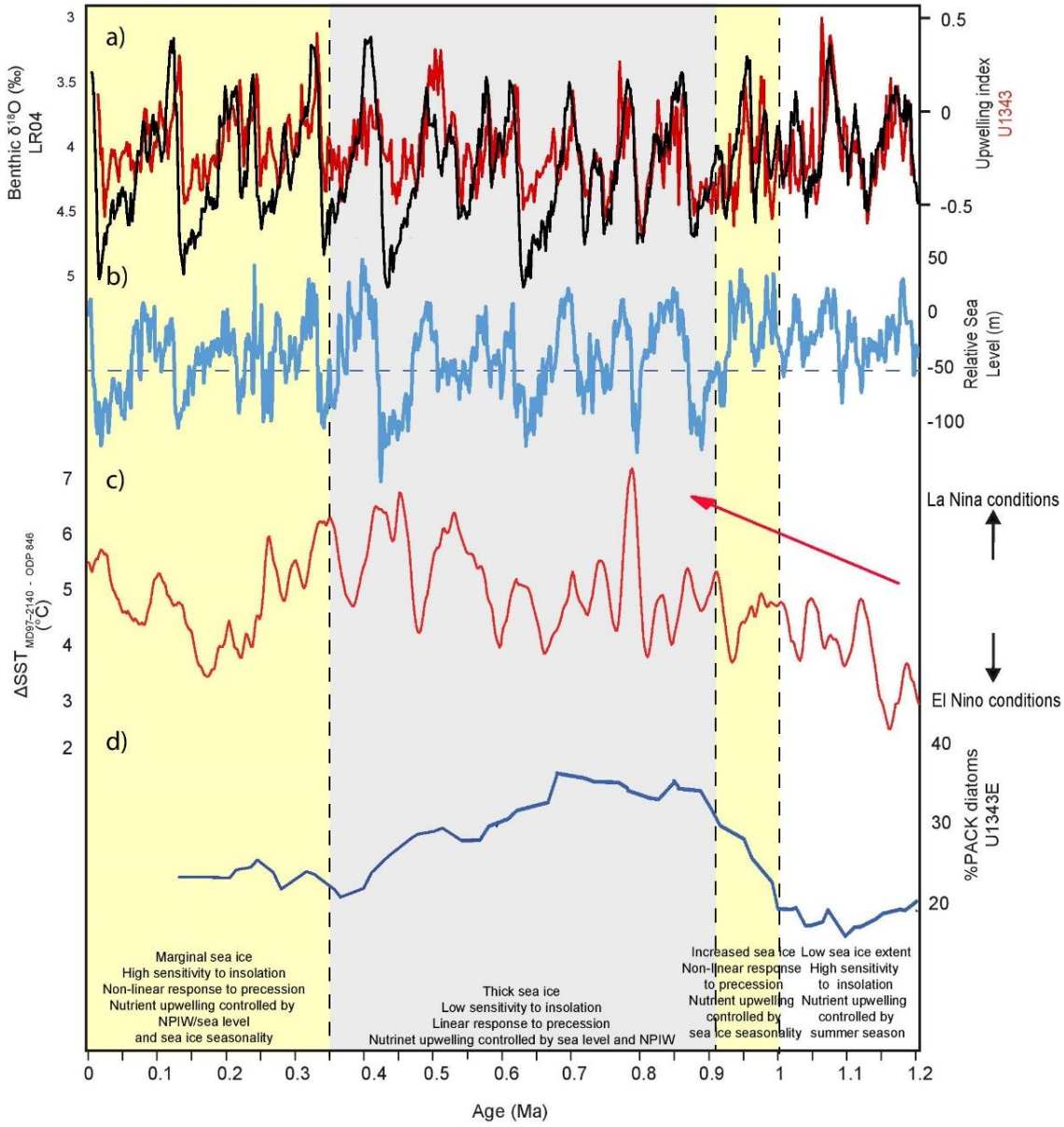


Figure 3.4 a) Comparison of upwelling index results (red) with global climate records including the LR04 benthic stack (Lisiecki & Raymo, 2005) (black), which represents a combined signal of global ice volume and temperature change. b) Relative sea level estimations of Elderfield et al., (2012) are also shown, and exhibits strong similarity to the upwelling index during and after the MPT. c) ΔSST temperature record from the tropical Pacific, which represents the East-West temperature gradient which drives Walker circulation strength, and shows an increase during the early Pleistocene, in line with increased abundance of pack ice associated diatoms at Site U1343 (Stroynowski et al., 2017) (d). Following wavelet analysis results (Figure 3.3) the control of sea ice on NPDW upwelling can be categorised into three states, described at the bottom of the figure and delineated with dashed lines (marked by white, yellow and grey coloured bars).

(Figure 3.3, Figure 3.4), where increased delivery of moisture and decreased heat transport to the high latitudes facilitated both ice sheet and sea ice growth (Gildor & Tziperman, 2001; Raymo & Nisancioglu, 2003; McClymont & Rosell-Melé, 2005). Intensification of the Walker circulation would also have propagated to the Bering Sea through causing a shift in the Aleutian Low and a weakening of the EAWM (Stroynowski et al., 2017), acting to enhance storm frequency and moisture availability in the northern Bering Sea and promoting BSC eddy activity, vertical mixing and sea ice growth (Luchin et al., 2002; Rodionov et al., 2007; Knudson & Ravelo, 2015b; Wang et al., 2018).

Initial precession forcing of nutrient upwelling between ~1.2 – 1 Ma occurs when sea ice volumes were lower and annual productivity was formed by a shorter melt-associated spring bloom period but dominated by a prominent summer bloom at the Bering Slope (Teraishi et al., 2016; Stroynowski et al., 2017). Opal MAR also followed a clear glacial-interglacial pattern, with high (low) productivity in warmer interglacials (colder glacials) (Kim et al., 2014). Therefore, precession forcing of the upwelling index during this early Pleistocene interval (white bar in Figure 3.4) likely reflects the sensitivity of the summer bloom (and marginal sea ice) to seasonal insolation. However, diatom evidence from the Bering slope indicates that sea ice began to expand through both glacials and interglacials between ~1 – 0.92 Ma (Teraishi et al., 2016; Stroynowski et al., 2017) (Figure 3.4, see also Chapter 4), coincident with the emergence of suborbital (~12 kyr) forcing.

Similar suborbital frequencies have been identified in proxy records from the high latitude North Atlantic Ocean and are proposed to occur either as a direct regional response to orbital forcing (Wara et al., 2000), or as a result of

atmospheric teleconnections, transporting heat and/or moisture from low to high latitudes (Hagelberg et al., 1994; Mcintyre & Molfino, 1996). In the tropical Pacific Ocean, suborbital cyclicity is thought to reflect a non-linear response of tropical climate to the monsoon system (Hagelberg et al., 1994). Therefore, I posit that as sea ice began to expand (yellow bar in Figure 3.4) and marginal sea ice conditions became more prominent at Site U1343, the emergence of suborbital frequency in the upwelling index likely reflects the sensitivity of sea ice to East Asian monsoonal/atmospheric forcing, which resulted in greater fluctuation of the sea ice margin and higher frequency variability in nutrient upwelling through modulation of the Aleutian Low. This is consistent with previous low resolution sea ice reconstructions which identify this interval as an "interim period" during which sea ice expansion was delayed by continued influence of warmer Alaskan Stream waters despite cooling temperatures (Detlef et al., 2018). Although it is possible that the 12 kyr cycle is simply an artefact of the high resolution of the upwelling index (2 kyr time-step), the emergence of an alternative suborbital cycle (~16 kyr) when wavelet analysis is performed at a larger time-step (6 kyr), may still support the suggestion that higher frequency variability in sea ice caused deep water upwelling to become asynchronous with global orbital forcing (Supplementary Figure 3.6).

Overall, despite evidence for NPIW in the southern Bering Sea back to at least 1.2 Ma (Knudson & Ravelo, 2015b), the significance of the precession forcing band in the early Pleistocene in our new records suggests that the seasonality (the balance between sea ice and summer seasons) played a more dominant control on nutrient upwelling strength before the MPT. Following intensification of the Walker circulation and sea ice expansion from ~1 Ma, a

switch from 23 kyr to 12 kyr cyclicity is likely a result of larger fluctuations in the position and duration of marginal sea ice (impacting diatom blooms), which is more sensitive to variability in the EAWM and the Aleutian Low.

3.4.4 Upwelling and NPIW expansion: the MPT

Although increased Walker circulation was likely important in the build up to the MPT conditions, this does not preclude the hypothesis that NPIW was also important, or the dominant control on upwelling strength during and/or after the MPT. At a critical threshold when significant land ice accumulated, sea level declined >50 m during the 900 kyr event and caused closure of the Bering Strait (Elderfield et al., 2012; Kender et al., 2018). The lack of obliquity and precession forcing bands during this short interval (~0.87 – 0.92 Ma), and prevalence of a harmonic of the eccentricity forcing only (Figure 3.3), suggests that sensitivity to seasonal insolation was significantly reduced, most likely due to prolonged pack ice cover, evidenced by diatom assemblages (Teraishi et al., 2016; Stroynowski et al., 2017) (see also Chapter 4). The coincidence of persistent sea ice cover and Bering Strait closure with suppression of deep water upwelling through MIS 23 up to the end of MIS 22, supports the idea that NPIW expanded and reduced vertical mixing and ventilation of NPDW across the subarctic Pacific region. Therefore, the upwelling index supports Kender et al. (2018) who suggests that retention of CO_2 in the deep subarctic North Pacific was an important mechanism in sustaining low subarctic Pacific upwelling, and reducing global pCO_2 during the MPT, and ultimately promoting longer glacial periods due to its cooling effect.

After the 900 kyr event (grey bar in Figure 3.4), strong glacial-interglacial variability in the upwelling index has been previously interpreted to

reflect continued control of glacially enhanced sea ice and NPIW formation on nutrient upwelling in the Bering Sea, causing both a reduced summer/autumn bloom season and acting as a physical barrier to deep water upwelling at the Bering slope (Worne et al., 2019). Wavelet analysis confirms significance of the longer ~100 kyr cycle consistent with global climate (LR04), and is present in the upwelling index after the MPT, up to ~0.4 Ma. This therefore supports that extreme sea level declines (following ice sheet accumulation) in glacials likely modulated NPIW expansion from the Bering Sea, which controlled nutrient upwelling at the slope with ~100 kyr cyclicity. Given that glacial sea level was lower, reduced prominence of the marginal sea ice season and increase in thicker sea ice caused lower sensitivity to changes in monsoonal/lower latitude climate, and therefore the disappearance of the 12 kyr cycles (Figure 3.3). However, re-emergence of ~23 kyr precession and ~41 kyr obliquity forcing bands (grey bar in Figure 3.4) suggests that sea ice seasonality still played an important role in determining nutrient upwelling strength within each glacial cycle, most likely through controlling the timing and duration or ice-associated spring and subsequent summer/autumn diatom blooms (Kim et al., 2014; Worne et al., 2019).

Overall, results indicate that MPT sea ice dynamics controlled nutrient upwelling strength in the Bering Sea via two mechanisms. Firstly, through NPIW expansion (following sea-level modulated Bering Strait closure (Kender et al., 2018; Worne et al., 2019), which acts to suppress upwelling during glacials as expressed in the LR04 global oxygen isotope stack. Secondly, through the active role of sea ice on seasonal primary productivity, which

continues to show some sensitivity to precession forcing during the middle Pleistocene.

3.4.5 Post-MPT

A second shift in the expression of the precession forcing, switching from a 23 kyr cyclicity to the 12 kyr cyclicity, occurs from ~0.4 Ma (yellow bar in Figure 3.4) and coincides with the Mid-Bruhnes Transition (MBT). The MBT represents another shift in global climate, after which the ~100 kyr glacial-interglacial cycles of the late Pleistocene became fully established (Barth et al., 2018). Post-MBT glacials (MIS 2, 4, 6, 8) exhibited lower continental ice volumes (Figure 3.1) while interglacials were characterised by increased warmth and higher pCO_2 (Hönisch et al., 2009; Barth et al., 2018). Wavelet analysis reveals the re-emergence of the suborbital forcing (12 kyr) of Bering Slope upwelling during this time, coincident with stronger EAWM in both glacial and interglacial periods (Liu et al., 2003). Warmer temperatures and a stronger EAWM would have caused reduced volumes of glacial sea ice, consistent with diatom assemblage results through this interval (Teraishi et al., 2016; Stroynowski et al., 2017). Given this, Site U1343 likely experienced more marginal sea ice conditions again after the MBT, with nutrient upwelling returning to become more sensitive to variability in Walker circulation-driven monsoonal and atmospheric systems.

Despite higher frequency variability in nutrient upwelling, NPIW would have continued to form in the Bering Sea during late Pleistocene glacials and acted as the first-order control on nutrient upwelling, due to Bering Strait closure which suppresses nutrient upwelling (Kender et al., 2018; Worne et al., 2019). This is supported by the development of clear glacial-interglacial

variability in nutrient utilisation ($\delta^{15}N_{U1343}$), where reduced magnitude of glacial-interglacial opal MAR variability indicates that the size of the nutrient pool varied, at least partially, independently from primary productivity (Figure 3.1). Indeed, Worne et al. (2019) noted that the correlation between nutrient upwelling and global pCO_2 was particularly strong over the last 0.35 Ma (Worne et al., 2019). Furthermore, Stroynowski et al. (2017) note that the long term correlation between abundance of pack ice associated diatoms and the ODP 1146 clay record (where clay mineral composition of sediments is representative of EAWM strength) also ends at 0.4 Ma (Liu et al., 2003), suggesting an additional control (other than sea ice) on productivity and nutrient utilisation after the MBT. Therefore, glacial expansion of NPIW (reducing the size of the nutrient pool) was likely still an important control on glacial-interglacial variability in the upwelling index over the last ~0.4 Ma, following trends in global climate and pCO_2, whilst sea ice volume and EAWM strength influenced the upwelling index by continuing to modulate primary productivity. This is consistent with spectral analysis of the post-MPT period (0 – 0.86 Ma) which shows strong significance at the 100 kyr cyclicity (Figure 3.2)

3.5 Conclusion

A significant ~41 kyr obliquity forcing in the upwelling index record from the Bering Sea indicates that the sea ice is sensitive to variation in summer insolation and latitudinal heat gradients, causing nutrient upwelling in the region to also follow global climate changes. During the early Pleistocene, when sea ice extent was low, summer insolation placed a key control on glacial-interglacial productivity. Emergence of a suborbital forcing band with 12 kyr cyclicity at ~1 Ma is coincident with enhanced Walker circulation, where

decreased poleward heat transport and increased moisture delivery facilitated sea ice expansion. Following this, increased but more highly fluctuating marginal sea ice conditions between MIS 28 – 24 were more sensitive to high frequency variability in monsoonal and atmospheric systems, which modulated the Aleutian Low. During the 900 kyr event, accumulation of continental ice sheets and sea level decline facilitated prolonged sea ice cover in the Bering Sea, which when combined with the closure of the Bering Strait caused expansion of a strong NPIW layer which suppressed nutrient upwelling at the Bering Slope. Southward propagation of NPIW and reduced vertical mixing/deep water ventilation in the subarctic North Pacific Ocean could have potentially contributed to low global pCO_2 and a long glacial period during MIS 22-23 (Kender et al., 2018).

After the 900 kyr event, persistence of the longer 123 kyr and 41 kyr forcing bands are consistent with global marine records (LR04 benthic stack); this supports the hypothesis that nutrient upwelling strength in the Bering Sea was controlled by NPIW formation, modulated by ice sheet growth/sea level decline which followed quasi-100 kyr glacial cycles (Kender et al., 2018; Worne et al., 2019). Given that sea ice volumes remained high during both glacials and interglacials after the MPT, precession-driven variability in sea ice seasonality is also identified with 23 kyr cyclicity. After MBT warming at ~0.4 Ma, reduced sea ice extent following re-strengthening of the EAWM caused more marginal sea ice conditions which are more sensitive to monsoonal/atmospheric systems, initiating re-emergence of suborbital frequency in nutrient upwelling. However, continued closure of the Bering Strait in post-MPT glacials promoted NPIW as an additional mechanism for suppressing nutrient upwelling, causing longer

glacial-interglacial variability in nutrient upwelling which continued to follow the global climate. Overall, I have determined the impact of MPT sea ice evolution in the Bering Sea on productivity, nutrient utilisation, and deep water ventilation at the Bering slope over the last 1.2 Ma. Further high resolution proxy reconstruction work is needed to better quantify the significance of these changes on global ocean-atmosphere CO_2 exchange and increasing glacial duration.

3.6 Supplementary information

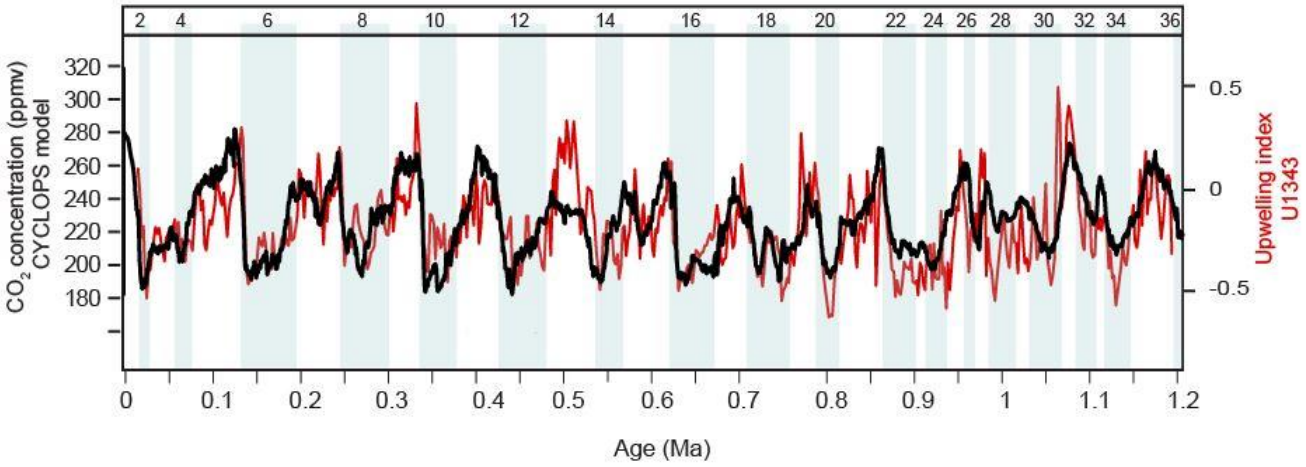


Figure 3.5 Comparison of upwelling index results (red) from 0 – 1.2 Ma with modelled atmospheric CO_2 concentrations (black) (Chalk et al., 2017).

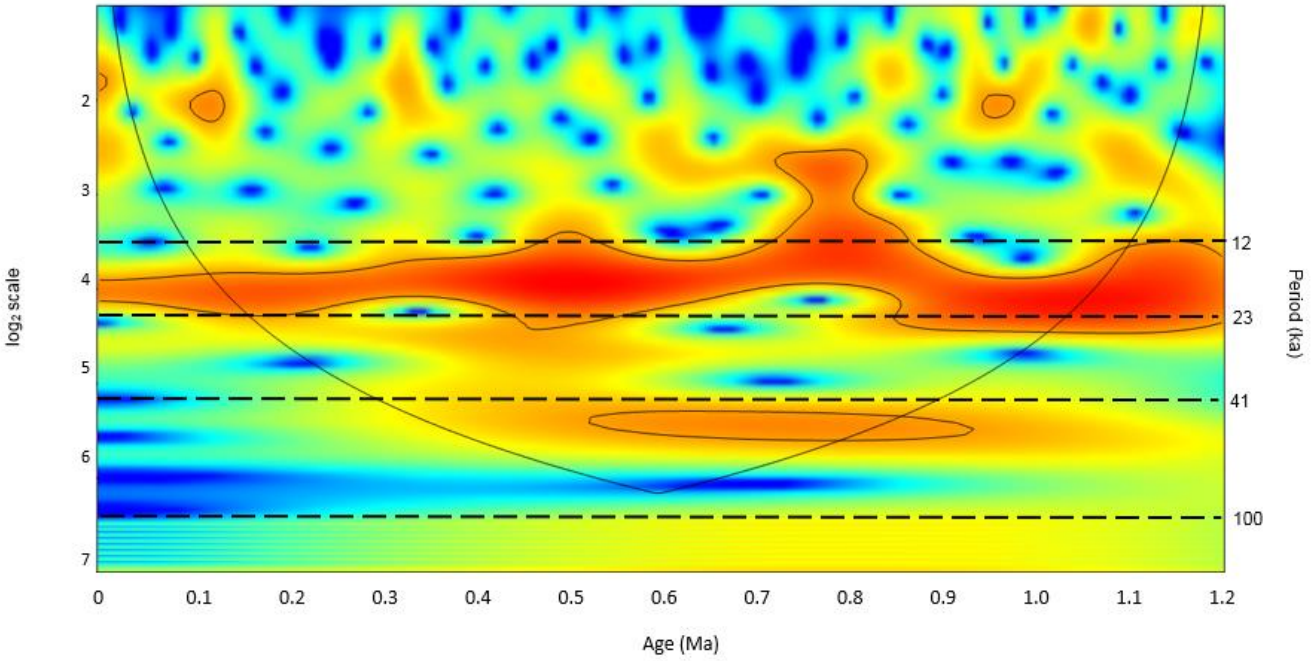


Figure 3.6 Wavelet analysis of the upwelling index from 0 – 1.2 Ma calculated at a larger timestep of 6 kyr, where red/warmer values indicate higher spectral power than blue/colder colours (temperature gradient). Dashed lines represent the periodicities of the Milankovitch orbital cycles, and the solid black line represents the cone of influence, above which results are considered significant.

Table 3.1 New age-depth tie points for Site U1343, building on Worne et al. (2019).

Depth (CCSF – A) (m)	**Age (kyr)**
0.96	10.15
14.23	57.38
36.72	131.41
48.03	181.46
59.73	219.06
68.72	242.57
79.52	279.96
96.24	335.14
114.56	396.17
119.35	424.39
129.90	480.93
145.02	512.78
152.01	545.32
161.63	580.48

173.39	621.39
174.57	641.03
184.09	700.03
188.27	725.84
191.58	753.63
203.57	790.75
209.04	812.86
227.39	865.95
238.34	917.46
254.16	959.01
266.14	983.50
272.57	1002.99
282.73	1031.59
296.57	1062.96
318.81	1124.99
336.91	1190.47

Chapter 4: Sea Ice in the Bering Sea during the Mid Pleistocene Transition

Savannah Worne[1]*, Zuzia Stroynowski[2], Sev Kender[3,4], George E. A. Swann[1],

[1]Centre for Environmental Geochemistry, School of Geography, University of Nottingham, Nottingham, NG7 2RD, UK

[2]Greene's Tutorial College, 2765-452 Estoril, Portugal

[3]Camborne School of Mines, University of Exeter, Penryn Campus, Penryn, Cornwall, TR10 9FE, UK

[4]British Geological Survey, Keyworth, Nottingham, NG12 5GG, UK

*Corresponding author. Email: savannah.worne@nottingham.ac.uk

Abstract

Expansion of high latitude sea ice during the Mid Pleistocene Transition (MPT, 0.6–1.2 Ma) is proposed to have significantly altered moisture availability, surface albedo, the efficiency of the biological pump, and net ocean-atmosphere CO_2 exchanges. One hypothesis postulates that sea ice controlled the timing of deglacials with expansion of sea ice at these times (the "sea ice switch hypothesis"). Other hypotheses suggests sea ice regulated glacial-interglacial ventilation of CO_2 through modulating deep water upwelling, nutrient availability and hence the biological pump. However, the low resolution/short timescale of existing sea ice reconstructions prevents a full evaluation of the role of sea ice dynamics on long term regional and global climate evolution. Here, a high resolution diatom assemblage record from Site U1343 in the green

belt region of the Bering slope is presented, to investigate subarctic sea ice evolution on glacial-interglacial timescales between 1.2 and 0.6 Ma. Results show gradual sea ice expansion occurred through the early-mid Pleistocene, suggesting that sea ice evolution was responding to global climate changes. Sea ice appears to have been primarily modulated by continental ice-sheet dynamics and sea level fluctuations, controlling water through-flow in the Bering Sea, likely facilitated by an amplified Walker circulation following cooling in the equatorial Pacific. Results do not support the sea ice switch hypothesis, as pack ice diatom abundances are highest at the glacial maxima during the MPT (rather than deglacials) and follow global climate changes in ice volume and sea level. Sustained high abundance of thick pack ice associated diatoms is coincident with sea level decline, low atmospheric CO_2, suppressed deep water upwelling and reduced export production at the Bering slope at 0.9 Ma. This supports the hypothesis that the increase in brines rejected during sea ice formation, coupled with closure of the Bering Strait at 0.9 Ma, caused expansion of NPIW across the subarctic Pacific Ocean. Overall, MPT sea ice and NPIW expansion contributed to the increased duration of glacials due to suppressed subarctic Pacific deep water CO_2 ventilation. As a result of larger volumes of post-MPT sea ice, the resultant impact on export production and regional upwelling likely also played an important role in global ocean-atmosphere dynamics on glacial-interglacial timescales.

4.1 Introduction

The Mid-Pleistocene Transition (MPT) represents a cooling of the global climate between ~1.2 - 0.6 Ma, during which glacial-interglacial cycles shifted from obliquity-dominant 41 kyr cycles, to lower frequency eccentricity-dominant 100 kyr (Lisiecki & Raymo, 2005), without any long term change in the external orbital forcing (Clark et al., 2006; McClymont et al., 2013). Onset of the MPT saw many climatic changes, including a decrease in sea surface temperature (SST) in the North Atlantic and tropical ocean upwelling systems, as well as changes in African and Asian aridity and monsoon intensity (McClymont et al., 2013). Notably, a long term increase in average global ice volume was observed through the MPT, particularly following the "900 kyr event", after which 100 kyr orbital cycles stabilised and became prominent in the proxy record (Lisiecki & Raymo, 2005). Post-MPT conditions are then characterised by less frequent but more extreme glacial periods, with colder SSTs and larger ice volumes (McClymont et al., 2013).

The cause of the MPT is still a highly debated topic, with several opposing hypotheses. As there was a stepwise increase in ice volume at 0.9 Ma, as evidenced by an increase in global seawater $\delta^{18}O$ (Pollard & DeConto, 2009; Elderfield et al., 2012), some proposals invoke changing ice sheets dynamics as the key proponent for the MPT; for example, a change in the relationship between ice sheets and the underlying bedrock which allowed ice sheets to increase in volume and thickness (Clark et al., 2006), or changing ice sheet response to insolation forcing due to decreasing atmospheric CO_2 (Berger et al., 1999; Hönisch et al., 2009). Potential mechanisms for the latter include reduced ventilation of CO_2 from the deep ocean to the atmosphere, for example via

suppressed polar upwelling, and/or increased efficiency of the biological pump as a result of changes in nutrient/dust supply (Clark et al., 2006; Martínez-Garcia et al., 2009). In either case, lower atmospheric CO_2 would act to cool the global climate and promote land ice accumulation. Alternatively, the "sea ice switch" (SIS) hypothesis for the MPT suggests that feedbacks between sea ice and ice sheets played a pivotal role in the MPT, where increased northern hemispheric sea ice modulated North American Ice Sheet (NAIS) growth and stability (Gildor & Tziperman, 2001; Tziperman & Gildor, 2003). The reduced poleward heat transport and increased delivery of moisture to the subarctic, as a result of an intensified Walker circulation following temperature declines in the equatorial Pacific, is also thought to have been an important precursor for ice sheet and sea ice growth at 0.9 Ma (McClymont & Rosell-Melé, 2005). Hypotheses for the MPT have however remained largely untested, due to a lack of high resolution and long term palaeoenvironmental records, from key high latitude locations such as the Bering Sea.

4.1.1 The Bering Sea and the MPT

The Bering Sea is located in the subarctic Pacific Ocean, where the Bering Strait at the northern boundary is the only connection between the Pacific, Arctic and Atlantic Oceans in the Northern Hemisphere. Modern surface waters in the Bering Sea are formed of subarctic Alaskan Stream waters, which enter through passes in the Aleutian island arc at the southern boundary, and then circulates in the basin to form the shelf-adjacent Bering Slope Current (BSC; Figure 1.3). Turbulent eddies in the BSC extend up to ~1 km water depth and cause upwelling of nutrient rich North Pacific Deep Water (NPDW) (Stabeno et al., 1999). This abundant nutrient supply fuels a high productivity region known as

the “green belt”, which is dominated by diatom productivity, primarily blooming in the spring/summer (Figure 1.3) (Springer et al., 1996). Seasonal sea ice melt also plays a critical role in this by promoting water column stability, allowing diatoms to remain in the photic zone and utilise available nutrients, as well as alleviating light availability (Hunt & Stabeno, 2002; Kim et al., 2012). Despite high nutrient availability, modern day green belt nutrient utilisation becomes iron limited in the summer (Takeda, 2011), leading to the region acting as a seasonal source of CO_2 to the atmosphere (Chen et al., 2014a; Cross et al., 2014).

Seasonal sea ice has formed in the Bering Sea since the onset of Northern Hemispheric glaciation (~2.6 Ma), and is expected to have been perennial or near-perennial during Pleistocene glacials (Stroynowski et al., 2015; Detlef et al., 2018). Sea ice is an essential component of palaeoclimate dynamics through its impact on surface albedo, regional moisture availability and restricting air-sea gas exchange. The importance of this is highlighted in the SIS hypothesis, which suggests that sea ice can regulate the growth and retreat of continental ice sheets through its role in the temperature−precipitation feedback (Gildor & Tziperman, 2001). Support for this hypothesis in the Bering Sea was previously found by Detlef et al., (2018), who presented a sedimentary lipid biomarker sea ice reconstruction at Site U1343 to demonstrate increased MPT sea ice and a shift in the seasonality of the sea ice maxima to the late glacial, consistent with the SIS sea ice/land ice hysteresis model. However the short time intervals covered by Detlef et al. (2018), and the low resolution nature of the record, limits assessment of the long term relationship between Bering Sea sea ice and productivity.

As nutrient rich NPDW upwells along the continental shelf, the Bering slope is also an important region for detecting changes in the high latitude deep water CO_2 ventilation. A previous study by Kender et al., (2018) from the Bering Sea green belt suggested that after sea level fell 50 m due to significant accumulation of land-ice at ~0.9 Ma (Figure 4.1d), the shallow Bering Strait became closed. As a result, brines which formed on the shelf during sea ice formation were forced to flow southward, sinking at the Bering slope to form North Pacific Intermediate Water (NPIW) (Knudson & Ravelo, 2015b; Kender et al., 2018). The presence of a large NPIW layer would have prevented eddies in the BSC from reaching NPDW, hence trapping nutrient rich waters in the deep Bering basin and reducing surface water CO_2 (Kender et al., 2018). Additionally, lowered sea level likely depressed BSC energy and hence eddy activity, further reducing vertical mixing (Kim et al., 2017). NPIW which formed in the glacial Bering Sea is also suggested to have propagated across the subarctic North Pacific, causing region-wide suppression of vertical mixing and isolation of CO_2 in the deep ocean (Kender et al., 2018; Worne et al., 2019) (Chapter 3). This is supported by a semi-quantitative "upwelling index", which demonstrates that glacials during and after the MPT exhibited reduced nutrient upwelling at the green belt, in line with global atmospheric pCO_2 (Worne et al., 2019) (Chapter 3). However, the low resolution and short temporal intervals of existing sea ice reconstructions from the Bering Sea (Teraishi et al., 2016; Detlef et al., 2018) prevent a full evaluation of the role of sea ice growth and brine formation as a mechanism for regional NPIW expansion and its impact on deep water upwelling and ocean-atmosphere CO_2 exchange.

Overall, MPT increases in sea ice and a reduction in upwelling of NPDW (nutrient supply) (Figure 4.1d-e), could have significantly altered moisture availability, surface albedo, photic zone CO_2, the efficiency of the biological pump, and hence net ocean-atmosphere CO_2 exchanges, over the MPT in the Bering Sea. Here a high resolution diatom assemblage record from Site U1343 in the green belt region of the Bering slope is presented, which is compared with previously published records for nutrient upwelling and productivity (Figure 4.1e-f), to permit a better assessment of the role of sea ice on both regional and global climate dynamics between 1.2 and 0.6 Ma, and over the MPT.

4.2 Methods

4.2.1 Core materials, age model and sedimentation rates

IODP Site U1343 (54°33.4'N, 176°49.0'E, water depth ~1, 950 m) is situated on a topographic high, adjacent to the continental shelf and proximal to the modern winter sea ice edge (Figure 1.3). Sediments from this site are primarily composed of silt with varying amounts of clay and diatoms, with minimal input of shelf-transported materials (Takahashi et al., 2011a). Regionally outstanding foraminiferal preservation at the Bering slope has provided an excellent opportunity to create a globally comparable and robust $\delta^{18}O$ age model, to help assess millennial scale sea ice variability in the Bering Sea. The age model for Site U1343 uses 1323 foraminiferal $\delta^{18}O$ measurements and has an average resolution of 450 years from 0.6 – 1.2 Ma (Worne et al., 2019) (Chapter 3) (Figure 4.1a).

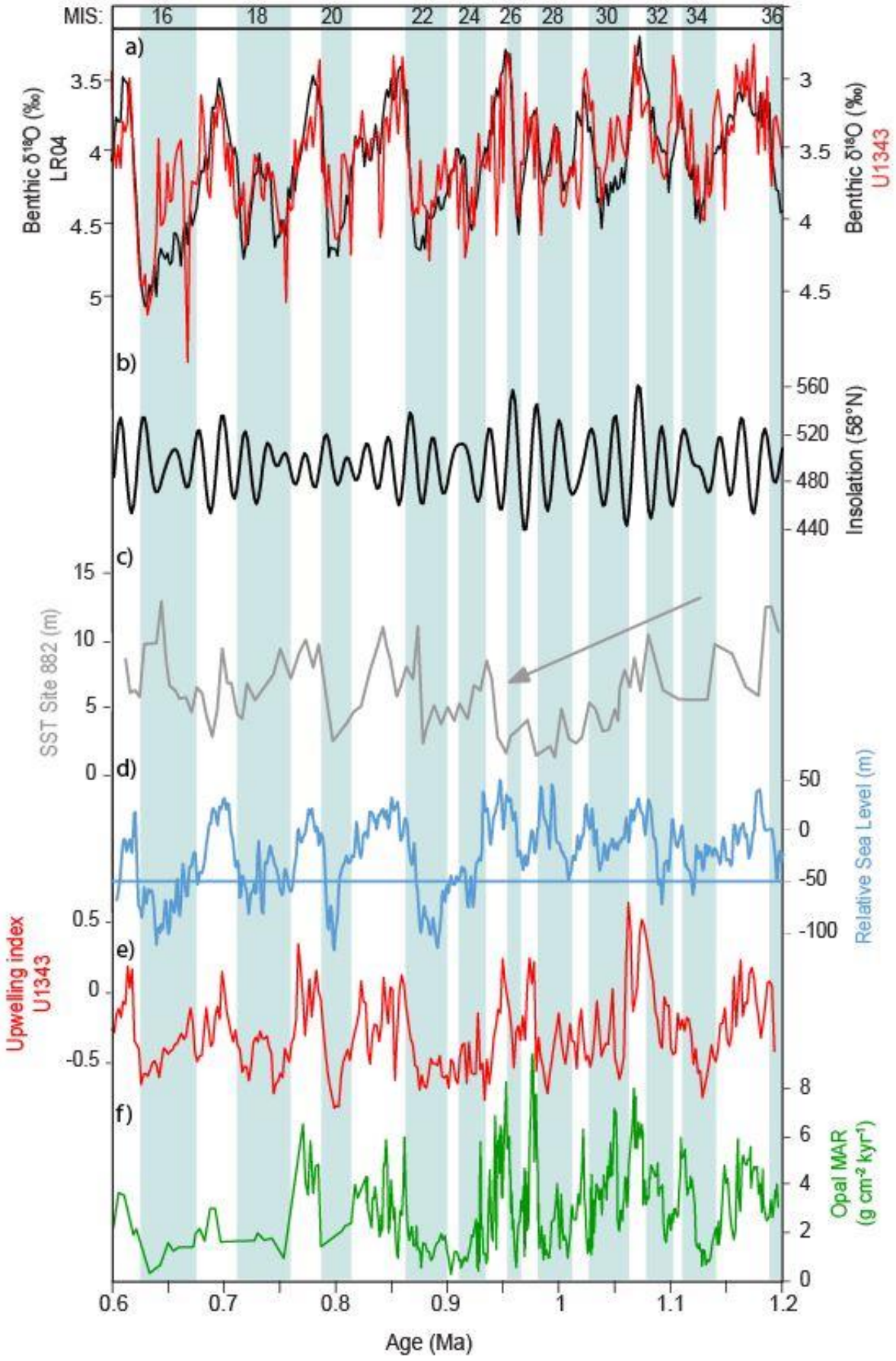

MIS:
16
18
20
22
24
26
28
30
32
34
36
a)
Benthic δ18O (‰)
LR04
Benthic δ18O (‰)
U1343
b)
Insolation (58°N)
c)
SST Site 882 (m)
d)
Relative Sea Level (m)
e)
Upwelling index
U1343
f)
Opal MAR
(g cm-2 kyr-1)
Age (Ma)

Figure 4.1 Published data from the subarctic Pacific Ocean between 0.6- 1.2 Ma which aid interpretation of diatom assemblage results presented here. A) Age model from Site U1343 between 0.6 – 1.2 Ma (red) compared to the global benthic LR04 stack (black). Blue shaded bars represent glacial periods identified in the LR04 stack, and labelled as the respective marine isotope stages (MIS) at the top of the figure. B) Solar insolation received at for 58°N. C) SST temperature from ODP Site 882 in the western subarctic Pacific Ocean (Martinez-Garcia et al., 2010). D) Relative sea level estimated using $\delta^{18}O$ data (Elderfield et al., 2012), where the blue line represents -50 m the modern depth of the Bering Strait, and values below the line are likely periods of Bering Strait closure (Kender et al., 2018; Chapter 3). E) Upwelling index results from Chapter 3, where higher values reflect increased strength of NPDW upwelling and lower values reflect suppressed nutrient upwelling. F) Opal mass accumulation results (MAR) from Kim et al. (2014) reflects siliceous productivity, where higher values are indicative of periods with higher total primary productivity.

4.2.2 Diatom assemblages

Enhanced productivity at the green belt has facilitated high preservation of diatom fossils in sediments at IODP Site U1343 (Kim et al., 2014). Previous low resolution studies undertaken at the site confirmed that regionally common sea ice species are well preserved throughout the record (Teraishi et al., 2016). 183 samples were selected to provide an average resolution of 3.4 kyr between 0.6 and 1.2 Ma, with a higher resolution section focussed between 0.8 and 1 Ma (average resolution of 2.2 kyr), and an average resolution of 4.9 kyr and 4.3 kyr from 0.6 – 0.8 Ma and 1 – 1.2 Ma, respectively.

Samples for diatom taxonomy were prepared and counted using established techniques (Battarbee & Kneen, 1982; Battarbee, 1986); ~0.015g of freeze-dried sediment was cleaned through recurrent heating with hydrogen peroxide and hydrochloric acid to remove organic matter. Two drops of weak ammonia (NH_3) solution was added to the final wash to help keep clay particles in suspension and reduce clumping of diatoms frustules (Battarbee, 1986). Glass microsphere solution of a known volume was added to the cleaned sediment to

enable calculation of diatom concentrations before being diluted to 10 ml of distilled water. Samples were then pipetted onto cover slips where they were left to settle overnight before they were mounted by heating with Naphrax®. All samples were identified to species level where possible, except for *Chaetoceros* resting and vegetative spores (RVS), which were grouped at genus level. A minimum of 300 valve counts were made across slide transects using an oil immersion lens and phase contrast at x1000 magnification. Using the total diatom count, the relative abundance (%) of each diatom species and genus was calculated.

To investigate the dynamics and evolution of sea ice expansion/melt on millennial timescales, the relative abundances of diatoms were grouped by their environmental tolerances as described by Stroynowski et al., (2017), with sea ice associated taxa grouped into three categories: indicators of thick pack ice (PACK), epontic or ice-dwelling species (ICE) and marginal sea ice species (MARG), with each group representing progressively less sea ice presence respectively (see Stroynowski et al., (2017) for further detail). Ordination analysis is used to confirm the control of sea ice on these ecological groupings, using R and the vegan package (R Core Team, 2017; Oksanen et al., 2018). A detrended correspondence analysis (DCA) was used to determine whether diatoms exhibited a linear or unimodal response to the latent variables. DCA produced a first axis gradient length of 0.45, indicating a linear response. A Principal Components Analysis (PCA), was then carried out with square root transformation of percentage data, to reduce the influence of dominant taxa.

4.2.3 Diatom concentration and accumulation rates

In order to assess absolute abundance changes in diatom assemblage, the concentration of diatom valves was calculated following Battarbee and Kneen (1982) (Equation 4.1):

$$Diatom\ concentration = \frac{\left(\frac{X_d * Y_{mi}}{X_{mi}}\right)}{Y_s} \qquad \text{Equation 4.1}$$

Where X_d is the number of diatoms valves counted, Y_{mi} is the number of microspheres introduced (ml), X_{mi} is the number of microspheres counted and Y_s is the mass of dry sediment used (g). Sedimentation rates (Chapter 3) were then applied to the concentration data to calculate a down-core diatom accumulation rate (DAR).

DAR results were also grouped ecologically to assess the difference in seasonal growth rates, with the aforementioned groups of sea ice related species combined together (henceforth "All Sea Ice") to examine winter conditions (Stroynowski et al., 2017). As *Chaetocero*s RVS is associated with the spring melt season, the DAR for this genus was grouped separately to investigate variability in the size of the spring bloom. Meanwhile, all other remaining species which are intolerant of sea ice conditions (i.e. not included in All Sea Ice or *Chaetoceros* RVS DAR) are grouped as "Non-Sea ice", for which the DAR is indicative of the rate of summer/autumn productivity.

4.3 Results and Discussion

4.3.1 Diatom ecologies and environmental inference

Over 94 species were identified and grouped by the ecological classifications described by Stroynowski et al., (2017) (Figure 4.2), which were confirmed

through PCA analysis (Figure 4.4) and identified a clear environmental gradient in which the first axis (sea ice) controlled 50% of the variability. The PACK group contains *Thalassiosira antarctica* var *borealis* RVS which has been shown to reflect thick multi-year or pack ice cover, where the resting stage (RS) is often dominant during periods of low species diversity and productivity (Sancetta, 1982; Caissie, 2012; Stroynowski et al., 2015, 2017). The ICE species group is dominated by *Fragilariopsis* spp., particularly *F. cylindrus*, for which the relative abundance has been shown to be directly related to the duration of sea ice cover in the eastern and southern Bering Sea (Caissie et al., 2010; Stroynowski et al., 2015). The MARG group is not dominated by a single species through the entire record, but shows an interesting succession in the dominance of different species, through periods of MPT ice growth and decline. Key taxa from the MARG group at Site U1343 include *Porosira glacialis* and *Stellarima microtrias*, which are both bipolar and grow in cold coastal waters adjacent to sea ice (Hasle & Sims, 1986; Stroynowski et al., 2017). In the Antarctic, these species grows in the summer months and are most abundant during years with at least 7.5 months of sea ice cover (Armand et al., 2005; Pike et al., 2009). The benthic grouping can be used to indicate periods of lower sea level and/or increased lateral shelf-slope exchange, as these species were most likely transported from the continental shelf (Stroynowski et al., 2017). This group is dominated by *Delphineis* spp. and *Navicula* spp., although individually neither genus exceeded 2% relative abundance. The most common taxa in the freshwater group were *Aulacoseira* spp. and *Cymatosira belgica*, but this group exhibits small millennial scale variability and low relative abundances (mean = 1%). This is consistent with previous studies at this site suggesting that small

peaks of neritic and freshwater species in some samples may indicate negligible riverine input into Bering Sea during periods of low sea level (Teraishi et al., 2016).

The other ecological groupings (pelagic, mat-forming and eastern shelf species) are dominated by one or a few species/genera, which are discussed individually. *Chaetoceros* RVS is considered a pelagic species as it thrives in the first spring bloom following sea ice melt, however palaeo-studies more commonly associate this taxa with high nutrient and turbulent waters such as at well-mixed current boundaries, or in the case of green belt, with BSC eddy activity and upwelling strength (Caissie, 2012; Stroynowski et al., 2015, 2017). There are three other key species in the pelagic group which have fluctuating but generally high relative abundances; *Neodenticula seminae*, which is an indicator of warm Alaskan Stream water which flows in from the subarctic Pacific gyre (Figure 1.3), *Actinocyclus curvatulus* (the dominant component of *Actinocyclus* spp.) which thrives in the low-nutrient summer dicothermal waters that follow sea ice melt, and *Shionodiscus trifultus* which has also been shown to prefer colder and more stratified waters, currently most dominant in the western side of Bering basin (Sancetta, 1982; Caissie, 2012; Ren et al., 2014; Stroynowski et al., 2015, 2017)

The mat-forming group is dominated by two genera, *Rhizosolenia* spp. (mostly *R. hebetata* f. *hebetata*) and *Coscinodiscus* spp. (predominantly *C. marginatus*). Both species bloom in the late summer/autumn months (August-November), requiring high nutrient availability and relatively warmer temperatures, where high abundances may reflect increased seasonality (Takahashi, 1986). While *C. marginatus* and other mat-forming species bloom

in the lower euphotic zone to utilise nutrients during the stratified autumn and winter season, *R. hebetata* has a competitive advantage during periods of low surface nutrient content, as it can sink below the nutricline using buoyancy-mediated migration (Kemp & Villareal, 2013; Stroynowski et al., 2015).

From the eastern shelf/coastal grouping, the most dominant species are *Paralia sulcata* and *Melosira sol* (grouped together from here onward) which are epibenthic species which dwell on the eastern Bering shelf, thriving in low light coastal brackish environments (Sancetta, 1982; McQuoid & Nordberg, 2003; Stroynowski et al., 2017). One species not included in the ecological groupings of Stroynowski et al., (2017) is *Stephanopyxis turris*, which has been shown to reflect either warmer water, shallower waters and/or amplified current speeds through the Aleutian passes at the southern boundary of the Bering Sea (Aizawa et al., 2005; Stroynowski et al., 2015) (Figure 1.3). Relative abundance of *P. sulcata/M. sol* and *S. turris* can therefore provide insight into the circulation of the Bering Sea gyre as well as wind strength and tidal mixing.

4.3.2 General trends in diatom abundances

There is clear glacial-interglacial variability in the relative abundance data, where higher abundances of PACK, ICE and MARG are generally consistent with increased sea ice during colder glacial periods (Figure 4.2a-c). One of the most dominant species found throughout the sample period is *T. antarctica* var *borealis* RS with a mean relative abundance of 26%, reaching up to 63% at its highest. As a result, the PACK group shows the highest mean relative abundance of the sea ice groups at 26%. ICE and MARG have mean relative abundances of 6%, reaching 24% and 25% at their maxima, respectively. Lower relative abundances of the ICE and MARG groups in comparison to other

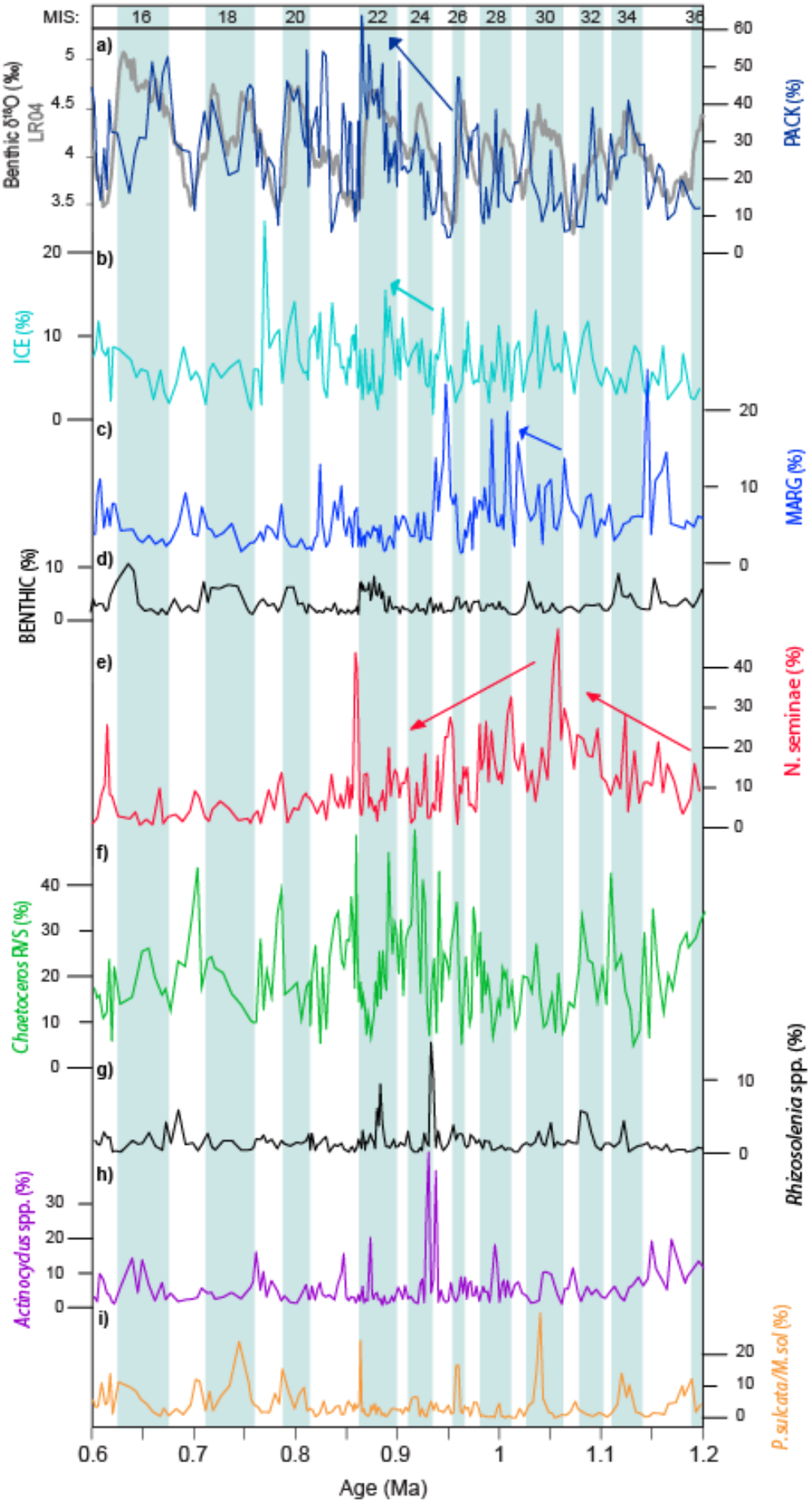

MIS:
16
18
20
22
24
26
28
30
32
34
36
a)
Benthic δ18O (‰)
LR04
PACK (%)
b)
ICE (%)
c)
MARG (%)
d)
BENTHIC (%)
e)
N. seminae (%)
f)
Chaetoceros RVS (%)
g)
Rhizosolenia spp. (%)
h)
Actinocyclus spp. (%)
i)
P.sulcata/M.sol (%)
Age (Ma)

Figure 4.2 Relative diatom abundance assemblage results from Site U1343 between 0.6 – 1.2 Ma, with species grouped by ecological tolerances or genus (see Section 4.3.1). a) Species associated with pack ice cover at Site U1343 (navy) shows similarity to global benthic LR04 stack (grey), particularly after the 900 kyr event (see Section 4.3.7). Blue bars represent glacial periods identified in the LR04 global stack and labelled by their respective glacial MIS numbers (Lisiecki & Raymo, 2005). Other sea ice associated species plotted include epontic diatoms (ICE) (b) and marginal sea ice (MARG) (c) also show increased abundance through the MPT. d) Benthic species show increased abundance in glacial periods when Site U1343 becomes more coastal while the abundance of *N. seminae* (e) is considered to be representative of Alaskan Stream water influence via the BSC which shows higher abundance during periods of higher sea level/lower sea ice. f) *Chaetoceros* RVS are indicative of high nutrient availability from deep water upwelling during spring sea ice melt (Stroynowski et al., 2017; Sancetta 1982). *Rhizosolenia* spp. (g) and *Actinocyclus* spp. (h) are summer/pelagic species, where both species are indicative of periods with strong water column stratification, while *P. sulcata/M. sol* (i) which dwells on the eastern Bering shelf can provide insight into Bering gyre strength.

reflects the longer annual duration of ice cover at Site U1343, which is more proximal to the ice margin. The benthic group has a low average relative abundance of 2%, but higher values up to 10% during glacial stands (Figure 4.2d), most likely as a result of sea level drop when the Bering shelf was exposed and Site U1343 became closer to the coast.

N. seminae has maximum relative abundance (50%) during early MIS 30, however a declining trend through the sample period decreases the mean contribution to 11% (Figure 4.2e). *N. seminae* generally shows peak and/or higher abundance during deglacials and interglacial periods, particularly in the earlier part of the record when sea levels were higher and Alaskan Stream waters flowed unrestricted into the Bering Sea (Stroynowski et al., 2015, 2017; Teraishi et al., 2016) (Figure 4.1d, Figure 4.2e). Simultaneous peaks in the abundance of *Chaetoceros* RVS during most deglacial periods (up to 52%; Figure 4.2f), most likely represents a spring surge in nutrient availability following sea ice retreat, where a longer melt associated bloom occurred under

high upwelling conditions. This is consistent with deglacial peaks and higher interglacial diatom productivity in the opal mass accumulation rate (MAR) record (Figure 4.2f).

Relative abundances of other species fluctuates more periodically throughout the record, most likely in response to pre-MPT cooling or climate changes associated with increased glacial duration and severity during and after the MPT (McClymont et al., 2013). Maximal abundance of *Actinocyclus* spp. (up to 46%) occurs during MIS 24 during the build up to MPT conditions (Figure 4.2e). The other key pelagic species, *S. trifultus,* never exceeds 18% abundance but shows sustained high values through MIS 28, remaining low for the rest of the study interval (Figure 4.5). The autumn mat-forming species *Rhizosolenia* spp. and *Coscinodiscus* spp. have average contributions of 1% and 2% respectively (Figure 4.2g, Figure 4.5). However, the timing of pulses in relative abundance of *Rhizosolenia* spp. (up to 15%) occur during palaeoceanographically important time periods (Figure 4.2g; See section 4.3.6). *P. sulcata/M. sol* has a mean relative abundance of 4% and has distinctive surges (up to 33%) around ~1, 0.86 and 0.75 Ma (Figure 4.2i). *S. turris* has an average contribution of 3% but a sustained increase in abundance (up to 29%) through MIS 21 and 26 (Figure 4.5).

While relative abundance of diatom species/groupings can provide information about the palaeoenvironment, the diatom concentrations give better insights into how these changing environments impacted productivity, nutrient cycling and the regional biological pump. The mean total concentration of diatoms over the analysed interval is 29.3 x 10^6 valves g^{-1}, with significantly higher concentrations in interglacials (mean = 35.1 x 10^6 valves g^{-1}) than

glacials (mean = 23.5 x 10^6 valves g^{-1}, $p < 0.01$). DAR range from 5559 x 10^6 to 8.81 x 10^6 valves cm^{-2} kyr^{-1} and exhibit parallel glacial-interglacial variability, where glacials are characterised by significantly lower DARs (mean = 831 x 10^6 valves cm^{-2} kyr^{-1}) than interglacials (mean = 1112 x 10^6 valves cm^{-2} kyr^{-1}, $p = < 0.05$). While the All Sea Ice DAR has a mean of 65 x 10^6 valves cm^{-2} kyr^{-1}, *Chaetocero*s RVS and Non-Sea ice species have higher mean DARs of 221 x 10^6 valves cm^{-2} kyr^{-1} and 400 x 10^6 valves cm^{-2} kyr^{-1}, respectively (Figure 4.3a-c).

4.3.3 Pre-MPT: MIS 36-25 (~1.2 – 0.96 Ma)

In the early Pleistocene, diatom assemblages show clear glacial-interglacial variability. Glacials prior to 1.1 Ma show increased abundances in the sea ice groupings with predominantly marginal sea ice conditions, although relatively high species diversity also indicates pronounced seasonality (Figure 4.2c). During the same interval, pre-MPT interglacial periods are dominated by *N. seminae*, *Actinocyclus* spp. and *P. sulcata/M. sol* (Figure 4.3), with a distinct increasing trend in *N. seminae* from 1.15 – 1.05 Ma. Dominance of these species, which thrive in warmer waters in the summer after the melt season, suggests there was a strong influence of Alaskan Stream waters transported from the lower subarctic through the Aleutian passes, stimulating green belt productivity under sustained strong BSC flow and nutrient upwelling from NPDW.

From ~1.05 Ma onwards however, relative abundance of *N. seminae* begins to decline through both glacials and interglacials until mid-MIS 22, suggesting decreasing influence of Alaskan Stream waters and reduced connectivity with the lower subarctic Pacific Ocean (Figure 4.2e). This is

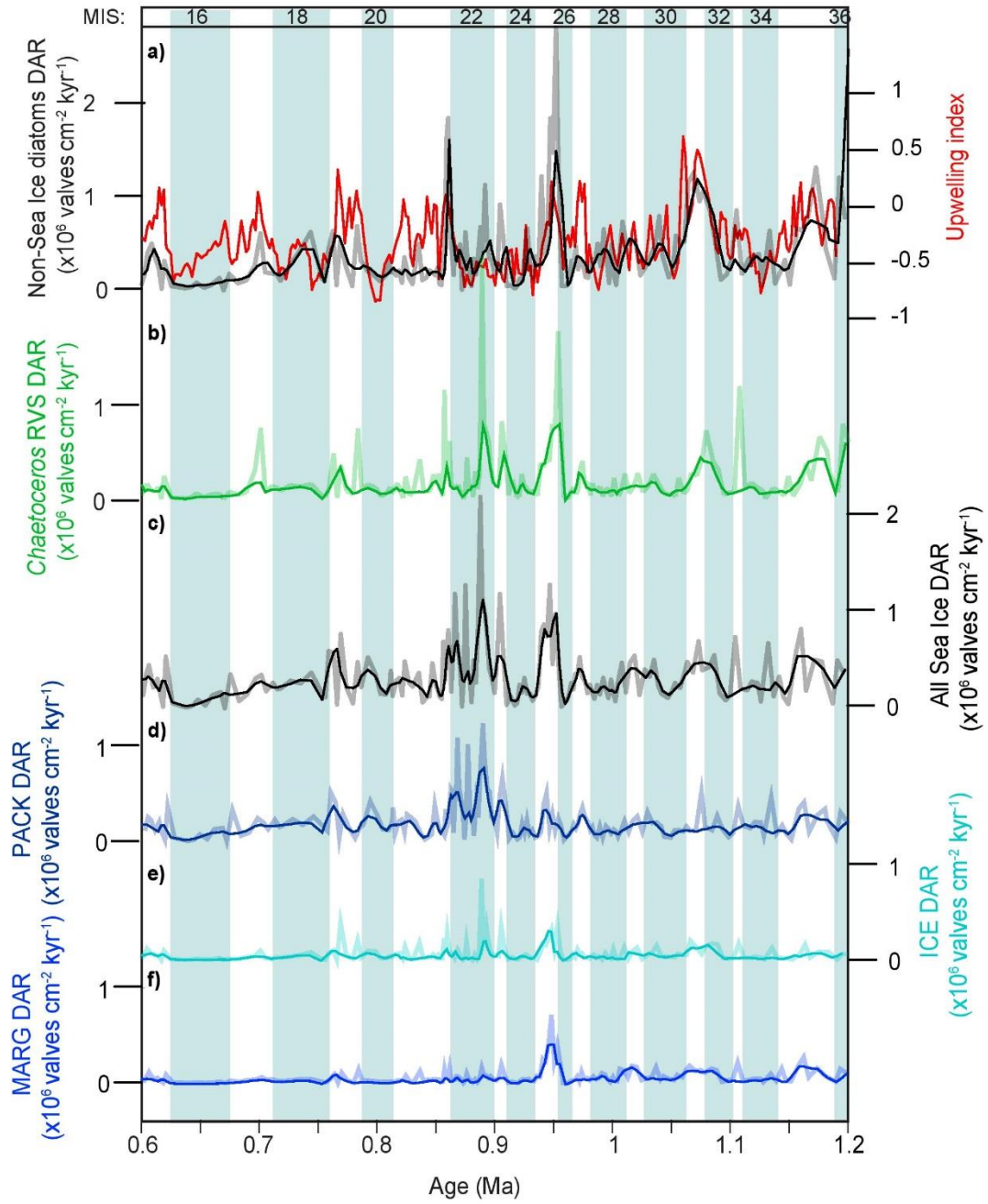


Figure 4.3 Diatom accumulation rates (DAR) (fainter, thicker lines) have been smoothed using a 2-point spline (darker, thinner lines), allowing investigation into variation in absolute abundance of diatom productivity, with glacial periosd depicted by the blue bars. a) Non-Sea Ice DAR (black) shows similar trends to the upwelling index results (Chapter 3), where higher Non-Sea Ice DAR occurs during periods of increased nutrient upwelling (red). Increased absolute abundance of *Chaetoceros* RVS (b) and All Sea Ice DAR (c) occur during the 900 kyr event. In particular, increased abundance of PACK DAR (d) and ICE DAR (e) contribute to the increase in All Sea Ice DAR during MIS 22. Increased absolute abundance of ICE and MARG DAR (f) also cause higher All Sea Ice DAR during MIS 25 when productivity is high (Figure 4.1).

region and more southerly Bering Sea sites, which also demonstrate decreased abundance of *N. seminae* through this period (Stroynowski et al., 2015, 2017; Teraishi et al., 2016). Corresponding increases in the relative abundance of sea ice related species, particularly the ICE and PACK groups (Figure 4.2b-c), are in agreement with lipid biomarker sea ice reconstruction work, suggesting a more prominent seasonal advance and retreat of sea ice margin, with maximal extent occurring in the mid-glacial interval (Detlef et al., 2018).

4.3.4 Interim Period: MIS 30-27 (~1.05 – 0.98 Ma)

Diatom assemblages show a clear succession in the dominance of MARG species and key pelagic taxa between MIS 30 and 27 (Figure 4.2c, Figure 4.5). During this interval, biomarker results from Detlef et al., (2018) identified an "interim period" which extended between ~1 – 0.95 Ma (mid-MIS 28 to MIS 26/25), characterised by persistent marginal ice conditions with smaller variations in the position of the winter and summer margin. This was attributed to continued inflow of relatively warmer Alaskan Stream waters into the Bering basin, as identified by previous low resolution diatom assemblage work of Teraishi et al. (2016), which prevented sea ice expansion despite SST cooling elsewhere in the subarctic Pacific Ocean (Figure 4.1c).

Higher resolution diatom assemblage results, presented here on the updated age model (Chapter 3) show that MARG species (in particular *P. glacialis*; Figure 4.5) exhibits an initial increase in relative abundance from a slightly earlier time around 1.05 Ma during mid-MIS 30 (Figure 4.2c). Following this, the relative abundance of MARG continues to increase through MIS 29-28, when there is a fairly stable relative abundance of *N. seminae* (~15%) and increased abundance of *S. trifultus* (~5%) (Figure 4.2e, Figure 4.5).

This indicates the continued influence of warmer waters from the lower subarctic Pacific Ocean in the Bering gyre, and is congruent with the interpretation of biomarker data (Detlef et al., 2018), which proposed that continued inflow of subarctic waters likely counteracted significant expansion of sea ice through the interim period. However, during the subsequent interglacial (MIS 27), increased relative abundance of PACK species and lower relative abundance of N. seminae advocates sea ice expansion when the influence of Alaskan Stream waters decreased, likely facilitated by a minima in insolation and minimal subarctic SST during this interval (Figure 4.1b-c, Figure 4.2a, e). Overall, using the higher resolution age model and diatom assemblage results for Site U1343, the interim period identified in the biomarker record appears to have started slightly earlier at 1.05 Ma when marginal ice species first began to increase in relative abundance during mid-MIS 30, and also ended slightly earlier at 0.98 Ma, when assemblage results indicated significantly reduced influence Alaskan Stream waters and sea ice expansion at MIS 27.

4.3.5 Build up to MPT conditions: MIS 27-25 (~0.98-0.94 Ma)

Following the interim period, the relative abundance of MARG decreases and is replaced by increased abundance of PACK and *Chaetoceros* RVS, indicating a period of sea ice growth with a stronger melt-associated bloom. This is consistent with interpretation of the biomarker results which suggest a more pronounced seasonal cycle with higher variability in the position of the sea ice margin after the interim period (Detlef et al., 2018). Additionally, there is increased relative abundance of *S. turris* (~10%) in MIS 27 and high relative abundance of *P. sulcata/M. sol* (~15%) throughout glacial MIS 26 (~0.95 – 0.97 Ma) (Figure 4.2i, Figure 4.5). Increased abundance of these laterally transported

species, coincident with lower relative abundance of *N. seminae*, suggests strong circulation persisted in the Bering basin despite sea ice growth and reduced Alaskan Stream inflow. As the modern sea ice distribution is controlled predominantly by northerly winds, in turn dependent on the intensity and location of the Aleutian Low (Rodionov et al., 2007), it is highly likely that atmospheric forcing played at least some role in this southward expansion of sea ice. This was posited by Knudson and Ravelo, (2015a), who also hypothesise that a shift in the Aleutian Low would have resulted in more northerly winds over the Bering Sea and hence enhanced both polynya growth regions, sea ice formation and its southerly extension (Rodionov et al., 2007). Increased windiness would also have acted to maintain gyre strength and increase BSC eddy activity and nutrient upwelling, which is supported by high productivity (opal MAR) and increased abundance of shelf-dwelling species (Figure 4.1f, Figure 4.2i, Figure 4.5).

During the following interglacial (MIS 25), maximum absolute abundance of Non Sea ice DAR (mean = 1061 x 10^6 valves cm^{-2} kyr^{-1}) is consistent with high opal MAR and increased interglacial nutrient upwelling (Figure 4.1f, Figure 4.3a). This is supported by increased relative abundance of *N. seminae*, indicatimg that Alaskan Stream waters influenced the Bering gyre and likely strengthened BSC flow through this interglacial (Figure 4.2e). However, simultaneous peaks in absolute abundance of All Sea ice (654 x 10^6 valves cm^{-2} kyr^{-1}) and *Chaetoceros* RVS (mean = 627 x 10^6 valves cm^{-2} kyr^{-1}) also suggest a sea ice dominant environment with an extended spring bloom period (Figure 4.3b-c). Maximal relative abundance of MARG species and increased abundance of ICE, but minimal abundance of PACK, reflects

dominance of marginal sea ice condition during MIS 25, with a longer melt period which sustained a large spring bloom (Figure 4.2a-c, Figure 4.3d-f).

Overall, the total DAR and export production during MIS 25 appears to have been amplified by both an extended sea ice melt and spring bloom following increased accumulation of sea ice during MIS 27-26 (Figure 4.6). Ample summer/autumn nutrient availability was also sustained by increased windiness and strong BSC flow, which will have increased nutrient upwelling and stimulated diatom productivity. Notably high productivity and longer spring and summer blooms suggests there was likely an increased efficiency in the biological pump, in which higher export production may have sequestered more CO_2 in the Bering basin, causing the green belt to act as a net CO_2 sink. Increased interglacial CO_2 drawdown could have contributed to lower global atmospheric CO_2, facilitating climate cooling in the build up to the 900-kyr event (Chalk et al., 2017).

4.3.6 The MPT and the 900 kyr event: MIS 24-22 (~0.94 – 0.87 Ma)

The final development before the establishment of peak MPT conditions saw a large and sudden increase in the relative abundance of *Actinocyclus* spp. and *Rhizosolenia* spp. during early MIS 24 (Figure 4.2g-h). Dominance of these species indicates that the Bering Sea slope region was highly stratified, with low-nutrient surface waters persistent through the summer and autumn. This stratification event is likely a result of the large scale melting of sea ice, which accumulated after the interim period. *R. hebetata* likely had a competitive advantage through utilising nutrients found below the nutricline, as other autumn mat-forming taxa were limited to the isolated nutrient pool in the photic zone. Furthermore, a shift in the relative abundance of sea ice groupings to

favour PACK and ICE (particularly *Fragilariopsis* spp.) over MARG, suggests an increase in the number of months with significant sea ice cover during this glacial (Caissie et al., 2010) (Figure 4.2a-c). A longer sea ice season would have caused a shift of the melt period to later in the year, causing a more highly stratified summer/autumn, during which vertical mixing would have also been restricted, causing lowered photic zone pCO_2. This is consistent with decreased nutrient upwelling and productivity (Figure 4.1e-f), where reduction of the marginal sea ice season and the associated spring/summer blooms would also have decreased net export production.

The "failed" interglacial at MIS 23, also known as the 900 kyr event, is considered the tipping point after which global climate begins to oscillate on 100-kyr timescales (Elderfield et al., 2012; McClymont et al., 2013; Kender et al., 2018). During this period, continental land ice began to rapidly accumulate, causing significantly decreased sea levels (Figure 4.1d). Diatom assemblages show this interval is characterised by a pulse in the absolute abundance of *Chaetoceros* RVS, peaks in both relative and absolute abundance of PACK and ICE species (Figure 4.2a-c, Figure 4.3b-e), and very low species diversity, even compared to previous low productivity glacials. A small but sustained increase in the relative abundance of benthic species throughout this glacial also reflects the exposure of the Bering shelf and hence more coastal location of Site U1343 following significant sea level drop (Figure 4.2d). Rapid sea level decline would have shoaled the eastern Aleutian passes and severely reduced inflow of the warmer Alaskan Stream into the Bering basin, promoting SST cooling and rapid sea ice accumulation. Reduced surface water flow would also have acted to lower BSC eddy activity, causing suppressed nutrient upwelling and low

productivity, supported by low Non-Sea Ice DAR (Figure 4.3a). The prevalence of *Chaetoceros* RVS and PACK species suggests the provision of a secondary nutrient supply, most likely from sea ice-derived nutrients, which is known to be a key source in the modern system (Aguilar-Islas et al., 2008) (Figure 4.3b-c) (see also Chapter 5).

The following glacial at MIS 22 is considered to be the first of the more severe 100 kyr glacial cycles (Lisiecki & Raymo, 2005). DAR results show evidence for significant sea ice expansion during this glacial, where the absolute abundance of All Sea ice species has a mean of 677 x 10^6 valves cm^{-2} kyr^{-1} (Figure 4.3c). As the glacial develops, there is a sudden drop in the relative abundance of ICE and *Chaetoceros* RVS species at the mid-glacial, suggesting extremely low nutrient and/or light conditions prevailed, where even epontic diatoms could not survive (Figure 4.2b, f). A mid-glacial peak in *Rhizosolenia* spp. also supports this, as this taxa would have been able to access nutrients at deeper depths and survive in low light conditions during the initial build-up of sea ice leading up to the late glacial (Figure 4.2g). Subsequently low species diversity and dominance of PACK species at the glacial maxima, reaching its maximal relative and absolute abundance, indicates the development and persistence of thick multi-year sea ice (Figure 4.2a, Figure 4.3d).

Overall, the 900 kyr event was characterised by a progressive shift in diatom assemblages, with initially increased abundance of PACK and ICE in MIS 23 and early MIS 22 reflecting build-up of thicker and more extensive sea ice. Peaks in the abundance of *Chaetoceros* RVS during this same period suggests there was an oscillation between a longer winter sea ice season and a sustained, but shorter, melt associated bloom in spring/summer. This indicates

there was a shift in the nutrient source for green belt productivity during the MPT, where melt-associated diatom productivity was sustained by shelf derived nutrients in the absence of upwelled nutrient-rich NPDW. Then, from mid-MIS 22, a sudden decrease in ICE and *Chaetoceros* RVS, and maximal PACK abundance suggests that only thick perennial sea ice conditions persisted on the Bering slope until deglaciation of MIS 22. The timing of this shift to a sustained pack ice environment is congruent with the glacial maxima identified in the global benthic $\delta^{18}O$ LR04 stack (Lisiecki & Raymo, 2005), suggesting MPT sea ice evolution in the Bering Sea reflects a global signal (Figure 4.2a).

4.3.7 Post-MPT: MIS 21-15 (~0.85 – 0.6 Ma)

At the end of the 900 kyr event, deglaciation at MIS 22/21 is characterised by a significant pulse in *N. seminae,* accompanied by high relative abundance of *P. sulcata/M. sol*, reaching values similar to the early Pleistocene (Figure 4.2e, i). This provides evidence for resumed circulation in the Bering basin and restored BSC strength following sea ice melt. A delayed deglacial peak in *Chaetoceros* RVS and persistently high abundance of coastal species *S. turris* through MIS 21 (Figure 4.2f, Figure 4.5) is consistent with a long sea ice retreat period following a rising sea level, where strong surface water circulation flow was maintained by increased deglacial windiness (Gray et al., 2018; Kender et al., 2018). Re-established BSC eddy activity at the deglaciation would have caused NPDW upwelling to recommence, raising nutrients which accumulated in the deep Bering basin to the photic zone and fuelling high interglacial productivity (Figure 4.1e-f).

After the MPT, from MIS 21 onwards, 100 kyr glacial-interglacial cycles are established. Longer and more severe post-MPT glacials are

characterised by higher abundances of PACK and increased relative abundance of benthic species, depicting a more sea-ice dominant environment with lower glacial sea level stands and persistent shallowing of Site U1343 (Figure 4.2a, d). Similarly, post-MPT interglacials generally exhibit higher abundance of ICE and MARG and lower *N. seminae* and *Actinocyclus* spp. than previous interglacials, suggesting the inflow of Alaskan Stream water was never fully restored as glacial sea level declines were larger after the MPT, enabling longer winter seasons with extended sea ice presence (Figure 4.2b-c, e, h) (Kender et al., 2018).

Trends in the relative abundance of PACK after the MPT strongly resemble the LR04 $\delta^{18}O$ stack, suggesting that sea ice expansion in the Bering Sea was responding to global climate changes (Figure 4.1a, Figure 4.2a). For example, a less substantial sea level drop and relatively warmer conditions during mid-glacial MIS 18 (~0.73 Ma) is reflected in reduced relative abundance of PACK. Furthermore, high relative abundance of PACK in early MIS 16 (~ 0.67 Ma) reflects the cold glacial conditions indicated by the LR04 stack, despite lighter $\delta^{18}O$ at Site U1343. Deglacial peaks in *Chaetoceros* RVS suggests strong melt associated spring blooms occurred following retreat of larger volumes of sea ice after the MPT (Figure 4.2f). Furthermore, lower Non-Sea Ice DARs in post-MPT interglacials after MIS 22 and variable but generally sustained high relative abundances of all sea ice groupings in both glacial and interglacial periods after the MPT, indicate shorter summer/autumn seasons with more sea ice dominant conditions, in comparison to pre-MPT cycles (Figure 4.2a-c, Figure 4.3a).

4.4 Wider impact: Assessing MPT Hypotheses

4.4.1 Intensified Walker circulation in the early Pleistocene

As subarctic Pacific Ocean SSTs declined through the early Pleistocene, lower surface ocean heat capacity and the resultant increase in salinity-driven stratification could have promoted sea ice expansion through MIS 27 (Brunelle et al., 2007; Detlef et al., 2018). However, high abundance of laterally transported species, observed here in the Bering Sea during MIS 27-25, suggests that increased storm frequency/windiness after the interim period was also likely pivotal in promoting increasing thickness and extent of sea ice. A potential mechanism to explain both enhanced storminess and increased sea ice formation in the Bering Sea is an intensified Walker circulation (Chapter 3). In the modern day, changes in the El-Niño Southern Oscillation (ENSO) have been shown to impact the position and intensity of the Aleutian Low, which has a large influence over the extent of sea ice in the Bering Sea (Rodionov et al., 2007). Evidence for equatorial deep water cooling and an increased zonal Pacific SST gradient, which emulate La Niña-like conditions when the Walker circulation is enhanced, is thought to have begun ~1.17 Ma, with evidence for equatorial continental cooling from ~1.05 Ma (Dupont et al., 2001; McClymont & Rosell-Melé, 2005). As the Walker circulation intensified in the early Pleistocene (McClymont & Rosell-Melé, 2005), a shift in the Aleutian Low and the resultant increase in windiness and moisture supply but decrease in poleward heat transport to the subarctic, would have promoted sea ice growth. This is supported by time series analysis of the upwelling index which showed variation at suborbital frequency and was interpreted to reflect the increased

sensitivity of marginal sea ice to fluctuations in the East Asian Winter Monsoon (EAWM), which also resulted from intensified Walker circulation (Chapter 3).

4.4.2 NPIW expansion and reduced CO_2 ventilation

During the interim period (1.05 – 0.98 Ma), continued inflow of warmer Alaskan stream waters prevented sea ice expansion in the Bering Sea. However, at the end of the interim period a threshold, where increased storm frequency and moisture availability promoted enough sea ice growth to shoal the eastern Aleutian passes and lower Bering Sea SST, likely facilitated further sea ice expansion. The resultant increase in seasonality in which the sea ice margin fluctuated more significantly, causing a strong spring and summer bloom, supported extremely high productivity during MIS 25 which was sustained by nutrients supplied from both upwelled NPDW and from sea-ice derived sources (Figure 4.1). Increased export production may also have caused the Bering Sea to act as a net CO_2 sink due to increased efficiency of the biological pump.

During early MIS 24, large-scale sea ice melt caused an intense stratification event which may have also been an important precursor to MPT conditions. Although sea ice did not extend directly into the lower subarctic Pacific Ocean, rapid melting of larger volumes of sea ice in the Bering Sea may have propagated to enhance stratification across the lower subarctic Pacific (e.g. ODP Site 882), preventing vertical mixing/upwelling and further reducing air-sea CO_2 exchange regionally. Although the Southern Ocean is considered the most dominant region for ocean-atmosphere CO_2 balance (Sigman et al., 2010), increased green belt CO_2 drawdown in MIS 25 and reduced CO_2 ventilation from the subarctic Pacific region in MIS 24, could certainly have been important components in the step-change observed during the 900 kyr event.

During the 900 kyr event, rapid accumulation of ice sheets caused larger declines in sea level during MIS 24 (Elderfield et al., 2012). Diatom assemblage evidence supports the development of more extensive sea ice, concurrent with sea level decline greater than 50 m, which likely caused closure of the Bering Strait (Figure 4.1d, Figure 4.2a) (Kender et al., 2018). Sea ice expansion at this time corroborates the notion that increased brine rejection likely facilitated NPIW expansion during the middle Pleistocene. If NPIW propagated from the Bering Sea and throughout the subarctic Pacific Ocean during MIS 24-22, reduced nutrient upwelling/vertical mixing would have acted to further prevent CO_2 ventilation to the atmosphere across the region. Modelling studies suggest that the subarctic North Pacific may have contributed ~30 ppm of CO_2 during deglacial periods (Rae et al., 2014). Therefore, suppression of abyssal carbon in the deep North Pacific Ocean would likely have contributed to the failure of full deglaciation at MIS 23. Although it is beyond the scope of this study to comment on the exact relationship between atmospheric pCO_2 and ice sheet dynamics, reduced CO_2 ventilation from the North Pacific Ocean, as a result of sea-ice driven stratification and NPIW formation, could have been key in lowering global pCO_2 and facilitating the large-scale ice sheet growth which occurred at ~0.9 Ma (Chalk et al., 2017).

4.4.3 Sea Ice Switch Hypothesis

As MPT conditions prevailed, persistent high relative and absolute abundances of sea ice diatoms, particularly those associated with pack ice, provide evidence for perennial or multi-year sea ice (Figure 4.2, Figure 4.3). As sea ice accumulation is self-limiting, where growth is eventually terminated by low moisture supply, and the insulating effect of sea ice on the surface ocean

(isolating from the cooler atmosphere) (Tziperman & Gildor, 2003), a large scale deglaciation occurred at MIS 21/22, after which 100 kyr glacial cycles were established. Larger volumes of sea ice during post-MPT deglacials would have modulated moisture availability and hence land ice growth and sea level change, as suggested by the SIS hypothesis. Support for this here in the Bering Sea is found in the delayed peaks in *Chaetoceros* RVS during deglacials, which suggest longer sea ice retreat phases, likely as a result of a larger volumes of sea ice.

However, strong similarity in relative abundance of PACK species and the LR04 benthic stack during post-MPT glacials, where sea ice maxima occur during the late glacial (simultaneous with ice sheet maxima), suggests that sea ice extent was mainly responding to climate changes, rather than leading it. Enhanced glacial sea ice formation after the MPT was therefore likely a response to persistently reduced inflow of warmer Alaskan Stream following ice sheet growth and large sea level declines.

Overall, the available data suggest that pre-MPT ice sheet expansion was likely modulated by ocean-atmosphere CO_2 exchange, rather than a direct shift in sea ice/land ice hysteresis. When ice growth became self-limited, the small rise in sea level rise following initial ice melt would have flooded the Bering Strait, causing regional collapse of NPIW which accumulated during the glacial, allowing ventilation of abyssal CO_2 across the subarctic Pacific Ocean. A sudden release of deep ocean CO_2 across the subarctic Pacific would have contributed to the speed of post-MPT deglaciation events (Rae et al., 2014; Gray et al., 2018; Kender et al., 2018). Following a larger sea ice retreat phase, NPIW collapse would have also resumed nutrient upwelling and facilitated high

interglacial primary productivity, despite more sea-ice heavy conditions. Overall, larger land ice volumes (and hence greater sea level changes) facilitated increased post-MPT sea ice growth and enhanced glacial NPIW formation. While sea ice growth would have modulated moisture availability causing gradual land ice accumulation during post-MPT glacials, expanded NPIW layer was more critical in regulating ocean-atmosphere CO_2 exchange, causing both glacial suppression and rapid deglacial release of CO_2, and explaining the "saw-tooth" shape of 100 kyr glacial - interglacial cycles.

4.5 Conclusion

Diatom assemblages have been used as faithful palaeoenvironmental proxies to reconstruct sea ice in the Bering Sea (Sancetta, 1982; Caissie, 2012; Stroynowski et al., 2015, 2017; Teraishi et al., 2016). Previous studies were limited by short timescales or low temporal resolution, and therefore assessment of long term sea ice evolution and dynamics during the Pleistocene has been limited. Here, the first millennial-scale resolution sea ice reconstruction for the subarctic Pacific Ocean through the enigmatic MPT period is presented. Early MPT assemblages align with previous low resolution results from Site U1343 (Teraishi et al., 2016), as well as other Bering slope records (Stroynowski et al., 2017), which show distinct glacial-interglacial variability and prominent seasonality. The "interim period" detected by the lipid biomarker sea ice reconstruction from Site U1343 (Detlef et al., 2018), is identified here at a slightly earlier time interval between 1.05 – 0.98 Ma. During this, the continued supply of relatively warmer Alaskan Stream waters into the Bering Sea acted to hinder sea ice expansion and minimise seasonality during MIS 29-28, despite SST decline in the lower subarctic Pacific Ocean.

Results show that Bering Sea sea ice expansion through the early-mid Pleistocene was likely facilitated by an amplified Walker circulation, following cooling in the equatorial Pacific and modulated by sea level-driven changes in Alaskan Stream inflow. Sea ice evolution was responding to global climate changes through the mid-late Pleistocene, primarily controlled by continental ice-sheet dynamics and sea level fluctuations. This is supported by spectral analysis of the upwelling index which suggests that nutrient upwelling and sea ice showed increased sensitivity to monsoon intensity and seasonality at suborbital periodicities (Chapter 3). During the MPT, extended sea ice in the Bering Sea was enabled by a significant sea level decline due to notable global continental ice sheet growth at 0.9 Ma, which significantly reduced warm Alaskan Stream water inflow. In turn, increased sea ice and reduced BSC strength caused expansion of a low nutrient NPIW layer which stifled upwelling of NPDW and lowered primary productivity (Kender et al., 2018) (Chapter 3). Results support the notion that the resultant expansion of NPIW across the subarctic Pacific Ocean was likely a contributor to both longer glacial periods (due to suppressed deep water CO_2 ventilation) and to the rapidity of deglaciation (following regional collapse of NPIW as sea levels begin to rise), alongside Southern Ocean driven CO_2 dynamics. As a result of larger volumes of post-MPT sea ice, the impact on export production and regional upwelling likely played an important role in global ocean-atmosphere dynamics on glacial-interglacial timescales through this interval.

4.6 Supporting information

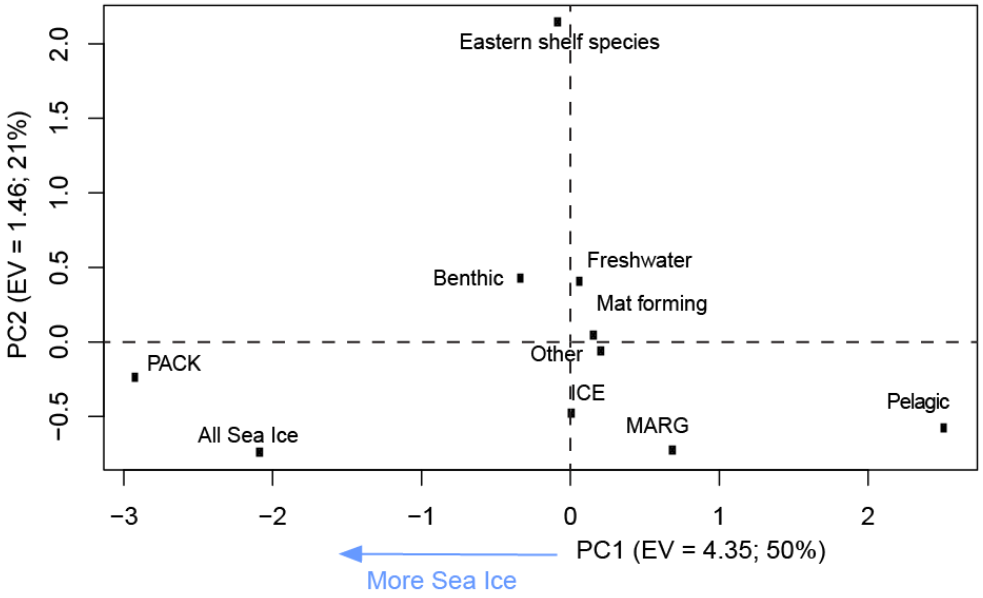


Figure 4.4 Principal Component Analysis (PCA) results confirm that sea ice explains 50% of variability in the diatom percentage data, where the volume of sea ice increases from pelagic open water conditions to thick pack ice environments (blue arrow). “All Sea Ice” group in the bottom left corner is a sum of the PACK, MARG and ICE groups.

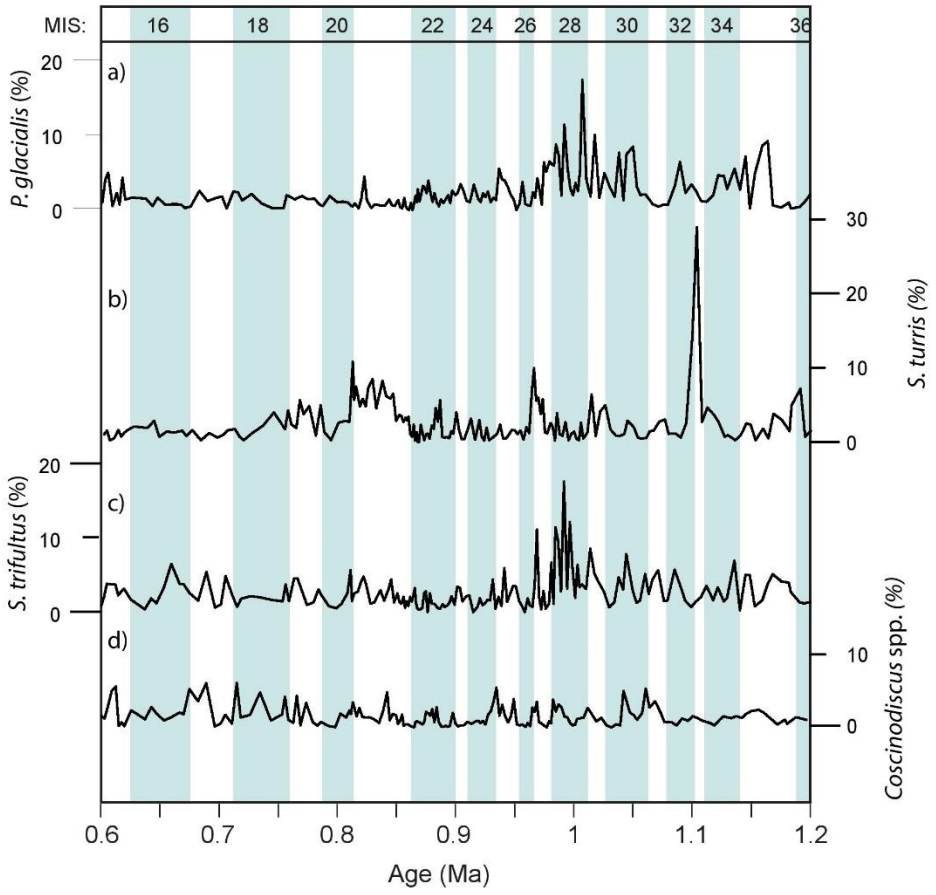


Figure 4.5 Relative abundance of other diatom species including marginal ice species *P. glacialis* (a), *S. turris* which is indicative of the strength of current speeds through the Aleutian island arc (b), *S. trifultus* which thrives in colder waters (c) and summer blooming species *Coscinodiscus* spp. (d)

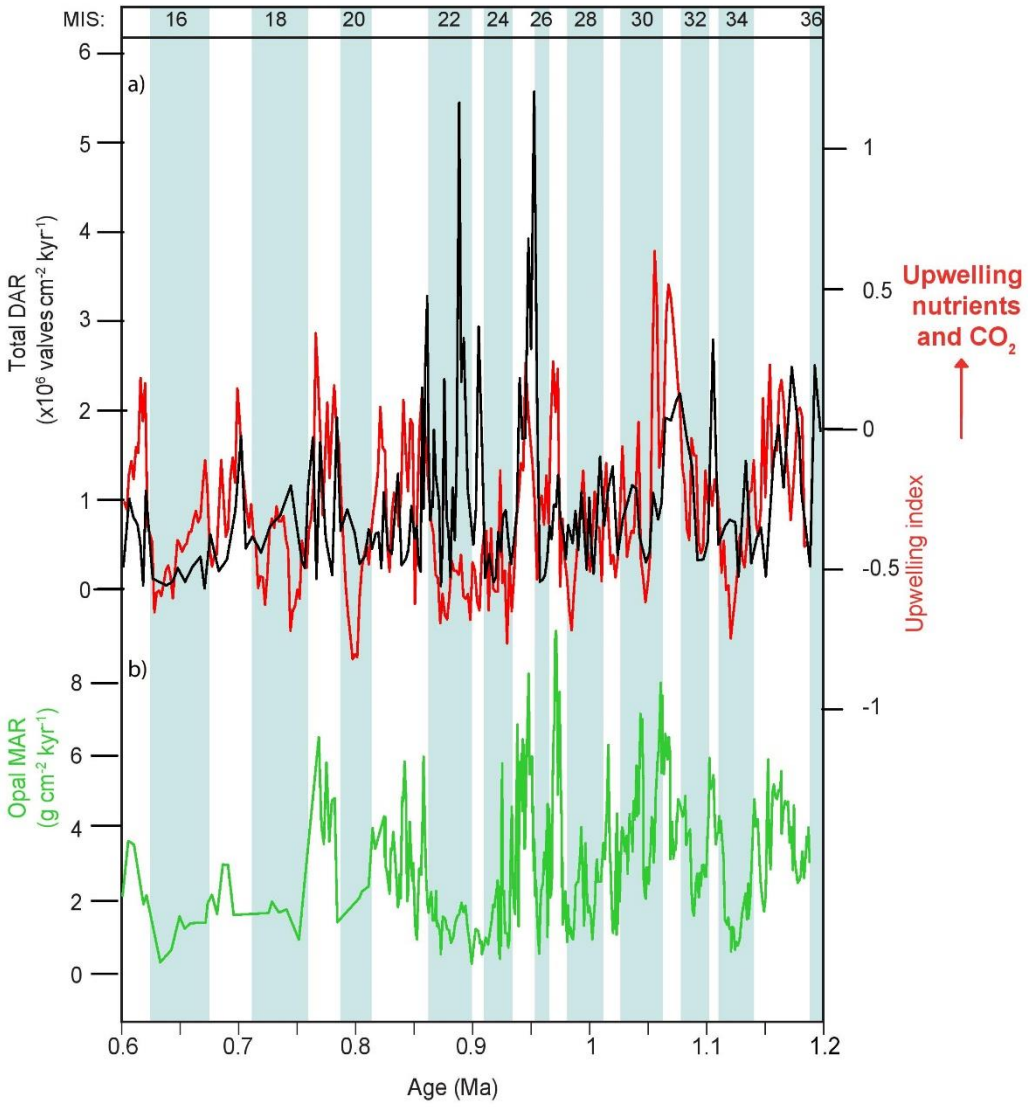


Figure 4.6 Total DAR (black) is compared to the upwelling index (red; Chapter 3) and shows similar trends with higher total DAR during periods of higher nutrient upwelling, with exception during the 900 kyr event (MIS 23-24) during which there is high Total DAR, despite low nutrient upwelling (a). Total DAR also shows strong similarity to opal MAR (Kim et al., 2014) with high Total DAR during periods of higher productivity (b).

Chapter 5: Increased efficiency of the subarctic Pacific biological pump during the Mid Pleistocene Transition

Savannah Worne[1]*, George E. A. Swann[1], Sev Kender[2,3] and Melanie J. Leng[3,4]

[1]Centre for Environmental Geochemistry, School of Geography, University of Nottingham, Nottingham, NG7 2RD, UK

[2]Camborne School of Mines, University of Exeter, Penryn Campus, Penryn, Cornwall, TR10 9FE, UK

[3]British Geological Survey, Keyworth, Nottingham, NG12 5GG, UK

[4]Centre for Environmental Geochemistry, School of Biosciences, University of Nottingham, Sutton Bonington Campus, Loughborough, NE12 5RD, UK

*Corresponding author. Email: savannah.worne@nottingham.ac.uk

Abstract

High latitude ocean-atmosphere CO_2 dynamics are often considered an important mechanism in shaping glacial-interglacial dynamics, with the efficiency by which carbon is buried in the deep ocean via the biological pump being highly variable through the Quaternary. During a shift to longer and more severe glacial periods during the Mid Pleistocene Transition (MPT), it has been suggested that iron fertilisation and increased efficiency of the biological pump in the Southern Ocean played a key role on lowering atmospheric pCO_2 and facilitating the "900 kyr event" during which land ice rapidly accumulated. Here silicon isotope measurements on diatoms ($\delta^{30}Si_{diatom}$) from the high productivity upwelling region adjacent to the Bering shelf, are used to assess the role of the

biological pump in the subarctic Pacific Ocean on the MPT. Findings provide evidence for an increase in the utilisation of silicic acid prior to the 900 kyr event, likely due to increased shelf borne iron as sea ice begins to expand following atmospheric and surface water cooling. During the 900 kyr event, low silicic acid utilisation but high nitrate utilisation and the dominance of diatom resting spore production suggests that the region became nitrate and light limited rather than iron, due to the development of thick pack ice and expansion of NPIW which suppressed nutrient upwelling. I posit that iron fertilisation from sea ice expansion, coupled with the preferential preservation and higher cellular carbon content of resting spores produced during this time, increased regional carbon export and contributed to low atmospheric pCO_2, in addition to changes in the Southern Ocean. Remnant iron and remineralised silicic acid at the Bering slope also likely propagated into the lower subarctic Pacific Ocean through NPIW, aiding high productivity across the region once upwelling/vertical mixing was restored. If the efficiency of biological pump was maintained in post-MPT deglacials across the subarctic region, this would have then contributed to a slower release of deep ocean carbon in the subarctic Pacific and hence longer glacial periods following the MPT.

5.1 Introduction

The Quaternary climate is typified by glacial-interglacial cycles, which are primarily modulated by the interplay between orbital forcing and ice sheet evolution. Between 1.2 and 0.6 Ma, a change in frequency of these cycles from 41 kyr to 100 kyr occurred, although no change in the long term solar budget of the Earth indicates that an internal feedback mechanism was a likely cause. This shift, known as the Mid Pleistocene Transition (MPT), is characterised by

global air and ocean cooling, with a rapid increase in land ice volume occurring during the "900 kyr event", after which glacials became more severe with continued accumulation of large ice volumes which causing sea level drops of 50 – 200 m (Lisiecki & Raymo, 2005; Elderfield et al., 2012; McClymont et al., 2013). There is little consensus on the cause of the MPT, although many proposals invoke high latitude ocean-atmosphere CO_2 dynamics as an important mechanism, despite being poorly constrained in the proxy records. For example, low resolution boron isotope measurements from the eastern equatorial Atlantic (Hönisch et al., 2009) and Caribbean Sea (Chalk et al., 2017), as well as modelled global pCO_2 records (Chalk et al., 2017) indicate that there was notably low atmospheric pCO_2 at ~0.9 Ma, consistent with rapid ice sheet growth and increased dissolved inorganic carbon (DIC) in ocean deep waters (Sigman et al., 2010; Elderfield et al., 2012; Diester-Haass et al., 2018; Farmer et al., 2019).

One mechanism which could have lowered atmospheric pCO_2 is termed the "biological pump", in which primary producers such as diatoms photosynthesise carbon found in surface waters and export it to the deep ocean (Sigman & Haug, 2004). This hypothesis is proposed to have been a key internal component in driving the severity and nature of glacial-interglacial climate through the Quaternary (Broecker, 1982), through either reduced upwelling of nutrients in equatorial and subtropical surface ocean productivity or increased polar and subpolar nutrient utilisation (Sigman & Haug, 2004). In the latter case, in high latitude regions, the efficiency of the biological pump is largely dependent on the availability of light and iron (from aeolian, upwelling deep water and shelf-derived sources), which are in turn modulated by sea ice,

intermediate/deep water formation and water column stratification (Sigman et al., 2010; Kim et al., 2014; Lear et al., 2016; Chalk et al., 2017; Kender et al., 2018). For example, under the Silicic Acid Leakage Hypothesis, glacial increases in aeolian iron input to the Southern Ocean would have lowered diatom silicic acid to nitrate utilisation ratios (Si:N), increasing the pool of unutilised silicic acid in the photic zone (Matsumoto et al., 2002b; Matsumoto & Sarmiento, 2008). The subsequent transfer of this pool of silicic acid to lower-latitudes would have promoted the growth of diatoms in those regions, increasing the net global export of carbon into ocean interior.

During the MPT, greater availability of iron in the Southern Ocean ("iron fertilisation"), either due to lower sea level or through atmospheric cooling/drying and changes in surface winds, is suggested to have facilitate a further increase in the biological uptake of CO_2 (Chalk et al., 2017). This increased efficiency of the biological pump is proposed to have caused a positive feedback during the 900 kyr event which promoted rapid ice sheet accumulation and increased glacial severity and duration (Chalk et al., 2017). However, sporadic measurements and a lack of high resolution records of atmospheric CO_2 and biological export, particularly through the 900kyr event, has limited full assessment of this mechanism.

Although the biological pump in the Southern Ocean, where ~30-50% of silicon export production occurs (Gnanadesikan, 1999; Reynolds, 2009), is considered the most significant region for high-latitude ocean-atmosphere CO_2 exchange, there is growing evidence that the subarctic Pacific Ocean could also play a key role in Quaternary climate dynamics (Haug et al., 1995, 2005; Sigman et al., 2010; Jaccard & Galbraith, 2018). In particular, the Bering Sea

in Northern subarctic Pacific Ocean is considered a key region for understanding deep water upwelling dynamics (Kender et al., 2018; Worne et al., 2019) (Chapter 3). At the Bering shelf slope, nutrient-rich (nitrate, silicic acid and phosphate) North Pacific Deep Water (NPDW) upwells due to large eddies in the shelf-adjacent Bering Slope Current (BSC), which fuel a region of seasonally high productivity known as the "green belt" (Figure 1.3). Modern annual green belt productivity is estimated at 175-275 g C m^{-2} yr^{-1} and is dominated by spring and summer diatom blooms (Springer et al., 1996). During the spring, iron-rich ice-entrained sediments from the shelf are released during sea ice melt which forms a key source of iron to the green belt (Aguilar-Islas et al., 2008). Sea ice then also modulates the success of diatom growth (and hence the biological pump) through its control on light availability and water column stability, as melt waters stratify the water column and allow diatoms to remain in the photic zone for longer to utilise more of the available nutrients (Aguilar-Islas et al., 2008). However, productivity becomes iron-limited in the summer when a HNLC environment with an inefficient biological pump develops, causing the region to become a seasonal source of CO_2 to the atmosphere (Aguilar-Islas et al., 2007; Takeda, 2011). Overall, the net annual efficiency of biological carbon export is therefore highly dependent on the strength of NPDW upwelling and the seasonality and duration of sea ice melt (Kim et al., 2011).

5.1.1 Paleoceanography of the Bering Sea

Between the onset of Northern Hemispheric Glaciation (NHG; ~2.7 Ma) and 1.25 Ma, export production in the Bering Sea was significantly higher than the adjacent subarctic Pacific region, particularly in interglacials (Kim et al., 2014; Swann et al., 2016). Climate cooling, Northern Hemispheric ice sheet expansion

and glacial sea level decline between ~1.25 and 0.9 Ma (Elderfield et al., 2012; Stroynowski et al., 2017; Detlef et al., 2018) is suggested to have reduced glacial export production in the Bering Sea green belt due to colder surface water temperatures and increased light limitation associated with the sea ice expansion, as well as reduced nutrient availability following lowered BSC eddy activity which weakens upwelling strength (Kim et al., 2014; Stroynowski et al., 2017; Detlef et al., 2018; Kender et al., 2018) (Chapter 4).

The subsequent 900 kyr event is considered a tipping point, after which closure of the Bering Strait during glacials caused significant expansion of North Pacific Intermediate Water (NPIW), which acted to further suppress the upwelling of nutrients to the photic zone in the Bering Sea (Kender et al., 2018) (Chapter 3). This is supported by geochemical proxy evidence (bulk sedimentary $\delta^{15}N$ ($\delta^{15}N_{bulk}$)) which suggests that nitrate utilisation was high despite lower productivity, indicating that there was as a reduction in nutrient supply to the green belt (Figure 5.1) (Kender et al., 2018) (Chapter 3). NPIW expansion is suggested to have propagated across the wider subarctic Pacific Ocean, causing the whole region to become a glacial sink of CO_2 during the MPT (Kender et al., 2018) (Chapter 3). Given that ~30 ppm of CO_2 was modelled to have been released from the subarctic Pacific region during the last deglaciation in response to the collapse of NPIW (Rae et al., 2014; Gray et al., 2018), the suppressed CO_2 upwelling during MPT glacials and subsequent delayed release of CO_2 from the subarctic Pacific region is proposed to have been a significant factor in the increased duration of post-MPT glacials (Kender et al., 2018) (Chapter 3-4).

5.1.2 Diatom silicon isotopes

Although there has been investigation into the role of increased sea ice, NPIW expansion and suppressed NPDW upwelling on deep water CO_2 ventilation (nutrient upwelling) in the subarctic Pacific Ocean (Haug et al., 1999, 2005; Rae et al., 2014; Gray et al., 2018), the influence of these oceanographic changes on Bering Sea green belt export production and the regional biological pump have not been constrained. Given that green belt productivity is dominated by diatoms, measuring the silicon isotope content of fossil diatom material ($\delta^{30}Si_{diatom}$) can be used as a proxy for silicic acid utilisation. As diatoms preferentially assimilate lighter ^{28}Si than ^{30}Si, the ratio of these isotopes can be used to assess variation in the rate of silicic acid utilisation and/or supply, as diatoms which grew during periods of higher utilisation/lower supply will have a higher proportion of ^{30}Si preserved in their frustules (higher $\delta^{30}Si_{diatom}$) (De La Rocha et al., 1997).

$\delta^{30}Si_{diatom}$ measurements have been used previously in palaeoceanographic studies from a range of locations globally, from the high latitude Southern Ocean (De La Rocha et al., 2011; Egan et al., 2012; Hendry & Brzezinski, 2014) and subarctic Pacific (Swann, 2010; Bailey et al., 2011; Maier et al., 2015) to the eastern equatorial Pacific (Pichevin et al., 2009, 2012) and tropical Atlantic Oceans (Griffiths et al., 2013). Studies of this nature have primarily focussed on investigating variation in the biological pump on shorter timescales, generally spanning either the last glacial-interglacial cycle or through the onset of NHG. Similar studies from the Bering Sea show an increase in silicic acid supply occurred during the onset of NHG, causing increased siliceous productivity (Swann et al., 2016), while low resolution $\delta^{30}Si_{diatom}$

results from the green belt have been shown to vary on glacial-interglacial timescales over the last 0.6 Ma, modulated by variation in sea ice (Kim & Khim, 2017). However to date, there has been no investigation into how silicic acid utilisation varied through the early/middle Pleistocene, and what impact this may have had on the biological pump and the MPT.

Here $\delta^{30}Si_{diatom}$ data from IODP Site U1343 in the green belt region near the Bering slope is presented, between 0.6 and 1.2 Ma. In combination with diatom assemblages, diatom productivity (opal MAR) (Kim et al., 2014), nitrate utilisation ($\delta^{15}N_{bulk}$; Worne et al., (2019) and Chapter 3) and nutrient upwelling (Worne et al., (2019) and Chapter 3) data from the same site, the cause and effect of MPT oceanographic changes on the green belt biological pump are investigated. Through this and quantification of relative changes in silicic acid utilisation and supply through the MPT, a representative assessment for regional variation in the biological pump and so ocean-atmosphere CO_2 exchange is made.

5.2 Methods

5.2.1 $\delta^{30}Si_{diatom}$

Using the high resolution age model for Site U1343, based on the orbital tuning of benthic foraminiferal $\delta^{18}O$ (Figure 5.1) (Chapter 3), 30 raw sediment samples were selected between 0.6 and 1.2 Ma, with an average resolution of ~23 kyr. Diatoms were extracted from these samples with 30% H_2O_2 and 5% HCl to remove organic material and carbonates, respectively (Swann et al., 2013). Samples were then repeatedly mixed with sodium polytungstate (SPT) at a series of specific gravities from 2.10 g/ml to 2.25 g/ml to isolate a pure diatom

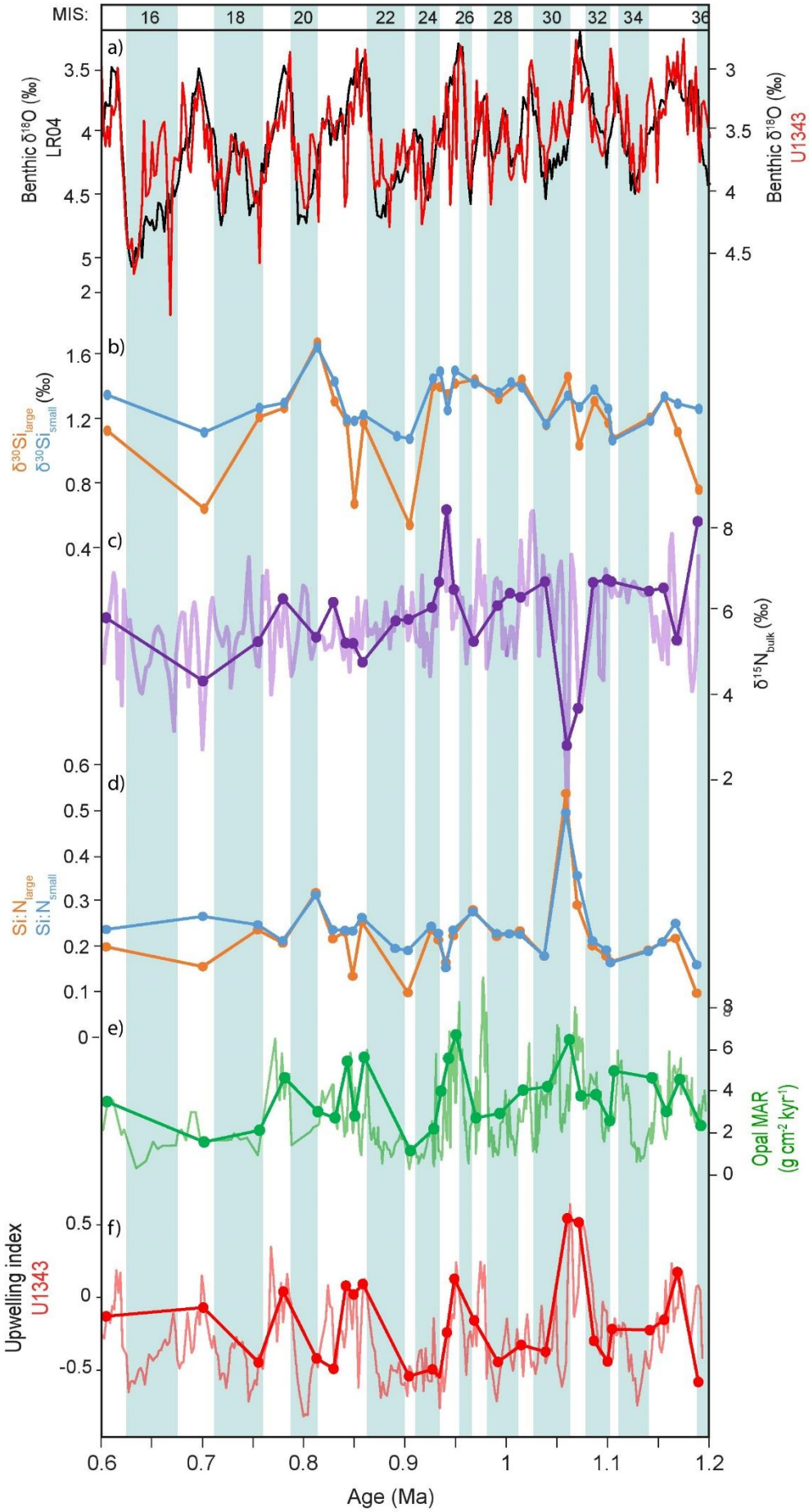

MIS:
16
18
20
22
24
26
28
30
32
34
36
a)
Benthic δ18O (‰) LR04
Benthic δ18O (‰) U1343
b)
δ30Si large
δ30Si small (‰)
c)
δ15Nbulk (‰)
d)
Si:N large
Si:N small
e)
Opal MAR (g cm-2 kyr-1)
f)
Upwelling index U1343
Age (Ma)

Figure 5.1 Geochemical proxy results from Site U1343 including the high resolution age model between 0.6 – 1.2 Ma (Chapter 3) (red) which is tuned to the LR04 global benthic stack (Lisiecki & Raymo, 2005) (black) (a). b) New $\delta^{30}Si_{diatom}$ results from Site U1343, measured on a larger >38 μm fraction ($\delta^{30}Si_{large}$; orange) and a smaller 20-38 μm fraction ($\delta^{30}Si_{small}$; blue). c) Bulk sedimentary $\delta^{15}N$ results from Chapter 3 (purple), where the fainter, thicker line is the raw data and is overlaid by darker, thinner low resolution line, where the data points (circles) align with those on which $\delta^{30}Si$ was measured. d) Si:N ratios for both the large (orange) and small (blue) fractions, calculated using the $\delta^{30}Si_{diatom}$ (a) and $\delta^{15}N_{bulk}$ (c) data. Opal mass accumulation rate (MAR) data from Kim et al. (2014) (e; green), and upwelling index results (f; red) from Chapter 3 are also plotted, where interpolated data points (circles) align with those on which $\delta^{30}Si$ was measured.

remove all non-diatom contaminants. Sample purity was confirmed through a combination of light microscopy (using a Zeiss Axiovert 40 C inverted microscope) and Scanning Light Microscopy (SEM), with contaminated samples subjected to another round of SPT cleaning or disregarded for isotope analysis. Once cleaned, 28 of the original samples contained sufficient clean material to be analysed for $\delta^{30}Si_{diatom}$ on the >38 μm ($\delta^{30}Si_{large}$), and 29 similarly suitable samples were analysed for 20-38 μm fractions ($\delta^{30}Si_{small}$). Samples were analysed for $\delta^{30}Si$ using a step-wise fluorination procedure and measured on a Finnigan MAT 253 (Leng & Sloane, 2008). Results were converted to the NBS28 scale using the within-run laboratory diatom standard BFC_{mod}, at the NERC Isotope Geosciences Facility at the British Geological Survey. This methods has been verified through an inter-laboratory calibration (Reynolds et al., 2006b), with replicate analysis of sample material from Site U1343, across the study interval, indicating an analytical reproducibility (1σ) of 0.01‰.

Given that diatom productivity is largely controlled by winter/spring sea ice dynamics and spring/summer nutrient upwelling strength, $\delta^{30}Si$ analysis was run on two size fractions (>38 μm and 20-38 μm) which contained larger summer species and smaller winter species, respectively (see Section 5.3.1 and

5.4.2). Comparison of $\delta^{30}Si_{large}$ and $\delta^{30}Si_{small}$ can therefore aid investigation into seasonal variability of silicic acid utilisation and supply, and its impact on export production and hence the biological pump through the MPT.

5.2.2 Diatom assemblage counts

To ensure that any difference between $\delta^{30}Si_{large}$ and $\delta^{30}Si_{small}$ are not an artefact of sieving or species-specific vital effects, diatom assemblage counts were completed on the >38 μm and 20-38 μm isotope samples, with a minimum of 300 valves identified to species level using an inverted light microscope. An exception was made for *Chaetoceros* RVS, which was grouped at genus level. Using the mean dimensions for each species (Leblanc et al., 2012), relative biovolumes (%biovolume) were calculated for each sample in order to assess the biological origin of isotope measurements.

5.2.3 Silicic acid utilisation

Silicon cycling at Site U1343 in the green belt is characterised by a continuous supply of silicic acid ($Si(OH_4)$) from upwelling of NPDW as well as from remineralisation of diatoms which occurs as they sink through the water column (Coachman et al., 1999; Egan et al., 2012). Following this, $\delta^{30}Si_{diatom}$ is determined by the original isotopic seawater composition of dissolved silicic acid upwelled to the surface waters ($\delta^{30}Si(OH)_4$), the fraction of silicic acid which is not utilised in the photic zone (f) and the fractionation factor between diatoms and the dissolved silicic acid (ε).

$$\delta^{30}Si_{diatom} = \delta^{30}Si(OH)_4 + \varepsilon * f \qquad \text{Equation 5.1}$$

By rearranging this equation and selecting end member values for both ε and $\delta^{30}Si(OH)_4$, changes in silicic acid utilisation (1 – *f*) can be calculated using the $\delta^{30}Si_{diatom}$ for both the large >38 μm fraction ($utilisation_{large}$) and smaller 20-38 μm fraction ($utilisation_{small}$).

$$\%Si(OH)_{4\ utilisation} = 1 - \frac{\delta^{30}Si_{diatom} - \delta^{30}Si(OH)_4}{\varepsilon} \qquad \text{Equation 5.2}$$

Previous studies from the subarctic Pacific Ocean and Bering Sea have used an $\delta^{30}Si(OH)_4$ value of 1.23‰ (Reynolds et al., 2006a; Swann et al., 2016; Kim & Khim, 2017), which is the nearest measurement of surface water $\delta^{30}Si_{seawater}$ in the subarctic Pacific Ocean (50°N, 167°E) (Reynolds et al., 2006a). However, a modelling study which considers global opal export fluxes to reconstruct global silicon cycling indicates that $\delta^{30}Si(OH)_4$ in the subarctic Pacific Ocean can be as high as 1.63‰ (Reynolds, 2009).

A generic ε value of ~ - 1.1 is often used in palaeoceanographic studies (Reynolds et al., 2006a; Swann et al., 2016; Kim & Khim, 2017), based on experimental work which demonstrates a constant fractionation factor that is independent of species and temperature (De La Rocha et al., 1997). However, recent culture studies indicate that ε can vary significantly between different polar and sub-polar marine species (Sutton et al., 2013). During the analysed interval, the raw (uncleaned) diatom assemblages at Site U1343 are dominated by two species: *Thalassiosira antarctica* var *borealis* and *Chaetoceros* RVS (Chapter 4). Although ε for these species have not been investigated, the Southern Ocean "bipolar twin" of *Thalassiosira antarctica* var. *borealis* (known as *Thalassiosira antarctica* var *antarctica*), which thrives in sea ice associated waters and blooms in autumn (Pike et al., 2009), has been shown to have an ε

of ~ -1.2‰ (Sutton et al., 2013). Some species within the *Chaetoceros* genus have been shown to have a significantly lower ε of -2.1‰, although the impact of this on the Site U1343 isotope record is likely to be low given that this taxa are generally <20 μm and so mostly removed during the sieving process. To fully account for inter-species variations in ε, mass-balance equations were used to determine the value of ε used in Equation 5.2 for each sample and size fraction using diatom relative abundance and %biovolume data, together with the aforementioned estimates of ε for *T. antarctica* var *borealis* and *Chaetoceros* RVS and a generic value of - 1.1 for other taxa. In doing this, I assume that the ε value calculated for *Chaetoceros brevis* (Sutton et al., 2013) is representative of the whole genus.

5.2.4 Silicic acid supply

To evaluate the cause of changes in silicic acid utilisation through the MPT, records of biogenic silica productivity (opal MAR) at Site U1343 (Kim et al., 2014) can be used to constrain the supply of silicic acid to the photic zone, relative to the youngest sample at 0.605 Ma (Horn et al., 2011), where the rate of supply at 0.605 Ma is equal to 0 (Equation 5.3). Through this, I assume that the rate of opal dissolution is constant over time and does not impose a first order control on the variability in the opal MAR record.

$$\%Si(OH)_{4\ supply} = \left(\left(\frac{Opal_{sample}\ /\ Opal_{0.605\ Ma}}{(1-f_{sample})\ /\ (1-f_{0.605\ Ma})}\right) - 1\right) * 100 \qquad \text{Equation 5.3}$$

5.3 Results

5.3.1 Diatom assemblages

The total number of diatom species identified was 43 in both the larger >38μm fraction ($species_{large}$) and the smaller 20-38 μm fraction ($species_{small}$). The most dominant species found in both size fractions analysed for $\delta^{30}Si_{diatom}$ was *Thalassiosira antarctica* var *borealis* RVS (henceforth *T. antarctica*), with a mean of 23% relative abundance in $species_{large}$ and 48% relative abundance in $species_{small}$ (Figure 5.2). This species is known to be dominant during periods of thick pack ice cover (Sancetta, 1982; Stroynowski et al., 2017), most notably during the 900 kyr event (~0.84 - 0.9 Ma), when maximal abundances occur in both $species_{large}$ and $species_{small}$ (up to ~90%; Figure 5.2), consistent with previous diatom assemblage work at Site U1343 (Teraishi et al., 2016) (Chapter 4).

Other prominent species in both size fractions include *Neodenticula seminae* and *Chaetoceros* RVS, where the former is used in palaeoceanographic studies as an indicator of Alaskan Stream water inflow into the Bering Sea gyre, and shows a decreasing trend through the MPT as sea levels decline (Stroynowski et al., 2017) (Chapter 4), and the latter is most dominant in the spring season, thriving in turbulent waters with high nutrient availability due to upwelling of NPDW (Caissie, 2012; Stroynowski et al., 2017). Key species which show consistently higher abundances in $species_{large}$ than $species_{small}$, include *Coscinodiscus marginatus* (mean abundance = 21%), and *Actinocyclus curvatulus* (mean abundance = 18%) (Figure 5.2). Both taxa primarily bloom in the summer/autumn season, where the former requires high nutrient availability

and warmer waters and reflects high seasonality, while the latter is more commonly associated with low nutrient and stratified waters which follow sea ice melt (Takahashi, 1986; Stroynowski et al., 2017). Increased abundances of these species in species$_{large}$ therefore reflects a period of high seasonality with a prominent summer bloom.

Additional sporadic peaks in species$_{large}$ include *Proboscia curvirostris* (maximum = 43%), *Stellarima microtrias* (maximum = 37%), *Paralia sulcata* and *Melosira sol* (grouped together as *P. sulcata/M. sol* (Chapter 4:); maximum = 25%), *Actinocyclus spp.* (maximum = 17%) and *Shionodiscus spp.* (maximum = 11%) are also observed (Figure 5.2, Figure 5.5). Peak abundance of *P. sulcata/M. sol* occur simultaneously with increased abundance of *T. antarctica* in species$_{large}$ (e.g. 0.85 and 0.91 Ma; Figure 5.2); these species are considered littoral and are typically found in higher abundance on the Bering shelf where they thrive in low light coastal environments (Sancetta, 1982; McQuoid & Nordberg, 2003; Stroynowski et al., 2017). Studies from the neighbouring Sea of Okhotsk which has a similar oceanographic regime to the Bering Sea, have suggested increased abundance of *P. sulcata* is indicative of periods with increased sea-ice transport of shelf-transported materials (Wang & Wang, 2008). Therefore combined increases in *T. antarctica* and *P. sulcata/M. sol* represent intervals of increase sea ice volume, where Site U1343 becomes more coastal following decreased sea levels and shallowing of Bering shelf waters. In general, species$_{small}$ showed less diversity, with *T. antarctica* consistently dominant over the analysed interval. Other than isolated peaks of *Stephanopyxis turris* (maximum = 29%), increased abundances of other taxa in species$_{small}$ were mostly as a result of fragmentation, for example at ~0.94 Ma a high

abundance of *A. curvatulus* was found in both $species_{large}$ and $species_{small}$, as fragments of larger valves (as well as smaller whole valves) had fallen through the sieve.

5.3.2 $\delta^{30}Si_{diatom}$

The mean $\delta^{30}Si_{diatom}$ for both size fractions ($\delta^{30}Si_{diatom}$) across the study interval was 1.29‰. Whilst mean values for the 20-38 μm fraction ($\delta^{30}Si_{small}$; mean = 1.36‰, σ = 0.14) are higher than the >38 μm fraction ($\delta^{30}Si_{large}$; mean = 1.23‰, σ = 0.28), both show a similar range of values and temporal trends through the majority of the record ($p > 0.05$) (Figure 5.1). Exceptions to this occur during early MIS 35 (~1.19 Ma), MIS 23 to mid-MIS 21 (0.90 – 0.84 Ma), and after MIS 18 (~0.75 – 0.6 Ma) when $\delta^{30}Si_{large}$ is notably lower than $\delta^{30}Si_{small}$, although $\delta^{30}Si_{small}$ also shows a smaller decrease at these times. Whilst the sample resolution is too low to assess glacial-interglacial variability in $\delta^{30}Si_{diatom}$, there appears to be decreased values in both size fractions during the 900 kyr event (0.90 – 0.84 Ma), particularly in the $\delta^{30}Si_{large}$ (mean = 0.84‰).

To ensure that a shift in the diatom assemblage were not the cause of the observed changes across the analysed record, due to either a change in seasonality in the $\delta^{30}Si_{diatom}$ signature linked to the timing of the diatom bloom or an inter-species fractionation (vital) effect, a multiple linear regression was performed between the offset of $\delta^{30}Si$ in each size fraction ($\delta^{30}Si_{large - small}$) and the relative abundance of each species in each fraction ($species_{large - small}$) (Figure 5.6). Results show that there is no significant relationship between the difference in species in each fraction and $\delta^{30}Si_{large - small}$ ($R^2 = -0.04$, $p > 0.05$). In addition, abundance results were grouped based on environmental preferences/habitat type identified by Stroynowski et al. (2017), including those

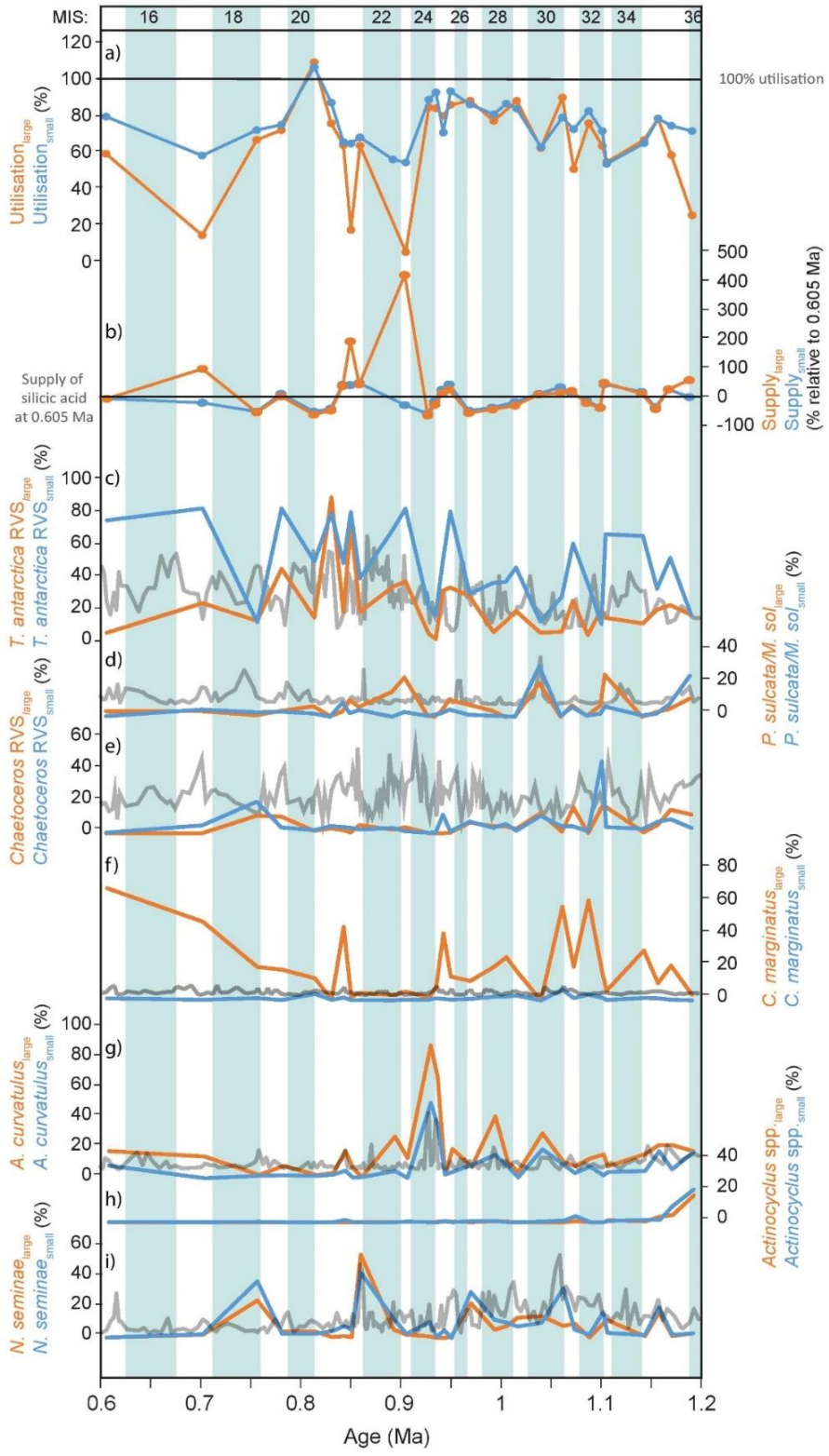


Figure 5.2 Silicic acid utilisation (a) and supply (relative to 0.605 Ma) (b) rates calculated on the larger >38 µm (orange) and smaller 20-38 µm (blue) fractions, with the black lines representing 100% utilisation (a) and supply at 0.605 Ma (b), respectively. c-i) Relative abundance of key diatom species (>~5-10% abundance) counted on the cleaned samples in both the large fraction ($species_{large}$; orange) and smaller fracter ($species_{small}$; blue) overlay the diatom assemblage results from the raw sediment (grey; Chapter 4).

associated with pack ice, marginal sea ice, epontic diatoms, pelagic taxa etc. Similar analyses confirms there was no relationship between the difference in the grouped relative abundances of the species in each fraction and $\delta^{30}Si_{large - small}$ (R^2= 0.18, p > 0.05), confirming that shifts in the species assemblages cannot account for the variability between $\delta^{30}Si_{large}$ and $\delta^{30}Si_{small}$ and instead reflect seasonal differences in photic zone silicic acid utilisation (see Section 5.4.2).

5.3.3 $\delta^{30}Si_{diatom}$:$\delta^{15}N_{bulk}$ (Si:N)

$\delta^{30}Si_{diatom}$:$\delta^{15}N_{bulk}$ (Si:N) ratios can be used as an indicator of iron availability/limitation, with diatoms utilising a larger proportion of silicic acid relative to nitrate when there is an iron deficiency, causing high diatom Si:N ratios (Hutchins & Bruland, 1998). The mean Si:N ratio over the analysed interval was 0.23, with similar values in the 20-38 μm fraction ($Si:N_{small}$; mean = 0.24) and the >38μm fraction ($Si:N_{large}$; mean = 0.22) (Figure 5.1). Both fractions show similar trends in the early-mid Pleistocene (0.95 – 1.2 Ma), with notably higher Si:N during early MIS 30 (1.06 Ma), although this is a reflection of anomalously low $\delta^{15}N_{bulk}$ value during this interval rather than a shift in $\delta^{30}Si_{diatom}$. Although low $\delta^{15}N_{bulk}$ excursions (< 4.5‰) may result from an influx of inorganic or terrestrial material, previous studies at Site U1343 confirm that these contributions do not drive glacial-interglacial variability (Kim et al., 2017; Kender et al., 2018; Worne et al., 2019) (Chapter 3). Furthermore, $\delta^{15}N_{bulk}$ has been proven to show similar trends to diatom-bound $\delta^{15}N$ ($\delta^{15}N_{db}$), where $\delta^{15}N_{bulk}$ often exhibits the same temporal trends but with lower amplitude of change (Galbraith et al., 2008). Consequently, the Si:N isotope ratios are a suitable method for evaluating long term variations between the utilisation of

these macronutrients through the study interval. During the 900 kyr event, $Si:N_{large}$ diverges from $Si:N_{small}$, with lower $Si:N_{large}$ values occurring between ~0.84 - 0.9 Ma (mean = 0.18 and 0.23, respectively). Following the $\delta^{30}Si_{diatom}$ trends, there is an offset between $Si:N_{large}$ and $Si:N_{small}$ during MIS 17 (~0.7 Ma), with $Si:N_{large}$ decreasing as $Si:N_{small}$ increases.

5.3.4 Silicic acid utilisation

Using standard values for the Bering Sea ($\delta^{30}Si(OH)_4$ = 1.23‰, ε = -1.1) (Reynolds et al., 2006a; Reynolds, 2009; Swann et al., 2016; Kim & Khim, 2017), the mean rate of silicic acid utilisation from both size fractions across the study interval is 107% with higher rates calculated using $\delta^{30}Si_{small}$ ($utilisation_{small}$; mean = 112%) than $\delta^{30}Si_{large}$ ($utilisation_{large}$; mean = 101%) (Figure 5.3). Although using the higher modelled $\delta^{30}Si(OH)_4$ value of 1.63‰ (Reynolds, 2009) causes a shift to lower utilisation rates (mean $utilisation_{large}$ = 65%; mean $utilisation_{small}$ = 75%) (Figure 5.2), it does not change the temporal trends (Figure 5.3). When using $\delta^{30}Si(OH)_4$ = 1.23‰, utilisation rates only drop below 100% during the 900 kyr event (0.85-0.91 Ma), most notably in $utilisation_{large}$ (mean = 65%).

$Utilisation_{large}$ show low values during early MIS 35 (~1.2 Ma) in the early Pleistocene, coinciding with low upwelling index values, high $\delta^{15}N_{bulk}$, and peak abundance of *Actinocyclus* spp. (predominantly *A. ochotensis* and *A. oculatus*; Chapter 4) (Figure 5.1, Figure 5.2); considered ancestor species of *A. curvatulus*, they are assumed to have similar ecologies (Sancetta & Silvestri, 1986; Shimada et al., 2009). Following this, an increasing trend in utilisation rates for both fractions between ~1.1 and 0.95 Ma is coincident with changes in

the diatom assemblages, which indicate that sea ice volumes began to increase (Chapter 4). During the 900 kyr event, low utilisation$_{large}$ values during MIS 23 (0.9 Ma) are consistent with low upwelling index values and peak abundance of *T. antarctica* in species$_{small}$. Species$_{large}$ also shows increased abundance of *T. antarctica*, as well as *P. sulcata/M. sol*. Similarly low utilisation$_{large}$ rates occur during early MIS 21 (0.84 Ma), when *T. antarctica* abundance is maximal in both fractions. After the 900 kyr event, utilisation rate calculated from each fraction are recoupled until MIS 17/18 (~0.70 Ma), when utilisation$_{large}$ decreases and remains diverged for the rest of the study interval.

5.3.5 Silicic acid supply

Applying the utilisation rates calculated using the larger $\delta^{30}Si(OH)_4$ value of 1.63‰ and an ε value of -1.1 (see Section 5.4.1 for justification for selecting these values), in combination with extrapolated opal MAR data from Site U1343 (Kim et al., 2014) (Figure 5.1), mean rates of $Si(OH)_4$ supply to the photic zone (henceforth "supply") were calculated. Supply rates are typically 25% higher through the study interval than those at 0.605 Ma in the larger >38 μm fraction (supply$_{large}$), with maximum supply occurring at 0.904 Ma and increased supply$_{large}$ during the 900 kyr event (~0.84 - 0.95 Ma). Alternatively, supply rates calculated from the smaller 20-38 μm fraction (supply$_{small}$) have a mean of 12% higher than supply rates at 0.605 Ma, with the maximal supply$_{small}$ occurring at 1.16 Ma. There is a slight increase in supply$_{small}$ around ~0.85 Ma which coincides with the end of the 900 kyr event. Generally, the range of supply rate values are much lower in supply$_{small}$ (-60% to 120%) than supply$_{large}$ (-56% to 415%) (Figure 5.2).

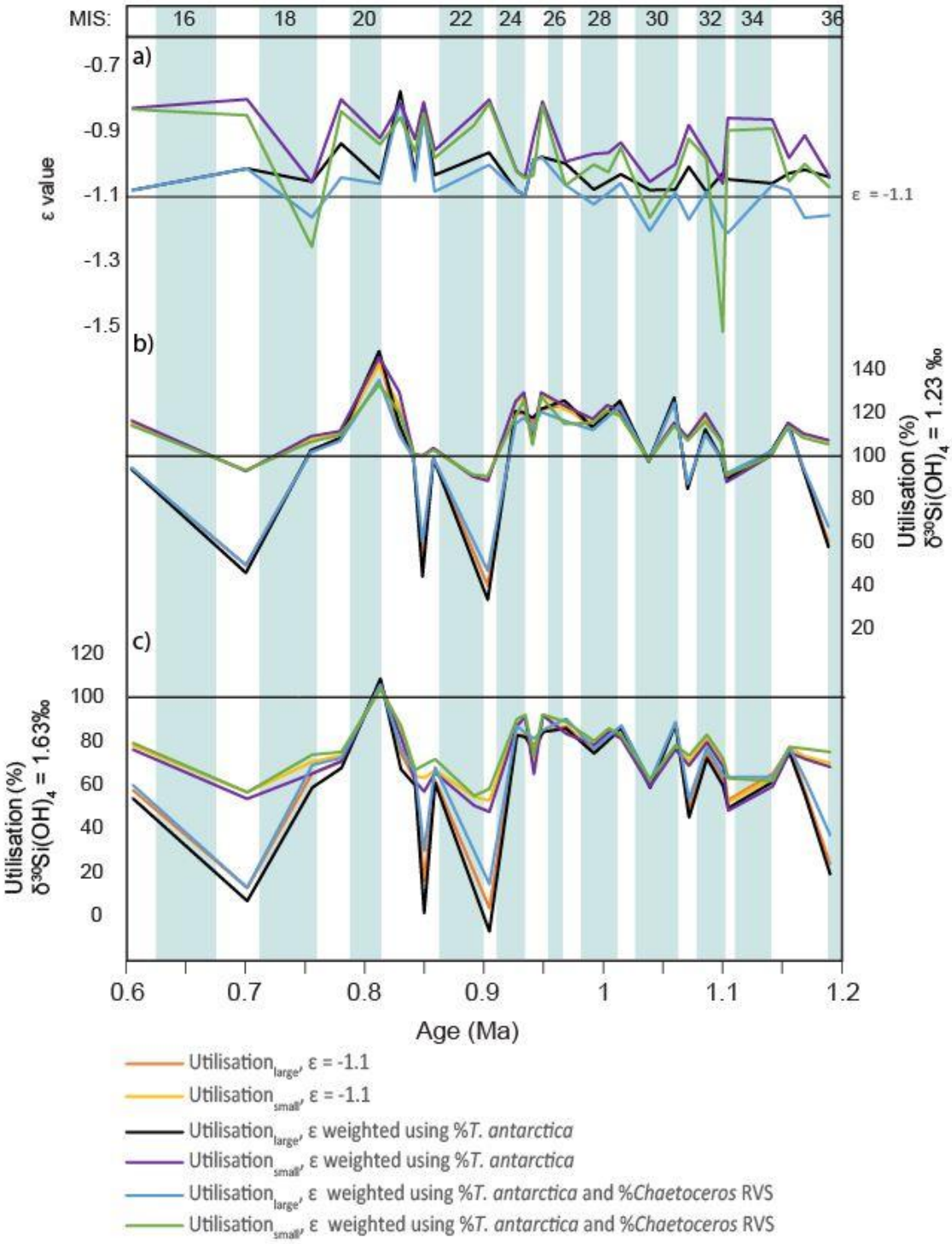


Figure 5.3 Investigation into the impact of selecting different diatom fractionation factors (ε) and $\delta^{30}Si(OH)_4$ values when calculating silicic acid utilisation. a) ε values weighted using the relative abundance of key species in each size fraction (*T. antarctica* RVS (black and purple lines) and *Chaetoceros* RVS (blue and green lines)) compared to the standard ε value of -1.1 (black line). The rate of silicic acid utilisation is then calculated for each size fraction and using each weighted ε values, an $\delta^{30}Si(OH)_4$ value of 1.23 (b) and 1.63 (c), where the black lines represents 100% silicic acid utilisation.

5.4 Discussion

5.4.1 Silicic acid utilisation – selecting ε and $\delta^{30}Si(OH)_4$

To calculate rates of silicic acid utilisation, a value for ε must be used (Equation 5.2). Laboratory evidence suggests the $\delta^{30}Si$ fractionation factor of diatoms may vary between species (Sutton et al., 2013), although there is no supporting evidence from similar studies in natural settings (Cardinal et al., 2007; Fripiat et al., 2012). Using species specific fractionation factors as part of a mass balance equation for two key taxa (*T. antarctica* and *Chaetoceros* RVS) (Sutton et al., 2013), which are consistently present through the study interval and dominate the assemblage during the 900 kyr event (Chapter 4), an investigation into the potential significance of these vital effects on utilisation rates is made. Results show that varying ε to consider the relative abundance and %biovolume of *T. antartcica* alone does not significantly alter the rate of $utilisation_{large}$ ($p > 0.5$ and $p > 0.5$, respectively) or $utilisation_{small}$ ($p > 0.5$ and $p > 0.5$, respectively), nor does varying the ε value to consider the combined relative abundance and %biovolume of *T. antarctica* and *Chaetoceros* RVS for $utilisation_{large}$ ($p > 0.5$ and $p > 0.05$, respectively) or $utilisation_{small}$ ($p > 0.5$ and, $p > 0.5$, respectively) (Figure 5.3). Therefore, the standard ε value of -1.1‰ is a suitable choice for assessing MPT changes in utilisation at Site U1343 and is used through the rest of the discussion.

In addition to ε, a suitable value for $\delta^{30}Si(OH)_4$ must also be used to calculate silicic acid utilisation (Equation 5.2). Previous studies from the subarctic Pacific Ocean and Bering Sea have used 1.23‰ (Reynolds et al., 2006a; Swann et al., 2016; Kim & Khim, 2017), which is the nearest measured

value, although a higher estimate of 1.63‰ is made by more recent modelling studies (Reynolds, 2009). Given that deep waters in the Bering Sea are known to be particularly silica rich (Tsunogai et al., 1979), I assume that the $\delta^{30}Si(OH)_4$ value of upwelling deep water at the Bering slope is more likely represented by the higher modelled value, rather than the those measured in the lower latitude subarctic Pacific Ocean. It is also important to consider the additional potential supply of surface water nutrients from the Alaskan Stream, which originates in the North East Pacific Ocean, and can be inferred from changes in the abundance of *N. seminae* (Sancetta, 1982; Stroynowski et al., 2017). The nearest measured $\delta^{30}Si(OH)_4$ values which may represent Alaskan Stream waters were taken in the Gulf of California, situated in the eastern equatorial Pacific (De La Rocha et al., 2000), where $\delta^{30}Si(OH)_4$ values peaked at 1.7‰, although palaeoceanographic studies from the same region use an $\delta^{30}Si(OH)_4$ value of 1.3‰ (Reynolds et al., 2006a; Pichevin et al., 2012). However, with *N. seminae* never exceeding a %biovolume of ~2.5% in either size fraction (Figure 5.7), it suggests that any $\delta^{30}Si(OH)_4$ signal from the Alaskan Stream would have contributed minimally to the $\delta^{30}Si_{diatom}$ record at Site U1343. Furthermore, the relative abundance of *N. seminae* varies similarly in both $species_{large}$ and $species_{small}$, so this signal will not impact any variation between $\delta^{30}Si_{large}$ and $\delta^{30}Si_{small}$ (Figure 5.2). Overall, given that using the different North Pacific Ocean $\delta^{30}Si(OH)_4$ values of 1.23‰ and 1.63‰ showed no temporal difference in the calculated rates of silicic acid utilisation (Figure 5.3), the higher estimate of 1.63‰ is selected here as it best agrees with modelled values for Bering Sea deep waters and can account for any potential signal from the influx of higher $\delta^{30}Si(OH)_4$ values from the Alaskan Stream (Reynolds, 2009) (Figure 5.2).

5.4.2 Seasonal investigation of $\delta^{30}Si_{diatom}$ using assemblage results

Given that $species_{large}$ generally has variable but higher abundance of summer/autumn species than $species_{small}$, the diatom assemblage data can be used to constrain for seasonal changes in silicic acid utilisation and supply. When $species_{large}$ is dominated by key summer species including *C. marginatus* and *A. curvatulus*, variability in $\delta^{30}Si_{large}$ reflects the changing nature/duration of silicic acid cycling during the summer/autumn bloom. Alternatively, when $species_{large}$ becomes dominated by *T. antarctica* and/or *P. sulcata/M. sol*, $\delta^{30}Si_{large}$ will reflect silicic acid utilisation during periods of reduced seasonality. Meanwhile, as the smaller fraction is more constantly dominated by *T. antarctica*, $\delta^{30}Si_{small}$ is consistently a better reflection of conditions during the early spring/sea ice season. Variation between the utilisation and supply rates calculated from the $\delta^{30}Si_{diatom}$ of each size fraction can therefore provide insight into the seasonal differences in silicic acid cycling. This is supported by the larger range of $supply_{large}$ values (compared to $supply_{small}$), which suggests that there is greater variability in the supply/availability of silicic acid for diatom productivity in the summer months than the winter/sea ice season (Figure 5.2). This is perhaps unsurprising, given that the rate of summer productivity can be more variable, as it is dependent on a number of factors including the length/duration of the spring melt season and the success of the preceding spring bloom. A year with a particularly large/long spring bloom will deplete nutrient availability for the summer/autumn period, while a year with a particularly short/early sea ice melt (occurring further north on the shelf) will reduce iron delivery to the green belt causing enhanced HNLC conditions (Aguilar-Islas et al., 2007, 2008).

5.4.3 Palaeoceanographic significance – the biological pump

5.4.3.1 Pre-900 kyr event

Conditions in the early Pleistocene show low rates of silicic acid utilisation ($utilisation_{large}$) but high nitrate utilisation. This causes reduced Si:N (increased nitrate use relative to silicic acid) (Figure 5.1, Figure 5.2) which indicates reduced iron availability during early interglacial MIS 35, limiting summer productivity (Figure 5.4a). This is consistent with the simultaneous prevalence of *Actinocyclus* spp. which suggests summer conditions were likely warm but characterised by low nutrient as a result of a stratified water column, (Stroynowski et al., 2017) which likely prevented macronutrient upwelling (Chapter 3). Following this, slightly increasing rates of silicic acid utilisation between 1.1 and 0.95 Ma either reflects reduced upwelling of nutrient rich NPDW, or an increase in the efficiency of the biological pump. Given that the Si:N is constant (with the exception of MIS 30; Figure 5.1, Figure 5.2), and there are no notable decreases in the upwelling index or rate of silicic acid supply, this trend likely reflects an increase in the availability of shelf-derived iron, probably delivered by sea ice which began to expand during this interval as indicated by sea ice associated taxa (Chapter 4) (Aguilar-Islas et al., 2008). Overall this supports the notion that increases in sea ice prior to the 900 kyr event could have increased the efficiency of the regional biological pump and contributed to increased glacial CO_2 drawdown in the build-up to the MPT (Chapter 4).

Anomalously high Si:N with no obvious change in the rate of silicic acid supply during MIS 30 (~1.06 Ma) appears to result from notably low $\delta^{15}N_{bulk}$ which could be a result of a short influx of inorganic nitrogen/terrigenous debris

input (Robinson et al., 2012) (Figure 5.1). However, this early glacial period also exhibits a peak in *C. marginatus* abundance in species$_{large}$ as well as high total abundance of *N. seminae* (Chapter 4) (Figure 5.2). It is possible that an influence of warmer Alaskan Stream waters caused reduced sea ice extent and restricted iron availability, causing increased utilisation of silicic acid relative to nitrate (Hutchins & Bruland, 1998). Alaskan Stream water is also likely to contain a higher Si:N than that upwelling from NPDW, given that the North East Pacific (from where the Alaskan Stream originates) is also an iron limited system (Marchetti et al., 2006). This short temporal fluctuation in nutrient utilisation is consistent with suggestions that pre-MPT conditions demonstrated high seasonality and an inconsistent sea ice margin (Detlef et al., 2018) (Chapter 4); further high resolution study of $\delta^{30}Si_{diatom}$ and $\delta^{15}N_{bulk}$ are necessary to better assess the significance of anomalously high Si:N and/or the potential influx of low $\delta^{15}N$ materials during MIS 30.

5.4.3.2 During and after the 900 kyr event

The 900 kyr event has been characterised as an interval of significant sea ice growth, sea level decline and closure of the Bering Strait, which caused expansion of NPIW across the subarctic Pacific region (Kender et al., 2018) (Chapter 3-4). Combined with lower Bering gyre energy from reduced Alaskan Stream inflow (also resulting from sea level decline) (Stroynowski et al., 2017) (Chapter 4), this MPT step-change represents a period of suppressed NPDW upwelling, reduced supply of nutrients to the photic zone and low primary productivity (low opal MAR; Figure 5.1) (Kim et al., 2014; Kender et al., 2018) (Chapter 3). Results here indicate that the 900 kyr event at MIS 23 also exhibits low $\delta^{30}Si_{diatom}$ and decreased silicic acid utilisation (particularly $\delta^{30}Si_{large}$ and

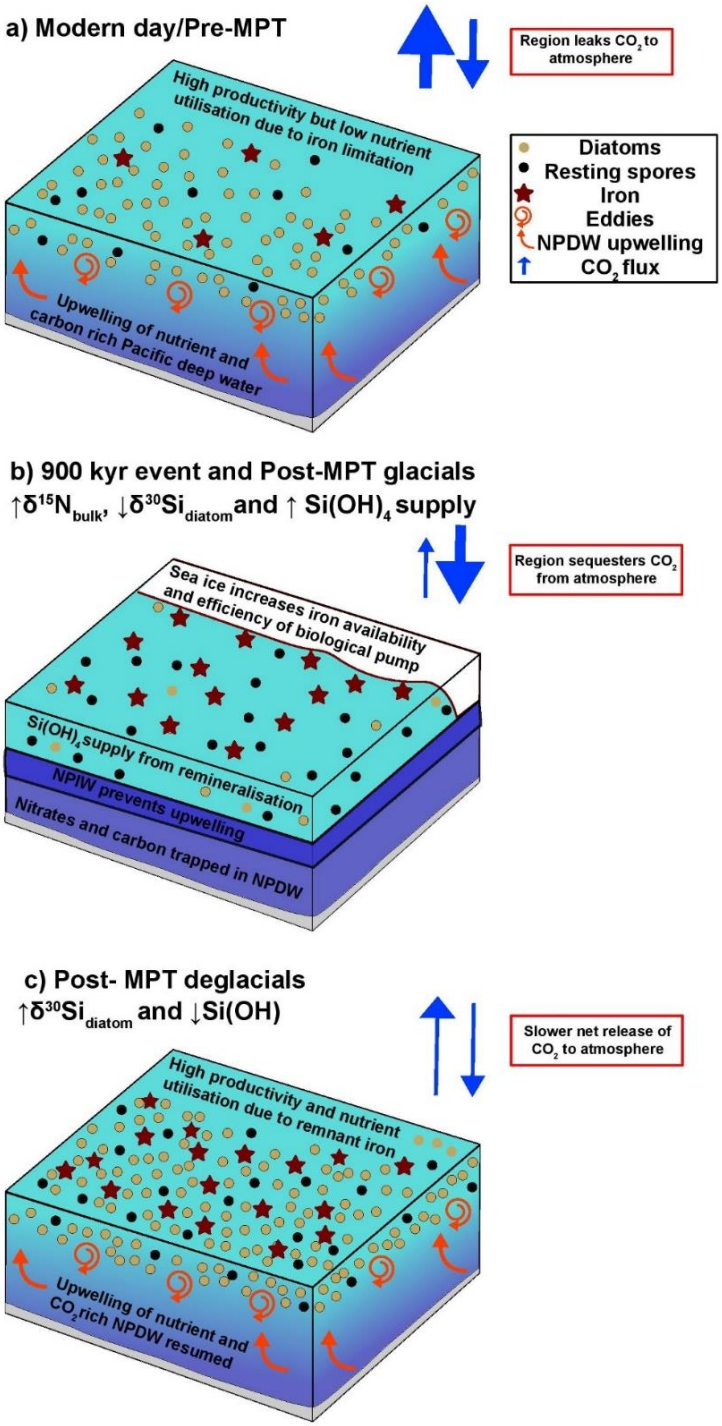


Figure 5.4 Box models representing the differing biogeochemical states at Site U1343 through the Pleistocene. a) Modern and Pre-MPT conditions are characterised by HNLC conditions which are iron limited, causing an inefficiency biological pump which leaks CO_2 to the atmosphere. b) During the 900 kyr event, increased shelf-derived iron supply from expanded sea ice increases the efficiency of the biological pump, with the green belt becoming nitrate-limited due to suppressed NPDW upwelling. c) After the MPT, deglacial periods exhibit resumed deep water upwelling, however enhanced productivity due to remnant iron in the photic zone stimulates the biological pump, causing a smaller net release of CO_2 to the atmosphere.

utilisation$_{large}$) (Figure 5.1, Figure 5.2). Combined with sustained levels of nitrate utilisation ($\delta^{15}N_{bulk}$) and lower Si:N$_{large}$ (Figure 5.1), these results are indicative of abundant iron availability, where diatoms used a larger proportion of nitrate relative to silicic acid (Hutchins & Bruland, 1998) (Figure 5.4b). Furthermore, the 900 kyr event shows a shift in species$_{large}$ from summer-blooming species *C. marginatus* to *T. antarctica* and *P. sulcata/M. sol* (Figure 5.2). *T. antarctica* resting spores (RS) are believed to form under periods of nutrient stress and/or low light intensities (Peters & Thomas, 1996), hence they are dominant during periods of thick pack ice and suppressed nutrient upwelling, when other species cannot survive (Caissie, 2012). Simultaneously increased *P. sulcata/M. sol* is consistent with low light availability and increased storm frequency (Chapter 4), supporting the supposition that an increased supply of shelf-derived iron from sea ice-entrained sediments, blown southward to the green belt (Wang & Wang, 2008), can explain the observed isotopic trends and decrease in Si:N during this interval.

Although $\delta^{30}Si_{small}$ (and utilisation$_{small}$) are low over this interval, the supply$_{large}$ rates shows maximal values during the 900 kyr event (Figure 5.2). In the modern Bering Sea, regeneration of silica is 4-5 time higher than in the adjacent deep waters of the North Pacific Ocean (Tsunogai et al., 1979; Coachman et al., 1999). *T. antarctica* RS are much more heavily silicified than their vegetative cell counterparts (Doucette & Fryxell, 1983), and therefore I posit that there was an abundant pool of silicic acid from remineralisation of resting spores, in the absence of upwelling NPDW. This would further aid explanation for low $\delta^{30}Si_{diatom}$, where the rate of utilisation would be lower due to a larger initial pool of silicic acid. Overall, development of thick pack ice

(Figure 5.2) (Chapter 4) caused limited light availability and reduced nutrient supply (through NPIW expansion and suppressed NPDW upwelling), and explains low opal MAR and utilisation$_{large}$ (Kender et al., 2018) (Figure 5.1). Meanwhile, continued iron supply from shelf-derived materials facilitated continued growth of resting spores despite HNLC conditions, where export production became limited by nitrate and low light availability, rather than iron (Figure 5.4b).

Despite warming interglacial conditions and resumed deep water upwelling during the MIS 22/21 deglaciation (increased upwelling index; Figure 5.1) (Chapter 3-4) the $\delta^{30}Si_{large}$ record diverges from $\delta^{30}Si_{small}$ again at 0.85 Ma, during which *T. antarctica* reaches peak relative abundance in both size fractions (Figure 5.2), indicating sustained dominance of a thick pack ice environment. This is consistent with hypotheses which suggests that delayed deglacial NPDW CO_2 ventilation across the subarctic Pacific Ocean may have been an important factor in increasing the duration of glacials after the MPT (Kender et al., 2018) (Chapter 3). Simultaneously, increased abundances of *T. antarctica* and rates of supply$_{large}$ again provides support for resting spore remineralisation as an important mechanism for silicic acid supply during periods of suppressed upwelling. Overall, the prevalence of pack ice and nitrate-limited conditions during the early part of MIS 21, evidenced by low $\delta^{30}Si_{large}$ and Si:N$_{large}$, but increased supply$_{large}$ (similar to at 0.94 Ma; Figure 5.1), suggests sea ice driven iron fertilisation in the early MIS 21 maintained a high efficiency of the biological pump, likely aiding delayed ocean-atmosphere CO_2 exchange through trapping organic carbon in the deep basins (Figure 5.4c).

Similar divergence between $\delta^{30}Si_{large}$ and $\delta^{30}Si_{small}$ during MIS 17 (~0.7 Ma; Figure 5.1) likely reflect increased interglacial volumes of sea ice in the 100-kyr post-MPT world (Stroynowski et al., 2017; Detlef et al., 2018) (Chapter 4). Although higher abundance of *C. marginatus* (and slight increases in *A. curvatulus*) reoccur in $species_{large}$, sustained prevalence of *T. antarctica* in $species_{small}$ is consistent with slightly increased $supply_{large}$, where remineralisation of heavily silicified resting spores is an important macronutrient source when NPDW upwelling is suppressed by sea ice. Simultaneous divergence between $\delta^{30}Si_{large}$ and $\delta^{30}Si_{small}$ and low $Si:N_{large}$ after MIS 17 is also indicative of severe winter/spring conditions where shelf derived iron was abundant (Figure 5.2), in line with previous suggestions that despite partial recovery of summer productivity/seasonality, post-MPT interglacial exhibited a more sea ice-dominant environment (Stroynowski et al., 2017; Detlef et al., 2018) (Chapter 4).

5.4.4 Wider implications

The impact of iron fertilisation on the Bering Sea green belt during the 900 kyr event may have wider significance for ocean-atmosphere CO_2 exchange and the nature of glacial-interglacial periodicity. Increased iron availability would have acted to increase the efficiency of the regional biological pump and caused the green belt to sequester a larger proportion of atmospheric CO_2 (Figure 5.4b). Furthermore, resting spores are known to have higher ratios of cellular carbon to nitrogen than their vegetative counterparts (McQuoid & Hobson, 1996), supported by evidence from the Southern Ocean which suggests that the selective preservation of *T. antarctica* and *Chaetoceros* resting spores (given their heavy silicification) forms the key component of seasonal and annual

carbon export (Rembauville et al., 2015, 2016). Dominance of *T. antarctica* RS and *Chaetoceros* RVS during the 900 kyr event (Chapter 4) will therefore have likely caused increased carbon burial despite low opal MAR (Figure 5.1, Figure 5.2). Although it is beyond the scope of this paper to quantify the impact these changes in green belt nutrient utilisation will have had on carbon cycling, I posit that increased resting spore formation combined with higher efficiency of the biological pump following iron fertilisation from shelf-derived sources, was an important component contributing to low pCO_2 during the MPT, alongside other changes occurring elsewhere in the marine system, including the Southern Ocean.

At the same time, NPIW formation and expansion is posited to have occurred in the Bering Sea, which proliferated through the subarctic Pacific Ocean, causing region-wide suppression of CO_2 ventilation (Kender et al., 2018) (Chapter 3). If the green belt region was iron-replete, it is highly plausible that excess iron and silicic acid would also have propagated in the NPIW as a regenerated nutrient source. Surface water samples from the western subarctic Pacific Ocean provide evidence for a similar propagation of iron in modern NPIW, which originates from the Sea of Okhotsk (Nishioka et al., 2007). Increased iron and silicic acid availability across the subarctic would act to increase the efficiency of the biological pump across the subarctic Pacific Ocean during the 900 kyr event, supported by high biogenic opal during MIS 23 at ODP Site 882 (Haug et al., 1995) (Figure 5.1). This provides further support for suppositions that NPIW was the likely linking mechanism between the Bering Sea and wider subarctic Pacific during mid-late Quaternary glacials (Kender et al., 2018) (Chapter 3), and that the biological pump of the subarctic North

Pacific is an important consideration for global ocean-atmosphere CO_2 dynamics (Jaccard & Galbraith, 2018).

Overall, although the Bering Sea green belt alone is unlikely to have placed a principal control on increasing the duration of post-MPT glacials, increased iron (and silicic acid) delivery to the larger subarctic Pacific region during the MPT and subsequent glacials, would have subsequently fuelled high deglacial productivity once sea levels began to rise and upwelling/vertical mixing of NPDW resumed (Kender et al., 2018). The resultant increase in export production would have caused higher rates of CO_2 sequestration and hence slower net release of CO_2 from the NPDW across the subarctic region (Figure 5.4c), which may have contributed to increased glacial duration globally. Further investigation into the rate of nutrient utilisation in the wider subarctic Pacific Ocean across the MPT would be necessary to fully constrain this mechanism, via higher resolution measurements, for example at IODP Site U1343 and ODP Site 882.

5.5 Conclusion

Understanding the role of high latitude upwelling systems, including sea ice dynamics and the biological pump, as controlling mechanisms for ocean-atmosphere CO_2 exchange and global climate, is of critical importance. Through comparison of multiple proxies from Site U1343, an assessment for the role of Bering Sea sea ice on subarctic Pacific Ocean biological export and deep ocean CO_2 ventilation through the MPT is made.

The 900 kyr event is considered to be characterised by low seasonality and a very short/no summer bloom period, due to reduced light and nutrient

availability following the development of thick pack ice and NPIW expansion (Kim et al., 2014; Stroynowski et al., 2017; Kender et al., 2018) (Chapter 3-4). Results here indicate that there was reduced silicic acid utilisation despite an increase in silicic acid supply to the photic zone during this interval (Aguilar-Islas et al., 2008). Therefore, it is proposed that expansion of NPIW after the closure of the Bering Strait suppressed macronutrient upwelling and caused the region to become nitrate- rather than iron-limited (Figure 5.4b). Low nitrate availability also explains the increased production of diatom resting spores which dominate MPT sediments at Site U1343, and likely caused increased CO_2 export production during the 900 kyr event, given their preferential preservation and higher cellular carbon content (Doucette & Fryxell, 1983; McQuoid & Hobson, 1996). Following nitrate-limitation, leftover iron (and silicic acid) which is unutilised at the green belt region could have propagated through the wider subarctic Pacific Ocean in NPIW, providing an important glacial nutrient source (Figure 5.4c). Low resolution evidence after the 900 kyr event indicates that more severe sea ice seasons persisted in both glacials and interglacials, with sea ice-derived iron continuing to provide an important supply for green belt and subarctic Pacific Ocean productivity, although further investigation is needed to assess the post-MPT impact of this mechanism on the silicon pump.

5.6 Supplementary information

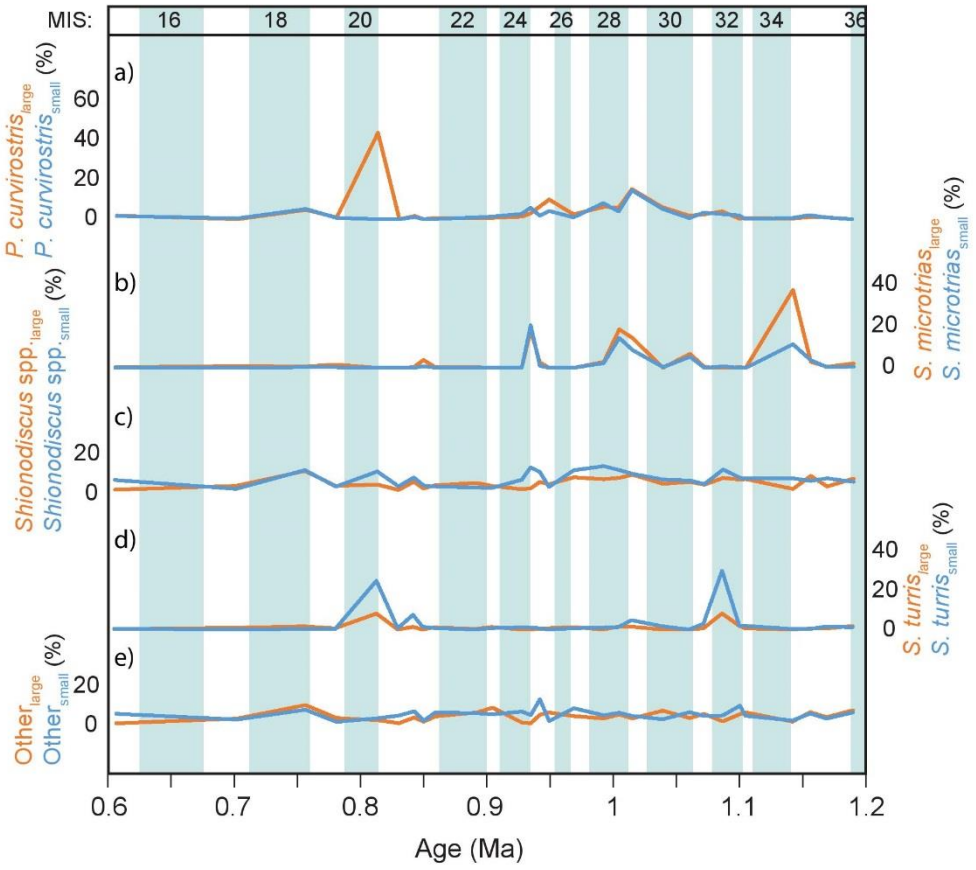


Figure 5.5 Relative abundance of other low abundance diatom species, in the >38 µm (orange) and 20-38 µm (blue) fractions.

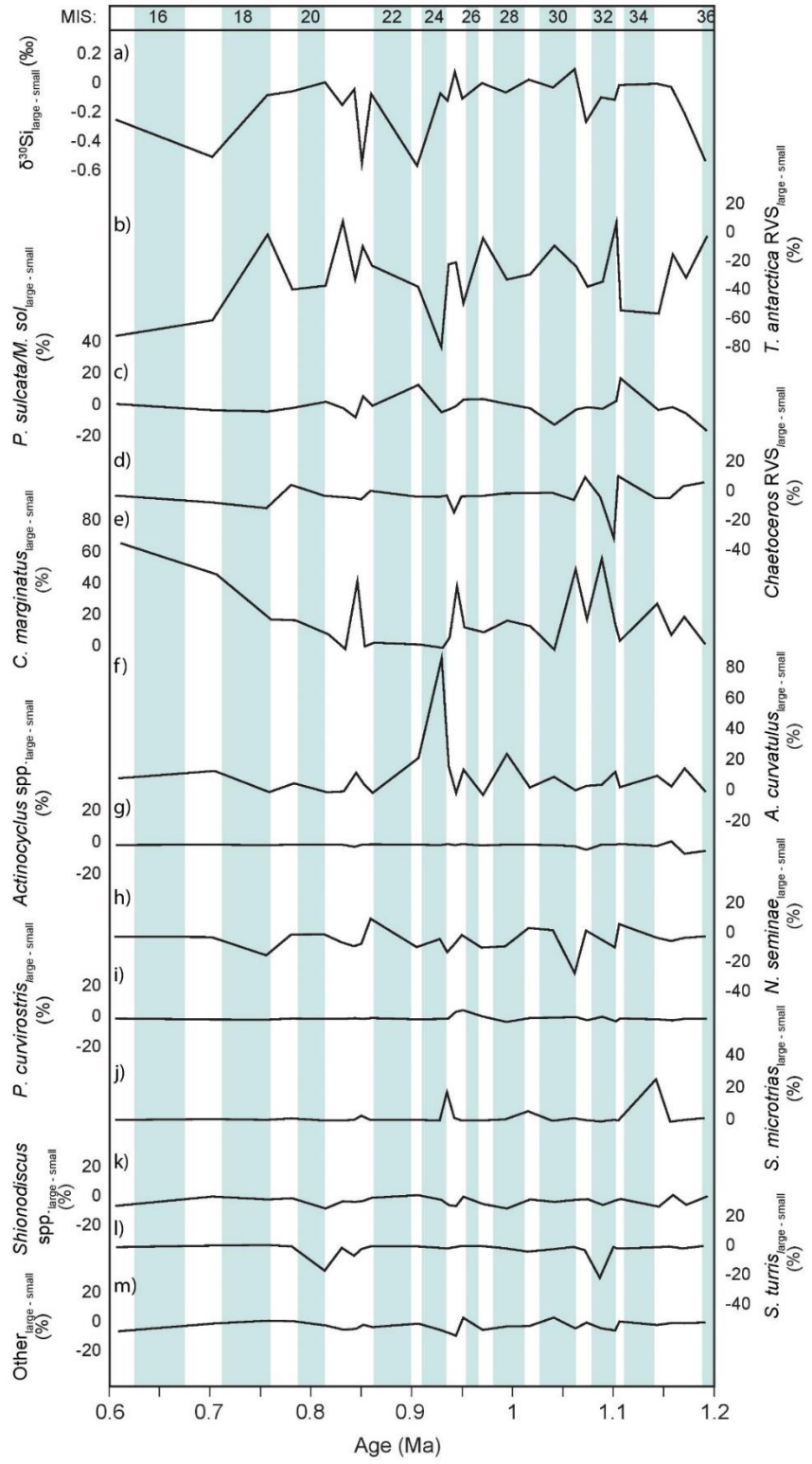


Figure 5.6 The offset between $\delta^{30}Si_{large}$ and $\delta^{30}Si_{small}$ (a) are compared to the offset between $species_{large}$ and $species_{small}$ (b-m) to ensure that the difference in assemblage composition between each fraction is not the primary cause of the isotopic differences between the two size fractions.

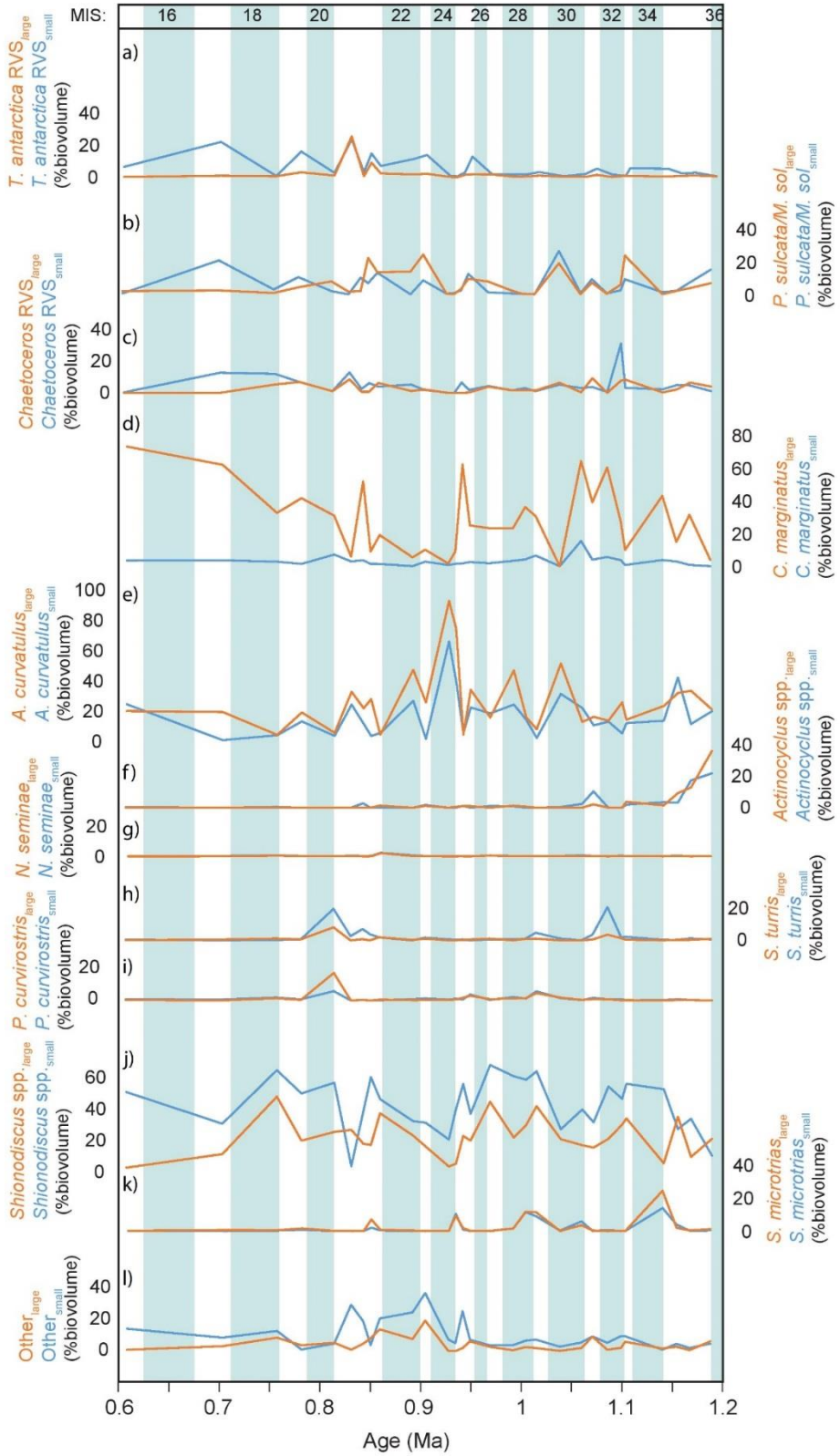


Figure 5.7 Relative biovolumes of each species (%biovolume) in the >38 µm (orange) and 20-38 µm (blue) fractions. Given that some species are considerably larger than others, the contribution of each species to the $\delta^{30}Si_{diatom}$ can be estimated using mean biovolume measurements of each species/genus (LeBlanc et al., 2012).

Chapter 6: Synthesis

6.1 Summary of thesis and advances to Bering Sea palaeoceanography

As the subarctic Pacific Ocean is not a region of significant deep water formation, it has been relatively understudied in comparison with the high latitude North Atlantic and Southern Oceans (Jaccard & Galbraith, 2018). As a result, previous understanding of Bering Sea palaeoceanography during the Pleistocene was largely limited to short term studies of the last glacial cycle. However, following proxy and modelling studies of the last deglacial which suggested that the collapse of NPIW in the subarctic Pacific region released ~30ppm of CO_2 from the resumed deep water ventilation (Okazaki et al., 2010; Rae et al., 2014), interest in the subarctic Pacific Ocean as an key area for understanding global palaeoclimate change has grown (Haug et al., 2005; Jaccard et al., 2005, 2010; Sigman et al., 2010; Jaccard & Galbraith, 2018).

Results from IODP Expedition 323 over the past 2 Myr have also highlighted the importance of the Bering Sea and subarctic Pacific region in Pleistocene climate dynamics. For example, expansion of NPIW to ~2,000 m water depth during the 900 kyr event following sea ice expansion in the Bering Sea and closure of the Bering Strait, is proposed to have suppressed NPDW upwelling during MIS 22 – 24 (~0.94-0.86 Ma), contributing to low global pCO_2, the failed interglacial at MIS 23 and longer post-MPT glacial periods (Kender et al., 2018). However, the short term nature of this study limits long term understanding of NPIW variability and deep water CO_2 ventilation from the subarctic Pacific Ocean. Despite long term evidence for glacial NPIW

formation in the Bering Sea to over 800m water depth since 1.2 Ma (Knudson & Ravelo, 2015b), the timing of more significant NPIW formation to greater depths in the Bering Sea, which could influence wider subarctic Pacific region oceanography, was also unresolved. Additionally, sea ice reconstructions from the Bering Sea were previously depicted only by low resolution diatom assemblage and lipid biomarker studies, which suggested that there was a broad increase in sea ice through the MPT, likely facilitated by weakened EAWM (Teraishi et al., 2016; Stroynowski et al., 2017; Detlef et al., 2018). However, poor time constraints in these studies meant the glacial-interglacial dynamics of enhanced sea ice growth through the middle Pleistocene remained largely unconstrained, with assessment of the onset and nature of increased sea ice duration/volume, and hence its role in potential NPIW expansion during the MPT, also unexplained.

Therefore, this research project aimed to address three key research questions, to assess the dynamics, timing/cyclicity and impact of sea ice evolution through the MPT (see Section 1.4). Through this thesis, creation of a long term and robust high resolution age model (Figure 6.1; Worne et al., (2019) and Chapter 3) has facilitated investigation into the glacial-interglacial palaeoceanography of the Bering Sea during the Pleistocene for the first time, as the previous age model did not have the resolution for this beyond the last few glacial cycles (Asahi et al. 2016). Using geochemical and palaeontological proxies from IODP Site U1343 on the Bering shelf slope, an assessment of the evolution and dynamics of sea ice, nutrient upwelling and primary productivity in the northern Bering Sea, and their impact on NPIW expansion, regional

carbon cycling and the biological pump is made, encompassing the enigmatic MPT and 900 kyr event.

Firstly, through novel calculation of an upwelling index (using bulk sedimentary $\delta^{15}N$ and opal MAR; Figure 6.1), the ultimate control of global climate on upwelling of NPDW at the Bering slope, particularly through glacial-interglacial changes in sea level and NPIW expansion following shoaling/closure of the Bering Strait and increased sea ice growth in glacials in the mid-late Pleistocene, was established (Worne et al., 2019) (Chapter 3). A tight correlation between the upwelling index and global pCO_2 records also indicates a common underlying mechanism between the two variables, suggested here to be a result of the continued propagation of NPIW across the subarctic Pacific Ocean which suppressed regional CO_2 ventilation (Figure 6.1) . Although oceanographic changes in sea level (global ice volume) and sea ice (controlling NPIW formation) are determined to be the primary influence on upwelling strength, results also support a secondary influence of atmospheric teleconnection, where the sea ice margin showed high sensitivity to variability in the EAWM following intensification of the Walker circulation in the early Pleistocene (Chapter 3).

During the 900 kyr event, diatom assemblage evidence supports previous findings which suggest the first closure of the Bering Strait occurred at this time (Kender et al., 2018), coincident with rapid increases in sea ice thickness and duration which combined to cause sustained suppression of NPDW upwelling at the Bering slope (Figure 6.2). Although sea ice was restricted to the Bering Sea, the simultaneous expansion and propagation of NPIW likely occurred across the subarctic Pacific Ocean and caused region-

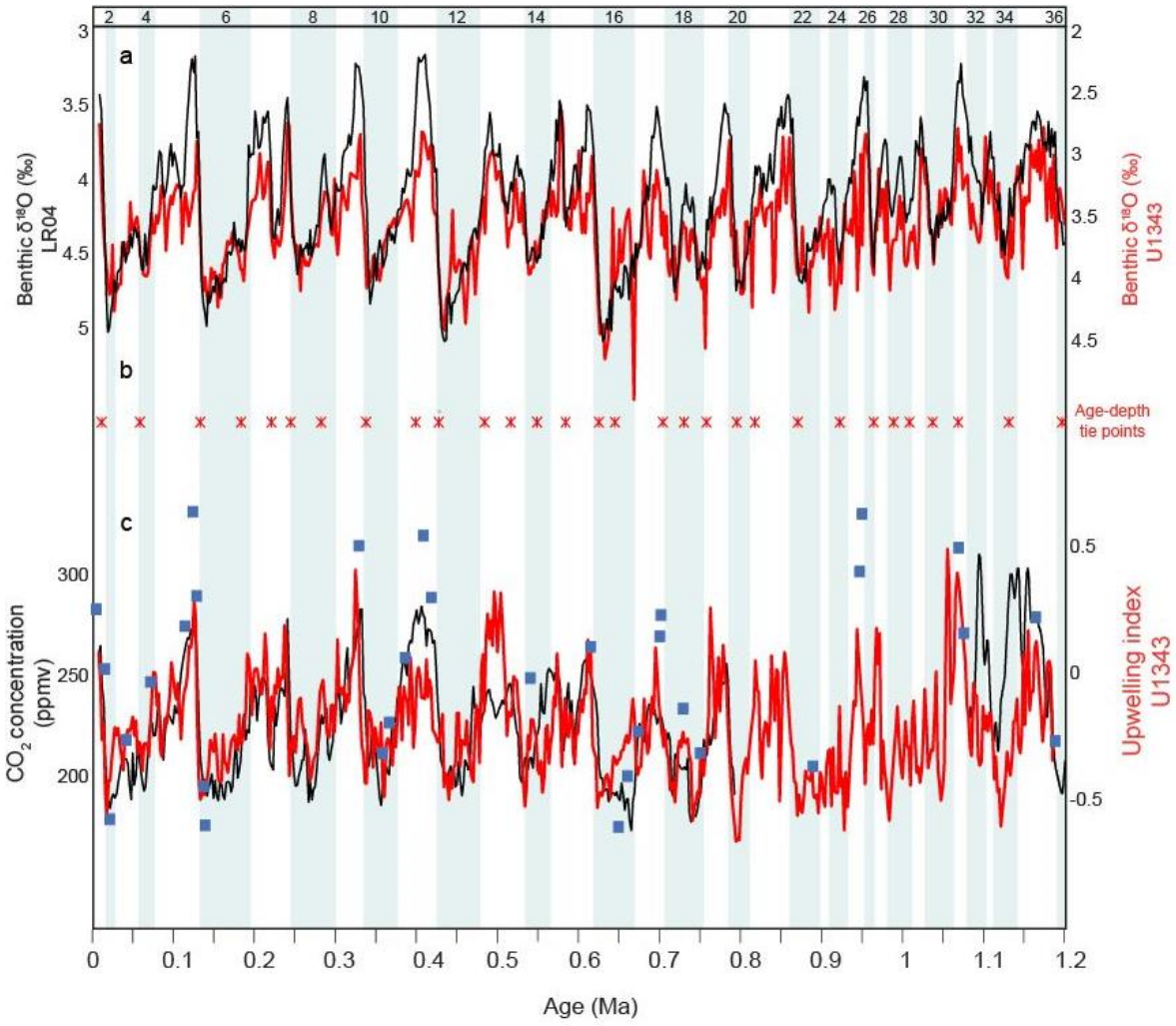


Figure 6.1 New age model (a) and upwelling index (c) results from Site U1343 (red) between 0 - 1.2 Ma. Age model was defined through selecting new tie points (b) to the LR04 global benthic stack (Lisiecki & Raymo, 2005) (a; black) during periods of rapid isotope change. New upwelling index (c; red) results show tight correlation with global pCO_2 from ice core records of the last 0.8 Ma (Lüthi et al., 2008) (c; black, 0 – 0.8 Ma) and boron-isotope derived estimates from Chalk et al., 2017 (c;black ~1.1 – 1.2 Ma) and Hönisch et al., (2009) (c;blue squares). Blue bars represent glacial periods, labelled at the top of the figure by the marine isotope stages (MIS) defined by the LR04 benthic stack.

wide suppression of CO_2 ventilation, contributing to low global pCO_2 during glacials after the MPT (Chapter 3 - 4). Furthermore, reduced NPDW upwelling and hence macronutrient supply at the Bering slope caused the green belt to become nitrate rather than iron-limited, supported by the dominance of diatom resting spore formation and a shift in Si:N utilisation (Figure 6.2). I hypothesise that iron which was left unutilised at the Bering slope likely propagated through

the lower subarctic Pacific in NPIW during MPT glacials, following a similar mechanism to that which is observed in the modern Okhotsk Sea, forming an important source of nutrients for glacial productivity in the HNLC environment of the lower subarctic Pacific Ocean (Chapter 5). In particular, when deep water upwelling was suppressed, iron fertilisation from Beringian NPIW likely caused increased efficiency of the biological pump in the subarctic region, which would have further contributed to low atmospheric global pCO_2 during the 900 kyr event, alongside other changes in the Southern Ocean.

6.2 Global significance and Future directions

Results from this thesis have a far-reaching global impact, for example the relative contribution of Beringian glacial NPIW to glacial-interglacial CO_2 ventilation from the subarctic Pacific Ocean to global climate changes during the Pleistocene, was likely more significant than previously thought, both through suppression of NPDW upwelling and as a source of nutrients delivered from the Bering shelf which enhanced the regional subarctic Pacific Ocean biological pump during glacials. This is in line with the growing awareness of the key role of the subarctic Pacific on long term global climate changes (Jaccard & Galbraith, 2018). Findings here also help to assess a number of hypotheses alongside our existing knowledge of the high latitude North Atlantic and Southern Ocean during the MPT (DeConto et al., 2007; Lear et al., 2016; Chalk et al., 2017), including the role of high latitude sea ice (SIS hypothesis; Chapter 4), subarctic Pacific Ocean CO_2 ventilation, NPIW expansion (Chapter 3) and the subpolar biological pump (Chapter 5).

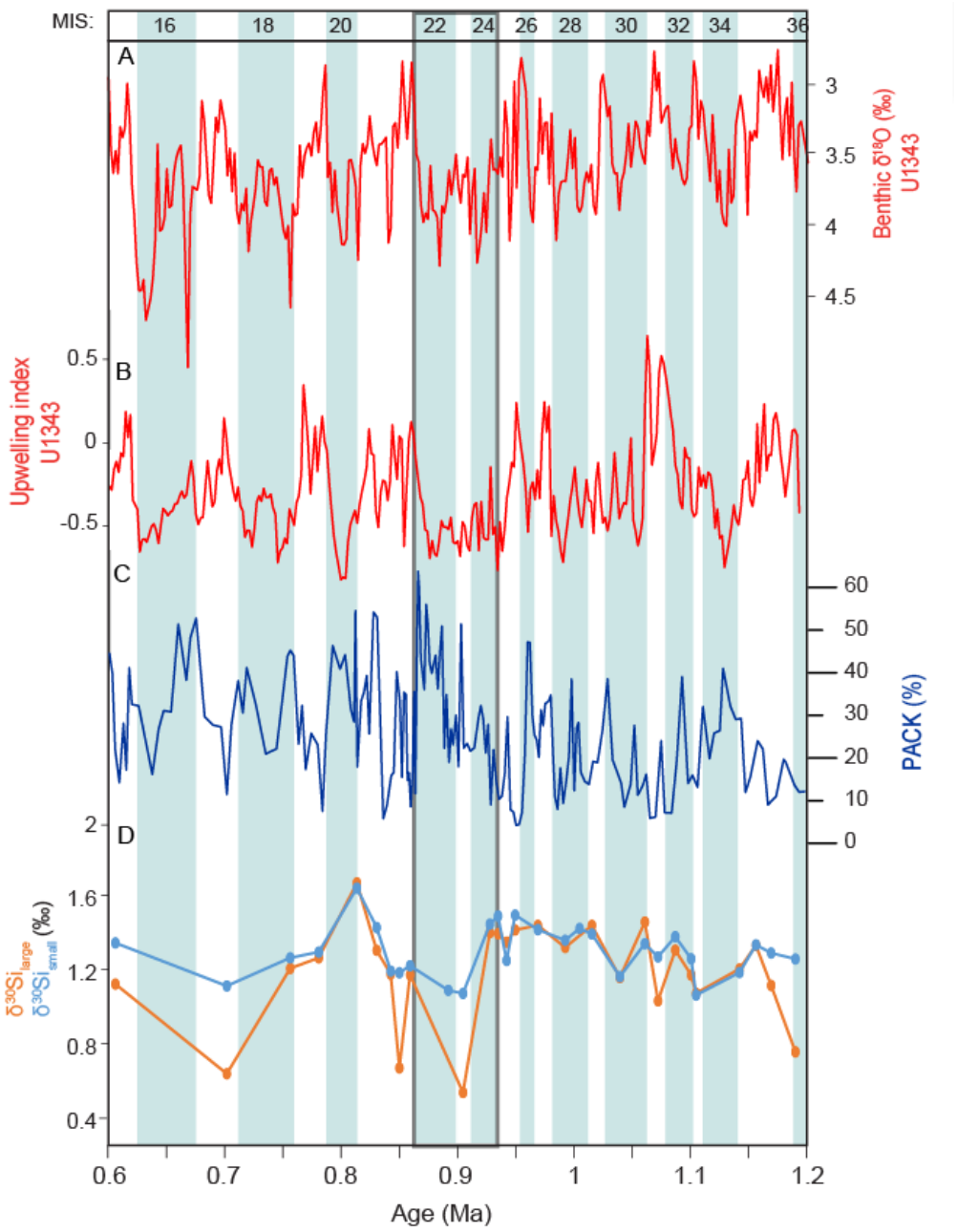


Figure 6.2 Key findings from 0.6 - 1.2 Ma. The new age model for Site U1343 (A) informs upwelling index results (B) which show suppressed nutrient upwelling during the 900 kyr event, coincident with increased abundance of pack ice associated diatoms (C). Simultaneously reduced $\delta^{30}Si_{diatom}$ (D) and Si:N (Chapter 5) are interpreted as a shift to nitrate-limited conditions (supported by diatom resting spore formation), with suppressed NPDW upwelling but increased sea ice formation causes iron to be left unutilised in the green belt region. Blue bars represent glacial periods, labelled by the marine isotope stages (MIS) defined by the LR04 benthic stack (Lisiecki & Raymo, 2005), where the darker band around MIS 22–24 represents the 900 kyr event.

Overall, new data presented in this thesis support high latitude sea ice in the Bering Sea as a critical control on glacial-interglacial deep water upwelling (through its role in intermediate water formation), which in turn responds to orbital-scale changes to global ice volume/sea level. Results also provides the first assessment for the role of suborbital scale changes in nutrient upwelling, likely forced by the interaction of sea ice and atmospheric teleconnection from the tropical Pacific, where the intensification of the Walker circulation and the resultant changes in moisture and heat delivery to high latitudes during the early Pleistocene was an important precursor for MPT sea ice evolution (and hence NPIW expansion and primary productivity).

In addition, the methodologies applied in this thesis are also significant to the wider palaeoceanographic community, for example the age model developed for Site U1343 (building on the previous work of Asahi et al., (2016) and Kender et al., (2018)) has the highest resolution for any site in the Bering Sea and wider North Pacific Ocean covering the Pleistocene epoch. It can therefore be used as a supplementary time constraint for neighbouring sites, when compared with records from other IODP Expedition 323 sites and other future expeditions in the subarctic region, such as those from IODP Expedition 341 to the Gulf of Alaska, the results of which will likely further enhance the spatial coverage of the region and our broader understanding of subarctic Quaternary palaeoceanography. Furthermore, the new calculation for the semi-quantitative upwelling index presented here can be applied to other sites with similar oceanographic regimes (as demonstrated by the short term upwelling calculation for ODP Site 882 from 8 to 146 kyr; Worne et al., (2019)). Through using the upwelling index calculation on other records from the subarctic Pacific

Ocean (for example future studies from the IODP Gulf of Alaska Expedition 341), a comparison with results presented in this thesis will allow a full assessment of the hypothesis that NPIW propagated throughout the subarctic Pacific Ocean during glacials, causing regionally suppressed ventilation of CO_2 during and after the MPT. Additionally, the upwelling index calculation is suitable for application to records from the Southern Ocean as deep water upwelling, productivity and nutrient utilisation there are also largely controlled by sea ice dynamics, similar to the Bering Sea. Through assessing the variability in nutrient upwelling strength in both high latitude regions, a better evaluation of the proposed hypotheses for the MPT which invoke high latitude sea ice-modulated ocean-atmosphere CO_2 exchange can be made, especially as the Southern Ocean is considered to be a larger influence on glacial-interglacial climate change (Sigman et al., 2010).

Another advancement to palaeoceanographic science in this PhD is provided thorough investigation of $\delta^{30}Si_{diatom}$ using two size fractions (Chapter 5), where a real-world assessment of diatom fractionation factors and the role of varying diatom assemblages (dominance of differing seasonal communities) on $\delta^{30}Si_{diatom}$ results has allowed development and validation of the proxy. Through comparison with diatom assemblages, results support minimal influence of species-specific vital effects and shifts in assemblage composition on $\delta^{30}Si_{diatom}$; this is important for both previous and future studies which rely on the accuracy of $\delta^{30}Si_{diatom}$ as a proxy for silicic acid utilisation through time, particularly as laboratory culture studies indicate different species exhibit variable fractionation of $\delta^{30}Si$ (Sutton et al., 2013). Renewed confidence in $\delta^{30}Si_{diatom}$ records facilitates further use of this proxy at other sites across the

wider subarctic Pacific Ocean and Southern Ocean which could provide insight into the relative contribution of the biological pump to glacial-interglacial CO_2 dynamics, as well as the potential for iron fertilisation/limitation as a control on the MPT (Chalk et al., 2017).

Future work in the Bering Sea could look to extend the existing diatom assemblage and $\delta^{30}Si_{diatom}$ record presented here, to understand how the onset of NHG at ~ 2.7 Ma and intensification of the Walker Circulation from 1.5 Ma impacted nutrient cycling, and the long term impact of sea ice expansion (through transporting shelf-derived iron and causing expanded NPIW) on deep water upwelling and the biological pump. In particular, a higher resolution $\delta^{30}Si_{diatom}$ record between 0.6 and 1.2 Ma (Chapter 5) would help to better understand the glacial-interglacial dynamics of sea ice-derived iron on limiting productivity/nutrient utilisation and therefore better assess the extent of variability in the biological pump through the MPT. Additional extension of the $\delta^{30}Si_{diatom}$ record through the late Pleistocene would also help to evaluate whether the hypothesised mechanism, where Beringian shelf-derived iron stimulated productivity throughout the subarctic Pacific region via NPIW during the 900 kyr event, continued to operate after the MPT and on orbital timescales.

As findings here principally emphasise the importance of high latitude sea ice in controlling ocean-atmosphere CO_2 dynamics, further work to improve the modelling of sea ice dynamics in climate models is recommended. Although there are some existing models which specifically model sea ice or Bering Strait closure (NPIW expansion), and have highlighted their importance in regulating ocean-atmosphere dynamics and global climate during the Pleistocene (Gildor

& Tziperman, 2001; Hu et al., 2010; Lee et al., 2017), computer power often limits model complexity (particularly when run over a long time period such as the Quaternary), necessitating the use of a basic sea ice model in simulations (Rae et al., 2014). Furthermore, a lack of proxy-derived sea ice data for the subarctic Pacific region (both the Bering Sea and Sea of Okhotsk) restricts modelling studies such as those run for the Southern Ocean and North Atlantic, for which sea ice distribution and snow mass balance simulations are among the most realistic of palaeoclimate studies (Pollard, 2000). Long term sea ice reconstruction and upwelling index results in this thesis therefore provide a useful conceptual framework/data resource for future modelling studies which assess CO_2 cycling in the subarctic Pacific Ocean on glacial-interglacial timescales through the Quaternary. In particular, further modelling of the role of NPIW expansion and Bering Strait closure as a boundary condition change during the MPT could aid in explanation of current discrepancies between modelled and proxy data (Hönisch et al., 2009; Rae et al., 2014; Chalk et al., 2017; Gray et al., 2018).

6.3 Conclusion

The key findings presented in this thesis corroborate the principal control of sea ice on orbital scale variability in nutrient upwelling at the Bering slope, following global changes in atmospheric pCO_2, continental ice sheet accumulation and sea level fluctuations. Results demonstrate periods of higher frequency variability in nutrient upwelling strength, interpreted here as response of marginal sea ice to atmospheric teleconnections (via the EAWM) following intensification of the Walker circulation in the early Pleistocene. Mostly, support is found for previous suppositions that the mechanism for this is through

enhanced glacial formation of NPIW since the 900 kyr event, acting to cause region-wide suppression of deep water CO_2 ventilation in the subarctic Pacific (Kender et al., 2018).

Alternatively, the palaeontologtical sea ice reconstruction presented here does not support the SIS hypothesis (Gildor & Tziperman, 2001; Detlef et al., 2018), where maximal sea ice occurs during the glacial maxima, and appears to mirror global climate cycles. Instead, larger glacial volumes of sea ice and more rapid deglacial phases (during which the expanded NPIW layer breaks down across the subarctic Pacific region) after the 900 kyr event, are more likely contributors to low glacial pCO_2 (modulating continental ice sheets) and longer glacial periods (Rae et al., 2014; Gray et al., 2018; Kender et al., 2018).

Through further geochemical analysis, an initial assessment of evolution in the efficiency of the Bering Sea biological pump during the MPT is made, indicating that the green belt became nitrate-limited during the 900 kyr event following reduced NPDW upwelling. Simultaneously expanded sea-ice likely caused increased shelf-derived iron to be left unutilised, which is speculated to have propagated to the wider subarctic Pacific Ocean in NPIW after closure of the Bering Strait. Following iron delivery, the increase the efficiency of the biological pump and enhanced CO_2 drawdown across the subarctic Pacific region may have further contributed to lower glacial atmospheric pCO_2, and hence longer glacial periods, in addition to changes in the Southern Ocean.

Overall, this thesis highlights the global significance of Bering Sea sea ice and its impact on regional nutrient upwelling and ocean-atomsphere CO_2 dynamics across the subarctic Pacific Ocean. Improved mechanistic

understanding of Bering Sea palaeoceanography and its relationship with the wider subarctic Pacific will aid future efforts to constrain the role of glacial-interglacial oceanographic variability in global climate, in complement to Southern Ocean-driven dynamics.

Chapter 7: References

Aguilar-Islas, A. M., Hurst, M. P., Buck, K. N., Sohst, B., Smith, G. J., Lohan, M. C., & Bruland, K. W. (2007). Micro- and macronutrients in the southeastern Bering Sea: Insight into iron-replete and iron-depleted regimes. *Progress in Oceanography*, *73*(2), 99–126. https://doi.org/10.1016/j.pocean.2006.12.002

Aguilar-Islas, A. M., Rember, R. D., Mordy, C. W., & Wu, J. (2008). Sea ice-derived dissolved iron and its potential influence on the spring algal bloom in the Bering Sea. *Geophysical Research Letters*, *35*(24), 10–14. https://doi.org/10.1029/2008GL035736

Aiello, I. W., & Ravelo, A. C. (2012). Evolution of marine sedimentation in the bering sea since the pliocene. *Geosphere*, *8*(6), 1231–1253. https://doi.org/10.1130/GES00710.1

Aizawa, C., Tanimoto, M., & Jordan, R. W. (2005). Living diatom assemblages from North Pacific and Bering Sea surface waters during summer 1999. *Deep-Sea Research Part II: Topical Studies in Oceanography*, *52*(16–18), 2186–2205. https://doi.org/10.1016/j.dsr2.2005.08.008

Alexander, V., & Niebauer, H. J. (1981). Oceanography of the eastern Bering Sea ice-edge zone in spring. *Limnology and Occeanography*, *26*(6), 1111–1125.

Armand, L. K., Crosta, X., Romero, O. E., & Pichon, J. J. (2005). The biogeography of major diatom taxa in Southern Ocean surface sediments: 3. Tropical/Subtropical species. *Palaeogeography, Palaeoclimatology, Palaeoecology*, *223*(1–2), 49–65. https://doi.org/10.1016/j.palaeo.2005.03.027

Asahi, H., Kender, S., Ikehara, M., Sakamoto, T., Takahashi, K., Ravelo, a. C. C., … Leng, M. J. J. (2016). Orbital-scale benthic foraminiferal oxygen isotope stratigraphy at the northern Bering Sea Slope Site U1343 (IODP Expedition 323) and its Pleistocene paleoceanographic significance. *Deep-Sea Research Part II: Topical Studies in Oceanography*, *125–126*, 66–83. https://doi.org/10.1016/j.dsr2.2014.01.004

Bailey, I., Liu, Q., Swann, G. E. A., Jiang, Z., Sun, Y., Zhao, X., & Roberts, A. P. (2011). Iron fertilisation and biogeochemical cycles in the sub-Arctic northwest Pacific during the late Pliocene intensification of northern hemisphere glaciation. *Earth and Planetary Science Letters*, *307*(3–4), 253–265. https://doi.org/10.1016/j.epsl.2011.05.029

Barth, A. M., Clark, P. U., Bill, N. S., He, F., & Pisias, N. G. (2018). Climate evolution across the Mid-Brunhes Transition. *Climate of the Past Discussions*, *2*(March), 1–31. https://doi.org/10.5194/cp-2018-20

Battarbee, R. W. (1986). Diatom analysis. In B. E. Berglund (Ed.), *Handbook of Holocene palaeoecology and palaeohydrology* (pp. 527–570). Retrieved from https://inis.iaea.org/search/search.aspx?orig_q=RN:19026440

Battarbee, R. W., & Kneen, M. J. (1982). The use of electronically counted microspheres in absolute diatom analysis. *Limnology and Oceanography*, *27*(1), 184–188. https://doi.org/10.4319/lo.1982.27.1.0184

Behl, R. J., & Kennett, J. P. (1996). Brief interstadial events in the Santa Barbara basin, NE Pacific, during the past 60 kyr. *Nature*, Vol. 379, pp. 243–246. https://doi.org/10.1038/379243a0

Berger, a., Li, X. S., & Loutre, M. F. (1999). Modelling northern hemisphere ice volume over the last 3Ma. *Quaternary Science Reviews*, *18*(1), 1–11. https://doi.org/10.1016/S0277-3791(98)00033-X

Billups, K., York, K., & Bradtmiller, L. I. (2018). Water Column Stratification in the Antarctic Zone of the Southern Ocean During the Mid-Pleistocene Climate Transition. *Paleoceanography and Paleoclimatology*, *33*(5), 432–442. https://doi.org/10.1029/2018PA003327

Broecker, W. S. (1982). Glacial to interglacial changes in ocean chemistry. *Progress in Oceanography*, *11*(2), 151–197. https://doi.org/10.1016/0079-6611(82)90007-6

Brunelle, B. G., Sigman, D. M., Cook, M. S., Keigwin, L. D., Haug, G. H., Plessen, B., … Jaccard, S. L. (2007). Evidence from diatom-bound nitrogen isotopes for subarctic Pacific stratification during the last ice age and a link to North Pacific denitrification changes. *Paleoceanography*, *22*(1), 1–17. https://doi.org/10.1029/2005PA001205

Buck, K. N., & Bruland, K. W. (2007). The physicochemical speciation of dissolved iron in the Bering Sea, Alaska. *Limnology and Oceanography*, *52*(5), 1800–1808. https://doi.org/10.4319/lo.2007.52.5.1800

Caissie, B. A. (2012). Diatoms as Recorders of Sea Ice in the Bering and Chukchi Seas : Proxy Development and Application. *Dissertations*, Paper 547.

Caissie, B. E., Brigham-Grette, J., Lawrence, K. T., Herbert, T. D., & Cook, M. S. (2010). Last Glacial Maximum to Holocene sea surface conditions at Umnak Plateau, Bering Sea, as inferred from diatom, alkenone, and stable isotope records. *Paleoceanography*, *25*(1). https://doi.org/10.1029/2008PA001671

Cardinal, D., Savoye, N., Trull, T. W., Dehairs, F., Kopczynska, E. E., Fripiat, F., … André, L. (2007). Silicon isotopes in spring Southern Ocean diatoms: Large zonal changes despite homogeneity among size fractions. *Marine Chemistry*, *106*(1-2 SPEC. ISS.), 46–62. https://doi.org/10.1016/j.marchem.2006.04.006

Chalk, T. B., Hain, M. P. M. P., Foster, G. L., Rohling, E. J., Badger, M. P. S., Cherry, S. G. S. G. S. G., … Wilson, P. A. P. A. P. A. (2017). Causes of ice age intensification across the Mid-Pleistocene Transition. *Proceedings of the National Academy of Sciences*, *114*(50), 201702143. https://doi.org/10.1073/pnas.1702143114

Chen, L., Gao, Z., Sun, H., Chen, B., & Cai, W. J. (2014a). Distributions and air-sea fluxes of CO2 in the summer Bering Sea. *Acta Oceanologica Sinica*, *33*(6), 1–8. https://doi.org/10.1007/s13131-014-0483-9

Chen, M. H., Zhang, Q., Zhang, L. L., Alvarez, C., Wang, R. J., Zarikian, C. A., & Wang, R. J. (2014b). Stratigraphic distribution of the radiolarian Spongodiscus biconcavus Haeckel at IODP Site U1340 in the Bering Sea and its paleoceanographic significance. *Palaeoworld*, *23*(1), 90–104. https://doi.org/10.1016/j.palwor.2013.11.001

Chung, Y. (1975). Areal Extent of the Benthic Front and Variation of the Scale Height in Pacific Deep and Bottom Waters. *Journal of Geophysical Research*, *80*(30).

Clark, P. U., Archer, D., Pollard, D., Blum, J. D., Rial, J. A., Brovkin, V., … Roy, M. (2006). The middle Pleistocene transition: characteristics, mechanisms, and implications for long-term changes in atmospheric pCO2. *Quaternary Science Reviews*, *25*(23–24), 3150–3184. https://doi.org/10.1016/j.quascirev.2006.07.008

Clark, P. U., & Pollard, D. (1998). Origin of the middle Pleistocene transition by ice sheet erosion of regolith. *Paleoceanography*, *13*(1), 1–9. https://doi.org/10.1029/97PA02660

Clement, J. L., Maslowski, W., Cooper, L. W., Grebmeier, J. M., & Walczowski, W. (2005). Ocean circulation and exchanges through the northern Bering Sea - 1979-2001 Model results. *Deep-Sea Research Part II: Topical Studies in Oceanography*, *52*(24–26), 3509–3540. https://doi.org/10.1016/j.dsr2.2005.09.010

Coachman, L. K., Whitledge, T. E., & Goering, J. J. (1999). Silica in Bering Sea Deep and Bottom Water. In *Dynamics of the Bering Sea* (pp. 285–386).

Cook, M. S., Ravelo, A. C., Mix, A., Nesbitt, I. M., & Miller, N. V. (2016). Tracing subarctic Pacific water masses with benthic foraminiferal stable isotopes during the LGM and late Pleistocene. *Deep-Sea Research Part II: Topical Studies in Oceanography*, *125–126*, 84–95. https://doi.org/10.1016/j.dsr2.2016.02.006

Cross, J. N., Mathis, J. T., Frey, K. E., Cosca, C. E., Danielson, S. L., Bates, N. R., … Evans, W. (2014). Annual sea-air CO2 fluxes in the Bering Sea: Insights fromnew autumn and winter observations of a seasonally ice-covered continental shelf. *Journal of Geophysical Research : Oceans*, *119*, 1–16. https://doi.org/10.1002/2013JC009579.Received

Crowley, T. J., & Hyde, W. T. (2008). Transient nature of late Pleistocene climate variability. *Nature*, *456*(7219), 226–230. https://doi.org/10.1038/nature07365

Crucifix, M. (2009). What causes glacial-interglacial cycles ? *PAGES News*, *17*(1), 39–40. https://doi.org/10.1029/2004PA001071

De La Rocha, C. L., Bescont, P., Croguennoc, A., & Ponzevera, E. (2011). The silicon isotopic composition of surface waters in the Atlantic and Indian sectors of the Southern Ocean. *Geochimica et Cosmochimica Acta*, *75*(18), 5283–5295. https://doi.org/10.1016/j.gca.2011.06.028

De La Rocha, C. L., Brzezinski, M. A., & Deniro, M. J. (2000). A first look at the distribution of the stable isotopes of silicon in natural waters. *Geochimica et Cosmochimica Acta*, *64*(14), 2467–2477.

De La Rocha, C. L., Brzezinski, M. A., & DeNiro, M. J. (1997). Fractionation of silicon isotopes by marine diatoms during biogenic silica formation. *Geochimica et Cosmochimica Acta*, *61*(23), 5051–5056. https://doi.org/10.1016/S0016-7037(97)00300-1

DeConto, R., Pollard, D., & Harwood, D. (2007). Sea ice feedback and Cenozoic evolution of Antarctic climate and ice sheets. *Paleoceanography*, *22*(3), 1–18. https://doi.org/10.1029/2006PA001350

Detlef, H., Belt, S. T., Sosdian, S. M., Smik, L., Lear, C. H., Hall, I. R., … Kender, S. (2018). Sea ice dynamics across the Mid-Pleistocene transition in the Bering Sea. *Nature Communications*, *9*(1). https://doi.org/10.1038/s41467-018-02845-5

Diester-Haass, L., Billups, K., & Lear, C. (2018). Productivity changes across the mid-Pleistocene climate transition. *Earth-Science Reviews*, *179*(July 2017), 372–391. https://doi.org/10.1016/j.earscirev.2018.02.016

Doucette, G. J., & Fryxell, G. A. (1983). Thalassiosira antarctica: vegetative and resting stage chemical composition of an ice-related marine diatom. *Marine Biology*, *78*(1), 1–6. https://doi.org/10.1007/BF00392964

Dupont, L. M., Donner, B., Schneider, R., & Wefer, G. (2001). Mid-Pleistocene environmental change in tropical Africa began as early as 1.05 Ma. *Geology*, *29*(3), 195–198. https://doi.org/10.1130/0091-7613(2001)029<0195:MPECIT>2.0.CO;2

Egan, K. E., Rickaby, R. E. M., Leng, M. J., Hendry, K. R., Hermoso, M., Sloane, H. J., … Halliday, A. N. (2012). Diatom silicon isotopes as a proxy for silicic acid utilisation: A Southern Ocean core top calibration. *Geochimica et Cosmochimica Acta*, *96*, 174–192. https://doi.org/10.1016/j.gca.2012.08.002

Elderfield, H., Ferretti, P., Greaves, M., Crowhurst, S. J., McCave, I. N., Hodell, D. a, & Piotrowski, A. M. (2012). Evolution of ocean

temperature. *Science*, *337*(August), 704–709. https://doi.org/10.1594/PANGAEA.786205

Farmer, J. R., Hönisch, B., Haynes, L. L., Kroon, D., Jung, S., Ford, H. L., … Kim, J. (2019). Deep Atlantic Ocean carbon storage and the rise of 100,000-year glacial cycles. *Nature Geoscience*. https://doi.org/10.1038/s41561-019-0334-6

Fripiat, F., Cavagna, A. J., Dehairs, F., De Brauwere, A., André, L., & Cardinal, D. (2012). Processes controlling the Si-isotopic composition in the Southern Ocean and application for paleoceanography. *Biogeosciences*, *9*(7), 2443–2457. https://doi.org/10.5194/bg-9-2443-2012

Fujii, Y., Nakano, T., Usui, N., Matsumoto, S., Tsujino, H., & Kamachi, M. (2013). Pathways of the North Pacific Intermediate Water identified through the tangent linear and adjoint models of an ocean general circulation model. *Journal of Geophysical Research: Oceans*, *118*(4), 2035–2051. https://doi.org/10.1002/jgrc.20094

Galbraith, E. D., Jaccard, S. L., Pedersen, T. F., Sigman, D. M., Haug, G. H., Cook, M., … Francois, R. (2007). Carbon dioxide release from the North Pacific abyss during the last deglaciation. *Nature*, *449*(7164), 890–893. https://doi.org/10.1038/nature06227

Galbraith, E. D., Kienast, M., Jaccard, S. L., Pedersen, T. F., Brunelle, B. D., Sigman, D. M., & Kiefer, T. (2008). Consistent relationship between global climate and surface nitrate utilization in the western subarctic Pacific throughout the last 500 ka. *Paleoceanography*, *23*(2), 1–11. https://doi.org/10.1029/2007PA001518

Gildor, H., & Tziperman, E. (2001). A sea ice climate switch mechanism for the 100-kyr glacial cycles. *Journal of Geophysical Research*, Vol. 106, p. 9117. https://doi.org/10.1029/1999JC000120

Gnanadesikan, A. (1999). A global model of silicon cycling: Sensitivity to eddy parameterization and dissolution. *Global Biogeochemical Cycles*, *13*(1), 199–220.

Gong, D. Y., & Ho, C. H. (2002). The Siberian High and climate change over middle to high latitude Asia. *Theoretical and Applied Climatology*, *72*(1–2), 1–9. https://doi.org/10.1007/s007040200008

Gong, X., Lembke-Jene, L., Lohmann, G., Knorr, G., Tiedemann, R., Zou, J. J., & Shi, X. F. (2019). Enhanced North Pacific deep-ocean stratification by stronger intermediate water formation during Heinrich Stadial 1. *Nature Communications*, *10*(1). https://doi.org/10.1038/s41467-019-08606-2

Gottschalk, J., Skinner, L. C., Lippold, J., Vogel, H., Frank, N., Jaccard, S. L., & Waelbroeck, C. (2016). Biological and physical controls in the

Southern Ocean on past millennial-scale atmospheric CO2changes. *Nature Communications*, *7*(May). https://doi.org/10.1038/ncomms11539

Gray, W. R., Rae, J. W. B., Wills, R. C. J., Shevenell, A. E., Taylor, B., Burke, A., … Lear, C. H. (2018). Deglacial upwelling, productivity and CO2 outgassing in the North Pacific Ocean. *Nature Geoscience*, *11*(5), 340–344. https://doi.org/10.1038/s41561-018-0108-6

Griffiths, J. D., Barker, S., Hendry, K. R., Thornalley, D. J. R., Van De Flierdt, T., Hall, I. R., & Anderson, R. F. (2013). Evidence of silicic acid leakage to the tropical Atlantic via Antarctic Intermediate Water during Marine Isotope Stage 4. *Paleoceanography*, *28*(2), 307–318. https://doi.org/10.1002/palo.20030

Hagelberg, T. K., Bond, G., & DeMenocal, P. (1994). Milankovitch band forcing of sub-Milankovitch climate variability during the Pleistocene. *Paleoceanography*, *9*(4), 545–558. https://doi.org/10.1029/94PA00443

Hammer, Ø., Harper, D. A. T., & Ryan, P. D. (2001). PAST: Paleontologtical Statistics Software Package for Education and Data Analysis. *Paleontologica Electronica*, *4*, 9. https://doi.org/10.1093/cid/ciq238

Hansell, D. a. A., Whitledge, T. E. E., & Goering, J. J. J. (1993). Patterns of nitrate utilization and new production over the Bering-Chukchi shelf. *Continental Shelf Research*, *13*(5–6), 601–627. https://doi.org/10.1016/0278-4343(93)90096-G

Hansell, D. A., Goering, J. J., Walsh, J. J., McRoy, C. P., Coachman, L. K., & Whitledge, T. E. (1989). Summer phytoplankton production and transport along the shelf break in the Bering Sea. *Continental Shelf Research*, *9*(12), 1085–1104. https://doi.org/10.1016/0278-4343(89)90060-5

Hasle, G. R., & Sims, P. A. (1986). The diatom genera stellarima and symbolophora with comments on the genus actinoptychus. *British Phycological Journal*, *21*(1), 97–114. https://doi.org/10.1080/00071618600650101

Haug, G. H., Ganopolski, A., Sigman, D. M., Rosell-mele, A., Swann, G. E. A., Tiedemann, R., … Eglinton, G. (2005). North Pacific seasonality and the glaciation of North America 2.7 million years ago. *Nature*, 821–825.

Haug, G. H., Maslin, M. a, Sarnthein, M., Stax, R., & Tiedemann, R. (1995). 20 . Evolution of Northwest Pacific Sedimentation Patterns Since 6 Ma (Site 882). *Proceedings of the Ocean Drilling Program. Scientific Results*, *145*(Site 882), 293–314.

Haug, G. H., Sigman, D. M., Tiedemann, R., Pedersen, T. F., & Sarntheink, M. (1999). Onset of permanent stratification in the subarctic Pacific Ocean. *Nature*, *401*(6755), 21–24. https://doi.org/10.1038/44550

Hendry, K. R., & Brzezinski, M. A. (2014). Using silicon isotopes to

understand the role of the Southern Ocean in modern and ancient biogeochemistry and climate. *Quaternary Science Reviews*, *89*, 13–26. https://doi.org/10.1016/j.quascirev.2014.01.019

Heslop, D., Dekkers, M. J., & Langereis, C. G. (2002). Timing and structure of the mid-Pleistocene transition: Records from the loess deposits of northern China. *Palaeogeography, Palaeoclimatology, Palaeoecology*, *185*(1–2), 133–143. https://doi.org/10.1016/S0031-0182(02)00282-1

Hönisch, B., Hemming, G. N., Archer, D., Siddall, M., & McManus, J. F. (2009). Atmospheric Carbon Dioxide Concentration Across the Mid-Pleistocene Transition. *Science*, *324*(5934), 1551–1554. https://doi.org/10.1126/science.1229223

Horikawa, K., Asahara, Y., Yamamoto, K., & Okazaki, Y. (2010). Intermediate water formation in the Bering Sea during glacial periods: Evidence from neodymium isotope ratios. *Geology*, *38*(5), 435–438. https://doi.org/10.1130/G30225.1

Horn, M. G., Beucher, C. P., Robinson, R. S., & Brzezinski, M. A. (2011). Southern ocean nitrogen and silicon dynamics during the last deglaciation. *Earth and Planetary Science Letters*, *310*(3–4), 334–339. https://doi.org/10.1016/j.epsl.2011.08.016

Hu, A., Meehl, G. A., Otto-Bliesner, B. L., Waelbroeck, C., Han, W., Loutre, M. F., … Rosenbloom, N. (2010). Influence of Bering Strait flow and North Atlantic circulation on glacial sea-level changes. *Nature Geoscience*, *3*(2), 118–121. https://doi.org/10.1038/ngeo729

Hunt, G. L., & Stabeno, P. J. (2002). Climate change and the control of energy flow in the southeastern Bering Sea. *Progress in Oceanography*, *55*(1-2 SPEC ISS.), 5–22. https://doi.org/10.1016/S0079-6611(02)00067-8

Hutchins, D. A., & Bruland, K. W. (1998). Iron-limited diatom growth and Si:N uptake ratios in a coastal upwelling regime. *Nature*, *393*(June), 561–564. https://doi.org/10.1038/31203

Ikenoue, T., Okazaki, Y., Takahashi, K., & Sakamoto, T. (2015). Bering sea radiolarian biostratigraphy and paleoceanography at IODP site U1341 during the last four million years. *Deep Sea Research Part II: Topical Studies in Oceanography*, (February 2016), 1–18. https://doi.org/10.1016/j.dsr2.2015.03.004

Ikenoue, T., Okazaki, Y., Takahashi, K., & Sakamoto, T. (2016). Bering Sea radiolarian biostratigraphy and paleoceanography at IODP Site U1341 during the last four million years. *Deep-Sea Research Part II: Topical Studies in Oceanography*, *125–126*(MARCH), 38–55. https://doi.org/10.1016/j.dsr2.2015.03.004

Imbrie, J., Boyle, I. E. a, Clemens, S. C., Duffy, A., Howard, I. W. R., Kukla, G., … Toggweiler, J. R. (1993). On the Structure and Origin of Major

Glacial Cycles 2. The 100,000 Year Cycle. *Paleoceanography*, *8*(6), 699–735. https://doi.org/10.1029/93pa02751

Itaki, T., Uchida, M., Kim, S., Shin, H.-S., Tada, R., & Khim, B.-K. (2009). Late Pleistocene stratigraphy and palaeoceanographic implications in northern Bering Sea slope sediments: evidence from the radiolarian species Cycladophora davisiana. *Journal of Quaternary Science*, *24*(8), 856–865. https://doi.org/10.1002/jqs

Iwasaki, S., Takahashi, K., Kanematsu, Y., Asahi, H., Onodera, J., & Ravelo, A. C. (2016). Paleoproductivity and paleoceanography of the last 4.3 Myrs at IODP Expedition 323 Site U1341 in the Bering Sea based on biogenic opal content. *Deep-Sea Research Part II: Topical Studies in Oceanography*, *125–126*, 145–154. https://doi.org/10.1016/j.dsr2.2015.04.005

Jaccard, S. L., & Galbraith, E. D. (2018). Push from the Pacific. *Nature Geoscience*, *11*(5), 299–300. https://doi.org/10.1038/s41561-018-0119-3

Jaccard, S. L., Galbraith, E. D., Sigman, D. M., & Haug, G. H. (2010). A pervasive link between Antarctic ice core and subarctic Pacific sediment records over the past 800 kyrs. *Quaternary Science Reviews*, *29*(1–2), 206–212. https://doi.org/10.1016/j.quascirev.2009.10.007

Jaccard, S. L., Haug, G. H., Sigman, D. M., Pedersen, T. F., Thierstein, H. R., & Röhl, U. (2005). Glacial/ Interglacial Changes in Subarctic North Pacific Stratification. *Science*, *308*(5724), 1003–1006. https://doi.org/10.1126/science.1108696

Jaccard, S. L., Hayes, C. T., Martinez-Garcia, A., Hodell, D. A., Anderson, R. F., Sigman, D. M., & Haug, G. H. (2013). Two modes of change in Southern Ocean productivity over the past million years. *Science*, *339*(March), 1419–1423.

Jaeger, J. M., Gulick, S. P. S., LeVay, L. J., & Scientists, E. 341. (2013). *Proceedings of the Integrated Ocean Drilling Program, Volume 341 Expedition Reports*. (341). https://doi.org/10.2204/iodp.pr.341.2014

Jang, K., Huh, Y., & Han, Y. (2017). Authigenic Nd isotope record of North Pacific Intermediate Water formation and boundary exchange on the Bering Slope. *Quaternary Science Reviews*, *156*, 150–163. https://doi.org/10.1016/j.quascirev.2016.11.032

Jouzel, J., Masson-Delmotte, V., Cattani, O., Dreyfus, G., Falourd, S., Hoffmann, G., … Wolff, E. W. (2007). Orbital and Millennial Antarctic Climate Variability over the Past 800,000 years. *Science*, *317*(August), 793–796. https://doi.org/10.1126/science.1141038

Kanematsu, Y., Takahashi, K., Kim, S., Asahi, H., & Khim, B. K. (2013). Changes in biogenic opal productivity with Milankovitch cycles during the last 1.3Ma at IODP Expedition 323 Sites U1341, U1343, and U1345

in the Bering Sea. *Quaternary International*, *310*, 213–220. https://doi.org/10.1016/j.quaint.2013.06.003

Kemp, A. E. S., & Villareal, T. A. (2013). High diatom production and export in stratified waters - A potential negative feedback to global warming. *Progress in Oceanography*, *119*, 4–23. https://doi.org/10.1016/j.pocean.2013.06.004

Kender, S., Ravelo, A. C., Worne, S., Swann, G. E. A., Leng, M. J., Asahi, H., … Hall, I. R. (2018). Closure of the Bering Strait caused Mid-Pleistocene Transition cooling. *Nature Communications*, *9*(5386). https://doi.org/10.1038/s41467-018-07828-0

Kim, S., & Khim, B.-K. (2017). Estimates of glacial silicic acid reduction over the last 600 ka in the Bering Sea using d30Si of diatom frustules. *Geochemical Journal*, Vol. 51, pp. 347–357.

Kim, S., Khim, B.-K., & Takahashi, K. (2016). Late Pliocene to early Pleistocene (2.4-1.25 Ma) paleoproductivity changes in the Bering Sea: IODP expedition 323 Hole U1343E. *Deep-Sea Research Part II: Topical Studies in Oceanography*, *125–126*, 155–162. https://doi.org/10.1016/j.dsr2.2015.04.003

Kim, S., & Khim, B. K. (2016). Reconstruction of nitrate utilization rate change based on diatom-bound nitrogen isotope values in the central slope area of the Bering sea during the early pleistocene (2.4−1.25 Ma). *Ocean and Polar Research*, *38*(3), 195–207. https://doi.org/10.4217/OPR.2016.38.3.195

Kim, S., Khim, B. K., Ikehara, M., & Takahashi, K. (2017). Relationship between δ15N values of bulk sediments and total organic carbon concentration in response to orbital-scale biogenic opal production in the Bering slope area over the last 600 kyrs. *Quaternary International*, *459*(3), 144–152. https://doi.org/10.1016/j.quaint.2017.05.041

Kim, S., Khim, B. K., Uchida, M., Itaki, T., & Tada, R. (2011). Millennial-scale paleoceanographic events and implication for the intermediate-water ventilation in the northern slope area of the Bering Sea during the last 71kyrs. *Global and Planetary Change*, *79*(1–2), 89–98. https://doi.org/10.1016/j.gloplacha.2011.08.004

Kim, S., Takahashi, K., Kanematsu, Y., Asahi, H., & Khim, B. K. (2012). Surface water productivity in the Bering Sea and the subarctic North Pacific in response to global climate cooling during the last 2.32 Myrs. *Geophysical Research Abstracts*, *14*, 3946.

Kim, S., Takahashi, K., Khim, B. K., Kanematsu, Y., Asahi, H., & Ravelo, A. C. (2014). Biogenic opal production changes during the Mid-Pleistocene Transition in the Bering Sea (IODP Expedition 323 Site U1343). *Quaternary Research (United States)*, *81*(1), 151–157. https://doi.org/10.1016/j.yqres.2013.10.001

Knauss, J. A. (1962). On Some Aspects of the Deep Circulation of the Pacific. *Journal of Geophysical Research*, *67*(10), 3943–3954.

Knudson, K. P., & Ravelo, A. C. (2015a). Enhanced subarctic Pacific stratification and nutrient utilization during glacials over the last 1.2 Myr. *Geophysical Research Letters*, *42*(22), 9870–9879. https://doi.org/10.1002/2015GL066317

Knudson, K. P., & Ravelo, A. C. (2015b). North Pacific Intermediate Water circulation enhanced by the closure of the Bering Strait. *Paleoceanography*, *30*(10), 1287–1304. https://doi.org/10.1002/2015PA002840

Ladd, C. (2014). Seasonal and interannual variability of the Bering Slope Current. *Deep-Sea Research Part II: Topical Studies in Oceanography*, *109*, 5–13. https://doi.org/10.1016/j.dsr2.2013.12.005

Lam, P. J., Robinson, L. F., Blusztajn, J., Li, C., Cook, M. S., McManus, J. F., & Keigwin, L. D. (2013). Transient stratification as the cause of the North Pacific productivity spike during deglaciation. *Nature Geoscience*, *6*(8), 622–626. https://doi.org/10.1038/ngeo1873

Lear, C. H., Billups, K., Rickaby, R. E. M., Diester-Haass, L., Mawbey, E. M., & Sosdian, S. M. (2016). Breathing more deeply: Deep ocean carbon storage during the mid-Pleistocene climate transition. *Geology*, *44*(12), 1035–1038. https://doi.org/10.1130/G38636.1

Leblanc, K., Arístegui, J., Armand, L., Assmy, P., Beker, B., Bode, A., … Yallop, M. (2012). A global diatom database – abundance, biovolume and biomass in the world ocean. *Earth System Science Data*, *4*(1), 149–165. https://doi.org/10.5194/essd-4-149-2012

Lee, J. E., Shen, A., Fox-Kemper, B., & Ming, Y. (2017). Hemispheric sea ice distribution sets the glacial tempo. *Geophysical Research Letters*, *44*(2), 1008–1014. https://doi.org/10.1002/2016GL071307

Leng, M. J., & Sloane, H. J. (2008). Combined oxygen and silicon isotope analysis of biogenic silica. *Journal of Quaternary Science*, *23*(4), 313–319.

Li, D., Zheng, L. W., Jaccard, S. L., Fang, T. H., Paytan, A., Zheng, X., … Kao, S. J. (2017). Millennial-scale ocean dynamics controlled export productivity in the subtropical North Pacific. *Geology*, *45*(7), 651–654. https://doi.org/10.1130/G38981.1

Li, F., & Wang, H. (2013). Relationship between Bering Sea Ice Cover and East Asian Winter Monsoon Year-to-Year Variations. *Advances in Atmospheric Sciences*, *30*(1), 48–56. https://doi.org/10.1007/s00376-012-2071-2.1.Introduction

Lisiecki, L. E., & Raymo, M. E. (2005). A Pliocene-Pleistocene stack of 57

globally distributed benthic δ18O records. *Paleoceanography*, *20*(1), 1–17. https://doi.org/10.1029/2004PA001071

Lisiecki, L. E., & Raymo, M. E. (2009). Diachronous benthic δ18O responses during late Pleistocene terminations. *Paleoceanography*, *24*(3), 1–14. https://doi.org/10.1029/2009PA001732

Liu, Z., Altabet, M. A., & Herbert, T. D. (2005). Glacial-interglacial modulation of eastern tropical North Pacific denitrification over the last 1.8-Myr. *Geophysical Research Letters*, *32*(23), 1–4. https://doi.org/10.1029/2005GL024439

Liu, Z., & Herbert, T. D. (2004). High-latitude influence on the eastern equatorial Pacific climate in the early Pleistocene epoch. *Nature*, *430*(July), 560–564. https://doi.org/10.1038/nature02295.1.

Liu, Z., Trentesaux, A., Clemens, S. C., Colin, C., Wang, P., Huang, B., & Boulay, S. (2003). Clay mineral assemblages in the northern South China Sea: Implications for East Asian monsoon evolution over the past 2 million years. *Marine Geology*, *201*(1–3), 133–146. https://doi.org/10.1016/S0025-3227(03)00213-5

Loose, B., Schlosser, P., Perovich, D., Ringelberg, D., Ho, D. T., Takahashi, T., … Tison, J. L. (2011). Gas diffusion through columnar laboratory sea ice: Implications for mixed-layer ventilation of CO2in the seasonal ice zone. *Tellus, Series B: Chemical and Physical Meteorology*, *63*(1), 23–39. https://doi.org/10.1111/j.1600-0889.2010.00506.x

Luchin, V. A., Semiletov, I. P., & Weller, G. E. (2002). Changes in the Bering Sea region: Atmosphere-Ice-Water system in the second half of the twentieth century. *Progress in Oceanography*, *55*(1-2 SPEC ISS.), 23–44. https://doi.org/10.1016/S0079-6611(02)00068-X

Lüthi, D., Le Floch, M., Bereiter, B., Blunier, T., Barnola, J. M., Siegenthaler, U., … Stocker, T. F. (2008). High-resolution carbon dioxide concentration record 650,000-800,000 years before present. *Nature*, *453*(7193), 379–382. https://doi.org/10.1038/nature06949

Maier, E., Méheust, M., Abelmann, A., Gersonde, R., Chapligin, B., Ren, J., … Tiedemann, R. (2015). Deglacial subarctic Pacific surface water hydrography and nutrient dynamics and links to North Atlantic climate variability and atmospheric CO2. *Paleoceanography*, *30*(7), 949–968. https://doi.org/10.1002/2014PA002763

Marchetti, A., Juneau, P., Whitney, F. A., Wong, C. S., & Harrison, P. J. (2006). Phytoplankton processes during a mesoscale iron enrichment in the NE subarctic Pacific: Part II-Nutrient utilization. *Deep-Sea Research Part II: Topical Studies in Oceanography*, *53*(20–22), 2114–2130. https://doi.org/10.1016/j.dsr2.2006.05.031

Marlow, J. R., Lange, C. B., Wefer, G., & Rosell-Mele, a. (2000). Upwelling

intensification as part of the Pliocene-Pleistocene climate transition. *Science*, *290*(5500), 2288–2291. https://doi.org/10.1126/science.290.5500.2288

Martínez-Garcia, A., Rosell-Melé, A., Geibert, W., Gersonde, R., Masqué, P., Gaspari, V., & Barbante, C. (2009). Links between iron supply, marine productivity, sea surface temperature, and CO2 over the last 1.1 Ma. *Paleoceanography*, *24*(1), 1–14. https://doi.org/10.1029/2008PA001657

Martínez-Garcia, A., Rosell-Melé, A., Jaccard, S. L., Geibert, W., Sigman, D. M., & Haug, G. H. (2011). Southern Ocean dust-climate coupling over the past four million years. *Nature*, *476*(7360), 312–315. https://doi.org/10.1038/nature10310

Martinez-Garcia, A., Rosell-Melé, A., McClymont, E. L., Gersonde, R., & Haug, G. H. (2010). Subpolar Link to Emergence of the Modern Equatorial Pacific Cold Tongue. *Science*, *328*(5985), 1550–1553.

März, C., Schnetger, B., Brumsack, H. J., März, C., Schnetger, B., & Brumsack, H. J. (2013). Nutrient leakage from the North Pacific to the Bering Sea (IODP site U1341) following the onset of Northern Hemispheric Glaciation? *Paleoceanography*, *28*(1), 68–78. https://doi.org/10.1002/palo.20011

Maslin, M. A., Haug, G. H., Sarnthein, M., & Tiedemann, R. (1996). The progressive intensification of northern hemisphere glaciation as seen from the North Pacific. *Geologische Rundschau*, *85*, 452–465. https://doi.org/10.1007/BF02369002

Maslin, M., Haug, G. H., Sarnthein, M., Tiedemann, R., Erlenkeuser, H., & Stax, R. (1995). Northwest Pacific Site 882 : the Initiation of Northern Hemisphere Glaciation. *Proceedings of the Ocean Drilling Program, Scientific Results, Vol. 145*, *145*, 315–329.

Matsumoto, K., Oba, T., Lynch-Stieglitz, J., & Yamamoto, H. (2002a). Interior hydrography and circulation of the glacial Pacific Ocean. *Quaternary Science Reviews*, *21*(14–15), 1693–1704. https://doi.org/10.1016/S0277-3791(01)00142-1

Matsumoto, K., & Sarmiento, J. L. (2008). A corollary to the silicic acid leakage hypothesis. *Paleoceanography*, *23*(2), 1–9. https://doi.org/10.1029/2007PA001515

Matsumoto, K., Sarmiento, J. L., & Brzezinski, M. A. (2002b). Silicic acid leakage from the Southern Ocean: A possible explanation for glacial atmospheric pCO2. *Global Biogeochemical Cycles*, *16*(3), 5-1-5–23. https://doi.org/10.1029/2001gb001442

Max, L., Lembke-Jene, L., Riethdorf, J. R., Tiedemann, R., Nürnberg, D., Kühn, H., & MacKensen, A. (2014). Pulses of enhanced north Pacific intermediate water ventilation from the Okhotsk Sea and Bering Sea

during the last deglaciation. *Climate of the Past*, *10*(2), 591–605. https://doi.org/10.5194/cp-10-591-2014

McClymont, E. L., & Rosell-Melé, A. (2005). Links between the onset of modern Walker circulation and the mid-Pleistocene climate transition. *Geology*, *33*(5), 389–392. https://doi.org/10.1130/G21292.1

McClymont, E. L., Rosell-Melé, A., Haug, G. H., & Lloyd, J. M. (2008). Expansion of subarctic water masses in the North Atlantic and Pacific oceans and implications for mid-Pleistocene ice sheet growth. *Paleoceanography*, *23*(4), 1–12. https://doi.org/10.1029/2008PA001622

McClymont, E. L., Sosdian, S. M., Rosell-Melé, A., & Rosenthal, Y. (2013). Pleistocene sea-surface temperature evolution: Early cooling, delayed glacial intensification, and implications for the mid-Pleistocene climate transition. *Earth-Science Reviews*, *123*, 173–193. https://doi.org/10.1016/j.earscirev.2013.04.006

Mcintyre, A., & Molfino, B. (1996). Forcing of Atlatic Equaotiral and Subpolar Millennial Cycles by Precession. *Science*, *274*(December), 0–3.

McQuoid, M. R., & Hobson, L. A. (1996). Diatom Resting Stages. *Journal of Phycology*, *32*(6), 889–902. https://doi.org/10.1111/j.0022-3646.1996.00889.x

McQuoid, M. R., & Nordberg, K. (2003). The diatom Paralia sulcata as an environmental indicator species in coastal sediments. *Estuarine, Coastal and Shelf Science*, *56*(2), 339–354. https://doi.org/10.1016/S0272-7714(02)00187-7

Melles, M., Minyuk, P. S., Nowaczyk, N. R., Deconto, R. M., Anderson, P. M., Andreev, A. A., … Wagner, B. (2012). 2.8 Million Years of Arctic Climate e from Lake El'gygytgyn, NE Russia. *Science*, *337*(June), 1–8. Retrieved from www.sciencemag.org

Mix, A. C., Pisias, N. G., Rugh, W., Wilson, J., Morey, A., & Hagelberg, T. K. (1995). Benthic Foraminifer Stable Isotope Record from Site 849 (0-5 Ma): Local and Global Climate Changes. *Proceedings of the Ocean Drilling Program, 138 Scientific Results*, *138*. https://doi.org/10.2973/odp.proc.sr.138.120.1995

Mizobata, K., & Saitoh, S. I. (2004). Variability of Bering Sea eddies and primary productivity along the shelf edge during 1998-2000 using satellite multisensor remote sensing. *Journal of Marine Systems*, *50*(1–2), 101–111. https://doi.org/10.1016/j.jmarsys.2003.09.014

Mudelsee, M., & Raymo, M. E. (2005). Slow dynamics of the Northern Hemisphere glaciation. *Paleoceanography*, *20*(4), 1–14. https://doi.org/10.1029/2005PA001153

Mudelsee, M., & Schulz, M. (1997). The Mid-Pleistocene climate transition:

onset of 100 ka cycle lags ice volume build-up by 280 Ka. *Earth and Planetary Science Letters*, *151*, 117–123.

Nishioka, J., Ono, T., Saito, H., Nakatsuka, T., Takeda, S., Yoshimura, T., … Tsuda, A. (2007). Iron supply to the western subarctic Pacific: Importance of iron export from the Sea of Okhotsk. *Journal of Geophysical Research: Oceans*, *112*(10). https://doi.org/10.1029/2006JC004055

Ohkushi, K., Itaki, T., & Nemoto, N. (2003a). Last Glacial-Holocene change in intermediate-water ventilation in the Northwestern Pacific. *Quaternary Science Reviews*, *22*(14), 1477–1484. https://doi.org/10.1016/S0277-3791(03)00082-9

Ohkushi, K., Suzuki, A., Kawahata, H., & Gupta, L. P. (2003b). Glacial-interglacial deep-water changes in the NW Pacific inferred from single foraminiferal δ18O and δ13C. *Marine Micropaleontology*, *48*(3–4), 281–290. https://doi.org/10.1016/S0377-8398(03)00023-9

Okazaki, Y., Timmermann, A., Menviel, L., Harada, N., Abe-Ouchi, A., Chikamoto, M. O., … Asahi, H. (2010). Deepwater Formation in the North Pacific During the Last Glacial Termination. *Science*, *329*(5988), 200–204. https://doi.org/10.1126/science.1190612

Oksanen, J., Guillaume Blanchet, F., Friendly, M., Kindt, R., Legendre, P., McGlinn, D., … Wagner, H. (2018). *vegan: Community Ecology Package. R package version 2.5-2.* Retrieved from https://cran.r-project.org/package=vegan

Pena, L. D., & Goldstein, S. L. (2014). Thermohaline circulation crisis and impacts during the mid-Pleistocene transition. *Science*, *345*(6194), 318–322. https://doi.org/10.1126/science.1249770

Peters, E., & Thomas, D. N. (1996). Prolonged nitrate exhaustion and diatom mortality: A comparison of polar and temperate Thalassiosira species. *Journal of Plankton Research*, *18*(6), 953–968. https://doi.org/10.1093/plankt/18.6.953

PICES. (2005). Western Subarctic Gyre BT - Marine Ecosystems of the North Pacific. *Marine Ecosystems of the North Pacific*, 1–11. Retrieved from papers2://publication/uuid/C059D00D-2AFB-4E5C-9CCC-5B9072529C6A

Pichevin, L. E., Reynolds, B. C., Ganeshram, R. S., Cacho, L., Pena, L., Keefe, K., & Ellam, R. M. (2009). Enhanced carbon pump inferred from relaxation of nutrient limitation in the glacial ocean. *Nature*, *459*(7250), 1114–1117. https://doi.org/10.1038/nature08101

Pichevin, L., Ganeshram, R. S., Reynolds, B. C., Prahl, F., Pedersen, T. F., Thunell, R., & McClymont, E. L. (2012). Silicic acid biogeochemistry in the Gulf of California: Insights from sedimentary Si isotopes.

Paleoceanography, *27*(2), 1–14. https://doi.org/10.1029/2011PA002237

Pike, J., Crosta, X., Maddison, E. J., Stickley, C. E., Denis, D., Barbara, L., & Renssen, H. (2009). Observations on the relationship between the Antarctic coastal diatoms Thalassiosira antarctica Comber and Porosira glacialis (Grunow) Jørgensen and sea ice concentrations during the late Quaternary. *Marine Micropaleontology*, *73*(1–2), 14–25. https://doi.org/10.1016/j.marmicro.2009.06.005

Pollard, D. (2000). Comparisons of ice-sheet surface mass budgets from Paleoclimate Modeling Intercomparison Project (PMIP) simulations. *Global and Planetary Change*, *24*(2), 79–106. https://doi.org/10.1016/S0921-8181(99)00071-5

Pollard, D., & DeConto, R. M. (2009). Modelling West Antarctic ice sheet growth and collapse through the past five million years. *Nature*, *458*(7236), 329–332. https://doi.org/10.1038/nature07809

Praetorius, S. K., Mix, A. C., Walczak, M. H., Wolhowe, M. D., Addison, J. A., & Prahl, F. G. (2015). North Pacific deglacial hypoxic events linked to abrupt ocean warming. *Nature*, *527*(7578), 362–366. https://doi.org/10.1038/nature15753

R Core Team. (2017). *R: A language and environment for statistical computing.* Retrieved from https://www.r-project.org/.

Rae, J. W. B., Sarnthein, M., Foster, G. L., Ridgewell, A., Grootes, P. M., & Elliott, T. (2014). Deep water formation in the North Pacific and deglacial CO2 rise. *Paleoceanography*, *29*, 1–23. https://doi.org/10.1002/2013PA002570.Received

Raymo, M. E. (1997). The timing of major climate terminations. *Paleoceanography*, *12*(4), 577–585. https://doi.org/10.1029/97PA01169

Raymo, M. E., Lisiecki, L. E., Nisancioglu, K. H., Hemispheres, S., & Instead, O. (2006). Plio-Pleistocene Ice Volume, Antarctic Climate, and the Global d18O Record. *Nature*, *313*(July), 492–495. https://doi.org/10.1126/science.1123296

Raymo, M. E., & Nisancioglu, K. H. (2003). The 41 kyr world: Milankovitch's other unsolved mystery. *Paleoceanography*, *18*(1), n/a-n/a. https://doi.org/10.1029/2002PA000791

Reed, R. K., Khen, G. V., Stabeno, P. J., & Verkhunov, A. V. (1993). Water properties and flow over the deep Bering Sea basin, summer 1991. *Deep-Sea Research Part I*, *40*(11–12), 2325–2334. https://doi.org/10.1016/0967-0637(93)90107-E

Rella, S. F., Tada, R., Nagashima, K., Ikehara, M., Itaki, T., Ohkushi, K., … Uchida, M. (2012). Abrupt changes of intermediate water properties on the northeastern slope of the Bering Sea during the last glacial and

deglacial period. *Paleoceanography*, *27*(3). https://doi.org/10.1029/2011PA002205

Rembauville, M., Blain, S., Armand, L., Quéguiner, B., & Salter, I. (2015). Export fluxes in a naturally iron-fertilized area of the Southern Ocean – Part 2: Importance of diatom resting spores and faecal pellets for export. *Biogeosciences*, *12*(11), 3171–3195. https://doi.org/10.5194/bg-12-3171-2015

Rembauville, M., Manno, C., Tarling, G. A., Blain, S., & Salter, I. (2016). Strong contribution of diatom resting spores to deep-sea carbon transfer in naturally iron-fertilized waters downstream of South Georgia. *Deep-Sea Research Part I: Oceanographic Research Papers*, *115*, 22–35. https://doi.org/10.1016/j.dsr.2016.05.002

Ren, J., Gersonde, R., Esper, O., & Sancetta, C. (2014). Diatom distributions in northern North Pacific surface sediments and their relationship to modern environmental variables. *Palaeogeography, Palaeoclimatology, Palaeoecology*, *402*, 81–103. https://doi.org/10.1016/j.palaeo.2014.03.008

Reynolds, B. C. (2009). Modeling the modern marine δ30Si distribution. *Global Biogeochemical Cycles*, *23*(2), 1–13. https://doi.org/10.1029/2008GB003266

Reynolds, B. C., Frank, M., & Halliday, A. N. (2006a). Silicon isotope fractionation during nutrient utilization in the North Pacific. *Earth and Planetary Science Letters*, *244*(1–2), 431–443. https://doi.org/10.1016/j.epsl.2006.02.002

Reynolds, B. C., Georg, R. B., Valley, J. W., & Halliday, A. N. (2006b). Co-variations of δ30Si and δ18O during contact metamorphism. *Geochimica et Cosmochimica Acta*, *70*(18), A529. https://doi.org/10.1016/j.gca.2006.06.974

Riethdorf, J.-R., Thibodeau, B., Ikehara, M., Nürnberg, D., Max, L., Tiedemann, R., & Yokoyama, Y. (2016). Surface nitrate utilization in the Bering sea since 180 kA BP: Insight from sedimentary nitrogen isotopes. *Deep-Sea Research Part II: Topical Studies in Oceanography*, *125–126*, 163–176. https://doi.org/10.1016/j.dsr2.2015.03.007

Robinson, R. S., Kienast, M., Luiza Albuquerque, A., Altabet, M., Contreras, S., De Pol Holz, R., … Yang, J. Y. (2012). A review of nitrogen isotopic alteration in marine sediments. *Paleoceanography*, *27*(4). https://doi.org/10.1029/2012PA002321

Rodionov, S. N., Bond, N. A., & Overland, J. E. (2007). The Aleutian Low, storm tracks, and winter climate variability in the Bering Sea. *Deep-Sea Research Part II: Topical Studies in Oceanography*, *54*(23–26), 2560–2577. https://doi.org/10.1016/j.dsr2.2007.08.002

Rodionov, S. N., Overland, J. E., & Bond, N. A. (2005). The Aleutian low and winter climatic conditions in the Bering Sea. Part I: Classification. *Journal of Climate*, *18*(1), 160–177. https://doi.org/10.1175/JCLI3253.1

Rodríguez-Sanz, L., Graham Mortyn, P., Martínez-Garcia, A., Rosell-Melé, A., & Hall, I. R. (2012). Glacial Southern Ocean freshening at the onset of the Middle Pleistocene Climate Transition. *Earth and Planetary Science Letters*, *345–348*, 194–202. https://doi.org/10.1016/j.epsl.2012.06.016

Sambrotto, R. N., Mordy, C., Zeeman, S. I., Stabeno, P. J., & Macklin, S. A. (2008). Physical forcing and nutrient conditions associated with patterns of Chl a and phytoplankton productivity in the southeastern Bering Sea during summer. *Deep-Sea Research Part II: Topical Studies in Oceanography*, *55*(16–17), 1745–1760. https://doi.org/10.1016/j.dsr2.2008.03.003

Sancetta, C. (1982). Distribution of diatom species in surface sediments of the Bering and Okhotsk seas. *Micropaleontology*, *28*(3), 221–257.

Sancetta, C., & Silvestri, S. (1986). Pliocene-Pleistocene Evolution of the North Pacific Ocean-Atmosphere System, Interpreted from Fossil Diatoms. *Paleoceanography*, *1*(2), 163–180. https://doi.org/10.1029/PA001i002p00163

Schlitzer, R. (2013). *eWOCE Gallery - Pacific*.

Schmieder, F., Von Dobeneck, T., & Bleil, U. (2000). The Mid-Pleistocene climate transition as documented in the deep South Atlantic Ocean: Initiation, interim state and terminal event. *Earth and Planetary Science Letters*, *179*(3–4), 539–549. https://doi.org/10.1016/S0012-821X(00)00143-6

Sexton, P. F., & Barker, S. (2012). Onset of "Pacific-style" deep-sea sedimentary carbonate cycles at the mid-Pleistocene transition. *Earth and Planetary Science Letters*, *321–322*, 81–94. https://doi.org/10.1016/j.epsl.2011.12.043

Shimada, C., Sato, T., Yamasaki, M., Hasegawa, S., & Tanaka, Y. (2009). Drastic change in the late Pliocene subarctic Pacific diatom community associated with the onset of the Northern Hemisphere Glaciation. *Palaeogeography, Palaeoclimatology, Palaeoecology*, *279*(3–4), 207–215. https://doi.org/10.1016/j.palaeo.2009.05.015

Sigman, D. M., DiFiore, P. J., Hain, M. P., Deutsch, C., Wang, Y., Karl, D. M., … Pantoja, S. (2009). The dual isotopes of deep nitrate as a constraint on the cycle and budget of oceanic fixed nitrogen. *Deep-Sea Research Part I: Oceanographic Research Papers*, *56*(9), 1419–1439. https://doi.org/10.1016/j.dsr.2009.04.007

Sigman, D. M., Hain, M. P., & Haug, G. H. (2010). The polar ocean and

glacial cycles in atmospheric CO2 concentration. *Nature*, *466*(7302), 47–55. https://doi.org/10.1038/nature09149

Sigman, D. M., & Haug, G. H. (2004). The Biological Pump in the Past. *Treatise on Geochemistry*, 491–528. https://doi.org/10.1016/b0-08-043751-6/06118-1

Snyder, C. W. (2016). Evolution of global temperature over the past two million years. *Nature*, *538*(7624), 226–228. https://doi.org/10.1038/nature19798

Sosdian, S. M., & Rosenthal, Y. (2009). Deep-Sea Temperature and Ice Volume Changes Across the Pliocene-Pleistocene Climate Transitions. *Science*, *325*(July), 306–309. https://doi.org/10.1126/science.1169938

Springer, A. M., Peter McRoy, C., & Flint, M. V. (1996). The Bering Sea Green Belt: Shelf-edge processes and ecosystem production. *Fisheries Oceanography*, *5*(3–4), 205–223. https://doi.org/10.1111/j.1365-2419.1996.tb00118.x

Stabeno, P. J., Kachel, N. B., Sullivan, M., & Whitledge, T. E. (2002). Variability of physical and chemical characteristics along the 70-m isobath of the southeast Bering Sea. *Deep-Sea Res. Pt. II*, *49*(26), 5931–5943. https://doi.org/10.1016/S0967-0645(02)00327-2

Stabeno, P. J., Schumacher, J. D., & Ohtani, K. (1999). The physical oceanography of the Bering Sea. *Dynamics of the Bering Sea*, 1–60. Retrieved from ftp://128.112.177.15/pub/edac/bering_sea/Stabeno_1999_bering_sea.pdf

Stroynowski, Z., Abrantes, F., & Bruno, E. (2017). The response of the Bering Sea Gateway during the Mid-Pleistocene Transition. *Palaeogeography, Palaeoclimatology, Palaeoecology*, *485*(March), 974–985. https://doi.org/10.1016/j.palaeo.2017.08.023

Stroynowski, Z., Ravelo, A. C., & Andreasen, D. (2015). A Pliocene to recent history of the Bering Sea at Site U1340A, IODP Expedition 323. *Paleoceanography*, *30*(12), 1641–1656. https://doi.org/10.1002/2015PA002866

Studer, A. S., Martínez-Garcia, A., Jaccard, S. L., Girault, F. E., Sigman, D. M., & Haug, G. H. (2012). Enhanced stratification and seasonality in the Subarctic Pacific upon Northern Hemisphere Glaciation-New evidence from diatom-bound nitrogen isotopes, alkenones and archaeal tetraethers. *Earth and Planetary Science Letters*, *351–352*, 84–94. https://doi.org/10.1016/j.epsl.2012.07.029

Sun, Y., Clemens, S. C., An, Z., & Yu, Z. (2006). Astronomical timescale and palaeoclimatic implication of stacked 3.6-Myr monsoon records from the Chinese Loess Plateau. *Quaternary Science Reviews*, *25*(1–2), 33–48. https://doi.org/10.1016/j.quascirev.2005.07.005

Sun, Y., Yin, Q., Crucifix, M., Clemens, S. C., Araya-Melo, P., Liu, W., … An, Z. (2019). Diverse manifestations of the mid-Pleistocene climate transition. *Nature Communications*, *10*(1), 1–11. https://doi.org/10.1038/s41467-018-08257-9

Sutton, J. N., Varela, D. E., Brzezinski, M. A., & Beucher, C. P. (2013). Species-dependent silicon isotope fractionation by marine diatoms. *Geochimica et Cosmochimica Acta*, *104*, 300–309. https://doi.org/10.1016/j.gca.2012.10.057

Sverdrup, K. A., & Armbrust, V. (2009). *An Introduction to the World's Oceans, 10th ed.* McGraw-Hill Education.

Swann, G. E. A. (2010). Salinity changes in the North West Paci fi c Ocean during the late Pliocene / early Quaternary from 2 . 73 Ma to 2 . 52 Ma. *Earth and Planetary Science Letters*, *297*(1–2), 332–338. https://doi.org/10.1016/j.epsl.2010.06.035

Swann, G. E. A., Pike, J., Snelling, A. M., Leng, M. J., & Williams, M. C. (2013). Seasonally resolved diatom δ18O records from the West Antarctica Peninsula over the last deglaciation. *Earth and Planetary Science Letters*, *364*(March 2017), 12–23. https://doi.org/10.1016/j.epsl.2012.12.016

Swann, G. E. A., Snelling, A. M., & Pike, J. (2016). Biogeochemical cycling in the Bering Sea over the onset of major Northern Hemisphere Glaciation. *Paleoceanography*, *31*(9), 1261–1269. https://doi.org/10.1002/2016PA002978

Takahashi, K. (1986). Seasonal fluxes of pelagic diatoms in the subarctic Pacific, 1982-1983. *Deep-Sea Research*, *33*(9), 1225–1251.

Takahashi, K., Fujitani, N., & Yanada, M. (2002). Long term monitoring of particle fluxes in the Bering Sea and the central subarctic Pacific Ocean, 1990-2000. *Progress in Oceanography*, *55*(1-2 SPEC ISS.), 95–112. https://doi.org/10.1016/S0079-6611(02)00072-1

Takahashi, K., Ravelo, A. C., Alvarez Zarikian, C. A., & Scientists, E. 323. (2011a). IODP Expedition 323-pliocene and pleistocene paleoceanographic changes in the Bering Sea. *Scientific Drilling*, (1), 4–13. https://doi.org/10.2204/iodp.sd.11.01.2011

Takahashi, K., Ravelo, A. C., Alvarez Zarikian, C. A., & Scientists, E. 323. (2011b). Site U1343. *Proceedings of the IODP*, *323*, *323*. https://doi.org/10.2204/iodp.proc.323.107.2011

Takeda, S. (2011). Iron and Phytoplankton Growth in the Subarctic North Pacific. *Aqua-BioScience Monographs*, *4*(2), 41–93. https://doi.org/10.5047/absm.2011.00402.0041

Talley, L. (2000). SIO 210 Talley Topic 4: North Pacific circulation and water

masses. Wind forcing. Retrieved from University College San Diego website: http://sam.ucsd.edu/sio210/lect_4/lecture_4.html

Talley, L. D. (1993). Distribution and Formation of North Pacific Intermediate Water. *Journal of Physical Oceanography*, *23*, 517–537.

Tanaka, S., & Takahashi, K. (2005). Late Quaternary paleoceanographic changes in the Bering Sea and the western subarctic Pacific based on radiolarian assemblages. *Deep-Sea Research Part II: Topical Studies in Oceanography*, *52*(16–18), 2131–2149. https://doi.org/10.1016/j.dsr2.2005.07.002

Teraishi, A., Suto, I., Onodera, J., & Takahashi, K. (2016). Diatom, silicoflagellate and ebridian biostratigraphy and paleoceanography in IODP 323 Hole U1343E at the Bering slope site. *Deep-Sea Research Part II: Topical Studies in Oceanography*, *125–126*, 18–28. https://doi.org/10.1016/j.dsr2.2013.03.026

Trujillo, A. P., & Thurman, H. V. (2011). *Essentials of Oceanography, 10th ed.* Prentic Hall, Pearson.

Tsunogai, S., Kusakabe, M., Iizumi, H., Koike, I., & Hattori, A. (1979). Hydrographic features of the deep water of the Bering Sea-the sea of Silica. *Deep Sea Research Part A, Oceanographic Research Papers*, *26*(6), 641–659. https://doi.org/10.1016/0198-0149(79)90038-4

Tziperman, E., & Gildor, H. (2003). On the mid-Pleistocene transition to 100-kyr glacial cycles and the asymmetry between glaciation and deglaciation times. *Paleoceanography*, *18*(1), 1-1-1–8. https://doi.org/10.1029/2001pa000627

VanLaningham, S., Pisias, N. G., Duncan, R. A., & Clift, P. D. (2009). Glacial-interglacial sediment transport to the Meiji Drift, northwest Pacific Ocean: Evidence for timing of Beringian outwashing. *Earth and Planetary Science Letters*, *277*(1–2), 64–72. https://doi.org/10.1016/j.epsl.2008.09.033

Wang, F., Li, Z., Wang, X., Li, B., & Chen, F. (2018). Variation and interplay of the Siberian High and westerlies in central-east Asia during the past 1200 kyr. *Aeolian Research*, *33*(December 2017), 62–81. https://doi.org/10.1016/j.aeolia.2018.05.003

Wang, W. L., & Wang, L. C. (2008). Reconstruction of oceanographic changes based on the diatom records of the central Okhotsk Sea over the last 500000 years. *Terrestrial, Atmospheric and Oceanic Sciences*, *19*(4), 403–411. https://doi.org/10.3319/TAO.2008.19.4.403(IMAGES)

Wara, M. W., Ravelo, A. C., & Revenaugh, J. S. (2000). The Pacemaker always rings twice. *Paleoceanography*, *15*(6), 616–624.

Wehrmann, L. M., Risgaard-Petersen, N., Schrum, H. N., Walsh, E. A., Huh,

Y., Ikehara, M., … Zarikian, C. A. (2011). Coupled organic and inorganic carbon cycling in the deep subseafloor sediment of the northeastern Bering Sea Slope (IODP Exp. 323). *Chemical Geology*, *284*(3–4), 251–261. https://doi.org/10.1016/j.chemgeo.2011.03.002

Worne, S., Kender, S., Swann, G. E. A., Leng, M. J., & Ravelo, A. C. (2019). Coupled climate and subarctic Pacific nutrient upwelling over the last 850, 000 years. *Earth and Planetary Science Letters*, *522*, 87–97.

Yasuda, I. (1997). The origin of the North Pacific Intermediate Water. *Journal of Geophysical Research: Oceans*, *102*(C1), 893–909. https://doi.org/10.1029/96jc02938

Yasuda, I. (2004). North Pacific Intermediate Water : Progress in SAGE (SubArctic Gyre Experiment) and Related Projects. *Journal of Oceanography*, *60*, 385–395.

Chapter 8: Appendix

8.1 Appendix 1: Closure of the Bering Strait caused Mid-Pleistocene Transition cooling

nature COMMUNICATIONS

ARTICLE

https://doi.org/10.1038/s41467-018-07828-0 OPEN

Closure of the Bering Strait caused Mid-Pleistocene Transition cooling

Sev Kender[1,2], Ana Christina Ravelo[3], Savannah Worne[4], George E.A. Swann[4], Melanie J. Leng[2,5], Hirofumi Asahi[6], Julia Becker[7], Henrieka Detlef[8], Ivano W. Aiello[9], Dyke Andreasen[3] & Ian R. Hall[10]

The Mid-Pleistocene Transition (MPT) is characterised by cooling and lengthening glacial cycles from 600–1200 ka, thought to be driven by reductions in glacial CO_2 in particular from ~900 ka onwards. Reduced high latitude upwelling, a process that retains CO_2 within the deep ocean over glacials, could have aided drawdown but has so far not been constrained in either hemisphere over the MPT. Here, we find that reduced nutrient upwelling in the Bering Sea, and North Pacific Intermediate Water expansion, coincided with the MPT and became more persistent at ~900 ka. We propose reduced upwelling was controlled by expanding sea ice and North Pacific Intermediate Water formation, which may have been enhanced by closure of the Bering Strait. The regional extent of North Pacific Intermediate Water across the subarctic northwest Pacific would have contributed to lower atmospheric CO_2 and global cooling during the MPT.

[1] Camborne School of Mines, University of Exeter, Penryn Campus, Penryn, Cornwall TR10 9FE, UK. [2] NERC Isotope Geosciences Facilities, British Geological Survey, Keyworth, Nottingham NG12 5GG, UK. [3] University of California, Santa Cruz, CA 95064, USA. [4] Centre for Environmental Geochemistry, School of Geography, University of Nottingham, University Park, Nottingham NG7 2RD, UK. [5] Centre for Environmental Geochemistry, School of Biosciences, University of Nottingham, Sutton Bonington Campus, Loughborough NE12 5RD, UK. [6] Center for Advanced Marine Core Research, Kochi University, B200 Monobe, Nankoku, Kochi 783-8502, Japan. [7] Department of Geosciences, State Museum of Natural History, 76133 Karlsruhe, Germany. [8] Department of Geoscience, Aarhus University, Høegh-Guldbergs Gade 2, 8000 Aarhus C, Denmark. [9] Moss Landing Marine Laboratories, 8272 Moss Landing Road, Moss Landing, CA 95039, USA. [10] School of Earth and Ocean Sciences, Cardiff University, Cardiff CF10 3AT, UK. Correspondence and requests for materials should be addressed to S.K. (email: s.kender@exeter.ac.uk)

The Mid-Pleistocene Transition (MPT) is the last major transition in Earth's climate, and appears as global cooling and glacial lengthening in two phases. Firstly, as gradual sea surface temperature (SST) reduction[1] and glacial intensification and lengthening (towards quasi 100 ka cycles), from about 1200 ka in SST and deep ocean $\delta^{18}O$ composite records. Secondly, there was abrupt ice sheet growth[2,3], and further SST reductions[1] from Marine Isotope Stage (MIS) 22–23 (at ~900 ka). The absence of noteworthy secular changes in Milankovitch forcing, and the weakness of the 100 ka eccentricity insolation cycle, indicates internal feedbacks within the Earth system rather than orbital forcing alone were the cause of these two phases[2,4]. There is currently no consensus on what internal forcing shifts led to the MPT. Hypotheses have pointed to Southern Ocean dust supply increases from ~1300 ka[5], the unusual insolation low over Antarctica at ~900 ka[2], changing North American ice sheet dynamics[4,6] and sea ice changes[7,8]. A secular decline in atmospheric CO_2 concentrations has been suggested as a central cause[5,6,9–11], and a slowdown in Atlantic meridional overturning circulation and North Atlantic Deep Water (NADW) production has led to the idea that there was enhanced CO_2 transfer from the surface ocean to the deep at ~900 ka[12]. These processes are not mutually exclusive, and could each be associated with a build-up of ice on North America for which there is ample evidence[4]. To sequester CO_2 in the deep ocean also likely requires stifled nutrient and CO_2-rich deep water upwelling at high latitudes to reduce outgassing, as proposed for the last glacial;[13,14] however, although recent records of Southern Ocean biogenic opal suggest glacial reductions in productivity occurred throughout the Pleistocene[15], there are so far no direct records of high latitude upwelling from either hemisphere with which to evaluate this potentially important mechanism for the MPT glacial CO_2 reduction.

The subarctic North Pacific (Fig. 1), including the marginal Bering Sea, is a high-nutrient, low-chlorophyll (HNLC) region limited by iron, and is in this respect similar to the subantarctic Southern Ocean where major nutrient consumption is incomplete and excess CO_2 today is vented to the atmosphere[13,16]. The subarctic North Pacific is particularly important, as ventilation of this region may have accounted for 30% of the last deglacial rise in atmospheric CO_2[17,18]. High-nutrient deep water in the modern subarctic Pacific is separated from the surface by a shallow seasonal halocline. While the stratification is strong enough to prevent major intermediate or deep water formation, nutrient- and CO_2-rich water sourced from North Pacific Deep Water (NPDW) upwells within eddies along the modern Bering Sea slope (termed the high productivity Green Belt) due to wind forcing, tidal mixing, instability and topographic interference[19,20]. Incomplete nutrient utilization occurs, likely due to iron and/or light limitation[16,21], leaving surface waters oversaturated compared with atmospheric CO_2 in the winter[22]. The modern Bering Sea intermediate water mass of low nitrate occurs above the halocline at ~300 m water depth[23], but eddies along the slope can reach down 400–1000 m[20].

Glacial reductions in Bering Sea Green Belt primary productivity are similar both to changes in subarctic Pacific primary productivity (ODP Site 882) over at least the last 800 ka[16,21,24,25], and to glacial reductions in productivity in the Indian Ocean sector of the Southern Ocean (ODP Site 745)[15], although the causes of reduced productivity are yet to be identified. For example, reductions in Pacific glacial productivity may be caused by light limitation due to a deepening of the mixed layer during summer[24], hypothetically linked to changing atmospheric weather systems and windiness. Alternatively, changes could be related to reduced glacial upwelling of nutrients[24] caused by enhanced halocline stratification[16,21] or the glacial expansion of the nutrient-poor North Pacific Intermediate Water (NPIW) which would have resulted in a less nutrient-rich source of upwelling water[26,27]. Additional possible causes in the Bering Sea are sea ice expansion[8,28], light limitation[25], ice-rafted debris[29], and reduced Fe-fertilization from riverine input and/or remobilization from shelf sediments[19]. A recent MPT productivity record from the Gulf of Alaska does not follow glacial cycles, and has demonstrated fertilization by glacigenic debris as an important process in that region[29].

In this study we produce the first high latitude nutrient upwelling record over the MPT and determine the causes of reduced glacial productivity in the Bering Sea over MIS 21–29 (840–1020 ka) by presenting new geochemical proxy records from Integrated Ocean Drilling Program (IODP) Site U1343 (1954 m water depth; 175° 49.0′W, 57° 33.4′N), located on a topographic high near the northern Bering Sea slope (Supplementary Fig. 1) within the high productivity Green Belt. We use bulk sediment $\delta^{15}N$ and $\delta^{13}C$ of organic carbon ($\delta^{13}C_{org}$) compared with organic carbon and previously published opal[25] accumulation rates to decipher changes in deep ocean

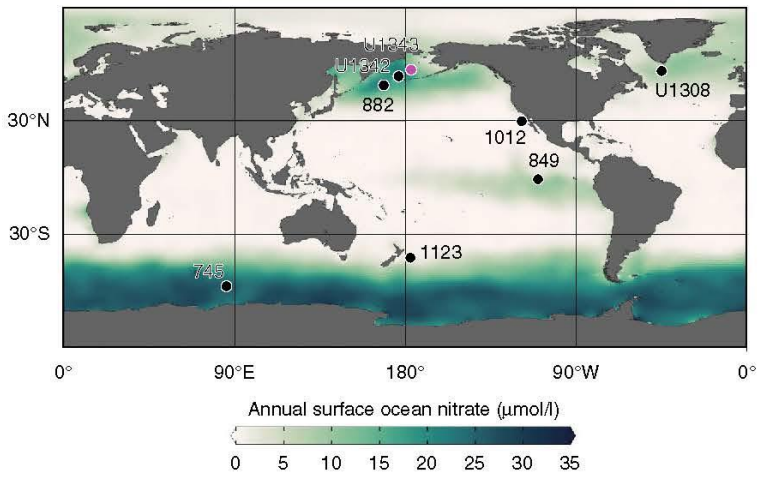


Fig. 1 Map of annual surface ocean nitrate concentration (μmol/l). Surface water data taken from the 2013 World Ocean Atlas database[67]. Circles show the locations of sediment cores referred to in the text. The new data in this paper come from Site U1343 (pink circle)

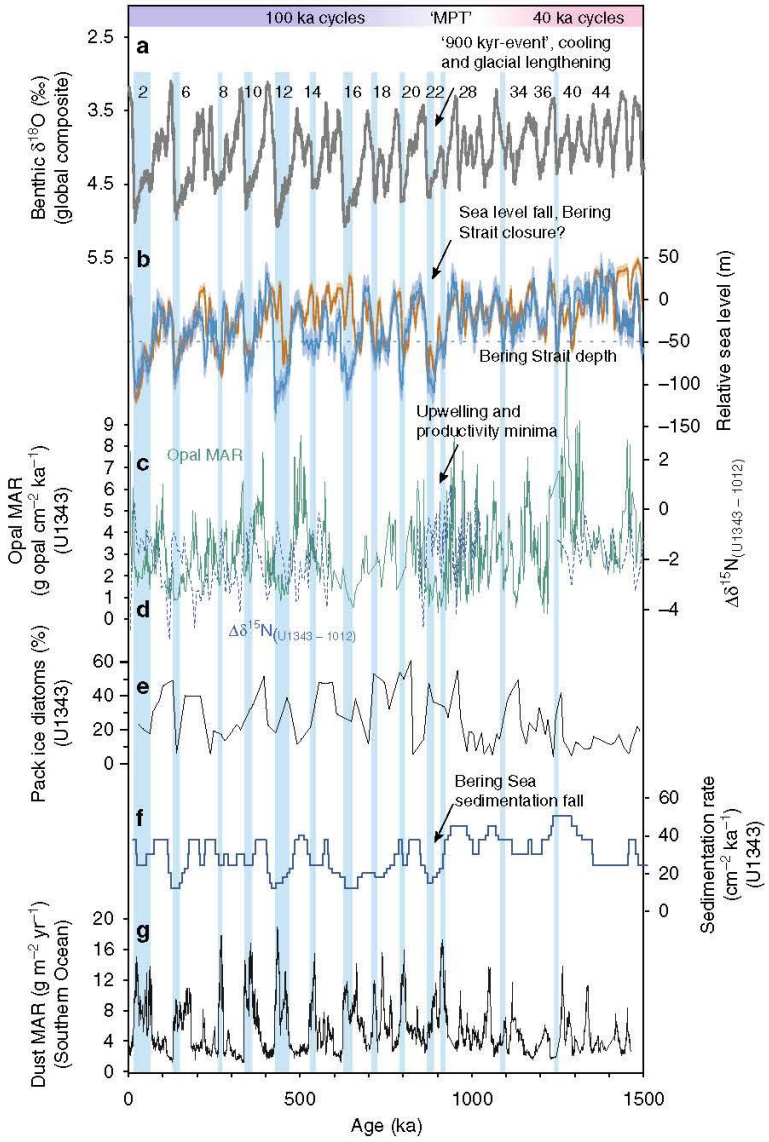


Fig. 2 Bering Sea productivity, nutrient utilization and sedimentation rate proxy records compared with global glacial-interglacial cycles for the past 1500 ka. The Mid-Pleistocene Transition (MTP) represents the transition from 40 ka glacial cycles to 100 ka glacial cycles. Major sea level falls below the current Bering Strait sill depth (horizontal dashed line) are indicated with blue vertical bars. From ~900 ka, reduced glacial productivity occurs with increased nutrient utilization. **a** Global benthic foraminiferal $\delta^{18}O$ composite (grey) LR04[30]. **b** Global sea level estimates from Site 1123 (blue)[2] and the Mediterranean (orange)[3]. **c** Opal mass accumulation rate (MAR) as a proxy for productivity (green) for Site U1343[25]. **d** Bulk sediment $\delta^{15}N$ for Site U1343, with Site 1012[48] subtracted ($\Delta\delta^{15}N$). U1343 $\delta^{15}N$ data from 850–1020 ka are from this study, other are data are previously published[39,68]. **e** Site U1343 percentage of diatom assemblages regarded as indicative of pack ice[69]. **f** Sedimentation rate (cm ka^{-1}) for Site U1343[33]. **g** Dust MAR from the Southern Ocean ODP Site 1090[5]

nutrient supply to the surface. Benthic foraminiferal $\delta^{18}O$ is used to provide evidence of NPIW expansion. We compare our new records of surface and deep ocean changes with global sea level estimates and published data from other subarctic sites to assess the potential links between cooling, sea ice expansion, closure of the Bering Strait, NPIW production, reduced high latitude CO_2 and nutrient upwelling, and development of the MPT. We find the increased presence of NPIW, and reduced nutrient upwelling, during glacial periods from the MPT onwards, and propose that coincident Bering Strait closure may have caused NPIW formation by retaining sea ice brines within the Bering Sea.

Results

Benthic foraminiferal isotopes. Our study focuses on the time period ~900 ka (MIS 21–29), which occurs within the MPT when sea levels fell, glacials began to lengthen, and productivity across the Bering Sea and North Pacific fell (Fig. 2a–c; Fig. 3). We produced a composite benthic foraminiferal $\delta^{18}O$ record at IODP

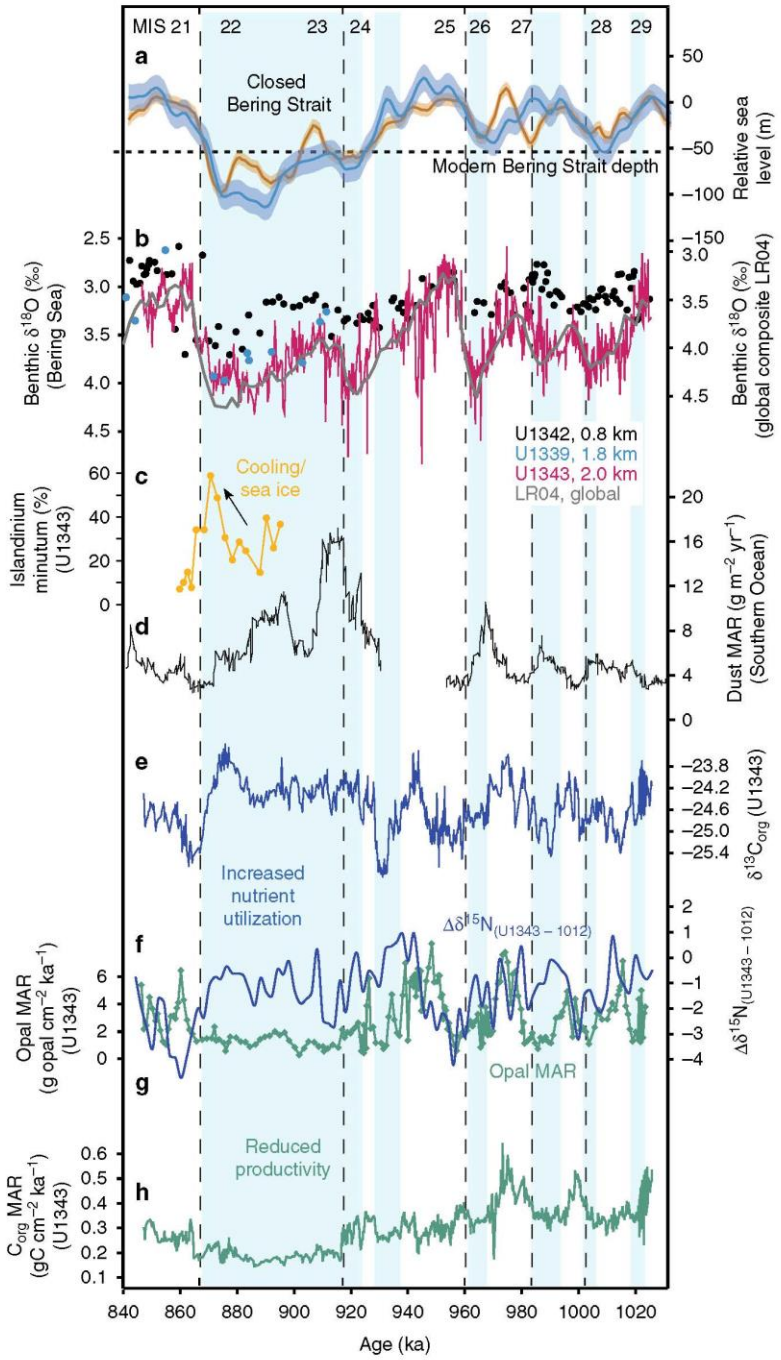


Fig. 3 Proxy data from Site U1343 for the time interval 850–1020 ka. Vertical blue bars are times of reduced productivity and elevated nutrient utilization indicating reduced deep water nutrient upwelling along the Bering Slope. **a** Global sea level estimates from Site 1123 (blue)[2] and the Mediterranean (orange)[3]. The current Bering Strait sill depth is indicated with a horizontal dashed line. **b** Benthic $\delta^{18}O$ data (this study) from U1343 (red), U1342 (black)[27], U1339 (blue)[36] and LR04 (grey)[30]. Data from U1339 and U1342 has been converted to the *Elphidium batialis* scale for direct comparison with U1343 data. **c** Dinoflagellate cyst *Islandinium minutum* % data for U1343 (this study). **d** Dust MAR from the Southern Ocean ODP Site 1090[5]. **e** Bulk sediment $\delta^{13}C_{org}$ for U1343 (this study). **f** Bulk sediment $\delta^{15}N$ for Site 1012[48] subtracted from U1343 ($\Delta\delta^{15}N$). **g** Opal mass accumulation rate (MAR) as a proxy for productivity (green) for Site U1343[25]. **h** Total organic carbon (C_{org}) mass accumulation rate (MAR) as a proxy for productivity for Site U1343 (this study)

Site U1343 (Fig. 3b) at high temporal resolution (average 200–300 y time step) and used this to create an age model by tuning it to the global composite benthic record LR04[30] (see Methods). The majority of our benthic $\delta^{18}O$ record follows long-term trends in LR04 (Fig. 3b, Supplementary Fig. 2a), providing no evidence that long-term changes in water mass occurred at this site (~2 km water depth) throughout almost all of the study interval. However, there is a prolonged negative offset towards relatively low $\delta^{18}O$ values centred at 880–870 ka during the MIS 22 glacial maximum (Fig. 3b; Supplementary Fig. 2b), and possible offsets at 930 ka although with less certainty (Supplementary Fig. 2c). These offsets toward low $\delta^{18}O$ values, which are exceptionally clear during MIS 22 at Site U1343, are more typical of shallower water Site U1342 (Fig. 3b). They are important as they contrast from the markedly enriched benthic $\delta^{18}O$ values in all global records including the eastern equatorial Pacific (Site 849)[31], deep South Pacific (Site 1123)[32] and North Atlantic (Site U1308) (Supplementary Fig. 2a).

We are confident the negative MIS 22 $\delta^{18}O$ offset seen in the Bering Sea records occurred at the glacial maximum (rather than occurring at the beginning of the deglacial) for three reasons. First, to shift the benthic $\delta^{18}O$ record to better match the global composite deglacial timing would require rapid and drastic changes in sedimentation rates, which are not seen elsewhere at Site U1343[33]. Second, manipulating the age model in this way would create an unusual three-step shape to the deglaciation, not seen in other records including the Pacific[2,31]. Third, our dinoflagellate cyst assemblages indicate that the relatively low $\delta^{18}O$ values are accompanied by a probable cooling and/or expansion of sea ice (Fig. 3c), indicative of a glacial maximum rather than deglaciation. The interval 870–880 ka is characterised by an increase in the proportion of dinoflagellate cyst *Islandinium minutum* which is a species known to become abundant in the modern Arctic and Atlantic when the temperature is approximately ~0–6 °C, and sea ice is >8 months/year[34]. The other abundant species in our samples, *Bitectatodinium* spp. and *Brigantedinium* spp. (Supplementary Data 1), are cosmopolitan and do not show strong preferences for temperature or sea ice[34], although *Islandinium* and *Bitectatodinium* are often associated with polynya[35].

The benthic foraminiferal $\delta^{13}C$ data show wide variability (Supplementary Fig. 3a). This is likely due to the different species habitats and possible authigenic carbonate overgrowth[36], although the majority of the species aside from *Elphidium* sit above the −2.5‰ threshold below which is considered indicative of possible authigenic carbonate for the Bering Sea[36]. In order to avoid authigenic carbonates, and the impact of changing species habitats, we plot the Site U1343 $\delta^{13}C$ of *Uvigerina* spp. which shows overall similar trends to $\delta^{13}C$ of *Uvigerina* spp. from equatorial Pacific Site 849 with a −1‰ offset (Supplementary Fig. 3b). Although there is scatter in the data, there is evidence for a positive $\delta^{13}C$ offset of Site U1343 from 849 during the MIS 22 glacial maximum, coinciding with the negative $\delta^{18}O$ offset of U1343 from the LR04 global stack.

MPT changes in primary productivity. Obtaining accurate proxies for export production can be a challenge due to preservation issues with both organic and inorganic compounds[24]. Bering Sea Site U1343 is uniquely valuable in this respect, as it sits within the highly productive Green Belt region dominated by diatom production such that the sediment is typically enriched in biogenic opal (the constituent of diatom frustules) at ~5–30%[25]. Because factors such as diagenesis and low opal export may compromise the preservation of opal[21,28], and any shifts in the balance of phytoplankton towards calcifiers could impact opal accumulation, absolute values may not constitute a quantitative proxy for export production. However, in this high flux region[37] the relative changes in opal accumulation are large and likely to reflect first-order changes in productivity. Site U1343 constitutes a continuous long record that has been orbitally-tuned using $\delta^{18}O$ stratigraphy over the past 1.2 Ma[33] allowing glacial-interglacial calculation of sedimentation and biogenic opal accumulation rates. As the age model is constructed with a relatively small number of tie points (see Methods), the resulting opal and total organic carbon mass accumulation rates (MARs) are likely to approximate true flux rates only on long glacial-interglacial timescales. The adjustment of opal and total organic carbon percentages to MAR does not change the overall pattern in a significant way, although it does lower the glacial MAR to some extent (Supplementary Fig. 4). Figure 2c shows that long term opal changes over the past 1.5 Ma exhibit highly fluctuating values, with generally higher accumulation rates before 900 ka, and higher rates during interglacials overall[25].

We generated a high resolution (average 200–300 yr time step) record of organic carbon (C_{org}) accumulation over the interval 840–1020 ka at Site U1343 (Fig. 3h, Supplementary Fig. 4), which is subject to different limitations to biogenic opal but is complementary as a productivity proxy[37]. Sedimentary C_{org} accumulation shows first-order trends similar to those found in the opal accumulation record (Fig. 3g), with cyclic higher values before 920 ka, and lowest values during MIS 22–23 thus lending confidence that opal accumulation at U1343 is indicative of export production. The more extreme decrease in C_{org} accumulation at ~920 ka compared to opal accumulation could be due either to reduced C_{org} preservation in comparison to opal[38], a shift away from calcareous phytoplankton towards siliceous, or changes to phytoplankton Si/C and Si/N uptake ratios due to changing Fe availability[39].

Surface nutrient supply and upwelling. We generated bulk sediment $\delta^{15}N$ (Supplementary Fig. 2e) and $\delta^{13}C_{org}$ (Fig. 3e) to provide insight into surface water nutrient utilization and possible causes for the observed changes in productivity. In some subarctic settings it is known that a significant proportion of total N can be bound up in inorganic form[40], but we do not believe this significantly affects our samples as total N versus total C_{org} shows no positive intercept on the total N axis (Supplementary Fig. 5). Although phytoplankton preferentially take up ^{14}N nitrate[41], variations in sediment $\delta^{15}N$ are controlled by a variety of factors: changes in the $\delta^{15}N$ of nitrate in advected and/or upwelled source water ($\delta^{15}N_{source}$), which can be impacted by local or regional water column denitrification (e.g., denitrification enriches the $\delta^{15}N_{source}$);[42] nitrate utilization during marine organic production (e.g., higher utilization of available nitrate results in higher $\delta^{15}N$ of exported organic matter);[42] diagenetic alteration;[43] and contributions of terrestrial organic material which has lower $\delta^{15}N$ (~3 ‰)[44] and $\delta^{13}C_{org}$ (−26‰)[45] values than marine organics. Diagenesis is unlikely a major influence in the high sedimentation rate and productive Bering Sea[21,46,47]. Although it is possible that increased terrestrial material caused low $\delta^{15}N$ and $\delta^{13}C_{org}$ during low export production intervals before 930 ka, we regard this as unlikely due to the relatively stable sediment accumulation rates from 920–1020 ka, and relatively low C/N values (indicative of a low terrestrial:marine ratio) that do not co-vary with $\delta^{15}N$ or $\delta^{13}C_{org}$ (Supplementary Fig. 6). Thus, observed variations in $\delta^{15}N$ at U1343 likely reflect nitrate utilization and/or changes in water column denitrification affecting $\delta^{15}N_{source}$.

From ~930–1020 ka (MIS 25–29) both opal accumulation and $\delta^{15}N$ exhibit significant cyclicity at the 28 ka band, with opal leading $\delta^{15}N$ (Supplementary Fig. 7b). In the latter part of the

cycles, reductions in opal accumulation are coincident with sustained high $\delta^{15}N$ (blue bars in Fig. 3 and Supplementary Fig. 7a). This suggests these times were characterised by lower productivity and elevated nutrient utilization, which can be explained by reduced upwelling of nutrient-rich deep water but sustained utilization from continued iron delivery[21]. To account for possible changes in the $\delta^{15}N_{source}$ of surface and/or subsurface water imported into the Bering Sea from the northeast Pacific (via the Alaskan Stream[28]), from our $\delta^{15}N$ record we subtract eastern North Pacific Site 1012[48] (Supplementary Fig. 2d–f). Although this site is thought to be subject to intense denitrification[48], it is considered to represent some component of the regional changes in $\delta^{15}N_{source}$ due to its similarity to $\delta^{15}N$ records of northeast Pacific sites over more recent glacial cycles[49]. The resulting $\Delta\delta^{15}N_{U1343\ 1012}$ (Fig. 3f, Supplementary Fig. 7) shows broadly similar trends to $\delta^{15}N$ between 930–1020 ka, supporting the observation that nutrient utilization (high $\delta^{15}N$) is lagging productivity (opal). The lag is more pronounced in $\Delta\delta^{15}N$ than $\delta^{15}N$, which may be real or possibly due to an issue with age model uncertainty of the two sites. The 28 ka cyclicity disappears after 930 ka, and $\Delta\delta^{15}N$ remains high and productivity (opal and C_{org} accumulation) low for the entirety of MIS 22–23 (Fig. 3f, g) signifying a prolonged reduction in upwelling nutrients.

The $\Delta\delta^{15}N_{U1343\ 1012}$ nutrient utilization proxy for U1343 is potentially impacted by the low-resolution nature of the Site 1012 record, by possible discrepancies between age models at both sites, and by possible denitrification. Although glacials have been considered times of reduced denitrification in the Bering Sea and subarctic North Pacific due to lower export production[21], peaks in Bering Sea $\delta^{15}N$ during deglacial oxygen minima have been proposed as possible denitrification signals[21]. To test this we compare the $\Delta\delta^{15}N_{U1343\ 1012}$ to the Site U1343 $\delta^{13}C_{org}$ (Fig. 3e) which is controlled by nutrient utilization, although also impacted by changes in surface water CO_2 and plankton community structure. Despite these potential limitations, for the majority of the record the major, long-term changes in $\delta^{13}C_{org}$ support the $\Delta\delta^{15}N_{U1343\ 1012}$ findings of cyclic changes before about 930 ka, higher nutrient utilization (removal of the bioavailable ^{12}C) throughout the entirety of MIS 22–23, with highest values during MIS 22 before a rapid return to low nutrient utilization during interglacial MIS 21 (Fig. 3e).

Discussion

The reductions in nutrient upwelling (high $\Delta\delta^{15}N$ and lower opal accumulation; blue bars in Fig. 3) between 930–1020 ka are predominantly restricted to glacial intervals between MIS 24–28, with nutrient upwelling and productivity increasing after each deglacial (dashed black lines in Fig. 3). Parts of this interval are characterised by covariation of utilization and productivity, which could be explained by variations in iron fertilization, perhaps from terrestrial sources to the region. Conversely, when productivity decreases and nutrient utilization increases (blue bars in Fig. 3), enhanced nutrient utilization cannot be accounted for by, for example, iron fertilization as this would increase productivity. Enhanced halocline stratification is unlikely to have caused these productivity minima along the Bering Slope (unlike at Bowers Ridge[21,47]) as the modern Pacific halocline is relatively shallow (upper 300 m) and eddies at the slope can reach down to 1 km water depth[20]. These strong eddies are also likely to rule out a change in the depth of the shallower mixed layer as the primary cause of reduced productivity. We propose the cause of the reduced glacial nutrient upwelling from 930–1020 ka was due to enhanced NPIW (Fig. 4a). NPIW today produces a temperature and salinity low centred at ~500 m in the North Pacific, which is sourced partly from winter Okhotsk Sea pack ice brine rejection,

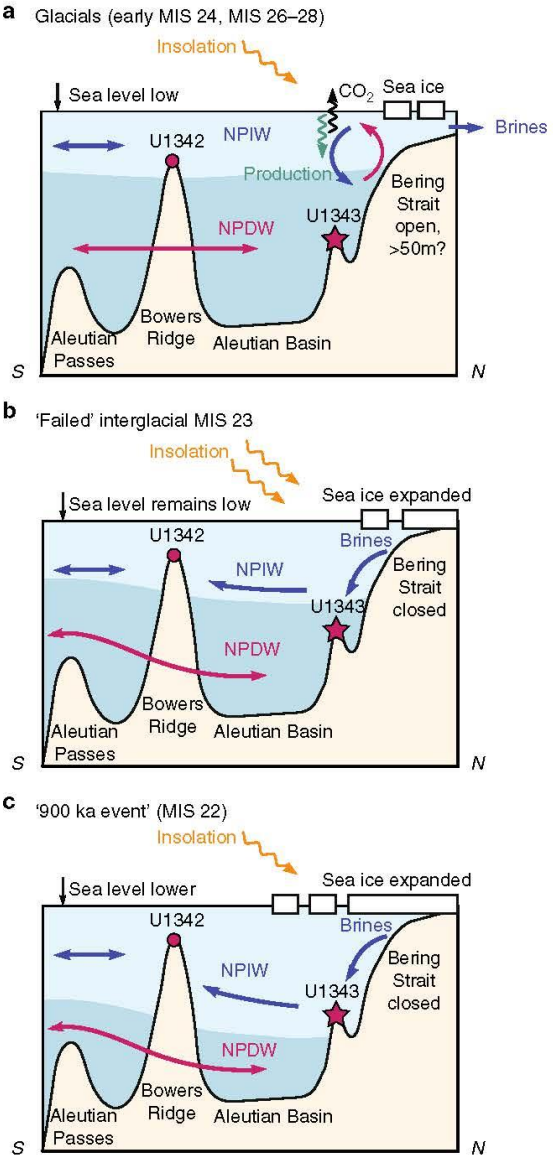


Fig. 4 Schematic Bering Sea cross section (N-S) showing palaeoceanographic interpretations. **a** Glacials between MIS 24–28 (before 930 ka). **b** 'Failed' interglacial MIS 23. **c** Glacial MIS 22 (the '900 ka event'). Interpretations of North Pacific Intermediate Water (NPIW) and North Pacific Deep Water (NPDW) are based on benthic $\delta^{18}O$ from Sites U1343 (this study) and U1342[27]. Arrows show the inferred flow of warmer (red) and colder (blue) currents

and exhibits low nutrients including nitrate[50]. Evidence for expanded NPIW during the last glacial maximum is extensive[26,27,36,51,52], with ε_{Nd} records identifying the Bering Sea as a probable source region for sea ice brine rejection during glacials[26,52]. The central Bering Sea appears to have been bathed in a relatively nutrient-poor (likely younger than deep Pacific) NPIW to at least ~0.8 km water depth during glacials over the past 1.2 Ma, evidenced by Site U1342 (Bowers Ridge) negative offsets in benthic foraminiferal $\delta^{18}O$ from deep Pacific end members[27]. These records

indicate that the lower boundary of NPIW deepened to >0.8 km water depth during glacials[27], offsetting shallow benthic $\delta^{18}O$ from U1343 values at ~2 km water depth (Fig. 3b). The proposed mechanism for producing relatively low Bering Sea deep water $\delta^{18}O$ is sea ice brine rejection, which can increase salinity without significantly altering $\delta^{18}O$, and is able to transport highly depleted $\delta^{18}O$ surface water to depth[27,36].

The shift away from precession (~23–28 ka) frequency in opal accumulation cycles at ~930 ka (Fig. 2c, Supplementary Fig. 8), suggests a change in the causal mechanisms driving export production during the MPT, possibly from a combination of NPIW and terrigenous nutrient influences before 930 ka, towards predominant NPIW control thereafter. During MIS 24–22, reduced nutrient upwelling (increased nutrient utilization and lower productivity) occurred for an extended period of time (>30 ka). This striking feature of the dataset is similar to $\delta^{15}N$ and opal accumulation records during the last glacial from Bowers Ridge (low glacial opal accumulation and higher $\delta^{15}N$)[21], and the last glacial cycle from the Bering Slope (Fig. 5). This provides evidence for both a more limited upwelling nutrient supply, and more complete nitrate utilization from continued iron delivery, during severe glacials[21]. During the 'failed' interglacial MIS 23, which directly contributed to the first quasi 100-ka cycle, nutrient upwelling remained low (blue bars in Fig. 3) likely due to the sustained expansion of NPIW, whilst insolation at 65°N was increasing (Fig. 4b). Subsequently, MIS 22 exhibited a further deepening of the lower boundary of NPIW to >2 km water depth, as evidenced by U1343 offsets in benthic $\delta^{18}O$ towards shallower water values (Fig. 3b) and potentially $\delta^{13}C$ (Supplementary Fig. 3) from global and Pacific records respectively, further removing the NPDW source of nutrients from the photic zone, and stifling both productivity and CO_2 outgassing (Fig. 4c). A lower resolution record from Site U1339 at 1.8 km water depth is consistent with this hypothesis, with benthic $\delta^{18}O$ values similar to Site U1343 (Fig. 3b). When considering the long-term record of nutrient utilization and primary productivity at Site U1343 (Figs. 1c, d, 5c), the data available show that severe glacials from MIS 22–24 onwards (MIS 2, 6, 8, 12 and 14) were coincident with longer productivity crashes and reduced nutrient upwelling (blue bars in Fig. 5). There is also evidence for deep expansion of NPIW to greater that 2 km from the lower resolution benthic $\delta^{18}O$ during these latter glacials (Fig. 5b). However, before ~930 ka productivity and nutrient utilization proxies indicate shorter-lived times of reduced nutrient upwelling, which we propose was due to less influence of NPIW in the early part of the MPT and before.

A cause for expanded NPIW has been suggested as enhanced sea ice and the production of brines, perhaps due to shifts in wind stress promoting polynya formation near the shelf[27]. Modelling of wind patterns over the last glacial does show significantly increased windiness over the Bering Sea[18]. A sea-ice controlled expansion of NPIW during glacials over the MPT is consistent with increased proportions of diatoms at the Bering Slope indicative of pack ice (Fig. 2e), although these records are of low resolution. Higher resolution but discontinuous IP_{25} and HBI III proxy records from U1343 were interpreted as glacial expansion of seasonal sea ice from 1150 ka, caused by high latitude atmospheric cooling[1], and then a more persistent seasonal/extended sea ice cover during glacials from MIS 22, possibly from reduced Pacific surface water influence[8]. Our dinoflagellate cyst assemblage record is consistent with an MIS 22 expansion of sea ice (Fig. 4c). Although a continuous and high-resolution sea ice proxy record from the Bering Sea is yet to be produced, further evidence for a sea ice control on NPIW and Bering Slope nutrient upwelling comes from sedimentation rate reductions along the slope during glacials particularly from MIS 22–24 onwards

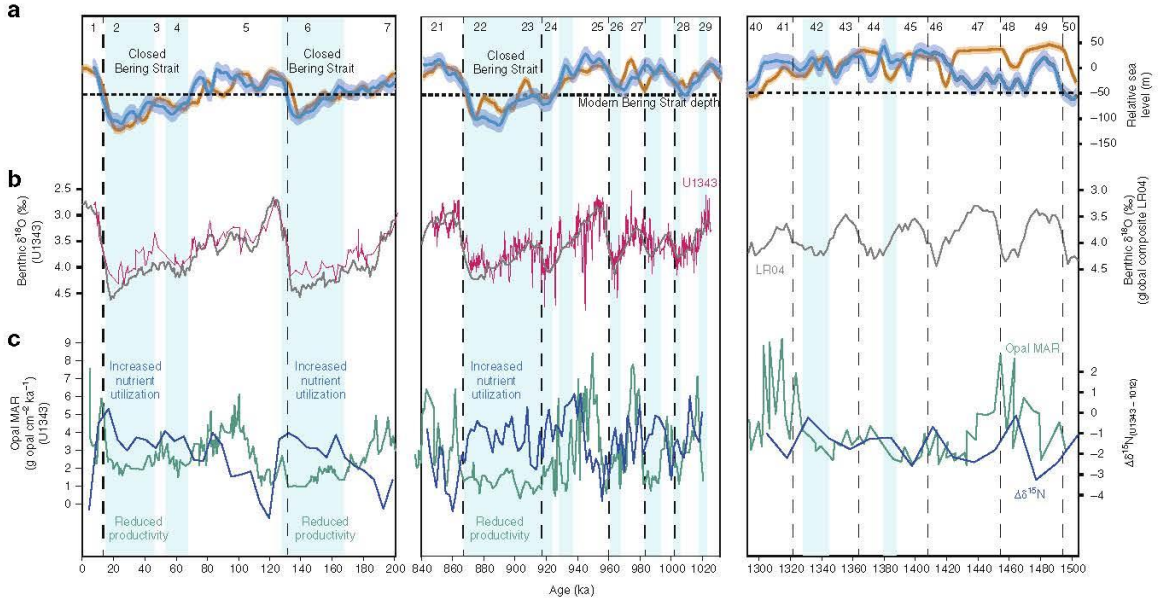


Fig. 5 Proxy data from Site U1343 compared with sea level, for three time periods over the past 1.5 Ma. Vertical blue bars are times of reduced productivity and elevated nutrient utilization indicating reduced deep water nutrient upwelling along the Bering Slope. **a** Global sea level estimates from Site 1123 (blue)[2] and the Mediterranean (orange)[3]. The current Bering Strait sill depth is indicated with a horizontal dashed line. **b** Benthic $\delta^{18}O$ data from U1343 (pink) and LR04 (grey)[30]. U1343 $\delta^{18}O$ data from 850–1020 ka are from this study, other data are published elsewhere[33]. **c** Bulk sediment $\delta^{15}N$ for Site 1012[48] subtracted from U1343 (blue) ($\Delta\delta^{15}N$). U1343 $\delta^{15}N$ data from 850–1020 ka are from this study, other are data are published elsewhere[39,68]. Opal mass accumulation rate (MAR) as a proxy for productivity (green) for Site U1343[25]

(Fig. 2f). Enhanced glaciation around the Bering Sea would have expanded shorefast and pack ice, known to inhibit modern day winter sedimentation[53].

Glacial expansions of sea ice influence may have been controlled by reduced air temperatures and/or increased windiness, and another factor promoting these conditions could have been closure of the Bering Strait[27]. Modern polynya brines formed in the Gulf of Anadyr and Anadyr Strait region of the Bering Sea flow into the Arctic[54]. A closed Bering Strait would have retained glacial brines within the Bering Sea. Modelling studies of a closed Bering Strait[55], although failing to predict expanded glacial NPIW perhaps due to limited modelling of Bering Sea shelf processes[27], do show entrained colder water within the Bering Sea. The first marked long-term period of reduced nutrient upwelling in our records was at MIS 22–24, which coincides with the first time sea level was below 50 m of the present[2,3] (Fig. 2b). The modern Bering Strait sill depth is 50 m. This region is thought to have undergone subsidence in the Pliocene[56] and first opened at about 4.8–5.5 Ma[57]. After an initial period of southward flow, the strait has been exchanging water with the Arctic in a (modern) northward flow since 3.3 Ma[58,59]. There is no direct evidence for how the water depth of the Bering Strait may have changed since, and it is possible that the strong currents did not allow significant sediment deposition and therefore any significant change from its current depth of ~50 m. We hypothesise that the failed MIS 23 deglacial may have directly coincided with the first closure of the Bering Strait (and subsequent closure during long glacials thereafter; Fig. 5a), retaining brines and NPIW in the Bering Sea, and cutting off the source of deep nutrients and CO_2 from the photic zone (Fig. 4b, c). This would have acted as a positive feedback on a process of global cooling already in motion. In addition to lower glacial temperatures and increased windiness, the idea of a closed Bering Strait promoting further enhanced sea ice, brines, NPIW and reduced nutrient upwelling along the Bering Slope, can only be supported by a comparison of upwelling with sea level records. Over the last 1.5 Ma, nutrient upwelling (offset between opal MAR and $\Delta\delta^{15}N$) has been lowest when sea level[2] was below 50 m of present (Table 1), compared to when global SST was below −3 °C of present, or deep ocean $\delta^{18}O$ (combined deep ocean temperature and ice volume) was above 4‰ (severe glacials). This provides some support for a closed Bering Strait having a stronger influence on NPIW and nutrient upwelling in the Bering Sea than either the average global surface or bottom water temperatures alone.

The regional significance of reduced MPT nutrient upwelling along the Bering Slope, caused by NPIW expansion (Fig. 5), is that NPIW would have inhibited CO_2 atmospheric exchange not only in the Bering Sea, but also across the subarctic North Pacific[13,16], creating a wide regional barrier for the upwelling of CO_2-rich deep water and associated primary productivity. Recent studies have highlighted the importance of North Pacific deep overturning[60] for increased outgassing of deep ocean CO_2 during the last deglacial[17,18], and the role that expanded NPIW may have played in suppressing North Pacific CO_2 ventilation to the atmosphere during the last glacial maximum[18]. A closed Bering Strait, therefore, could have contributed to MPT cooling by promoting local sea ice[8] and regionally-extensive NPIW and reduced nutrient upwelling (this study). NPIW would have created an effective barrier to deep North Pacific overturning, and subsequent atmospheric ventilation of CO_2. In this scenario, overturning of the North Pacific from the MPT onwards was only instigated at the termination of severe glacial conditions and associated global ocean circulation changes such as a shutdown of Atlantic Meridional Overturning Circulation[60].

The initial cause of MPT cooling remains enigmatic, but our new records show the North Pacific and the Bering Strait were important components within this global climate shift. Atmospheric cooling in high latitudes began at ~1.2 Ma[1] and may have been associated with a reduction in atmospheric CO_2 from enhanced dust fertilization in the Southern Ocean[5] (Fig. 2g). There is evidence for increases in Bering Sea sea ice from at least 1.2 Ma[8], and possible associated expansion of NPIW from reduced primary productivity at 1.2 Ma (Fig. 2c). These pieces of evidence suggest both the North Pacific and the Southern Ocean were likely ventilating less CO_2 to the atmosphere during glacials from the early phase of the MPT, although further records are needed to test this and ascertain timings. The second step in the development of the MPT, the severe ice sheet expansion[3] and glacial lengthening at ~900 ka (MIS 22–24; Fig. 2a), has been suggested to be associated with further CO_2 decline from deep ocean reorganisation and sequestration of CO_2 (ref. [12]). In agreement with this, we find that MIS 22–24 was associated with a severe and extended period of reduced Bering Slope nutrient upwelling and NPIW expansion to >2 km water depth, similar to subsequent severe glacials (Fig. 5), which would have further inhibited any CO_2 ventilation across the subarctic North Pacific. We suggest closure of the Bering Strait was contributory to this expanded NPIW, either as a threshold response crossed due to an as yet undefined boundary condition change, or as a boundary condition change in itself such as a hypothetical shoaling of the strait through sediment accumulation. This could be tested with future coring of the Bering Strait to ascertain its sedimentation rate history. Southern Ocean productivity proxies are currently of low resolution[15], and although they show consistently increased glacial water column stratification, thought critical for sequestration of glacial CO_2 (ref. [14]), they do not show a clear increase in stratification over the MPT[15] highlighting the potential importance of NPIW in increased oceanic sequestration of CO_2 during the MPT. Although a further enhancement of dust deposition across the Southern Ocean may have contributed to MIS 22–24 cooling and CO_2 decline (Fig. 2g), we note that dust deposition was actually decreasing into the MIS 22 glacial maximum (Fig. 3d) whilst nutrient upwelling on the Bering Slope remained inhibited and NPIW expanded, thus supporting changes in upwelling of the North Pacific as an important mechanism of CO_2 reduction compared with Southern Ocean dust fertilization.

The cause of MPT glacial lengthening is still unknown, but it may have emerged from the 'skipping' of insolation peaks[61–63] ultimately due to lower glacial CO_2 associated with oceanic processes described here. The lower global temperature may have been able to sustain larger ice volumes that could withstand melting and override these skipped insolation peaks. In this

Table 1 Average nutrient upwelling for glacial and interglacial phases

Proxy	'Midpoint'	Opal MAR-$\Delta\delta^{15}N$: warmer than midpoint	Opal MAR-$\Delta\delta^{15}N$: cooler than midpoint
Sea level[2]	-50 m	5.91	3.66
Global SST[70]	-3 °C	6.11	4.68
Deep ocean $\delta^{18}O$ (LR04)[30]	+4‰	6.54	4.38

Average extent of nutrient upwelling (opal MAR-$\Delta\delta^{15}N$) for different proxies, for both above and below their 1.5 Ma approximate glacial 'midpoint' values (for the dataset available, Fig. 2). For sea level[2], -50 m from modern is chosen as the current depth of the Bering Strait. For global sea surface temperature[70] (SST), -3 °C from modern is chosen as -6 °C was the last glacial maximum. For global benthic $\delta^{18}O$ (ref. 30), + 4‰ is the midpoint between the ~3–5‰ glacial-interglacial range. The lowest value of average nutrient upwelling (opal MAR-$\Delta\delta^{15}N$) is when sea level is below 50 m of present.

mid-late Pleistocene state, abrupt deglacials were likely triggered by a breakdown in Southern Ocean stratification and enhanced CO_2 ventilation[14], followed by reduced NPIW in the North Pacific and further enhanced CO_2 ventilation[18]. Our records cannot address the boundary condition changes at ~1.2 Ma that instigated global cooling, which could have been from changing ice sheet dynamics described in the 'regolith hypothesis'[4]. However, they do suggest that enhanced glacial drawdown of CO_2 occurred during the MPT and in particular from ~900 ka (MIS 22–23), due at least in part to NPIW expansion across the subarctic North Pacific and associated reduced upwelling. Further high-resolution continuous sea ice and upwelling records over the last 1.5 Ma, from both the subarctic North Pacific and the Southern Ocean, and numerical modelling studies with integrated shelf processes, are now needed to explore the full climatic impacts of a closed Bering Strait and development of the MPT.

Methods

Site U1343. Surface water in the Bering Sea enters from the North Pacific, primarily from the relatively warm Alaskan Stream (Supplementary Fig. 1a)[20]. Deep water that bathes Site U1343 is fed from NPDW, which enters and exits the Bering Sea through various passes in the Aleutian Island Arc (sill depths <4000 m). The clastic sediments from Site U1343 are predominantly fine clay and biogenic material[64]. There are no transported shelf-characteristic benthic foraminifera recorded[65], which is to be expected as Site U1343 is situated on a topographic high separated from the shelf (Supplementary Fig. 1b), and is at ~1954 m depth. There were no obvious current-formed sedimentary features recorded by shipboard sedimentologists. Bioturbation is recorded as centimetre scale mottling of ash layers and gradational lithological transitions, and no long bioturbation features (e.g., burrows) were recorded[65]. Therefore, our maximum sampling frequency of 8 cm (ave. ~250 yrs) was designed to override the major effects of bioturbation. We sampled between 219.87 and 281.74 m composite core depth (m CCSF-A). Site U1343 was double piston-cored to ~262 m CCSF, and the constructed splice leaves no apparent coring gaps in this section[65].

Foraminiferal isotopes. For $\delta^{18}O$ and $\delta^{13}C$ of benthic foraminifera (Supplementary Data 2), bulk samples were freeze-dried, weighed, processed through a 63 µm sieve with de-ionised water, and oven dried at <40 °C. Analysis was carried out on a range of benthic foraminiferal species (Supplementary Fig. 9), focusing on *Elphidium batialis* or *Uvigerina bifurcata* wherever abundant specimens were available. We measured ~830 benthic foraminiferal samples. For each sample, ~5 well-preserved shells were selected from the >150–250 µm fraction. Analyses were performed using a Finnigan MAT252 mass spectrometer with automated carbonate preparation device at Cardiff University stable isotope facility, and an Iso-Prime mass spectrometer with a Multicarb preparation system at the NERC Isotope Geosciences Laboratory at the British Geological Survey. Stable isotope results were calibrated to the VPDB scale by international standards. The analytical precision is better than ± 0.08‰ at Cardiff, and ± 0.05‰ at NIGL.

Bulk sediment geochemistry. We measured ~740 samples for total organic carbon (TOC) and isotopes of C_{org} ($\delta^{13}C_{org}$) (Supplementary Data 3). Around 500 mg sample was added to 5% HCl to remove calcite, rinsed in deionized water, dried at 40 °C, ground to a fine powder and homogenized. The samples were combusted using a Costech ECS4010 elemental analyser at approximately 1050 °C, and then analysed using a VG Optima dual inlet mass spectrometer at the NERC Isotope Geosciences Laboratory (British Geological Survey). $\delta^{13}C_{org}$ is expressed as per mil (‰) in conventional delta notation relative to the $^{13}C/^{12}C$ ratio calculated to the Vienna Pee Dee Belemnite (VPDB) scale, utilising within-run laboratory and international standards. Analytical reproducibility for the within-run standards was <0.1‰ for $\delta^{13}C$, and <0.7% for TOC.

For $\delta^{15}N$, ~215 bulk sediment samples (unacidified) were run on a Carlo Erba 1108 elemental analyzer, interfaced to a Thermo Finnigan Delta Plus XP IRMS at the University of California, Santa Cruz (Supplementary Data 4). $\delta^{15}N$ is expressed as per mil (‰) in conventional delta notation relative to atmospheric nitrogen. Precision for $\delta^{15}N$ is 0.2‰, based on replicates and in-house sediment standards.

Total organic carbon (TOC) mass accumulation rate (C_{org} MAR) was calculated as (dry bulk density) × (sedimentation rate) × (wt %TOC). Opal MAR was calculated as (dry bulk density) × (sedimentation rate) × (wt %opal). Measured dry bulk density was only carried out on U1343 Hole A, and the bottom part of Hole E (ref. [65]). We therefore estimated dry bulk density for the U1343 splice by converting the depths to composite m CCSF values, and modelling a 9-point loess smoothing spline for the entire record. We then estimated sample dry bulk density values to the nearest 10 m (by linear interpolation).

Age model. We constructed a composite benthic foraminiferal $\delta^{18}O$ record to provide a more precise age model for this interval than previously provided by $\delta^{18}O$ stratigraphy[33] (Supplementary Fig. 10). With just five age-depth tie points (triangles in Supplementary Fig. 2, Supplementary Table 1) based on major deglacials, we obtain a good match ($r^2 = 0.78$, Supplementary Fig. 11) between U1343 and the global composite stack[30] (LR04) when our record is smoothed, with a consistent offset of ~0.5‰. This correlation suggests no significant missing intervals, as is expected with high sedimentation rates at U1343. Although our age model is markedly more precise than previously reported for U1343, when comparing our records with other locations it should be noted that up to 10^3 yr offsets exist between $\delta^{18}O$ records in different ocean basins[33].

To estimate offsets between species and construct the composite benthic foraminiferal $\delta^{18}O$ record, we firstly removed all $\delta^{18}O$ data points where the values for $\delta^{13}C$ were below −5‰ (signifying potential diagenetic alteration), and removed all significantly high/low $\delta^{18}O$ data points if there was a replicate measurement for that sample. We then calculated offsets between all species compared with *Elphidium* (Supplementary Figs 9, 12, Supplementary Table 2). We defined the *Elphidium-Uvigerina* offset by combining all our paired *Elphidium/Uvigerina* data with previously published data from U1343[33]. This produced an *Elphidium-Uvigerina* offset of 0.87 ± 0.2‰. We applied this, as we found the offsets between *U. senticosa* and *U. bifurcata* were not outside of this range, and prefer to use the more robust offset calculated from the larger dataset. We note that our value is slightly larger than the offset provided by Asahi et al. (ref. [33]). We used the previously defined offsets for *Globobulimina pacifica* (0.85 ± 0.22‰) and *Nonionella labradorica* (0.65 ± 0.27‰) from U1343[33], as our data were collected on a much lower number of samples and produced similar offset values (0.86 and 0.62‰, respectively). To estimate offsets for the other species, we calculated a smoothing spline because we did not have paired measurements in enough samples. The offsets for the species *Islandiella norcrossi, Valvulineria aurucana, Lenticulina* spp. and *Cassidulina* spp. were estimated by subtracting their values from the smoothing spline value at that location (Supplementary Table 2).

Dinoflagellate cysts. Palynological samples were chemically treated following the procedure used at GEOTOP[66]. Briefly, 5 cc of wet sediment were sieved through 10 and 106 µm to discard coarse sand and silt, and fine clay. The fraction between 106 and 10 µm was then treated with warm HCL (10%) and HF (49%) several times to dissolve carbonate, silicate, and aluminosilicates. The residue was finally mounted between a slide and cover slide in glycerin gel. Organic-walled dinoflagellate cysts were counted using an optical microscope at magnification of ×400 to ×1000 . At least 300 dinoflagellate cysts were counted for each sample when possible, otherwise the entire slide was scanned and the average count is 214 cysts (Supplementary Data 1).

Data availability

All data generated during this study supporting its findings are available within the paper and the supplementary information.

Received: 18 February 2018 Accepted: 28 November 2018
Published online: 19 December 2018

References

1. McClymont, E. L., Sosdian, S. M., Rosell-Melé, A. & Rosenthal, Y. Pleistocene seasurface temperature evolution: early cooling, delayed glacial intensification, and implications for the mid-Pleistocene climate transition. *Earth Sci. Rev.* **123**, 173–193 (2013).
2. Elderfield, H. et al. Evolution of ocean temperature and ice volume through the Mid-Pleistocene climate transition. *Science* **337**, 704–709 (2012).
3. Rohling, E. J. et al. Sea-level and deep-sea-temperature variability over the past 5.3 million years. *Nature* **508**, 477–482 (2014).
4. Clark, P. U. et al. The middle Pleistocene transition: characteristics, mechanisms, and implications for long-term changes in atmospheric pCO_2. *Quat. Sci. Rev.* **25**, 3150–3184 (2006).
5. Martínez-Garcia, A. et al. Southern Ocean dust–climate coupling over the past four million years. *Nature* **476**, 312–315 (2011).
6. Chalk, T. B. et al. Causes of ice age intensification across the Mid-Pleistocene Transition. *Proc. Natl Acad. Sci. USA* **114**, 13114–13119 (2017).
7. Gildor, H. & Tziperman, E. A sea ice climate switch mechanism for the 100-kyr glacial cycles. *J. Geophys. Res.* **106**, 9117–9133 (2001).
8. Detlef, H. et al. Sea ice dynamics across the Mid-Pleistocene transition in the Bering Sea. *Nat. Commun.* **9**, 941 (2018).
9. Hönisch, B., Hemming, N. G., Archer, D., Siddall, M. & McManus, J. F. Atmospheric carbon dioxide concentration across the mid-Pleistocene transition. *Science* **324**, 1551–1554 (2009).
10. Raymo, M. E. The timing of major climate terminations. *Paleoceanography* **12**, 577–585 (1997).

11. Diester-Haass, L., Billups, K. & Lear, C. Productivity changes across the mid-Pleistocene climate transition. *Earth-Sci. Rev.* **179**, 372–391 (2018).
12. Pena, L. D. & Goldstein, S. L. Thermohaline circulation crisis and impacts during the mid-Pleistocene transition. *Science* **345**, 318–322 (2014). 6194.
13. Sigman, D. M., Hain, M. P. & Haug, G. H. The polar ocean and glacial cycles in atmospheric CO_2 concentration. *Nature* **466**, 47–55 (2010).
14. Basak, C. et al. Breakup of last glacial deep stratification in the South Pacific. *Science* **359**, 900–904 (2018).
15. Billups, K., York, K. & Bradtmiller, L. I. Water column stratification in the Antarctic Zone of the Southern Ocean during the Mid-Pleistocene climate transition. *Paleoceanogr. Paleoclimatology* **33**, 432–442 (2018).
16. Jaccard, S. L. et al. Glacial/interglacial changes in subarctic North Pacific stratification. *Science* **308**, 1003–1006 (2005).
17. Rae, J. W. B. et al. Deep water formation in the North Pacific and deglacial CO_2 rise. *Paleoceanography* **29**, 645–667 (2014).
18. Gray, W. R. et al. Deglacial upwelling, productivity and CO_2 outgassing in the North Pacific Ocean. *Nat. Geosci.* **11**, 340–344 (2018).
19. Springer, A. M., McRoy, P. C. & Flint, M. V. The Bering Sea Green Belt: shelf-edge processes and ecosystem production. *Fish. Oceanogr.* **5**, 205–223 (1996).
20. Stabeno, P. J., Schumacher, J. D. & Ohtani, K. in *Dynamics of the Bering Sea* (eds Loughlin, T.R. & Ohtani, K.) 1–28 (University of Alaska Sea Grant, Fairbanks, 1999).
21. Brunelle, B. G. et al. Evidence from diatom-bound nitrogen isotopes for subarctic Pacific stratification during the last ice age and a link to North Pacific denitrification changes. *Paleoceanography* **22**, PA1215 (2007).
22. Ishii, M. et al. Air-sea CO_2 flux in the Pacific Ocean for the period 1990–2009. *Biogeosciences* **11**, 709–734 (2014).
23. Luchin, V. A., Menovshchikov, V. A., Lavrentiev, V. M. & Reed, R. K. in *Dynamics of the Bering Sea* (eds Loughlin, T.R. & Ohtani, K.) 61–92 (University of Alaska Sea Grant, Fairbanks, 1999).
24. Jaccard, S. L., Galbraith, E. D., Sigman, D. M. & Haug, G. H. A pervasive link between Antarctic ice core and subarctic Pacific sediment records over the past 800 kyrs. *Quat. Sci. Rev.* **29**, 206–212 (2010).
25. Kim, S. et al. Biogenic opal production changes during the mid-Pleistocene transition in the Bering Sea (IODP expedition 323 site U1343). *Quat. Res* **81**, 151–157 (2014).
26. Horikawa, K., Asahara, Y., Yamamoto, K. & Okazaki, Y. Intermediate water formation in the Bering Sea during glacial periods: evidence from neodymium isotope ratios. *Geology* **38**, 435–438 (2010).
27. Knudson, K. P. & Ravelo, A. C. North Pacific Intermediate Water circulation enhanced by the closure of the Bering Strait. *Paleoceanography* **30**, 1287–1304 (2015).
28. Stroynowski, Z., Ravelo, A. C. & Andreasen, D. A Pliocene to recent history of the Bering Sea at Site U1340A, IODP Expedition 323. *Paleoceanography* **30**, 1641–1656 (2015).
29. Müller, J. et al. Cordilleran ice-sheet growth fueled primary productivity in the Gulf of Alaska, northeast Pacific Ocean. *Geology* **46**, 307–310 (2018).
30. Lisiecki, L. E. & Raymo, M. E. A Pliocene-Pleistocene stack of 57 globally distributed benthic $\delta^{18}O$ records. *Paleoceanography* **20**, PA1003 (2005).
31. Mix, A. C. et al. Benthic foraminifer stable isotope record from Site 849 (0–5Ma): Local and global climate changes. In *Proc. Ocean Drilling Program, Scientific Results 138* (eds Pisias, N.G. et al.) 371–412 (Ocean Drilling Program, College Station, Texas, 1995).
32. Hall, I. R., McCave, I. N., Shackleton, N. J., Weedon, G. P. & Harris, S. E. Intensified deep Pacific inflow and ventilation in Pleistocene glacial times. *Nature* **412**, 809–812 (2001).
33. Asahi, H. et al. Orbital-scale benthic foraminiferal oxygen isotope stratigraphy at the northern Bering Sea Slope Site U1343 (IODP Expedition 323) and its Pleisocene paleoceanographic significance. *Deep-Sea Res. II* **125-126**, 66–83 (2016).
34. de Vernal, A. et al. Dinoflagellate cyst assemblages as tracers of sea-surface conditions in the northern North Atlantic, Arctic and sub-arctic seas: the new "n = 677" database and application for quantitative paleoceanographical reconstruction. *J. Quat. Sci.* **16**, 681–699 (2001).
35. Hamel, D. de Vernal, A., Gosselin, M. & Hillaire-Marcel, C. Organic-walled microfossils and geochemical tracers: sedimentary indicators of productivity changes in the North Water and northern Baffin Bay (High Arctic) during the last centuries. *Deep-Sea Res. II* **49**, 5277–5295 (2002).
36. Cook, M. S. et al. Tracing subarctic Pacific water masses with benthic foraminiferal stable isotopes during the LGM and late Pleistocene. *Deep-Sea Res. II* **125–126**, 84–95 (2016).
37. Takahashi, K., Fujitani, N. & Yanada, M. Long term monitoring of particle fluxes in the Bering Sea and the central subarctic Pacific Ocean, 1990–2000. *Prog. Oceanogr.* **55**, 95–112 (2002).
38. Wehrmann, L. M., Arndt, S., März, C., Ferdelman, T. G. & Brunner, B. The evolution of early diagenetic signals in Bering Sea subseafloor sediments in response to varying organic carbon deposition over the last 4.3 Ma. *Geochim. Cosmochim. Acta* **109**, 175–196 (2013).
39. Kim, S., Khim, B.-K., Ikehara, M. & Takahashi, K. Relationship between $\delta^{15}N$ values of bulk sediments and total organic carbon concentration in response to orbital-scale biogenic opal production in the Bering slope area over the last 600 kyrs. *Quat. Int.* **459**, 144–152 (2017).
40. Schubert, C. J. & Calvert, S. E. Nitrogen and carbon isotopic composition of marine and terrestrial organic matter in Arctic Ocean sediments: implications for nutrient utilization and organic matter composition. *Deep-Sea. Res. I* **48**, 789–810 (2001).
41. Altabet, M. A. & Francois, R. Sedimentary nitrogen isotopic ratio as a recorder for surface ocean nitrate utilization. *Glob. Biogeochem. Cycles* **8**, 103–116 (1994).
42. Sigman, D. M., DiFiore, P. J., Hain, M. P., Deutsch, C. & Karl, D. M. Sinking organic matter spreads the nitrogen isotope signal of pelagic denitrification in the North Pacific. *Geophys. Res. Lett.* **36**, L08605 (2009).
43. Robinson, R. S., Etourneau, J., Martinez, P. M. & Schneider, R. Expansion of pelagic denitrification during early Pleistocene cooling. *Earth. Planet. Sci. Lett.* **389**, 52–61 (2014).
44. McClelland, J. W. et al. River export of nutrients and organic matter from the North Slope of Alaska to the Beaufort Sea. *Water Resour. Res.* **50**, 1823–1839 (2014).
45. Guo, L. & Macdonald, R. W. Source and transport of terrigenous organic matter in the upper Yukon River: Evidence from isotope ($\delta^{13}C$, $\delta^{14}C$, and $\delta^{15}N$) composition of dissolved, colloidal, and particulate phases. *Glob. Biogeochem. Cycles* **20**, GB2011 (2006).
46. Altabet, M. A. et al. The nitrogen isotope biogeochemistry of sinking particles from the margin of the Eastern North Pacific. *Deep-Sea Res. I* **46**, 655–679 (1999).
47. Knudson, K. P. & Ravelo, A. C. Enhanced subarctic Pacific stratification and nutrient utilization during glacials over the last 1.2 Myr. *Geophys. Res. Lett.* **42**, 9870–9879 (2015).
48. Liu, Z., Altabet, M. A. & Herbert, T. D. Plio-Pleistocene denitrification in the eastern tropical North Pacific: Intensification at 2.1 Ma. *Geochem. Geophys. Geosystems* **9**, 11 (2008).
49. Galbraith, E. D. et al. Consistent relationship between global climate and surface nitrate utilization in the western subarctic Pacific throughout the last 500 ka. *Paleoceanography* **23**, PA2212 (2008).
50. Whitney, F. A., Bograd, S. J. & Ono, T. Nutrient enrichment of the subarctic Pacific Ocean pycnocline. *Geophys. Res. Lett.* **40**, 2200–2205 (2013).
51. Matsumoto, K., Oba, T., Lynch-Stieglitz, J. & Yamamoto, H. Interior hydrography and circulation of the glacial Pacific Ocean. *Quat. Sci. Rev.* **21**, 1693–1704 (2002).
52. Jang, K., Huh, Y. & Han, Y. Authigenic Nd isotope record of North Pacific Intermediate water formation and boundary exchange on the Bering Slope. *Quat. Sci. Rev.* **156**, 150–163 (2017).
53. Drake, D. E., Totman, C. E. & Wiberg, P. L. Sediment transport during the winter on the Yukon prodelta, Norton Sound, Alaska. *J. Sediment. Res.* **49**, 1171–1180 (1979).
54. Cavalleri, D. J. & Martin, S. The contribution of Alaskan, Siberian, and Canadian coastal polynyas to the cold halocline layer of the Arctic Ocean. *J. Geophys. Res.* **99**, 18343–18362 (1994).
55. Hu, A. X. et al. Influence of Bering Strait flow and North Atlantic circulation on glacial sea-level changes. *Nat. Geosci.* **3**, 118–121 (2010).
56. Dumitru, T. A. et al. Cretaceous to recent extension the Bering Strait region, Alaska. *Tectonics* **14**, 549–563 (1995).
57. Marincovich, L. Jr. & Gladenkov, A. Y. An early opening of the Bering Strait. *Nature* **397**, 149–151 (1999).
58. Marincovich, L. Jr. Central American paleogeography controlled Pliocene Arctic Ocean molluscan migrations. *Geology* **28**, 551–554 (2000).
59. Horikawa, K. et al. Pliocene cooling enhanced by flow of low-salinity Bering Sea water to the Arctic Ocean. *Nat. Commun.* **6**, 7587 (2015).
60. Okazaki, Y. et al. Deepwater formation in the North Pacific during the Last Glacial termination. *Science* **329**, 200–204 (2010).
61. Tzedakis, P. C., Crucifix, M., Mitsui, T. & Wolff, E. W. A simple rule to determine which insolation cycles lead to interglacials. *Nature* **542**, 427–432 (2017).
62. Ganopolski, A. & Calov, R. The role of orbital forcing, carbon dioxide and regolith in 100 kyr glacial cycles. *Clim. Past.* **7**, 1415–1425 (2011).
63. Abe-Ouchi, A. et al. Insolation-driven 100,000-year glacial cycles and hysteresis of ice-sheet volume. *Nature* **500**, 190–193 (2013).
64. Aiello, I. W. & Ravelo, A. C. Evolution of marine sedimentation in the Bering Sea since the Pliocene. *Geosphere* **8**, 1231–1253 (2012).
65. Expedition 323 Scientists. Site U1343. In *Proc. Integrated Ocean Drilling Program, 323* (eds Takahashi, K. et al.) (Tokyo, IODP Management International, Inc., 2011).
66. de Vernal, A., Hillaire-Marcel, C. & Bilodeau, G. . Reduced meltwater outflow from the Laurentide ice margin during the Younger Dryas. *Nature* **381**, 774–777 (1996).

67. Garcia, H. E. et al. World Ocean Atlas 2013, Volume 4: Dissolved Inorganic Nutrients (phosphate, nitrate, silicate). *NOAA Atlas NESDIS76* (eds Levitus, S. & Mishonov, A.) 25 (NOAA National Centers for Environmental Information, Silver Spring, 2014).
68. Kim, S., Khim, B. K. & Takahashi, K. Late Pliocene to early Pleistocene (2.4–1.25 Ma) paleoproductivity changes in the Bering sea: IODP Expedition 323 Hole U1343E. *Deep-Sea Res. II* **125-126**, 155–162 (2016).
69. Stroynowski, Z., Abrantes, F. & Bruno, E. The response of the Bering Sea Gateway during the Mid-Pleistocene Transition. *Palaeogeogr. Palaeoclim. Palaeoecol.* **485**, 974–985 (2017).
70. Snyder, C. W. Evolution of global temperature over the past two million years. *Nature* **538**, 226–228 (2016).

Acknowledgements

We thank Taoufik Radi (Université du Québec à Montréal) for generating dinoflagellate cyst data, the International Ocean Discovery Program for providing samples, and the Expedition 323 captain, staff and technical crew of the JOIDES *Resolution*. This research was funded by Natural Environment Research Council (NERC) Isotope Geosciences Facilities Steering Committee grants IP/1141/1109, IP/1413/1113 and IP-1620-0516 (to S. K.), and research project NRF-2015M1A5A1037243 from the National Research Foundation of Korea funded by the Ministry of Science and ICT (to H.A.; PI S.I. Nam of the Korea Polar Research Institute).

Author contributions

S.K devised the study, M.J.L, J.B., I.R.H. and S.K. generated the foraminiferal isotope data, A.C.R, M.J.L. and D.A. generated the bulk sediment isotope data. All authors contributed to the ideas and writing of the manuscript.

Additional information

Supplementary Information accompanies this paper at https://doi.org/10.1038/s41467-018-07828-0.

Competing interests: The authors declare no competing interests.

Reprints and permission information is available online at http://npg.nature.com/reprintsandpermissions/

Journal peer review information: *Nature Communications* thanks the anonymous reviewers for their contribution to the peer review of this work.

Publisher's note: Springer Nature remains neutral with regard to jurisdictional claims in published maps and institutional affiliations.

Open Access This article is licensed under a Creative Commons Attribution 4.0 International License, which permits use, sharing, adaptation, distribution and reproduction in any medium or format, as long as you give appropriate credit to the original author(s) and the source, provide a link to the Creative Commons license, and indicate if changes were made. The images or other third party material in this article are included in the article's Creative Commons license, unless indicated otherwise in a credit line to the material. If material is not included in the article's Creative Commons license and your intended use is not permitted by statutory regulation or exceeds the permitted use, you will need to obtain permission directly from the copyright holder. To view a copy of this license, visit http://creativecommons.org/licenses/by/4.0/.

© The Author(s) 2018

8.2 Data tables

Table 8.1 New benthic foraminiferal $\delta^{18}O$ data presented in Chapters 2 and 3.

Sample ID	Depth (m CCSF-A)	Age (kyr)	Species	$\delta^{13}C$ ‰	$\delta^{18}O$ ‰	$\delta^{18}O$ ‰ (tuned to *E. batialis*)
U1343C-1H-2 W, 79.5--81.5 cm	2.31	14.93	*G. auriculata*	-1.70	4.67	3.82
U1343C-1H-3 W, 89.0--91.0 cm	3.90	20.61	*C. teretis*	-0.36	5.44	4.88
U1343C-1H-3 W, 89.0--91.0 cm	3.90	20.61	*G. auriculata*	-0.93	5.86	5.01
U1343C-1H-4 W, 22.0--24.0 cm	4.73	23.56	*G. auriculata*	-1.65	4.41	3.56
U1343C-1H-4 W, 90.0--92.0 cm	5.41	25.98	*G. auriculata*	-0.93	5.11	4.26
U1343C-1H-5 W, 10.0--12.0 cm	6.11	28.47	*U. senticosa*	-0.64	5.04	4.17
U1343E-1H-3 W, 59.0--61.0 cm	7.08	31.93	*U. senticosa*	-0.49	4.89	4.02
U1343E-1H-4 W, 88.0--90.0 cm	8.87	38.30	*E. batialis*	-2.21	3.79	3.79
U1343E-1H-5 W, 38.5--40.5 cm	9.87	41.88	*E. batialis*	-2.54	3.70	3.70
U1343C-2H-3 W, 77.0--79.0 cm	10.94	45.65	*G. auriculata*	-1.09	4.52	3.67
U1343C-2H-5 W, 36.0--38.0 cm	13.53	54.87	*U. bifurcata*	-1.80	4.34	3.47
U1343E-2H-4 W, 90.0--92.0 cm	17.33	67.60	*I. norcrossi*	-1.39	4.55	4.07
U1343E-2H-4 W, 90.0--92.0 cm	17.33	67.60	*G. aurciulata*	-1.99	4.83	3.98
U1343E-2H-5 W, 98.0--100.0 cm	18.91	72.80	*Valvulineria sp.*	-3.60	4.14	3.89
U1343A-3H-4 W, 109.0--111.0 cm	20.44	77.82	*G. aurciulata*	-1.29	4.32	3.47
U1343A-3H-5 W, 72.0--74.0 cm	21.57	81.54	*E. batialis*	-2.30	3.51	3.51
U1343E-3H-2 W, 120.0--122.0 cm	24.23	90.29	*G. auriculata*	-1.21	4.66	3.81
U1343A-4H-6 W, 31.0--33.0 cm	32.78	118.44	*E. batialis*	-1.90	3.63	3.63
U1343E-4H-1 W, 129.0--131.0 cm	33.74	121.60	*E. batialis*	-2.20	3.31	3.31
U1343E-4H-3 W, 71.0--73.0 cm	36.16	129.57	*U. senticosa*	-2.51	3.60	2.73
U1343E-4H-3 W, 71.0--73.0 cm	36.16	129.57	*U. bifurcata*	-3.26	3.82	2.95
U1343E-4H-3 W, 132.0--134.0 cm	36.77	131.63	*U. bifurcata*	-1.20	4.36	3.49

U1343E-4H-4 W, 26.0--28.0 cm	37.21	133.58	*U. senticosa*	-0.84	4.74	3.87
U1343E-4H-4 W, 26.0--28.0 cm	37.21	133.58	*G. auriculata*	-0.85	4.82	3.97
U1343E-4H-4 W, 26.0--28.0 cm (2)	37.21	133.58	*G. auriculata*	-0.88	4.84	3.99
U1343E-4H-4 W, 76.0--78.0 cm	37.71	135.79	*U. senticosa*	-0.74	4.95	4.08
U1343E-4H-4 W, 76.0--78.0 cm	37.71	135.79	*U. bifurcata*	-1.42	5.01	4.14
U1343E-4H-4 W, 109.0--111.0 cm	38.04	137.25	*U. bifurcata*	-1.44	5.01	4.14
U1343E-4H-5 W, 10.0--12.0 cm	38.55	139.51	*U. senticosa*	-0.79	4.93	4.06
U1343E-4H-5 W, 52.0--54.0 cm	38.97	141.36	*U. senticosa*	-0.66	5.09	4.22
U1343E-4H-5 W, 102.0--104.0 cm	39.47	143.58	*U. senticosa*	-0.72	4.96	4.09
U1343C-5H-3 W, 52.0--54.0 cm	40.94	150.10	*U. senticosa*	-0.76	4.80	3.93
U1343C-5H-4 W, 66.0--68.0 cm	42.58	157.35	*U. senticosa*	-2.96	5.11	4.24
U1343C-5H-4 W, 129.0--131.0 cm	43.21	160.14	*U. senticosa*	-0.79	4.73	3.86
U1343C-5H-5 W, 76.0--78.0 cm	44.12	164.17	*U. senticosa*	-0.73	4.68	3.81
U1343E-5H-3 W, 8.0--10.0 cm	45.16	168.79	*U. senticosa*	-0.79	4.63	3.76
U1343E-5H-3 W, 109.0--111.0 cm	46.17	173.26	*U. senticosa*	-0.85	4.56	3.69
U1343A-6H-1 W, 99.0--101.0 cm	47.76	180.26	*U. senticosa*	-0.87	4.63	3.76
U1343A-6H-2 W, 137.5--139.5 cm	49.35	185.71	*G. auriculata*	-4.09	4.92	4.07
U1343E-6H-3 W, 130.0--132.0 cm	58.93	216.48	*E. batialis*	-1.96	3.10	3.10
U1343E-6H-4 W, 109.0--111.0 cm	60.22	220.34	*G. auriculata*	-1.43	4.55	3.70
U1343E-6H-5 W, 76.0--78.0 cm	61.22	222.96	*U. senticosa*	-0.78	4.69	3.82
U1343A-8H-4 W, 76.0--78.0 cm	72.35	255.15	*U. senticosa*	-1.11	4.60	3.73
U1343A-8H-5 W, 10.0--12.0 cm	73.19	258.06	*E. batialis*	-2.95	3.74	3.74
U1343A-8H-5 W, 96.0--98.0 cm	74.05	261.04	*G. auriculata*	-1.46	4.75	3.90
U1343A-8H-6 W, 36.0--38.0 cm	74.90	263.98	*U. senticosa*	-1.15	4.73	3.86
U1343E-8H-1 W, 46.0--48.0 cm	75.54	266.19	*U. senticosa*	-1.06	4.76	3.89
U1343E-8H-5 W, 8.0--10.0 cm	80.09	281.85	*U. senticosa*	-0.54	4.31	3.44

U1343E-8H-6 W, 31.0--33.0 cm	81.82	287.56	*U. bifurcata*	-1.34	4.11	3.24
U1343A-9H-3 W, 119.0--121.0 cm	82.48	289.73	*G. auriculata*	-1.78	4.16	3.31
U1343A-9H-4 W, 40.0--42.0 cm	83.19	292.07	*U. senticosa*	-0.91	4.27	3.40
U1343A-9H-4 W, 108.0--110.0 cm	83.87	294.31	*G. auriculata*	-1.61	4.49	3.64
U1343A-9H-5 W, 66.0--68.0 cm	84.90	297.71	*U. senticosa*	-1.15	4.02	3.15
U1343C-10H-2 W, 38.0--40.0 cm	85.54	299.81	*G. auriculata*	-1.52	4.51	3.66
U1343C-10H-2 W, 107.0--109.0 cm	86.23	302.08	*G. pacifica*	-1.73	4.66	3.81
U1343C-10H-3 W, 96.0--98.0 cm	87.62	306.67	*E. batialis*	-3.15	3.44	3.44
U1343C-10H-4 W, 19.0--21.0 cm	88.35	309.08	*U. senticosa*	-2.50	4.17	3.30
U1343A-10H-5 W, 140.0--142.0 cm	96.25	335.14	*E. batialis*	-2.79	3.36	3.36
U1343A-10H-6 W, 68.5--70.5 cm	97.03	337.76	*U. senticosa*	-1.05	4.94	4.07
U1343C-11H-2 W, 112.0--114.0 cm	97.56	339.53	*E. batialis*	-3.58	3.91	3.91
U1343C-11H-2 W, 112.0--114.0 cm	97.56	339.53	*U. senticosa*	-1.04	4.90	4.03
U1343C-11H-3 W, 30.0--32.0 cm	98.24	341.79	*U. senticosa*	-1.02	4.87	4.00
U1343C-11H-4 W, 88.0--90.0 cm	100.32	348.72	*U. senticosa*	-1.85	4.72	3.85
U1343C-11H-5 W, 8.0--10.0 cm	101.02	351.05	*U. senticosa*	-1.03	4.68	3.81
U1343C-11H-5 W, 96.5--98.5 cm	101.91	354.00	*U. senticosa*	-1.05	4.88	4.01
U1343C-11H-6 W, 36.5--38.5 cm	102.81	357.00	*U. senticosa*	-1.88	4.76	3.89
U1343C-11H-7 W, 30.0--32.0 cm	104.24	361.78	*U. senticosa*	-1.12	4.54	3.67
U1343A-11H-5 W, 80.0--82.0 cm	105.80	366.96	*U. senticosa*	-2.94	4.47	3.60
U1343A-11H-6 W, 69.5--71.5 cm	107.11	371.34	*G. auriculata*	-1.88	4.33	3.48
U1343C-12H-2 W, 28.0--30.0 cm	108.03	374.40	*U. senticosa*	-0.69	4.45	3.58
U1343A-12H-3 W, 80.0--82.0 cm	113.82	393.67	*Nonionella*	-9.27	4.39	3.74
U1343A-12H-5 W, 79.0--81.0 cm	116.81	409.38	*E. batialis*	-3.06	2.85	2.85
U1343A-12H-6 W, 20.0--23.0 cm	117.72	414.78	*G. auriculata*	-1.30	3.91	3.06
U1343A-12H-6 W, 54.0--56.0 cm	118.06	416.75	*G. auriculata*	-1.39	3.82	2.97

U1343A-12H-6 W, 88.0--90.0 cm	118.40	418.76	*G. auriculata*	-1.94	3.72	2.87
U1343A-12H-6 W, 108.5--110.5 cm	118.60	419.97	*G. auriculata*	-1.85	4.27	3.42
U1343C-13H-2 W, 119.0--121.0 cm	119.15	423.19	*G. auriculata*	-1.30	4.35	3.50
U1343C-13H-5 W, 8.0--10.0 cm	122.46	441.04	*U. bifurcata*	-2.67	4.86	3.99
U1343C-13H-5 W, 63.0--65.0 cm	123.01	443.99	*E. batialis*	-4.32	3.43	3.43
U1343C-13H-5 W, 107.0--109.0 cm	123.45	446.35	*U. bifurcata*	-1.54	4.85	3.98
U1343A-13H-3 W, 87.5--89.5 cm	125.11	455.27	*G. auriculata*	-2.26	4.73	3.88
U1343A-13H-4 W, 30.0--32.0 cm	126.04	460.23	*C. parkerianus*	-1.59	4.38	4.38
U1343A-13H-5 W, 102.0--104.0 cm	128.26	472.13	*G. auriculata*	-6.66	4.98	4.13
U1343A-14H-4 W, 30.0--32.0 cm	137.41	496.75	*E. batialis*	-1.64	3.08	3.08
U1343A-14H-4 W, 145.0--147.0 cm	138.56	499.18	*N. labradorica*	-0.69	4.09	3.44
U1343A-14H-5 W, 109.0--111.0 cm	139.70	501.58	*G. auriculata*	-1.05	4.14	3.29
U1343A-14H-6 W, 80.0--82.0 cm	140.83	503.96	*G. auriculata*	-1.02	4.03	3.18
U1343C-15H-4 W, 53.0--55.0 cm	144.00	510.64	*E. batialis*	-1.86	3.56	3.56
U1343C-15H-5 W, 6.0--8.0 cm	144.93	512.60	*E. batialis*	-1.66	3.82	3.82
U1343C-15H-5 W, 88.0--90.0 cm	145.75	516.20	*E. batialis*	-1.66	3.54	3.54
U1343C-15H-6 W, 23.0--25.0 cm	146.60	520.15	*E. batialis*	-2.20	3.27	3.27
U1343C-15H-6 W, 88.0--90.0 cm	147.25	523.17	*U. senticosa*	-0.95	4.07	3.20
U1343C-15H-7 W, 31.0--33.0 cm	147.96	526.48	*E. batialis*	-1.92	3.53	3.53
U1343A-15H-5 W, 36.0--38.0 cm	148.71	529.94	*E. batialis*	-4.14	3.83	3.83
U1343A-15H-5 W, 36.0--38.0 cm	148.71	529.94	*G. pacifica*	-1.81	4.12	3.27
U1343A-15H-5 W, 36.0--38.0 cm	148.71	529.94	*G. pacifica*	-1.32	4.57	3.72
U1343A-15H-6, 0.0 cm	149.85	535.24	*G. auriculata*	-1.69	4.47	3.62
U1343A-15H-6, 30.0 cm	150.15	536.64	*G. pacifica*	-1.29	4.40	3.55
U1343A-15H-6, 62.0 cm	150.47	538.12	*E. batialis*	-2.56	3.99	3.99
U1343A-15H-6, 62.0 cm	150.47	538.12	*U. senticosa*	-0.86	4.81	3.94

U1343A-15H-6, 102.0 cm	150.87	539.99	*G. auriculata*	-1.32	4.80	3.95
U1343A-15H-6, 112.0 cm	150.97	540.45	*U. senticosa*	-0.92	4.79	3.92
U1343A-15H-7, 30.0 cm	151.58	543.29	*G. pacifica*	-1.18	4.79	3.94
U1343A-15H-7, 68.0 cm	151.96	545.06	*E. batialis*	-2.99	4.27	4.27
U1343A-15H-7, 68.0 cm	151.96	545.06	*G. Pacifica*	-1.11	4.87	4.02
U1343E-17H-3, 68.0 cm	152.05	545.45	*E. batialis*	-2.84	3.87	3.87
U1343E-17H-4, 46.0 cm	153.33	550.13	*E. batialis*	-2.35	3.78	3.78
U1343E-17H-4, 68.0 cm	153.55	550.93	*U. senticosa*	-0.95	4.66	3.79
U1343E-17H-5, 30.0 cm	154.67	555.03	*Valvulineria sp.*	-1.08	4.12	3.87
U1343E-17H-5, 102.0 cm	155.39	557.66	*G. Pacifica*	-1.25	4.43	3.58
U1343A-16H-2, 68.0 cm	156.23	560.75	*E. batialis*	-2.94	3.75	3.75
U1343A-16H-3, 52.0 cm	157.57	565.65	*E. batialis*	-2.07	3.53	3.53
U1343A-16H-3, 109.0 cm	158.14	567.73	*Valvulineria sp.*	-1.13	3.52	3.27
U1343A-16H-4, 118.0 cm	159.73	573.55	*E. batialis*	-1.65	3.57	3.57
U1343A-16H-6, 37.0 cm	161.69	580.70	*E. batialis*	-1.82	3.23	3.23
U1343A-16H-6, 68.0 cm	162.00	581.78	*E. batialis*	-2.99	3.44	3.44
U1343A-16H-6, 102.0 cm	162.34	582.96	*E. batialis*	-4.60	4.03	4.03
U1343E-18H-4, 46.0 cm	163.22	586.02	*E. batialis*	-2.45	3.70	3.70
U1343E-18H-5, 87.0 cm	164.92	591.93	*U. birfurcata*	-1.19	4.22	3.35
U1343E-18H-6, 16.0 cm	165.83	595.08	*C. parkeraniu s*	-1.26	4.01	4.01
U1343E-18H-6, 68.0 cm	166.21	596.42	*E. batialis*	-4.14	3.59	3.59
U1343A-17H-2, 52.0 cm	167.39	600.52	*U. senticosa*	-0.60	4.34	3.47
U1343E-18H-8, 26.0 cm	168.09	602.96	*E. batialis*	-2.02	3.61	3.61
U1343A-17H-2, 134.0 cm	168.21	603.36	*E. batialis*	-3.07	3.67	3.67
U1343A-17H-3, 23.0 cm	168.50	604.37	*E. batialis*	-1.90	3.59	3.59
U1343A-17H-3, 52.0 cm	168.79	605.38	*E. batialis*	-1.74	3.63	3.63

U1343A-17H-3, 77.0 cm	169.04	606.25	*U. bifurcata*	-1.30	4.34	3.47
U1343A-17H-3, 102.0 cm	169.29	607.12	*E. batialis*	-2.66	3.53	3.53
U1343A-17H-3, 126.0 cm	169.53	607.96	*E. batialis*	-1.79	3.63	3.63
U1343A-17H-4, 16.0 cm	169.84	609.03	*E. batialis*	-3.34	3.51	3.51
U1343A-17H-4, 37.0 cm	170.05	609.76	*E. batialis*	-2.56	3.15	3.15
U1343A-17H-4, 86.0 cm	170.54	611.47	*E. batialis*	-2.28	3.41	3.41
U1343A-17H-4, 118.0 cm	170.86	612.58	*G. auriculata*	-0.74	4.18	3.33
U1343A-17H-4, 134.0 cm	171.02	613.14	*G. auriculata*	-0.91	4.33	3.48
U1343A-17H-5, 23.0 cm	171.41	614.49	*E. batialis*	-1.92	3.21	3.21
U1343A-17H-5, 37.0 cm	171.55	614.98	*E. batialis*	-6.89	3.54	3.54
U1343A-17H-5, 52.0 cm	171.70	615.50	*G. auriculata*	-0.93	3.93	3.08
U1343A-17H-5, 68.0 cm	171.86	616.06	*E. batialis*	-2.52	2.99	2.99
U1343A-17H-5, 86.0 cm	172.04	616.68	*E. batialis*	-6.08	3.38	3.38
U1343A-17H-5, 126.0 cm	172.44	618.07	*U. bifurcata*	-1.11	4.11	3.24
U1343C-18H-2, 54.0 cm	172.92	619.76	*G. auriculata*	-1.75	4.54	3.69
U1343A-17H-6, 45.0 cm	173.13	620.47	*U. bifurcata*	-1.59	4.38	3.51
U1343A-17H-6, 45.0 cm	173.13	620.47	*G. auriculata*	-1.82	4.58	3.73
U1343A-17H-6, 62.0 cm	173.30	621.06	*U. bifurcata*	-1.58	4.41	3.54
U1343A-17H-6, 77.0 cm	173.45	622.35	*G. pacifica*	-1.75	4.90	4.05
U1343C-18H-2, 126.0 cm	173.64	625.60	*G. auriculata*	-1.08	5.29	4.44
U1343C-18H-2, 142.0 cm	173.80	628.27	*U. birfurcata*	-1.38	5.31	4.44
U1343A-17H-6, 122.0 cm	173.90	629.84	*U. birfurcata*	-1.83	5.18	4.31
U1343C-18H-3, 8.0 cm	173.96	630.94	*G. auriculata*	-1.14	5.53	4.68
U1343C-18H-3, 46.0 cm	174.34	637.28	*E. batialis*	-2.35	4.44	4.44
U1343C-18H-3, 62.0 cm	174.50	639.95	*U. birfurcata*	-1.66	4.96	4.09
U1343C-18H-3, 109.0 cm	174.97	643.54	*E. batialis*	-3.03	4.02	4.02

U1343C-18H-4, 16.0 cm	175.54	647.07	*E. batialis*	-2.63	4.00	4.00
U1343C-18H-4, 37.0 cm	175.75	648.37	*E. batialis*	-3.14	3.83	3.83
U1343C-18H-4, 37.0 cm	175.75	648.37	*G. auriculata*	-1.69	4.76	3.91
U1343C-18H-4, 62.0 cm	176.00	649.92	*G. pacifica*	-1.60	4.61	3.76
U1343C-18H-4, 89.0 cm	176.27	651.59	*U. bifurcata*	-1.85	4.71	3.84
U1343C-18H-4, 118.0 cm	176.56	653.39	*G. auriculata*	-1.15	4.76	3.91
U1343C-18H-5, 68.0 cm	177.56	659.59	*E. batialis*	-2.93	3.46	3.46
U1343C-18H-5, 118.0 cm	178.06	662.68	*E. batialis*	-2.98	3.40	3.40
U1343C-18H-6, 0.0 cm	178.38	664.67	*G. Pacifica*	-1.64	4.72	3.87
U1343A-18H-3, 37.0 cm	178.94	668.14	*G. Pacifica*	-4.10	4.93	4.08
U1343A-18H-3, 37.0 cm	178.94	668.14	*E. batialis*	-5.75	5.02	5.02
U1343C-18H-6, 118.0 cm	179.56	671.98	*G. auriculata*	-1.40	4.56	3.71
U1343A-18H-4, 16.0 cm	180.03	674.89	*E. batialis*	-2.85	3.73	3.73
U1343A-18H-4, 45.0 cm	180.32	676.69	*E. batialis*	-2.71	3.74	3.74
U1343A-18H-4, 77.0 cm	180.64	678.67	*E. batialis*	-3.12	3.59	3.59
U1343A-18H-4, 102.0 cm	180.89	680.22	*E. batialis*	-3.05	3.04	3.04
U1343A-18H-5, 68.0 cm	182.05	687.41	*E. batialis*	-4.67	3.96	3.96
U1343E-20H-2, 52.0 cm	182.63	690.94	*E. batialis*	-9.93	4.16	4.16
U1343E-20H-4, 16.0 cm	184.94	705.24	*G. auriculata*	-1.19	4.50	3.65
U1343E-20H-4, 46.0 cm	185.24	707.09	*G. auriculata*	-1.78	4.47	3.62
U1343E-20H-4, 109.0 cm	185.87	711.02	*E. batialis*	-2.84	3.71	3.71
U1343E-20H-5, 0.0 cm	186.28	713.52	*E. batialis*	-7.56	4.08	4.08
U1343E-20H-5, 0.0 cm	186.28	713.52	*C. teretis*	-3.69	4.56	4.00
U1343E-20H-5, 23.0 cm	186.51	714.95	*E. batialis*	-4.86	3.96	3.96
U1343E-20H-5, 77.0 cm	187.05	718.28	*E. batialis*	-4.71	3.69	3.69
U1343E-20H-5, 102.0 cm	187.30	719.83	*E. batialis*	-6.49	4.21	4.21

U1343E-20H-6, 0.0 cm	187.78	722.80	*E. batialis*	-3.09	3.71	3.71
U1343C-19H-4, 0.0 cm	188.06	724.54	*E. batialis*	-2.61	3.77	3.77
U1343C-19H-4, 52.0 cm	188.58	728.44	*E. batialis*	-2.58	3.56	3.56
U1343C-19H-4, 77.0 cm	188.83	730.53	*E. batialis*	-2.18	3.68	3.68
U1343C-19H-4, 102.0 cm	189.08	732.63	*E. batialis*	-1.79	3.83	3.83
U1343C-19H-4, 126.0 cm	189.32	734.64	*G. auriculata*	-1.27	4.66	3.81
U1343C-19H-5, 8.0 cm	189.64	737.32	*G. auriculata*	-1.05	4.50	3.65
U1343C-19H-5, 30.0 cm	189.86	739.17	*E. batialis*	-3.01	3.53	3.53
U1343C-19H-5, 52.0 cm	190.08	741.01	*E. batialis*	-2.72	3.66	3.66
U1343C-19H-5, 86.0 cm	190.42	743.86	*E. batialis*	-3.36	3.66	3.66
U1343C-19H-5, 86.0 cm	190.42	743.86	*E. batialis*	-3.45	3.73	3.73
U1343C-19H-5, 86.0 cm	190.42	743.86	*G. auriculata*	-2.00	4.49	3.64
U1343C-19H-5, 86.0 cm	190.42	743.86	*G. auriculata*	-1.88	4.63	3.78
U1343E-21H-2, 30.0 cm	191.54	753.24	*C. teretis*	-0.83	4.63	4.07
U1343E-21H-2, 109.0 cm	192.29	755.82	*E. batialis*	-7.94	4.90	4.90
U1343E-21H-3, 45.0 cm	193.19	758.60	*E. batialis*	-3.95	3.72	3.72
U1343E-21H-3, 78.0 cm	193.52	759.62	*C. teretis*	-0.54	4.38	3.82
U1343E-21H-3, 109.0 cm	193.83	760.58	*C. parkeraniu s*	-1.49	4.38	4.38
U1343C-20H-3, 52.0 cm	196.51	768.89	*E. batialis*	-2.19	3.52	3.52
U1343C-20H-3, 126.0 cm	197.25	771.18	*E. batialis*	-2.45	3.35	3.35
U1343C-20H-4, 66.0 cm	198.05	773.66	*Valvulineri a sp.*	-1.09	3.79	3.54
U1343C-20H-4, 109.0 cm	198.48	774.99	*G. auriculata*	-1.52	4.23	3.38
U1343C-20H-5, 8.0 cm	198.97	776.51	*E. batialis*	-2.46	3.32	3.32
U1343C-20H-5, 46.0 cm	199.35	777.69	*E. batialis*	-2.42	3.17	3.17
U1343C-20H-5, 96.0 cm	199.85	779.24	*E. batialis*	-3.10	3.67	3.67
U1343C-20H-5, 134.0 cm	200.23	780.41	*E. batialis*	-1.87	3.37	3.37

U1343C-20H-6, 30.0 cm	200.69	781.84	*E. batialis*	-1.93	3.36	3.36
U1343C-20H-6, 46.0cm	200.79	782.15	*E. batialis*	-2.06	3.25	3.25
U1343E-22H-2, 102.0 cm	203.89	792.07	*G. auriculata*	-1.29	4.87	4.02
U1343E-22H-3, 68.0 cm	204.95	796.36	*G. auriculata*	-1.52	4.68	3.83
U1343E-22H-3, 118.0 cm	205.45	798.38	*G. auriculata*	-1.40	4.83	3.98
U1343E-22H-4, 86.0 cm	206.53	802.75	*C. teretis*	-1.04	4.61	4.05
U1343A-21H-1, 95.0 cm	206.70	803.43	*G. Pacifica*	-1.35	4.85	4.00
U1343A-21H-2, 18.0 cm	206.96	804.46	*E. batialis*	-4.37	3.73	3.73
U1343A-21H-2, 126.0 cm	208.04	808.83	*I. norcorssi*	-1.31	4.00	3.52
U1343A-21H-3, 16.0cm	208.36	810.13	*E. batialis*	-3.06	3.61	3.61
U1343A-21H-3, 23.0 cm	208.43	810.41	*E. batialis*	-2.23	3.85	3.85
U1343A-21H-3, 45.0cm	208.65	811.30	*I. norcrossi*	-1.24	4.26	3.78
U1343A-21H-3, 52.0 cm	208.72	811.58	*I. norcrossi*	-1.21	4.17	3.69
U1343A-21H-3, 96.0 cm	209.16	813.21	*G. auriculata*	-1.57	4.61	3.76
U1343A-21H-3, 134.0 cm	209.54	814.32	*C. parkeraniu s*	-1.99	4.41	4.41
U1343A-21H-4, 68.0cm	210.28	816.46	*E. batialis*	-7.31	4.43	4.43
U1343A-21H-4, 86.0cm	210.46	816.98	*E. batialis*	-6.15	3.75	3.75
U1343A-21H-4, 96.0 cm	210.56	817.27	*Valvulineri a sp.*	-3.07	4.12	3.87
U1343A-21H-4, 118.0cm	210.78	817.91	*Valvulineri a sp.*	-1.68	3.64	3.39
U1343A-21H-5, 8.0 cm	211.08	818.77	*I. norcrossi*	-1.77	4.12	3.64
U1343A-21H-5, 16.0cm	211.16	819.01	*I. norcrossi*	-1.17	4.05	3.57
U1343A-21H-5, 45.0cm	211.45	819.85	*I. norcrossi*	-1.02	3.98	3.50
U1343A-21H-5, 62.0 cm	211.62	820.33	*E. batialis*	-2.53	3.44	3.44
U1343A-21H-5, 96.0 cm	211.96	821.32	*I. norcrossi*	-0.77	4.56	4.08
U1343A-21H-5, 109.0 cm	212.09	821.70	*I. norcrossi*	-1.07	4.22	3.74
U1343A-21H-5, 118.0 cm	212.18	821.95	*E. batialis*	-2.38	3.44	3.44

U1343A-21H-6, 8.0 cm	212.53	822.97	*E. batialis*	-2.81	3.10	3.10
U1343A-21H-6, 23.0 cm	212.68	823.40	*E. batialis*	-2.16	3.30	3.30
U1343A-21H-7, 37.0 cm	213.42	825.55	*E. batialis*	-4.05	3.50	3.50
U1343E-23H-4, 37.0 cm	215.03	830.22	*E. batialis*	-1.82	3.81	3.81
U1343E-23H-6, 58.0 cm	217.34	836.90	*U. bifurcata*	-1.65	4.27	3.40
U1343A-22H-2, 50.0 cm	218.11	839.11	*C. parkeraniu s*	-1.31	4.15	4.15
U1343A-22H-3, 10.0 cm	219.21	842.30	*C. parkeraniu s*	-1.51	3.99	3.99
U1343A-22H-4, 118.0 cm	221.80	849.79	*E. batialis*	-1.89	3.30	3.30
U1343E-30H-2, 106.0 cm	282.50	1030.95	*U. bifurcata*	-1.28	4.27	3.40
U1343E-30H-3, 112.0 cm	284.06	1034.61	*E. batialis*	-2.66	3.65	3.65
U1343E-30H-4, 18.0 cm	284.62	1035.87	*E. batialis*	-2.97	3.62	3.62
U1343E-30H-4, 75.0 cm	285.19	1037.17	*E. batialis*	-2.53	3.71	3.71
U1343E-30H-4, 132.0 cm	285.76	1038.46	*G. auriculata*	-1.47	4.62	3.77
U1343E-30H-5, 32.0 cm	286.26	1039.59	*E. batialis*	-2.70	3.71	3.71
U1343E-30H-6, 60.0 cm	288.04	1043.63	*E. batialis*	-2.60	3.62	3.62
U1343E-31H-1, 112.0 cm	290.56	1049.34	*E. batialis*	-1.93	3.63	3.63
U1343E-31H-2, 32.0 cm	291.26	1050.92	*E. batialis*	-1.94	3.69	3.69
U1343E-31H-6, 10.0 cm	297.04	1064.27	*E. batialis*	-1.41	3.29	3.29
U1343E-31H-6, 66.0 cm	297.60	1065.83	*E. batialis*	-2.02	3.12	3.12
U1343E-31H-7, 32.0 cm	298.76	1069.06	*E. batialis*	-0.83	3.18	3.18
U1343E-32H-5, 100.0 cm	303.72	1082.90	*E. batialis*	-3.04	3.24	3.24
U1343E-32H-6, 0.0 cm	304.22	1084.29	*I. norcrossi*	-1.06	4.06	3.58
U1343E-32H-6, 106.0 cm	305.28	1087.25	*E. batialis*	-2.74	2.72	2.72
U1343E-32H-7, 10.0 cm	305.82	1088.76	*E. batialis*	-3.38	3.02	3.02
U1343E-32H-7, 66.0 cm	306.38	1090.32	*I. norcrossi*	-1.11	4.09	3.61

U1343E-32H-8, 79.0 cm	307.96	1094.73	*I. norcrossi*	-1.05	4.18	3.70
U1343E-33H-1, 10.0 cm	308.76	1096.96	*E. batialis*	-2.00	3.40	3.40
U1343E-33H-2, 44.0 cm	309.10	1097.91	*E. batialis*	-1.84	3.55	3.55
U1343E-33H-3, 87.0 cm	310.76	1102.53	*I. norcrossi*	-2.05	3.20	2.72
U1343E-33H-4, 32.0 cm	311.70	1105.16	*E. batialis*	-1.29	3.45	3.45
U1343E-33H-5, 100.0 cm	313.88	1111.24	*U. bifurcata*	-1.24	4.23	3.36
U1343E-33H-6, 100.0 cm	315.37	1115.41	*E. batialis*	-2.38	3.23	3.23
U1343E-33H-7, 36.0 cm	316.02	1117.20	*E. batialis*	-3.17	3.46	3.46
U1343E-33H-4, 134.0 cm	316.02	1117.20	*G. auriculata*	-1.54	3.92	3.07
U1343E-33H-7, 111.0 cm	316.76	1119.28	*E. batialis*	-2.80	3.45	3.45
U1343E-33H-CC, 60.0 cm	317.68	1121.84	*G. auriculata*	-1.56	4.68	3.83
U1343E-33H-7, 102.0 cm	318.54	1124.23	*E. batialis*	-3.27	3.34	3.34
U1343E-34H-1, 60.0 cm	318.54	1124.23	*E. batialis*	-2.12	4.00	4.00
U1343E-34H-1, 102.0 cm	318.96	1125.53	*I. norcrossi*	-1.19	4.29	3.81
U1343E-34H-1, 102.0 cm	318.96	1125.53	*G. auriculata*	-1.51	4.82	3.97
U1343E-34H-2, 0.0 cm	319.36	1126.98	*U. bifurcata*	-1.40	4.57	3.70
U1343E-34H-3, 32.0 cm	321.09	1133.24	*I. norcrossi*	-1.04	4.42	3.94
U1343E-34H-3, 74.0 cm	321.51	1134.76	*U. senticosa*	-0.78	4.50	3.63
U1343E-34H-3, 112.0 cm	321.89	1136.13	*I. norcrossi*	-1.21	4.26	3.78
U1343E-34H-5, 0.0 cm	323.66	1142.54	*E. batialis*	-1.76	3.75	3.75
U1343E-34H-5, 108.0 cm	324.75	1146.46	*G. auriculata*	-3.83	4.33	3.48
U1343E-34H-5, 100.0 cm	326.22	1151.80	*U. birfurcata*	-1.46	4.36	3.49
U1343E-35H-2, 44.0 cm	327.57	1156.69	*E. batialis*	-1.86	3.34	3.34
U1343E-35H-3, 60.0 cm	329.23	1162.70	*E. batialis*	-2.32	2.95	2.95
U1343E-35H-3, 60.0 cm	329.23	1162.70	*U. bifurcata*	-0.87	3.94	3.07
U1343E-35H-3, 100.0 cm	329.63	1164.15	*I. norcrossi*	-1.98	4.06	3.58

U1343E-35H-4, 60.0 cm	330.75	1168.19	*U. bifurcata*	-1.39	3.71	2.84
U1343E-35H-7, 106.0 cm	336.90	1190.46	*E. batialis*	-1.40	3.23	3.23
U1343E-36H-2, 18.0 cm	336.90	1190.46	*E. batialis*	-2.81	3.32	3.32
U1343E-35H-8, 18.0 cm	337.38	1192.19	*E. batialis*	-1.94	3.18	3.18
U1343E-35H-8, 60.0 cm	338.32	1195.60	*E. batialis*	-1.52	3.34	3.34
U1343E-36H-4, 92.0 cm	340.64	1203.99	*E. batialis*	-3.51	2.95	2.95
U1343E-36H-5, 32.0 cm	341.54	1207.25	*E. batialis*	-2.31	3.65	3.65
U1343E-36H-5, 87.0 cm	342.09	1209.24	*E. batialis*	-2.09	3.70	3.70
U1343E-36H-5, 130.0 cm	342.52	1210.79	*E. batialis*	-2.90	3.71	3.71
U1343E-36H-6, 74.0 cm	343.46	1214.19	*E. batialis*	-3.69	2.51	2.51
U1343E-36H-6, 144.0 cm	344.16	1216.73	*G. auriculata*	-0.91	4.93	4.08
U1343E-36H-6, 25.0 cm	344.75	1218.84	*E. batialis*	-2.87	3.75	3.75
U1343E-36H-6, 74.0 cm	345.90	1223.00	*U. bifurcata*	-1.14	4.51	3.64
U1343E-37H-1, 20.0 cm	346.14	1223.90	*E. batialis*	-2.13	4.95	4.95
U1343E-36H-7, 49.0 cm	346.50	1225.17	*G. auriculata*	-2.31	3.93	3.08
U1343E-36H-CC, 18.0 cm	346.50	1225.17	*G. auriculata*	-1.27	4.84	3.99

Table 8.2 Benthic foraminiferal $\delta^{18}O$ from Asahi et al. (2016), Kender et al. (2018) and new data presented in this thesis, combined to form the new updated high resolution age model for Site U1343 between 0 and 1.2 Ma (Chapter 2-3).

Depth (m CCSF-A)	Age (kyr)	$\delta^{18}O$ ‰ (tuned to *E. batialis*)	Reference
0.01	6.76	2.80	Asahi et al., (2016)
0.35	7.97	2.74	Asahi et al., (2016)
0.83	9.68	3.21	Asahi et al., (2016)
1.16	10.85	2.94	Asahi et al., (2016)
1.23	11.10	3.41	Asahi et al., (2016)
2.31	14.93	3.82	Chapter 2
3.35	18.65	4.04	Asahi et al., (2016)
3.83	20.36	4.14	Asahi et al., (2016)
3.90	20.61	4.88	Chapter 2
3.90	20.61	5.01	Chapter 2
4.23	21.78	4.17	Asahi et al., (2016)
4.73	23.56	3.56	Chapter 2
5.33	25.70	4.32	Asahi et al., (2016)
5.34	25.73	4.08	Asahi et al., (2016)
5.41	25.98	4.26	Chapter 2
5.73	27.12	3.90	Asahi et al., (2016)
6.11	28.47	4.17	Chapter 2
6.21	28.83	4.31	Asahi et al., (2016)
6.45	29.68	4.11	Asahi et al., (2016)
6.80	30.91	3.99	Asahi et al., (2016)
6.83	31.04	4.11	Asahi et al., (2016)
7.08	31.93	4.02	Chapter 2
7.17	32.23	4.08	Asahi et al., (2016)
7.31	32.74	4.07	Asahi et al., (2016)
7.71	34.17	4.03	Asahi et al., (2016)

7.95	35.02	4.04	Asahi et al., (2016)
8.01	35.24	3.67	Asahi et al., (2016)
8.53	37.09	3.73	Asahi et al., (2016)
8.87	38.30	3.79	Chapter 2
9.21	39.51	3.63	Asahi et al., (2016)
9.45	40.36	3.96	Asahi et al., (2016)
9.64	41.04	3.96	Asahi et al., (2016)
9.87	41.88	3.70	Chapter 2
10.03	42.43	3.69	Asahi et al., (2016)
10.31	43.42	3.73	Asahi et al., (2016)
10.51	44.12	3.75	Asahi et al., (2016)
10.71	44.85	3.57	Asahi et al., (2016)
10.94	45.65	3.67	Chapter 2
10.95	45.70	3.34	Asahi et al., (2016)
11.63	48.14	3.61	Asahi et al., (2016)
13.53	54.87	3.47	Chapter 2
14.88	59.53	3.96	Asahi et al., (2016)
14.89	59.56	3.75	Asahi et al., (2016)
15.17	60.49	3.93	Asahi et al., (2016)
15.34	61.05	3.90	Asahi et al., (2016)
15.45	61.41	3.93	Asahi et al., (2016)
15.97	63.12	3.99	Asahi et al., (2016)
16.27	64.11	3.96	Asahi et al., (2016)
16.41	64.56	3.89	Asahi et al., (2016)
16.55	65.02	3.90	Asahi et al., (2016)
16.63	65.28	3.93	Asahi et al., (2016)
17.33	67.60	3.98	Chapter 2
17.33	67.60	4.07	Chapter 2
17.89	69.44	3.79	Asahi et al., (2016)

17.95	69.64	3.86	Asahi et al., (2016)
18.07	70.03	3.70	Asahi et al., (2016)
18.17	70.36	3.79	Asahi et al., (2016)
18.27	70.69	3.46	Asahi et al., (2016)
18.35	70.95	3.46	Asahi et al., (2016)
18.47	71.35	3.47	Asahi et al., (2016)
18.57	71.68	3.67	Asahi et al., (2016)
18.67	72.01	3.45	Asahi et al., (2016)
18.91	72.80	3.89	Chapter 2
18.97	73.00	3.43	Asahi et al., (2016)
19.40	74.40	3.70	Asahi et al., (2016)
19.69	75.35	3.67	Asahi et al., (2016)
20.44	77.82	3.47	Chapter 2
21.19	80.29	3.55	Asahi et al., (2016)
21.47	81.23	3.65	Asahi et al., (2016)
21.57	81.54	3.51	Chapter 2
22.69	85.22	3.10	Asahi et al., (2016)
23.17	86.81	3.39	Asahi et al., (2016)
23.27	87.13	3.38	Asahi et al., (2016)
23.77	88.77	3.46	Asahi et al., (2016)
23.80	88.87	3.58	Asahi et al., (2016)
24.23	90.29	3.81	Chapter 2
24.25	90.36	3.59	Asahi et al., (2016)
24.49	91.15	3.47	Asahi et al., (2016)
24.50	91.20	3.58	Asahi et al., (2016)
25.01	92.87	3.46	Asahi et al., (2016)
25.99	96.10	3.32	Asahi et al., (2016)
26.37	97.34	3.44	Asahi et al., (2016)

26.81	98.79	3.33	Asahi et al., (2016)
28.31	103.72	3.23	Asahi et al., (2016)
28.99	105.97	3.25	Asahi et al., (2016)
29.31	107.02	3.24	Asahi et al., (2016)
29.81	108.66	3.24	Asahi et al., (2016)
30.12	109.68	3.75	Asahi et al., (2016)
31.32	113.63	3.28	Asahi et al., (2016)
32.47	117.42	3.48	Asahi et al., (2016)
32.78	118.44	3.63	Chapter 2
32.81	118.54	3.53	Asahi et al., (2016)
33.09	119.46	3.53	Asahi et al., (2016)
33.74	121.60	3.31	Chapter 2
33.79	121.76	3.41	Asahi et al., (2016)
34.27	123.34	3.34	Asahi et al., (2016)
34.77	124.99	3.22	Asahi et al., (2016)
35.02	125.82	3.30	Asahi et al., (2016)
35.40	127.06	3.09	Asahi et al., (2016)
35.88	128.66	2.73	Asahi et al., (2016)
36.16	129.57	2.73	Chapter 2
36.16	129.57	2.95	Chapter 2
36.19	129.67	2.92	Asahi et al., (2016)
36.77	131.63	3.49	Chapter 2
36.79	131.72	3.49	Asahi et al., (2016)
36.92	132.31	3.61	Asahi et al., (2016)
37.10	133.11	4.17	Asahi et al., (2016)
37.21	133.58	3.87	Chapter 2
37.21	133.58	3.97	Chapter 2
37.21	133.58	3.99	Chapter 2
37.49	134.82	4.07	Asahi et al., (2016)
37.71	135.79	4.08	Chapter 2

37.71	135.79	4.14	Chapter 2
37.99	137.03	4.15	Asahi et al., (2016)
38.04	137.25	4.14	Chapter 2
38.29	138.36	3.90	Asahi et al., (2016)
38.40	138.84	4.03	Asahi et al., (2016)
38.55	139.51	4.06	Chapter 2
38.87	140.92	4.21	Asahi et al., (2016)
38.97	141.36	4.22	Chapter 2
39.39	143.22	4.14	Asahi et al., (2016)
39.47	143.58	4.09	Chapter 2
39.79	144.99	4.03	Asahi et al., (2016)
39.91	145.54	3.89	Asahi et al., (2016)
40.59	148.53	4.02	Asahi et al., (2016)
40.94	150.10	3.93	Chapter 2
40.99	150.30	4.00	Asahi et al., (2016)
41.39	152.07	3.99	Asahi et al., (2016)
41.47	152.43	3.97	Asahi et al., (2016)
41.87	154.20	4.25	Asahi et al., (2016)
42.24	155.86	3.96	Asahi et al., (2016)
42.45	156.78	3.97	Asahi et al., (2016)
42.58	157.35	4.24	Chapter 2
43.21	160.14	3.86	Chapter 2
43.34	160.72	4.00	Asahi et al., (2016)
43.92	163.30	3.67	Asahi et al., (2016)
43.92	163.30	3.72	Asahi et al., (2016)
44.12	164.17	3.81	Chapter 2
44.40	165.42	3.67	Asahi et al., (2016)
44.92	167.73	3.74	Asahi et al., (2016)
45.04	168.26	3.69	Asahi et al., (2016)
45.16	168.79	3.76	Chapter 2

45.90	172.06	3.61	Asahi et al., (2016)
46.17	173.26	3.69	Chapter 2
46.31	173.88	3.89	Asahi et al., (2016)
46.40	174.25	3.28	Asahi et al., (2016)
46.42	174.36	3.80	Asahi et al., (2016)
46.55	174.92	3.75	Asahi et al., (2016)
46.92	176.58	3.72	Asahi et al., (2016)
47.11	177.38	3.56	Asahi et al., (2016)
47.24	177.99	3.76	Asahi et al., (2016)
47.40	178.70	3.69	Asahi et al., (2016)
47.73	180.16	3.83	Asahi et al., (2016)
47.76	180.26	3.76	Chapter 2
47.83	180.60	3.84	Asahi et al., (2016)
47.93	181.04	3.86	Asahi et al., (2016)
48.01	181.39	3.79	Asahi et al., (2016)
48.13	181.80	3.88	Asahi et al., (2016)
48.30	182.33	3.97	Asahi et al., (2016)
48.32	182.39	3.77	Asahi et al., (2016)
49.35	185.71	4.07	Chapter 2
49.82	187.21	3.75	Asahi et al., (2016)
52.72	196.52	3.35	Asahi et al., (2016)
54.22	201.34	3.35	Asahi et al., (2016)
55.72	206.16	2.97	Asahi et al., (2016)
56.47	208.58	3.24	Asahi et al., (2016)
56.95	210.13	3.36	Asahi et al., (2016)
57.07	210.49	3.33	Asahi et al., (2016)
57.46	211.76	3.24	Asahi et al., (2016)
57.59	212.18	3.34	Asahi et al., (2016)

57.77	212.76	3.08	Asahi et al., (2016)
58.27	214.36	3.15	Asahi et al., (2016)
58.37	214.67	3.04	Asahi et al., (2016)
58.37	214.69	3.23	Asahi et al., (2016)
58.85	216.23	3.01	Asahi et al., (2016)
58.93	216.48	3.10	Chapter 2
59.10	217.02	3.08	Asahi et al., (2016)
59.47	218.22	3.22	Asahi et al., (2016)
59.95	219.63	3.58	Asahi et al., (2016)
60.22	220.34	3.70	Chapter 2
60.24	220.39	3.79	Asahi et al., (2016)
60.80	221.86	3.73	Asahi et al., (2016)
61.22	222.96	3.82	Chapter 2
62.02	225.04	3.83	Asahi et al., (2016)
62.30	225.78	3.63	Asahi et al., (2016)
63.25	228.27	3.70	Asahi et al., (2016)
63.81	229.72	3.74	Asahi et al., (2016)
64.87	232.50	3.67	Asahi et al., (2016)
66.38	236.46	3.33	Asahi et al., (2016)
66.45	236.63	3.31	Asahi et al., (2016)
66.57	236.95	3.23	Asahi et al., (2016)
66.67	237.21	3.07	Asahi et al., (2016)
66.77	237.47	3.30	Asahi et al., (2016)
66.85	237.68	3.20	Asahi et al., (2016)
66.98	238.01	3.16	Asahi et al., (2016)
67.07	238.25	3.06	Asahi et al., (2016)
67.17	238.52	3.12	Asahi et al., (2016)
68.11	240.98	2.47	Asahi et al., (2016)

68.74	242.64	2.93	Asahi et al., (2016)
68.85	243.03	3.07	Asahi et al., (2016)
68.96	243.40	3.07	Asahi et al., (2016)
69.08	243.82	3.27	Asahi et al., (2016)
69.18	244.17	3.30	Asahi et al., (2016)
69.28	244.51	3.31	Asahi et al., (2016)
69.36	244.79	3.33	Asahi et al., (2016)
69.48	245.20	3.44	Asahi et al., (2016)
69.58	245.55	3.54	Asahi et al., (2016)
69.68	245.90	3.51	Asahi et al., (2016)
69.76	246.17	3.56	Asahi et al., (2016)
69.88	246.59	3.44	Asahi et al., (2016)
69.98	246.93	3.45	Asahi et al., (2016)
70.08	247.28	3.63	Asahi et al., (2016)
70.28	247.97	3.65	Asahi et al., (2016)
70.34	248.18	3.93	Asahi et al., (2016)
70.34	248.18	3.82	Asahi et al., (2016)
71.75	253.07	3.69	Asahi et al., (2016)
71.83	253.35	3.84	Asahi et al., (2016)
72.08	254.22	3.88	Asahi et al., (2016)
72.35	255.15	3.73	Chapter 2
72.54	255.81	4.12	Asahi et al., (2016)
73.19	258.06	3.74	Chapter 2
73.30	258.43	3.77	Asahi et al., (2016)
73.33	258.55	3.69	Asahi et al., (2016)
73.33	258.55	3.72	Asahi et al., (2016)
74.05	261.04	3.90	Chapter 2
74.90	263.98	3.86	Chapter 2

75.54	266.19	3.89	Chapter 2
76.93	270.99	3.75	Asahi et al., (2016)
78.47	276.32	3.71	Asahi et al., (2016)
78.85	277.65	3.76	Asahi et al., (2016)
80.09	281.85	3.44	Chapter 2
80.35	282.71	3.44	Asahi et al., (2016)
81.46	286.36	3.27	Asahi et al., (2016)
81.54	286.63	3.22	Asahi et al., (2016)
81.82	287.56	3.24	Chapter 2
81.85	287.66	3.29	Asahi et al., (2016)
82.48	289.73	3.31	Chapter 2
83.04	291.58	3.38	Asahi et al., (2016)
83.19	292.07	3.40	Chapter 2
83.36	292.63	3.55	Asahi et al., (2016)
83.87	294.31	3.64	Chapter 2
84.49	296.36	3.64	Asahi et al., (2016)
84.59	296.68	3.86	Asahi et al., (2016)
84.90	297.71	3.15	Chapter 2
85.41	299.38	3.35	Asahi et al., (2016)
85.54	299.81	3.66	Chapter 2
86.23	302.08	3.81	Chapter 2
86.38	302.58	3.56	Asahi et al., (2016)
86.50	302.98	3.50	Asahi et al., (2016)
86.60	303.31	3.70	Asahi et al., (2016)
87.45	306.13	3.37	Asahi et al., (2016)
87.62	306.67	3.44	Chapter 2
87.73	307.03	3.57	Asahi et al., (2016)
88.02	308.00	3.24	Asahi et al., (2016)
88.35	309.08	3.30	Chapter 2
88.41	309.28	3.32	Asahi et al., (2016)
89.91	314.23	3.44	Asahi et al., (2016)

90.80	317.18	3.13	Asahi et al., (2016)
93.61	326.43	3.19	Asahi et al., (2016)
93.79	327.04	3.08	Asahi et al., (2016)
94.19	328.35	2.86	Asahi et al., (2016)
95.11	331.38	2.80	Asahi et al., (2016)
95.41	332.39	3.72	Asahi et al., (2016)
96.25	335.14	3.36	Chapter 2
96.75	336.84	4.16	Asahi et al., (2016)
97.03	337.76	4.07	Chapter 2
97.56	339.53	3.91	Chapter 2
97.56	339.53	4.03	Chapter 2
98.24	341.79	4.00	Chapter 2
98.41	342.34	4.06	Asahi et al., (2016)
98.75	343.48	4.01	Asahi et al., (2016)
99.36	345.52	3.78	Asahi et al., (2016)
99.83	347.09	3.87	Asahi et al., (2016)
100.32	348.72	3.85	Chapter 2
101.02	351.05	3.81	Chapter 2
101.34	352.12	3.95	Asahi et al., (2016)
101.91	354.00	4.01	Chapter 2
102.78	356.91	3.88	Asahi et al., (2016)
102.81	357.00	3.89	Chapter 2
103.00	357.65	3.87	Asahi et al., (2016)
103.11	358.02	3.74	Asahi et al., (2016)
103.44	359.11	3.78	Asahi et al., (2016)
103.76	360.16	3.67	Asahi et al., (2016)
104.24	361.78	3.67	Chapter 2
105.23	365.06	3.56	Asahi et al., (2016)
105.26	365.16	3.52	Asahi et al., (2016)
105.80	366.96	3.60	Chapter 2
106.68	369.89	3.53	Asahi et al., (2016)

107.11	371.34	3.48	Chapter 2
108.03	374.40	3.58	Chapter 2
109.28	378.57	3.51	Asahi et al., (2016)
111.97	387.52	3.34	Asahi et al., (2016)
113.28	391.88	3.48	Asahi et al., (2016)
113.82	393.67	3.74	Chapter 2
114.78	397.42	3.11	Asahi et al., (2016)
115.49	401.61	3.18	Asahi et al., (2016)
115.82	403.55	3.12	Asahi et al., (2016)
116.28	406.29	2.77	Asahi et al., (2016)
116.81	409.38	2.85	Chapter 2
117.72	414.78	3.06	Chapter 2
117.78	415.10	2.86	Asahi et al., (2016)
118.06	416.75	2.97	Chapter 2
118.40	418.76	2.87	Chapter 2
118.60	419.97	3.42	Chapter 2
119.15	423.19	3.50	Chapter 2
119.28	423.94	3.43	Asahi et al., (2016)
119.36	424.41	3.69	Asahi et al., (2016)
120.54	430.74	4.32	Asahi et al., (2016)
121.03	433.39	4.48	Asahi et al., (2016)
121.57	436.26	4.13	Asahi et al., (2016)
121.84	437.74	4.13	Asahi et al., (2016)
122.46	441.04	3.99	Chapter 2
123.01	443.99	3.43	Chapter 2
123.45	446.35	3.98	Chapter 2
124.50	451.97	3.84	Asahi et al., (2016)
125.11	455.27	3.88	Chapter 2
126.04	460.23	4.38	Chapter 2
126.94	465.05	3.72	Asahi et al., (2016)
127.50	468.06	3.65	Asahi et al., (2016)
128.26	472.13	4.13	Chapter 2

128.54	473.63	3.84	Asahi et al., (2016)
131.22	483.72	3.22	Asahi et al., (2016)
131.26	483.80	3.43	Asahi et al., (2016)
131.32	483.93	3.04	Asahi et al., (2016)
131.34	483.97	3.64	Asahi et al., (2016)
131.70	484.73	3.20	Asahi et al., (2016)
134.42	490.46	2.98	Asahi et al., (2016)
136.40	494.63	2.95	Asahi et al., (2016)
136.74	495.34	3.09	Asahi et al., (2016)
137.37	496.67	3.00	Asahi et al., (2016)
137.41	496.75	3.08	Chapter 2
137.63	497.22	3.11	Asahi et al., (2016)
138.23	498.49	3.24	Asahi et al., (2016)
138.56	499.18	3.44	Chapter 2
138.87	499.83	3.11	Asahi et al., (2016)
139.70	501.58	3.29	Chapter 2
139.74	501.66	3.14	Asahi et al., (2016)
139.91	502.02	3.12	Asahi et al., (2016)
140.77	503.83	3.62	Asahi et al., (2016)
140.83	503.96	3.18	Chapter 2
140.96	504.23	3.53	Asahi et al., (2016)
142.36	507.18	3.26	Asahi et al., (2016)
144.00	510.64	3.56	Chapter 2
144.93	512.60	3.82	Chapter 2
145.16	513.45	3.58	Asahi et al., (2016)
145.69	515.92	3.60	Asahi et al., (2016)
145.75	516.20	3.54	Chapter 2
146.17	518.15	3.51	Asahi et al., (2016)
146.60	520.15	3.27	Chapter 2
146.66	520.42	3.17	Asahi et al., (2016)

147.25	523.17	3.20	Chapter 2
147.64	524.97	3.54	Asahi et al., (2016)
147.96	526.48	3.53	Chapter 2
148.61	529.47	3.52	Asahi et al., (2016)
148.71	529.94	3.27	Chapter 2
148.71	529.94	3.72	Chapter 2
148.71	529.94	3.83	Chapter 2
148.89	530.78	3.64	Asahi et al., (2016)
149.85	535.24	3.62	Chapter 2
150.11	536.45	3.86	Asahi et al., (2016)
150.15	536.64	3.55	Chapter 2
150.47	538.12	3.94	Chapter 2
150.47	538.12	3.99	Chapter 2
150.87	539.99	3.95	Chapter 2
150.97	540.45	3.92	Chapter 2
151.39	542.41	3.89	Asahi et al., (2016)
151.47	542.78	3.87	Asahi et al., (2016)
151.54	543.10	3.64	Asahi et al., (2016)
151.55	543.16	3.64	Asahi et al., (2016)
151.58	543.29	3.94	Chapter 2
151.63	543.53	3.69	Asahi et al., (2016)
151.69	543.81	3.97	Asahi et al., (2016)
151.79	544.27	3.80	Asahi et al., (2016)
151.87	544.64	3.62	Asahi et al., (2016)
151.95	545.02	3.78	Asahi et al., (2016)
151.96	545.06	4.02	Chapter 2
151.96	545.06	4.27	Chapter 2
152.03	545.37	3.84	Asahi et al., (2016)
152.05	545.45	3.87	Chapter 2
152.11	545.67	3.60	Asahi et al., (2016)
152.19	545.96	3.70	Asahi et al., (2016)
152.27	546.25	3.61	Asahi et al., (2016)

152.35	546.54	3.48	Asahi et al., (2016)
152.43	546.84	3.50	Asahi et al., (2016)
152.51	547.13	3.62	Asahi et al., (2016)
152.59	547.42	3.75	Asahi et al., (2016)
152.67	547.71	3.75	Asahi et al., (2016)
152.75	548.00	3.81	Asahi et al., (2016)
152.79	548.16	3.92	Asahi et al., (2016)
152.89	548.52	3.85	Asahi et al., (2016)
152.97	548.81	3.78	Asahi et al., (2016)
153.05	549.10	3.93	Asahi et al., (2016)
153.13	549.40	3.70	Asahi et al., (2016)
153.19	549.62	3.79	Asahi et al., (2016)
153.33	550.13	3.78	Chapter 2
153.37	550.27	3.82	Asahi et al., (2016)
153.45	550.57	3.81	Asahi et al., (2016)
153.55	550.93	3.79	Chapter 2
153.61	551.15	3.57	Asahi et al., (2016)
153.69	551.45	3.64	Asahi et al., (2016)
153.77	551.74	3.70	Asahi et al., (2016)
153.85	552.03	3.66	Asahi et al., (2016)
153.93	552.32	3.70	Asahi et al., (2016)
154.01	552.62	3.64	Asahi et al., (2016)
154.09	552.91	3.51	Asahi et al., (2016)
154.47	554.30	3.65	Asahi et al., (2016)
154.67	555.03	3.87	Chapter 2
154.95	556.05	3.42	Asahi et al., (2016)
155.03	556.35	3.42	Asahi et al., (2016)
155.11	556.64	3.62	Asahi et al., (2016)

155.39	557.66	3.58	Chapter 2
155.51	558.10	3.50	Asahi et al., (2016)
155.59	558.39	3.54	Asahi et al., (2016)
155.67	558.69	3.43	Asahi et al., (2016)
155.79	559.13	3.09	Asahi et al., (2016)
155.81	559.21	3.28	Asahi et al., (2016)
155.89	559.49	3.29	Asahi et al., (2016)
156.05	560.08	3.52	Asahi et al., (2016)
156.23	560.75	3.75	Chapter 2
156.37	561.25	3.82	Asahi et al., (2016)
156.45	561.54	3.62	Asahi et al., (2016)
156.53	561.83	3.47	Asahi et al., (2016)
156.61	562.12	3.29	Asahi et al., (2016)
156.69	562.42	2.99	Asahi et al., (2016)
156.77	562.71	3.41	Asahi et al., (2016)
156.85	563.00	3.29	Asahi et al., (2016)
156.85	563.01	3.28	Asahi et al., (2016)
156.93	563.29	3.04	Asahi et al., (2016)
157.01	563.59	2.92	Asahi et al., (2016)
157.17	564.17	3.35	Asahi et al., (2016)
157.40	565.01	2.78	Asahi et al., (2016)
157.57	565.65	3.53	Chapter 2
158.14	567.73	3.27	Chapter 2
159.73	573.55	3.57	Chapter 2
160.31	575.67	2.97	Asahi et al., (2016)
160.79	577.42	2.62	Asahi et al., (2016)
161.22	578.99	2.63	Asahi et al., (2016)
161.33	579.41	2.91	Asahi et al., (2016)

161.41	579.70	2.83	Asahi et al., (2016)
161.57	580.29	2.66	Asahi et al., (2016)
161.63	580.50	3.06	Asahi et al., (2016)
161.69	580.70	3.23	Chapter 2
161.81	581.13	3.44	Asahi et al., (2016)
162.00	581.78	3.44	Chapter 2
162.21	582.52	3.65	Asahi et al., (2016)
162.29	582.80	3.80	Asahi et al., (2016)
162.34	582.96	4.03	Chapter 2
162.45	583.35	3.97	Asahi et al., (2016)
162.53	583.63	3.17	Asahi et al., (2016)
162.61	583.91	3.52	Asahi et al., (2016)
162.86	584.76	3.60	Asahi et al., (2016)
162.94	585.03	3.39	Asahi et al., (2016)
163.02	585.31	3.42	Asahi et al., (2016)
163.10	585.59	3.25	Asahi et al., (2016)
163.16	585.80	3.65	Asahi et al., (2016)
163.22	586.01	3.48	Asahi et al., (2016)
163.22	586.02	3.70	Chapter 2
163.26	586.15	3.60	Asahi et al., (2016)
163.42	586.70	3.84	Asahi et al., (2016)
163.50	586.98	3.46	Asahi et al., (2016)
163.58	587.26	3.57	Asahi et al., (2016)
163.74	587.82	3.66	Asahi et al., (2016)
163.82	588.09	3.56	Asahi et al., (2016)
163.90	588.37	3.60	Asahi et al., (2016)
163.98	588.65	3.76	Asahi et al., (2016)
164.06	588.94	3.62	Asahi et al., (2016)

164.19	589.38	3.68	Asahi et al., (2016)
164.27	589.66	3.40	Asahi et al., (2016)
164.35	589.94	3.53	Asahi et al., (2016)
164.43	590.22	3.81	Asahi et al., (2016)
164.49	590.42	3.44	Asahi et al., (2016)
164.59	590.77	3.45	Asahi et al., (2016)
164.67	591.05	3.33	Asahi et al., (2016)
164.75	591.33	3.31	Asahi et al., (2016)
164.83	591.61	3.36	Asahi et al., (2016)
164.91	591.88	3.28	Asahi et al., (2016)
164.92	591.93	3.35	Chapter 2
164.97	592.09	3.07	Asahi et al., (2016)
165.07	592.44	3.33	Asahi et al., (2016)
165.15	592.72	3.38	Asahi et al., (2016)
165.23	593.00	3.15	Asahi et al., (2016)
165.39	593.55	2.99	Asahi et al., (2016)
165.47	593.83	3.37	Asahi et al., (2016)
165.77	594.88	3.71	Asahi et al., (2016)
165.83	595.08	4.01	Chapter 2
165.93	595.43	3.37	Asahi et al., (2016)
165.99	595.64	3.22	Asahi et al., (2016)
166.08	595.95	3.37	Asahi et al., (2016)
166.17	596.27	3.41	Asahi et al., (2016)
166.21	596.42	3.59	Chapter 2
166.25	596.54	3.35	Asahi et al., (2016)
166.33	596.82	3.49	Asahi et al., (2016)
166.41	597.10	3.32	Asahi et al., (2016)
166.49	597.38	3.36	Asahi et al., (2016)

166.57	597.66	3.53	Asahi et al., (2016)
166.65	597.94	3.27	Asahi et al., (2016)
166.73	598.21	3.55	Asahi et al., (2016)
166.81	598.49	3.08	Asahi et al., (2016)
166.89	598.77	3.31	Asahi et al., (2016)
166.95	598.98	3.29	Asahi et al., (2016)
167.03	599.26	3.17	Asahi et al., (2016)
167.11	599.53	3.19	Asahi et al., (2016)
167.19	599.81	3.19	Asahi et al., (2016)
167.25	600.02	2.93	Asahi et al., (2016)
167.34	600.33	3.22	Asahi et al., (2016)
167.39	600.52	3.47	Chapter 2
167.43	600.65	3.45	Asahi et al., (2016)
167.51	600.93	3.13	Asahi et al., (2016)
167.59	601.20	3.09	Asahi et al., (2016)
167.67	601.48	3.34	Asahi et al., (2016)
167.75	601.76	3.12	Asahi et al., (2016)
167.82	602.00	3.46	Asahi et al., (2016)
168.09	602.96	3.61	Chapter 2
168.21	603.36	3.67	Chapter 2
168.50	604.37	3.59	Chapter 2
168.79	605.38	3.63	Chapter 2
168.84	605.57	3.45	Asahi et al., (2016)
169.04	606.25	3.47	Chapter 2
169.29	607.12	3.53	Chapter 2
169.53	607.96	3.63	Chapter 2
169.84	609.03	3.51	Chapter 2
170.05	609.76	3.15	Chapter 2
170.44	611.11	4.00	Asahi et al., (2016)
170.54	611.47	3.41	Chapter 2
170.86	612.58	3.33	Chapter 2
171.02	613.14	3.48	Chapter 2

171.41	614.49	3.21	Chapter 2
171.55	614.98	3.54	Chapter 2
171.70	615.50	3.08	Chapter 2
171.86	616.06	2.99	Chapter 2
172.04	616.68	3.38	Chapter 2
172.44	618.07	3.24	Chapter 2
172.92	619.76	3.69	Chapter 2
173.13	620.47	3.51	Chapter 2
173.13	620.47	3.73	Chapter 2
173.30	621.06	3.54	Chapter 2
173.45	622.35	4.05	Chapter 2
173.64	625.60	4.44	Chapter 2
173.80	628.27	4.44	Chapter 2
173.90	629.84	4.31	Chapter 2
173.96	630.94	4.68	Chapter 2
174.34	637.28	4.44	Chapter 2
174.50	639.95	4.09	Chapter 2
174.57	641.04	3.99	Asahi et al., (2016)
174.60	641.24	3.12	Asahi et al., (2016)
174.97	643.54	4.02	Chapter 2
175.54	647.07	4.00	Chapter 2
175.75	648.37	3.83	Chapter 2
175.75	648.37	3.91	Chapter 2
176.00	649.92	3.76	Chapter 2
176.05	650.19	3.19	Asahi et al., (2016)
176.27	651.59	3.84	Chapter 2
176.56	653.39	3.91	Chapter 2
177.06	656.46	3.57	Asahi et al., (2016)
177.56	659.59	3.46	Chapter 2
177.82	661.15	3.46	Asahi et al., (2016)
178.06	662.68	3.40	Chapter 2
178.38	664.67	3.87	Chapter 2
178.94	668.14	4.08	Chapter 2
178.94	668.14	5.02	Chapter 2
179.56	671.98	3.71	Chapter 2
180.03	674.89	3.73	Chapter 2
180.32	676.69	3.74	Chapter 2
180.64	678.67	3.59	Chapter 2
180.89	680.22	3.04	Chapter 2
181.02	681.02	3.13	Asahi et al., (2016)

182.05	687.41	3.96	Chapter 2
182.45	689.83	3.44	Asahi et al., (2016)
182.63	690.94	4.16	Chapter 2
182.75	691.69	3.20	Asahi et al., (2016)
183.05	693.54	3.42	Asahi et al., (2016)
183.35	695.40	3.09	Asahi et al., (2016)
184.17	700.48	3.32	Asahi et al., (2016)
184.47	702.34	3.71	Asahi et al., (2016)
184.59	703.10	3.30	Asahi et al., (2016)
184.94	705.24	3.65	Chapter 2
185.12	706.35	3.79	Asahi et al., (2016)
185.24	707.09	3.62	Chapter 2
185.42	708.21	3.45	Asahi et al., (2016)
185.72	710.06	3.90	Asahi et al., (2016)
185.87	711.02	3.71	Chapter 2
186.02	711.92	3.97	Asahi et al., (2016)
186.20	713.04	4.04	Asahi et al., (2016)
186.28	713.52	4.00	Chapter 2
186.28	713.52	4.08	Chapter 2
186.32	713.77	3.80	Asahi et al., (2016)
186.51	714.95	3.96	Chapter 2
186.62	715.63	3.90	Asahi et al., (2016)
186.92	717.48	3.79	Asahi et al., (2016)
187.05	718.28	3.69	Chapter 2
187.22	719.33	3.92	Asahi et al., (2016)
187.30	719.83	4.21	Chapter 2
187.52	721.19	3.86	Asahi et al., (2016)
187.70	722.33	4.00	Asahi et al., (2016)
187.78	722.80	3.71	Chapter 2
187.82	723.04	4.01	Asahi et al., (2016)
188.06	724.54	3.77	Chapter 2

188.12	724.90	3.98	Asahi et al., (2016)
188.43	727.17	3.47	Asahi et al., (2016)
188.58	728.44	3.56	Chapter 2
188.76	729.93	3.56	Asahi et al., (2016)
188.83	730.53	3.68	Chapter 2
189.02	732.11	3.57	Asahi et al., (2016)
189.08	732.63	3.83	Chapter 2
189.32	734.64	3.81	Chapter 2
189.41	735.38	3.94	Asahi et al., (2016)
189.64	737.32	3.65	Chapter 2
189.86	739.17	3.53	Chapter 2
190.08	741.01	3.66	Chapter 2
190.42	743.86	3.64	Chapter 2
190.42	743.86	3.66	Chapter 2
190.42	743.86	3.73	Chapter 2
190.42	743.86	3.78	Chapter 2
191.28	751.06	4.08	Asahi et al., (2016)
191.54	753.24	4.07	Chapter 2
191.58	753.58	4.04	Asahi et al., (2016)
191.88	754.54	3.91	Asahi et al., (2016)
192.18	755.47	3.39	Asahi et al., (2016)
192.20	755.53	3.95	Asahi et al., (2016)
192.29	755.82	4.90	Chapter 2
192.48	756.40	3.79	Asahi et al., (2016)
192.78	757.33	3.96	Asahi et al., (2016)
193.19	758.60	3.72	Chapter 2
193.38	759.19	3.40	Asahi et al., (2016)
193.52	759.62	3.82	Chapter 2
193.55	759.73	3.70	Asahi et al., (2016)
193.83	760.58	4.38	Chapter 2
193.98	761.05	3.89	Asahi et al., (2016)
194.19	761.71	3.70	Asahi et al., (2016)
194.28	761.98	3.91	Asahi et al., (2016)

194.58	762.91	3.56	Asahi et al., (2016)
194.88	763.83	3.33	Asahi et al., (2016)
195.18	764.76	3.86	Asahi et al., (2016)
195.68	766.31	3.60	Asahi et al., (2016)
195.78	766.62	3.32	Asahi et al., (2016)
196.08	767.55	3.67	Asahi et al., (2016)
196.38	768.48	3.32	Asahi et al., (2016)
196.51	768.89	3.52	Chapter 2
196.68	769.41	3.51	Asahi et al., (2016)
196.98	770.34	3.40	Asahi et al., (2016)
197.25	771.18	3.35	Chapter 2
198.05	773.66	3.54	Chapter 2
198.48	774.99	3.38	Chapter 2
198.97	776.51	3.32	Chapter 2
199.35	777.69	3.17	Chapter 2
199.85	779.24	3.67	Chapter 2
200.21	780.35	3.39	Asahi et al., (2016)
200.23	780.41	3.37	Chapter 2
200.69	781.84	3.36	Chapter 2
200.79	782.15	3.25	Chapter 2
201.41	784.08	3.03	Asahi et al., (2016)
201.71	785.01	2.55	Asahi et al., (2016)
202.01	785.94	2.87	Asahi et al., (2016)
202.31	786.87	2.90	Asahi et al., (2016)
202.61	787.80	3.76	Asahi et al., (2016)
202.90	788.70	3.27	Asahi et al., (2016)
202.91	788.73	3.20	Asahi et al., (2016)
203.21	789.66	3.50	Asahi et al., (2016)
203.51	790.59	3.62	Asahi et al., (2016)
203.59	790.84	3.61	Asahi et al., (2016)

203.81	791.75	3.48	Asahi et al., (2016)
203.89	792.07	4.02	Chapter 2
204.15	793.13	3.72	Asahi et al., (2016)
204.31	793.77	3.53	Asahi et al., (2016)
204.61	794.98	3.89	Asahi et al., (2016)
204.91	796.20	3.83	Asahi et al., (2016)
204.95	796.36	3.83	Chapter 2
205.19	797.33	3.95	Asahi et al., (2016)
205.45	798.38	3.98	Chapter 2
205.48	798.50	3.90	Asahi et al., (2016)
205.55	798.77	3.95	Asahi et al., (2016)
205.71	799.43	4.01	Asahi et al., (2016)
206.01	800.64	4.23	Asahi et al., (2016)
206.53	802.75	4.05	Chapter 2
206.61	803.07	4.09	Asahi et al., (2016)
206.70	803.43	4.00	Chapter 2
206.91	804.28	4.11	Asahi et al., (2016)
206.96	804.46	3.73	Chapter 2
207.05	804.85	3.54	Asahi et al., (2016)
208.04	808.83	3.52	Chapter 2
208.36	810.13	3.61	Chapter 2
208.43	810.41	3.85	Chapter 2
208.56	810.94	3.50	Asahi et al., (2016)
208.65	811.30	3.78	Chapter 2
208.72	811.58	3.69	Chapter 2
209.16	813.21	3.76	Chapter 2
209.54	814.32	4.41	Chapter 2
210.03	815.73	3.07	Asahi et al., (2016)
210.28	816.46	4.43	Chapter 2
210.46	816.98	3.75	Chapter 2
210.56	817.27	3.87	Chapter 2
210.78	817.91	3.39	Chapter 2
211.08	818.77	3.64	Chapter 2
211.16	819.01	3.57	Chapter 2

211.45	819.85	3.50	Chapter 2
211.62	820.33	3.44	Chapter 2
211.96	821.32	4.08	Chapter 2
212.09	821.70	3.74	Chapter 2
212.18	821.95	3.44	Chapter 2
212.53	822.97	3.10	Chapter 2
212.68	823.40	3.30	Chapter 2
213.20	824.92	3.10	Asahi et al., (2016)
213.42	825.55	3.50	Chapter 2
213.50	825.79	3.43	Asahi et al., (2016)
213.80	826.66	3.29	Asahi et al., (2016)
214.10	827.53	3.34	Asahi et al., (2016)
214.25	827.94	3.49	Asahi et al., (2016)
214.55	828.82	3.53	Asahi et al., (2016)
215.00	830.13	3.57	Asahi et al., (2016)
215.03	830.22	3.81	Chapter 2
215.30	831.00	3.66	Asahi et al., (2016)
215.60	831.87	3.45	Asahi et al., (2016)
215.90	832.73	3.24	Asahi et al., (2016)
216.07	833.23	2.99	Asahi et al., (2016)
216.20	833.60	3.62	Asahi et al., (2016)
216.49	834.44	3.20	Asahi et al., (2016)
216.67	834.95	3.48	Asahi et al., (2016)
216.80	835.34	3.27	Asahi et al., (2016)
217.10	836.21	3.44	Asahi et al., (2016)
217.34	836.90	3.40	Chapter 2
217.40	837.07	3.22	Asahi et al., (2016)
217.70	837.94	3.33	Asahi et al., (2016)
218.11	839.11	4.15	Chapter 2
219.21	842.30	3.99	Chapter 2
219.80	843.99	3.31	Asahi et al., (2016)

219.88	844.23	2.97	Kender et al., (2018)
219.97	844.49	3.12	Kender et al., (2018)
220.07	844.78	3.08	Kender et al., (2018)
220.13	844.96	3.16	Kender et al., (2018)
220.20	845.16	3.27	Kender et al., (2018)
220.29	845.42	3.25	Kender et al., (2018)
220.33	845.54	2.91	Asahi et al., (2016)
220.37	845.65	3.26	Kender et al., (2018)
220.45	845.88	3.22	Kender et al., (2018)
220.54	846.14	3.33	Kender et al., (2018)
220.61	846.35	3.41	Kender et al., (2018)
220.69	846.58	3.43	Kender et al., (2018)
220.77	846.81	3.38	Kender et al., (2018)
220.84	847.01	3.06	Kender et al., (2018)
220.94	847.30	3.28	Kender et al., (2018)
220.98	847.42	3.16	Kender et al., (2018)
221.06	847.65	3.13	Kender et al., (2018)
221.13	847.85	3.25	Kender et al., (2018)
221.23	848.14	3.62	Kender et al., (2018)
221.38	848.57	3.18	Kender et al., (2018)
221.47	848.83	3.30	Kender et al., (2018)
221.57	849.12	3.23	Kender et al., (2018)
221.63	849.30	3.33	Kender et al., (2018)
221.70	849.50	3.27	Kender et al., (2018)
221.80	849.79	3.30	Chapter 2
221.87	849.99	3.21	Kender et al., (2018)
221.95	850.22	3.06	Kender et al., (2018)

222.01	850.40	3.20	Kender et al., (2018)
222.09	850.63	3.00	Kender et al., (2018)
222.17	850.86	3.14	Kender et al., (2018)
222.24	851.06	3.02	Kender et al., (2018)
222.31	851.26	2.97	Kender et al., (2018)
222.38	851.47	3.10	Kender et al., (2018)
222.53	851.90	2.81	Kender et al., (2018)
222.63	852.19	2.91	Kender et al., (2018)
222.69	852.36	2.96	Kender et al., (2018)
222.78	852.62	2.92	Kender et al., (2018)
222.84	852.80	2.88	Kender et al., (2018)
222.97	853.17	3.08	Kender et al., (2018)
223.03	853.35	3.02	Kender et al., (2018)
223.08	853.49	3.07	Kender et al., (2018)
223.19	853.81	3.10	Kender et al., (2018)
223.27	854.04	3.15	Kender et al., (2018)
223.35	854.27	3.24	Kender et al., (2018)
223.42	854.47	3.18	Kender et al., (2018)
223.50	854.71	3.30	Kender et al., (2018)
223.58	854.94	3.27	Kender et al., (2018)
223.65	855.14	3.36	Kender et al., (2018)
223.72	855.34	3.32	Kender et al., (2018)
223.79	855.55	3.27	Kender et al., (2018)
223.88	855.81	3.46	Kender et al., (2018)
223.94	855.98	3.40	Kender et al., (2018)
224.01	856.20	3.19	Kender et al., (2018)

224.04	856.27	3.28	Kender et al., (2018)
224.09	856.43	3.46	Kender et al., (2018)
224.19	856.70	3.27	Kender et al., (2018)
224.24	856.86	3.22	Kender et al., (2018)
224.31	857.06	3.24	Kender et al., (2018)
224.38	857.27	3.13	Kender et al., (2018)
224.44	857.43	3.28	Kender et al., (2018)
224.51	857.63	3.23	Kender et al., (2018)
224.63	857.99	3.14	Kender et al., (2018)
224.69	858.16	3.22	Kender et al., (2018)
224.78	858.42	3.15	Kender et al., (2018)
224.87	858.68	3.13	Kender et al., (2018)
224.97	858.97	2.94	Kender et al., (2018)
225.03	859.15	2.95	Kender et al., (2018)
225.10	859.35	3.01	Kender et al., (2018)
225.19	859.61	3.37	Kender et al., (2018)
225.27	859.84	2.76	Kender et al., (2018)
225.35	860.07	2.89	Kender et al., (2018)
225.41	860.25	2.97	Kender et al., (2018)
225.59	860.77	2.81	Kender et al., (2018)
225.65	860.92	2.82	Asahi et al., (2016)
225.74	861.20	2.93	Kender et al., (2018)
225.81	861.40	3.04	Kender et al., (2018)
225.97	861.87	3.09	Kender et al., (2018)
226.11	862.27	3.12	Asahi et al., (2016)
226.19	862.50	2.76	Kender et al., (2018)

226.28	862.76	3.05	Kender et al., (2018)
226.28	862.76	3.10	Kender et al., (2018)
226.37	863.02	3.19	Kender et al., (2018)
226.47	863.31	2.75	Kender et al., (2018)
226.47	863.31	3.29	Kender et al., (2018)
226.53	863.49	3.21	Kender et al., (2018)
226.60	863.69	3.42	Kender et al., (2018)
226.69	863.95	3.46	Kender et al., (2018)
226.77	864.18	3.61	Kender et al., (2018)
226.85	864.41	3.63	Kender et al., (2018)
226.90	864.55	3.67	Asahi et al., (2016)
227.09	865.11	3.53	Kender et al., (2018)
227.14	865.23	4.10	Asahi et al., (2016)
227.17	865.34	3.58	Kender et al., (2018)
227.24	865.54	3.70	Kender et al., (2018)
227.31	865.74	3.61	Kender et al., (2018)
227.38	865.95	3.54	Kender et al., (2018)
227.46	866.32	3.54	Kender et al., (2018)
227.53	866.65	3.41	Kender et al., (2018)
227.63	867.12	3.56	Kender et al., (2018)
227.69	867.40	3.61	Kender et al., (2018)
227.87	868.25	3.94	Kender et al., (2018)
227.96	868.67	3.98	Kender et al., (2018)
228.04	869.04	3.89	Kender et al., (2018)
228.10	869.31	3.90	Kender et al., (2018)
228.12	869.42	4.13	Kender et al., (2018)

228.14	869.50	4.33	Asahi et al., (2016)
228.18	869.68	3.90	Kender et al., (2018)
228.19	869.75	3.98	Kender et al., (2018)
228.26	870.06	3.96	Kender et al., (2018)
228.26	870.08	3.82	Kender et al., (2018)
228.33	870.39	3.97	Kender et al., (2018)
228.33	870.41	4.08	Kender et al., (2018)
228.48	871.10	3.86	Asahi et al., (2016)
228.48	871.11	3.90	Kender et al., (2018)
228.50	871.19	4.02	Kender et al., (2018)
228.58	871.58	3.75	Kender et al., (2018)
228.58	871.58	3.88	Kender et al., (2018)
228.73	872.29	4.00	Kender et al., (2018)
228.82	872.71	3.93	Kender et al., (2018)
228.87	872.93	4.11	Kender et al., (2018)
228.92	873.18	3.80	Kender et al., (2018)
228.96	873.35	3.96	Kender et al., (2018)
228.98	873.46	3.95	Kender et al., (2018)
229.04	873.73	3.86	Kender et al., (2018)
229.05	873.79	4.02	Kender et al., (2018)
229.06	873.83	4.04	Asahi et al., (2016)
229.12	874.10	3.88	Kender et al., (2018)
229.14	874.22	3.75	Kender et al., (2018)
229.19	874.43	3.82	Kender et al., (2018)
229.19	874.43	3.84	Kender et al., (2018)
229.22	874.59	3.80	Kender et al., (2018)

229.28	874.86	4.02	Kender et al., (2018)
229.34	875.14	3.76	Asahi et al., (2016)
229.36	875.23	3.81	Kender et al., (2018)
229.44	875.61	3.94	Kender et al., (2018)
229.56	876.18	3.40	Asahi et al., (2016)
229.60	876.36	3.83	Kender et al., (2018)
229.64	876.55	3.54	Asahi et al., (2016)
229.68	876.74	3.59	Kender et al., (2018)
229.76	877.11	3.87	Kender et al., (2018)
229.90	877.77	3.98	Kender et al., (2018)
229.94	877.96	3.93	Asahi et al., (2016)
229.97	878.10	3.73	Kender et al., (2018)
230.06	878.52	4.24	Kender et al., (2018)
230.12	878.80	3.96	Kender et al., (2018)
230.22	879.28	4.20	Kender et al., (2018)
230.37	879.98	3.88	Kender et al., (2018)
230.46	880.40	4.10	Kender et al., (2018)
230.56	880.87	3.93	Kender et al., (2018)
230.56	880.87	4.03	Kender et al., (2018)
230.58	880.97	3.87	Asahi et al., (2016)
230.69	881.48	3.92	Kender et al., (2018)
230.78	881.91	4.07	Kender et al., (2018)
230.78	881.91	4.20	Kender et al., (2018)
230.84	882.19	3.64	Asahi et al., (2016)
230.86	882.28	4.06	Kender et al., (2018)
230.94	882.66	4.07	Kender et al., (2018)

231.05	883.18	4.04	Asahi et al., (2016)
231.14	883.61	3.97	Asahi et al., (2016)
231.18	883.79	4.19	Kender et al., (2018)
231.26	884.16	4.32	Kender et al., (2018)
231.44	885.01	3.97	Asahi et al., (2016)
231.47	885.15	4.03	Kender et al., (2018)
231.56	885.57	4.08	Kender et al., (2018)
231.62	885.86	3.91	Kender et al., (2018)
231.74	886.43	3.66	Asahi et al., (2016)
231.78	886.61	3.98	Kender et al., (2018)
231.87	887.03	4.02	Kender et al., (2018)
232.04	887.84	3.91	Asahi et al., (2016)
232.12	888.21	3.87	Kender et al., (2018)
232.19	888.54	3.94	Kender et al., (2018)
232.28	888.96	3.79	Kender et al., (2018)
232.28	888.96	4.19	Kender et al., (2018)
232.34	889.25	3.69	Asahi et al., (2016)
232.36	889.34	4.12	Kender et al., (2018)
232.44	889.71	3.83	Kender et al., (2018)
232.56	890.28	3.78	Asahi et al., (2016)
232.60	890.46	3.82	Kender et al., (2018)
232.64	890.66	3.60	Asahi et al., (2016)
232.68	890.84	3.70	Kender et al., (2018)
232.76	891.22	3.87	Kender et al., (2018)
232.83	891.55	3.35	Kender et al., (2018)
232.90	891.87	3.59	Kender et al., (2018)

232.94	892.07	3.61	Asahi et al., (2016)
232.97	892.20	3.87	Kender et al., (2018)
233.05	892.58	3.78	Kender et al., (2018)
233.05	892.58	3.95	Kender et al., (2018)
233.12	892.91	3.87	Kender et al., (2018)
233.22	893.38	3.83	Kender et al., (2018)
233.24	893.48	3.80	Asahi et al., (2016)
233.28	893.66	3.77	Kender et al., (2018)
233.37	894.08	3.77	Kender et al., (2018)
233.46	894.51	4.26	Kender et al., (2018)
233.54	894.89	3.48	Asahi et al., (2016)
233.56	894.98	4.31	Kender et al., (2018)
233.62	895.26	3.91	Kender et al., (2018)
233.62	895.26	4.05	Kender et al., (2018)
233.69	895.59	3.61	Kender et al., (2018)
233.78	896.01	3.64	Kender et al., (2018)
233.84	896.30	3.57	Asahi et al., (2016)
233.86	896.39	3.63	Kender et al., (2018)
233.92	896.67	3.79	Kender et al., (2018)
234.06	897.33	3.55	Asahi et al., (2016)
234.10	897.52	3.88	Kender et al., (2018)
234.14	897.71	3.53	Asahi et al., (2016)
234.18	897.89	3.43	Kender et al., (2018)
234.26	898.27	3.56	Kender et al., (2018)
234.26	898.27	3.63	Kender et al., (2018)
234.33	898.60	3.46	Kender et al., (2018)

234.33	898.60	3.72	Kender et al., (2018)
234.40	898.93	3.52	Kender et al., (2018)
234.40	898.93	3.61	Kender et al., (2018)
234.44	899.12	3.50	Asahi et al., (2016)
234.47	899.26	3.57	Kender et al., (2018)
234.47	899.26	3.78	Kender et al., (2018)
234.56	899.68	3.89	Kender et al., (2018)
234.64	900.06	3.64	Kender et al., (2018)
234.64	900.06	3.68	Kender et al., (2018)
234.72	900.43	3.36	Kender et al., (2018)
234.72	900.43	3.63	Kender et al., (2018)
234.74	900.53	3.22	Asahi et al., (2016)
234.78	900.71	3.49	Kender et al., (2018)
234.78	900.71	3.74	Kender et al., (2018)
234.87	901.14	3.62	Kender et al., (2018)
234.87	901.14	3.72	Kender et al., (2018)
234.96	901.56	3.50	Kender et al., (2018)
234.96	901.56	3.81	Kender et al., (2018)
235.04	901.94	3.70	Asahi et al., (2016)
235.06	902.03	3.84	Kender et al., (2018)
235.06	902.03	3.89	Kender et al., (2018)
235.12	902.31	3.70	Kender et al., (2018)
235.19	902.64	3.60	Kender et al., (2018)
235.28	903.06	3.57	Kender et al., (2018)
235.34	903.35	3.62	Asahi et al., (2016)
235.36	903.44	3.67	Kender et al., (2018)

235.44	903.82	3.65	Kender et al., (2018)
235.53	904.24	3.60	Kender et al., (2018)
235.60	904.57	3.71	Kender et al., (2018)
235.60	904.57	3.73	Kender et al., (2018)
235.68	904.94	3.51	Kender et al., (2018)
235.76	905.32	3.38	Kender et al., (2018)
235.83	905.65	3.51	Kender et al., (2018)
235.90	905.98	3.65	Kender et al., (2018)
235.94	906.17	3.64	Asahi et al., (2016)
235.97	906.31	3.55	Kender et al., (2018)
236.06	906.73	3.51	Kender et al., (2018)
236.12	907.01	3.55	Kender et al., (2018)
236.22	907.48	3.43	Kender et al., (2018)
236.28	907.77	3.28	Kender et al., (2018)
236.37	908.19	3.69	Kender et al., (2018)
236.40	908.33	3.56	Kender et al., (2018)
236.40	908.33	3.60	Kender et al., (2018)
236.46	908.61	3.52	Kender et al., (2018)
236.54	908.99	3.58	Asahi et al., (2016)
236.56	909.08	3.64	Kender et al., (2018)
236.56	909.08	3.65	Kender et al., (2018)
236.62	909.36	3.69	Kender et al., (2018)
236.62	909.36	3.37	Kender et al., (2018)
236.71	909.79	4.40	Kender et al., (2018)
236.80	910.21	3.69	Kender et al., (2018)
236.82	910.31	3.91	Asahi et al., (2016)

236.90	910.68	3.67	Kender et al., (2018)
236.96	910.96	3.74	Kender et al., (2018)
237.03	911.29	3.94	Kender et al., (2018)
237.12	911.71	3.76	Kender et al., (2018)
237.20	912.09	3.74	Kender et al., (2018)
237.37	912.89	3.52	Kender et al., (2018)
237.44	913.22	3.78	Kender et al., (2018)
237.52	913.60	3.64	Kender et al., (2018)
237.60	913.97	3.56	Kender et al., (2018)
237.67	914.30	3.64	Kender et al., (2018)
237.67	914.30	3.93	Kender et al., (2018)
237.74	914.63	3.57	Kender et al., (2018)
237.81	914.96	3.52	Kender et al., (2018)
237.81	914.96	3.71	Kender et al., (2018)
237.90	915.38	3.70	Kender et al., (2018)
237.96	915.66	3.77	Kender et al., (2018)
238.06	916.13	4.43	Kender et al., (2018)
238.12	916.42	3.81	Kender et al., (2018)
238.13	916.44	3.65	Asahi et al., (2016)
238.21	916.84	3.87	Kender et al., (2018)
238.21	916.84	3.94	Kender et al., (2018)
238.30	917.26	3.65	Kender et al., (2018)
238.40	917.61	3.96	Kender et al., (2018)
238.46	917.77	4.03	Kender et al., (2018)
238.53	917.95	4.16	Kender et al., (2018)
238.62	918.19	4.03	Kender et al., (2018)

238.70	918.40	4.07	Kender et al., (2018)
238.70	918.40	4.13	Kender et al., (2018)
238.78	918.61	4.03	Kender et al., (2018)
238.78	918.61	4.11	Kender et al., (2018)
238.87	918.85	4.77	Kender et al., (2018)
238.94	919.03	4.17	Kender et al., (2018)
239.02	919.24	3.87	Kender et al., (2018)
239.02	919.24	3.97	Kender et al., (2018)
239.10	919.45	3.96	Kender et al., (2018)
239.17	919.63	3.92	Kender et al., (2018)
239.24	919.82	4.00	Kender et al., (2018)
239.31	920.00	3.98	Kender et al., (2018)
239.31	920.00	4.03	Kender et al., (2018)
239.39	920.21	3.79	Kender et al., (2018)
239.39	920.21	3.96	Kender et al., (2018)
239.46	920.40	4.02	Kender et al., (2018)
239.56	920.66	4.12	Kender et al., (2018)
239.62	920.82	3.80	Kender et al., (2018)
239.71	921.05	4.04	Kender et al., (2018)
239.80	921.29	3.92	Kender et al., (2018)
239.91	921.58	3.87	Kender et al., (2018)
239.91	921.58	4.11	Kender et al., (2018)
239.96	921.71	3.88	Kender et al., (2018)
240.12	922.13	3.70	Kender et al., (2018)
240.20	922.34	3.63	Kender et al., (2018)
240.28	922.55	3.61	Kender et al., (2018)

240.37	922.79	3.71	Kender et al., (2018)
240.44	922.97	3.28	Kender et al., (2018)
240.46	923.01	3.65	Asahi et al., (2016)
240.52	923.18	3.88	Kender et al., (2018)
240.60	923.39	3.77	Kender et al., (2018)
240.67	923.58	4.07	Kender et al., (2018)
241.06	924.60	3.97	Kender et al., (2018)
241.38	925.44	3.64	Kender et al., (2018)
241.40	925.49	3.79	Kender et al., (2018)
241.44	925.60	3.80	Kender et al., (2018)
241.46	925.65	3.83	Kender et al., (2018)
241.51	925.78	4.74	Kender et al., (2018)
241.53	925.83	3.64	Kender et al., (2018)
241.63	926.09	3.67	Asahi et al., (2016)
241.72	926.33	3.73	Kender et al., (2018)
241.76	926.43	3.26	Asahi et al., (2016)
241.80	926.54	3.72	Kender et al., (2018)
241.88	926.75	3.64	Kender et al., (2018)
242.02	927.12	3.54	Kender et al., (2018)
242.09	927.31	3.39	Kender et al., (2018)
242.18	927.54	3.41	Kender et al., (2018)
242.24	927.70	3.36	Kender et al., (2018)
242.34	927.96	3.46	Kender et al., (2018)
242.36	928.00	3.38	Asahi et al., (2016)
242.40	928.12	3.45	Kender et al., (2018)
242.58	928.59	3.15	Kender et al., (2018)

242.68	928.86	3.74	Kender et al., (2018)
242.74	929.01	3.07	Kender et al., (2018)
242.90	929.43	3.27	Kender et al., (2018)
242.96	929.58	3.51	Asahi et al., (2016)
243.21	930.25	3.65	Kender et al., (2018)
243.47	930.92	3.58	Asahi et al., (2016)
244.93	934.77	3.64	Kender et al., (2018)
245.08	935.16	3.33	Kender et al., (2018)
245.15	935.35	3.44	Kender et al., (2018)
245.25	935.61	3.41	Kender et al., (2018)
245.59	936.50	3.63	Kender et al., (2018)
245.72	936.84	3.45	Kender et al., (2018)
245.72	936.84	3.45	Kender et al., (2018)
246.21	938.13	3.67	Kender et al., (2018)
246.29	938.34	3.45	Kender et al., (2018)
246.46	938.79	3.37	Kender et al., (2018)
246.48	938.83	3.33	Asahi et al., (2016)
246.50	938.89	3.81	Kender et al., (2018)
246.59	939.13	3.56	Kender et al., (2018)
246.81	939.71	3.07	Kender et al., (2018)
246.90	939.94	3.05	Kender et al., (2018)
246.90	939.94	3.18	Kender et al., (2018)
246.90	939.94	3.22	Kender et al., (2018)
246.99	940.18	3.17	Kender et al., (2018)
246.99	940.18	3.25	Kender et al., (2018)
246.99	940.18	3.35	Kender et al., (2018)

247.07	940.38	3.40	Asahi et al., (2016)
247.09	940.44	3.17	Kender et al., (2018)
247.09	940.44	3.48	Kender et al., (2018)
247.15	940.60	3.06	Kender et al., (2018)
247.15	940.60	3.21	Kender et al., (2018)
247.15	940.60	3.61	Kender et al., (2018)
247.22	940.78	2.96	Kender et al., (2018)
247.22	940.78	3.28	Kender et al., (2018)
247.31	941.02	2.82	Kender et al., (2018)
247.31	941.02	3.26	Kender et al., (2018)
247.35	941.11	3.42	Asahi et al., (2016)
247.67	941.96	3.42	Asahi et al., (2016)
247.71	942.07	3.12	Kender et al., (2018)
247.75	942.18	3.21	Kender et al., (2018)
247.79	942.28	3.10	Kender et al., (2018)
247.82	942.36	3.23	Kender et al., (2018)
247.86	942.47	3.33	Kender et al., (2018)
247.90	942.57	3.26	Kender et al., (2018)
247.93	942.65	3.19	Kender et al., (2018)
247.97	942.74	3.24	Asahi et al., (2016)
247.98	942.78	3.35	Kender et al., (2018)
248.05	942.96	3.21	Kender et al., (2018)
248.19	943.33	3.97	Kender et al., (2018)
248.27	943.53	2.74	Asahi et al., (2016)
248.28	943.57	4.09	Kender et al., (2018)
248.44	943.99	4.12	Kender et al., (2018)

248.57	944.32	3.14	Asahi et al., (2016)
248.59	944.38	3.72	Kender et al., (2018)
248.68	944.62	3.16	Kender et al., (2018)
248.76	944.83	3.24	Kender et al., (2018)
248.76	944.83	3.37	Kender et al., (2018)
248.84	945.04	3.25	Kender et al., (2018)
248.87	945.11	3.25	Asahi et al., (2016)
248.91	945.22	3.18	Kender et al., (2018)
248.91	945.22	3.20	Kender et al., (2018)
249.00	945.46	4.84	Kender et al., (2018)
249.08	945.67	3.40	Kender et al., (2018)
249.16	945.88	3.50	Kender et al., (2018)
249.16	945.88	3.70	Kender et al., (2018)
249.25	946.12	3.34	Kender et al., (2018)
249.25	946.12	3.96	Kender et al., (2018)
249.32	946.30	3.46	Kender et al., (2018)
249.40	946.51	3.08	Kender et al., (2018)
249.48	946.72	2.97	Kender et al., (2018)
249.48	946.72	3.15	Kender et al., (2018)
249.53	946.84	2.70	Asahi et al., (2016)
249.55	946.91	2.95	Kender et al., (2018)
249.55	946.91	2.98	Kender et al., (2018)
249.63	947.12	3.01	Kender et al., (2018)
249.63	947.12	3.34	Kender et al., (2018)
249.69	947.27	3.49	Kender et al., (2018)
249.78	947.51	3.54	Kender et al., (2018)

249.84	947.67	3.03	Kender et al., (2018)
249.94	947.93	3.00	Kender et al., (2018)
250.00	948.09	2.86	Kender et al., (2018)
250.00	948.09	2.96	Kender et al., (2018)
250.00	948.09	2.96	Kender et al., (2018)
250.18	948.56	3.32	Kender et al., (2018)
250.41	949.16	3.16	Kender et al., (2018)
250.82	950.24	3.89	Kender et al., (2018)
250.90	950.45	3.20	Kender et al., (2018)
250.90	950.45	3.49	Kender et al., (2018)
250.97	950.64	3.02	Kender et al., (2018)
251.06	950.89	3.15	Asahi et al., (2016)
251.10	950.98	3.12	Kender et al., (2018)
251.21	951.27	2.98	Kender et al., (2018)
251.21	951.27	3.09	Kender et al., (2018)
251.25	951.37	2.83	Kender et al., (2018)
251.26	951.40	2.79	Kender et al., (2018)
251.32	951.56	3.24	Kender et al., (2018)
251.36	951.67	3.19	Asahi et al., (2016)
251.38	951.71	2.79	Kender et al., (2018)
251.39	951.74	2.93	Kender et al., (2018)
251.48	951.98	2.99	Kender et al., (2018)
251.51	952.05	2.84	Kender et al., (2018)
251.54	952.13	2.91	Kender et al., (2018)
251.60	952.29	2.92	Kender et al., (2018)
251.60	952.29	3.12	Kender et al., (2018)

251.64	952.40	2.77	Kender et al., (2018)
251.70	952.55	2.91	Kender et al., (2018)
251.76	952.71	2.88	Kender et al., (2018)
251.79	952.79	3.03	Kender et al., (2018)
251.83	952.90	2.90	Kender et al., (2018)
251.88	953.03	2.71	Kender et al., (2018)
251.88	953.03	2.75	Kender et al., (2018)
251.98	953.29	2.87	Kender et al., (2018)
252.04	953.45	2.80	Kender et al., (2018)
252.11	953.63	2.66	Kender et al., (2018)
252.20	953.87	2.97	Kender et al., (2018)
252.28	954.08	2.73	Kender et al., (2018)
252.36	954.29	2.80	Kender et al., (2018)
252.36	954.29	2.93	Kender et al., (2018)
252.45	954.52	2.75	Kender et al., (2018)
252.45	954.52	2.78	Kender et al., (2018)
252.52	954.71	3.29	Kender et al., (2018)
252.56	954.83	2.74	Asahi et al., (2016)
252.60	954.92	3.52	Kender et al., (2018)
252.68	955.13	3.08	Kender et al., (2018)
252.75	955.31	2.75	Kender et al., (2018)
252.84	955.55	2.80	Kender et al., (2018)
252.89	955.68	2.97	Kender et al., (2018)
252.97	955.90	2.79	Asahi et al., (2016)
252.98	955.92	2.97	Kender et al., (2018)
252.98	955.92	3.01	Kender et al., (2018)

253.04	956.07	2.92	Kender et al., (2018)
253.14	956.34	3.08	Kender et al., (2018)
253.20	956.49	2.90	Kender et al., (2018)
253.29	956.73	2.71	Kender et al., (2018)
253.29	956.73	2.75	Kender et al., (2018)
253.38	956.97	2.84	Kender et al., (2018)
253.46	957.19	2.35	Asahi et al., (2016)
253.48	957.23	2.78	Kender et al., (2018)
253.54	957.39	2.79	Kender et al., (2018)
253.61	957.57	2.96	Kender et al., (2018)
253.70	957.81	3.36	Kender et al., (2018)
253.78	958.02	3.02	Kender et al., (2018)
253.86	958.23	3.00	Kender et al., (2018)
254.02	958.65	3.22	Kender et al., (2018)
254.10	958.86	3.30	Kender et al., (2018)
254.18	959.06	3.31	Kender et al., (2018)
254.25	959.20	3.14	Kender et al., (2018)
254.32	959.34	3.44	Kender et al., (2018)
254.36	959.44	3.87	Asahi et al., (2016)
254.40	959.51	3.38	Kender et al., (2018)
254.48	959.67	2.83	Kender et al., (2018)
254.54	959.79	3.50	Kender et al., (2018)
254.64	960.00	3.52	Kender et al., (2018)
254.64	960.00	3.67	Kender et al., (2018)
254.70	960.12	3.54	Kender et al., (2018)
254.79	960.30	3.52	Kender et al., (2018)

254.88	960.49	3.64	Kender et al., (2018)
254.96	960.66	3.57	Asahi et al., (2016)
254.98	960.69	3.75	Kender et al., (2018)
255.04	960.82	3.59	Kender et al., (2018)
255.11	960.96	3.69	Kender et al., (2018)
255.18	961.10	3.62	Kender et al., (2018)
255.28	961.31	3.72	Kender et al., (2018)
255.28	961.31	3.72	Kender et al., (2018)
255.28	961.31	3.72	Kender et al., (2018)
255.36	961.47	3.69	Kender et al., (2018)
255.49	961.74	3.70	Asahi et al., (2016)
255.52	961.80	3.68	Kender et al., (2018)
255.52	961.80	3.76	Kender et al., (2018)
255.56	961.89	4.10	Asahi et al., (2016)
255.60	961.96	3.93	Kender et al., (2018)
255.68	962.12	3.56	Kender et al., (2018)
255.68	962.12	3.70	Kender et al., (2018)
255.75	962.27	3.73	Kender et al., (2018)
255.84	962.45	4.26	Kender et al., (2018)
255.89	962.55	4.00	Kender et al., (2018)
255.98	962.74	3.72	Kender et al., (2018)
256.04	962.86	3.75	Kender et al., (2018)
256.04	962.86	3.86	Kender et al., (2018)
256.12	963.02	3.96	Kender et al., (2018)
256.16	963.11	3.43	Asahi et al., (2016)
256.29	963.37	4.14	Kender et al., (2018)

256.38	963.55	3.82	Kender et al., (2018)
256.46	963.73	3.09	Asahi et al., (2016)
256.48	963.76	4.43	Kender et al., (2018)
256.54	963.88	3.94	Kender et al., (2018)
256.61	964.02	3.94	Kender et al., (2018)
256.61	964.02	3.97	Kender et al., (2018)
256.70	964.21	3.86	Kender et al., (2018)
256.70	964.21	3.93	Kender et al., (2018)
256.74	964.29	3.33	Asahi et al., (2016)
256.76	964.32	3.76	Kender et al., (2018)
256.76	964.32	3.94	Kender et al., (2018)
256.86	964.54	3.82	Kender et al., (2018)
256.98	964.79	3.49	Asahi et al., (2016)
257.02	964.86	3.85	Kender et al., (2018)
257.02	964.86	3.92	Kender et al., (2018)
257.10	965.03	3.84	Kender et al., (2018)
257.18	965.19	3.82	Kender et al., (2018)
257.25	965.33	4.59	Kender et al., (2018)
257.35	965.54	3.86	Kender et al., (2018)
257.39	965.63	3.84	Asahi et al., (2016)
257.47	965.78	3.78	Kender et al., (2018)
257.54	965.93	3.42	Kender et al., (2018)
257.54	965.93	3.68	Kender et al., (2018)
257.64	966.13	3.61	Kender et al., (2018)
257.64	966.13	3.85	Kender et al., (2018)
257.70	966.25	3.54	Kender et al., (2018)

257.79	966.44	3.88	Kender et al., (2018)
257.87	966.60	3.80	Kender et al., (2018)
257.88	966.62	3.87	Kender et al., (2018)
257.96	966.79	3.17	Asahi et al., (2016)
257.98	966.83	3.88	Kender et al., (2018)
258.03	966.93	3.79	Kender et al., (2018)
258.10	967.07	3.94	Kender et al., (2018)
258.11	967.09	3.72	Kender et al., (2018)
258.19	967.25	3.70	Kender et al., (2018)
258.20	967.27	3.87	Kender et al., (2018)
258.25	967.38	3.79	Kender et al., (2018)
258.28	967.44	3.67	Kender et al., (2018)
258.28	967.44	3.81	Kender et al., (2018)
258.33	967.54	3.78	Kender et al., (2018)
258.36	967.60	3.69	Kender et al., (2018)
258.41	967.70	3.71	Kender et al., (2018)
258.41	967.70	3.80	Kender et al., (2018)
258.48	967.85	3.69	Kender et al., (2018)
258.49	967.87	3.09	Asahi et al., (2016)
258.55	967.99	3.62	Kender et al., (2018)
258.62	968.13	3.37	Kender et al., (2018)
258.71	968.32	3.79	Kender et al., (2018)
258.77	968.44	3.69	Kender et al., (2018)
258.87	968.64	3.81	Kender et al., (2018)
258.93	968.77	3.45	Kender et al., (2018)
259.02	968.95	3.76	Kender et al., (2018)

259.11	969.14	3.73	Kender et al., (2018)
259.21	969.34	3.55	Kender et al., (2018)
259.27	969.46	3.52	Kender et al., (2018)
259.34	969.61	3.63	Kender et al., (2018)
259.43	969.79	3.38	Kender et al., (2018)
259.43	969.79	3.51	Kender et al., (2018)
259.51	969.95	3.04	Kender et al., (2018)
259.59	970.12	3.26	Kender et al., (2018)
259.68	970.30	3.37	Kender et al., (2018)
259.75	970.44	3.31	Kender et al., (2018)
259.75	970.44	3.39	Kender et al., (2018)
259.91	970.77	3.13	Kender et al., (2018)
259.91	970.77	3.27	Kender et al., (2018)
259.98	970.91	3.13	Kender et al., (2018)
259.98	970.91	3.37	Kender et al., (2018)
260.05	971.06	3.26	Kender et al., (2018)
260.05	971.06	3.37	Kender et al., (2018)
260.27	971.51	3.58	Kender et al., (2018)
260.37	971.71	3.61	Kender et al., (2018)
260.43	971.83	3.60	Kender et al., (2018)
260.52	972.02	3.47	Kender et al., (2018)
260.55	972.08	3.07	Asahi et al., (2016)
260.60	972.18	3.53	Kender et al., (2018)
260.81	972.61	3.08	Kender et al., (2018)
260.81	972.61	3.29	Kender et al., (2018)
260.84	972.67	2.87	Kender et al., (2018)

260.93	972.86	3.05	Kender et al., (2018)
261.01	973.02	2.58	Kender et al., (2018)
261.09	973.18	3.52	Kender et al., (2018)
261.25	973.51	3.50	Kender et al., (2018)
261.25	973.51	3.53	Kender et al., (2018)
261.33	973.67	3.39	Kender et al., (2018)
261.33	973.67	3.50	Kender et al., (2018)
261.41	973.84	3.46	Kender et al., (2018)
261.41	973.84	3.60	Kender et al., (2018)
261.48	973.98	3.24	Kender et al., (2018)
261.48	973.98	3.61	Kender et al., (2018)
261.55	974.12	3.40	Kender et al., (2018)
261.55	974.12	3.45	Kender et al., (2018)
261.62	974.27	3.36	Kender et al., (2018)
261.62	974.27	3.62	Kender et al., (2018)
261.71	974.45	3.46	Kender et al., (2018)
261.71	974.45	3.54	Kender et al., (2018)
261.77	974.57	3.08	Kender et al., (2018)
261.77	974.57	3.35	Kender et al., (2018)
261.87	974.78	3.34	Kender et al., (2018)
261.87	974.78	3.39	Kender et al., (2018)
261.93	974.90	3.41	Kender et al., (2018)
261.93	974.90	3.49	Kender et al., (2018)
262.02	975.08	3.16	Kender et al., (2018)
262.02	975.08	3.43	Kender et al., (2018)
262.11	975.27	3.09	Kender et al., (2018)

262.11	975.27	3.11	Kender et al., (2018)
263.13	977.35	3.40	Kender et al., (2018)
263.13	977.35	3.59	Kender et al., (2018)
263.17	977.44	3.10	Asahi et al., (2016)
263.23	977.56	3.52	Kender et al., (2018)
263.23	977.56	3.76	Kender et al., (2018)
263.31	977.72	3.39	Kender et al., (2018)
263.31	977.72	3.51	Kender et al., (2018)
263.38	977.86	3.40	Kender et al., (2018)
263.38	977.86	3.59	Kender et al., (2018)
263.45	978.01	3.42	Kender et al., (2018)
263.45	978.01	3.71	Kender et al., (2018)
263.57	978.25	3.43	Kender et al., (2018)
263.57	978.25	3.61	Kender et al., (2018)
263.59	978.30	3.31	Asahi et al., (2016)
263.64	978.40	3.21	Kender et al., (2018)
263.64	978.40	3.51	Kender et al., (2018)
263.87	978.87	3.28	Kender et al., (2018)
263.92	978.97	3.10	Kender et al., (2018)
263.92	978.97	3.36	Kender et al., (2018)
264.00	979.13	2.92	Kender et al., (2018)
264.00	979.13	3.28	Kender et al., (2018)
264.02	979.18	2.91	Asahi et al., (2016)
264.05	979.23	3.15	Kender et al., (2018)
264.05	979.23	3.35	Kender et al., (2018)
264.13	979.40	3.17	Kender et al., (2018)

264.13	979.40	3.40	Kender et al., (2018)
264.19	979.52	3.32	Kender et al., (2018)
264.19	979.52	3.45	Kender et al., (2018)
264.25	979.64	3.29	Kender et al., (2018)
264.25	979.64	3.40	Kender et al., (2018)
264.50	980.15	3.17	Kender et al., (2018)
264.63	980.42	3.45	Kender et al., (2018)
264.67	980.51	3.42	Asahi et al., (2016)
264.73	980.62	3.37	Kender et al., (2018)
264.81	980.79	3.47	Kender et al., (2018)
264.88	980.93	3.46	Kender et al., (2018)
264.95	981.07	3.59	Kender et al., (2018)
265.07	981.32	3.71	Kender et al., (2018)
265.09	981.37	3.46	Asahi et al., (2016)
265.37	981.93	3.40	Kender et al., (2018)
265.37	981.93	3.69	Kender et al., (2018)
265.42	982.03	3.92	Kender et al., (2018)
265.52	982.25	3.57	Asahi et al., (2016)
265.63	982.46	3.10	Kender et al., (2018)
265.69	982.59	3.47	Kender et al., (2018)
265.75	982.71	3.49	Kender et al., (2018)
265.86	982.93	3.10	Kender et al., (2018)
265.86	982.93	3.65	Kender et al., (2018)
265.88	982.98	3.44	Asahi et al., (2016)
265.93	983.08	3.42	Kender et al., (2018)
266.09	983.40	3.39	Asahi et al., (2016)

266.13	983.49	3.42	Kender et al., (2018)
266.13	983.49	3.88	Kender et al., (2018)
266.17	983.62	3.32	Asahi et al., (2016)
266.23	983.78	3.68	Kender et al., (2018)
266.23	983.78	3.81	Kender et al., (2018)
266.23	983.78	4.01	Kender et al., (2018)
266.31	984.03	3.75	Kender et al., (2018)
266.31	984.03	4.13	Kender et al., (2018)
266.38	984.24	3.46	Kender et al., (2018)
266.38	984.24	3.72	Kender et al., (2018)
266.45	984.45	3.72	Kender et al., (2018)
266.57	984.81	3.78	Kender et al., (2018)
266.59	984.89	3.15	Asahi et al., (2016)
266.64	985.02	3.80	Kender et al., (2018)
266.73	985.30	4.00	Kender et al., (2018)
266.79	985.48	3.33	Kender et al., (2018)
266.87	985.72	3.70	Kender et al., (2018)
266.92	985.87	3.77	Kender et al., (2018)
267.00	986.12	3.77	Kender et al., (2018)
267.13	986.51	3.60	Kender et al., (2018)
267.19	986.69	3.57	Kender et al., (2018)
267.25	986.87	3.60	Kender et al., (2018)
267.36	987.21	3.69	Kender et al., (2018)
267.43	987.42	3.67	Kender et al., (2018)
267.43	987.42	3.73	Kender et al., (2018)
267.63	988.02	3.68	Kender et al., (2018)

267.67	988.16	3.20	Asahi et al., (2016)
267.73	988.33	3.70	Kender et al., (2018)
267.81	988.57	3.55	Kender et al., (2018)
267.88	988.78	3.63	Kender et al., (2018)
267.88	988.78	3.65	Kender et al., (2018)
267.95	988.99	3.45	Kender et al., (2018)
268.07	989.36	3.58	Kender et al., (2018)
268.23	989.84	3.61	Kender et al., (2018)
268.23	989.84	3.72	Kender et al., (2018)
268.29	990.02	3.68	Kender et al., (2018)
268.42	990.42	3.67	Kender et al., (2018)
268.42	990.42	3.68	Kender et al., (2018)
268.42	990.42	3.78	Kender et al., (2018)
268.69	991.24	3.70	Kender et al., (2018)
268.75	991.42	3.67	Kender et al., (2018)
268.75	991.42	3.69	Kender et al., (2018)
269.13	992.57	3.68	Kender et al., (2018)
269.38	993.33	3.62	Kender et al., (2018)
269.45	993.54	3.63	Kender et al., (2018)
269.45	993.54	3.86	Kender et al., (2018)
269.57	993.90	3.52	Kender et al., (2018)
269.57	993.90	3.61	Kender et al., (2018)
269.64	994.11	3.53	Kender et al., (2018)
269.79	994.57	3.49	Kender et al., (2018)
269.87	994.81	3.55	Kender et al., (2018)
270.17	995.72	3.18	Asahi et al., (2016)

270.43	996.51	3.37	Kender et al., (2018)
270.43	996.51	3.58	Kender et al., (2018)
270.47	996.64	3.06	Asahi et al., (2016)
270.53	996.81	3.19	Kender et al., (2018)
270.53	996.81	3.61	Kender et al., (2018)
270.61	997.05	3.57	Kender et al., (2018)
270.61	997.05	3.61	Kender et al., (2018)
270.68	997.26	3.49	Kender et al., (2018)
270.68	997.26	3.51	Kender et al., (2018)
270.75	997.48	3.35	Kender et al., (2018)
270.75	997.48	3.45	Kender et al., (2018)
270.75	997.48	3.48	Kender et al., (2018)
270.87	997.84	3.37	Kender et al., (2018)
270.87	997.84	3.43	Kender et al., (2018)
270.89	997.92	3.51	Asahi et al., (2016)
270.94	998.05	3.64	Kender et al., (2018)
271.03	998.33	3.48	Kender et al., (2018)
271.03	998.33	3.60	Kender et al., (2018)
271.09	998.51	3.45	Kender et al., (2018)
271.09	998.51	3.49	Kender et al., (2018)
271.17	998.75	3.36	Kender et al., (2018)
271.17	998.75	3.44	Kender et al., (2018)
271.22	998.90	3.51	Kender et al., (2018)
271.22	998.90	3.55	Kender et al., (2018)
271.30	999.14	3.47	Kender et al., (2018)
271.30	999.14	3.56	Kender et al., (2018)

271.32	999.22	3.48	Asahi et al., (2016)
271.35	999.29	3.55	Kender et al., (2018)
271.35	999.29	3.65	Kender et al., (2018)
271.43	999.54	3.55	Kender et al., (2018)
271.43	999.54	3.59	Kender et al., (2018)
271.51	999.78	3.78	Kender et al., (2018)
271.55	999.92	3.09	Asahi et al., (2016)
271.61	1000.08	3.52	Kender et al., (2018)
271.61	1000.08	3.65	Kender et al., (2018)
271.69	1000.32	3.61	Kender et al., (2018)
271.69	1000.32	3.63	Kender et al., (2018)
271.76	1000.54	3.63	Kender et al., (2018)
271.83	1000.75	3.67	Kender et al., (2018)
271.95	1001.11	3.70	Kender et al., (2018)
271.95	1001.11	3.83	Kender et al., (2018)
271.97	1001.19	3.51	Asahi et al., (2016)
272.02	1001.32	3.69	Kender et al., (2018)
272.17	1001.78	3.53	Kender et al., (2018)
272.17	1001.78	3.71	Kender et al., (2018)
272.25	1002.02	3.73	Kender et al., (2018)
272.25	1002.02	3.88	Kender et al., (2018)
272.30	1002.17	3.78	Kender et al., (2018)
272.30	1002.17	3.79	Kender et al., (2018)
272.38	1002.42	3.68	Kender et al., (2018)
272.38	1002.42	3.72	Kender et al., (2018)
272.38	1002.42	3.73	Kender et al., (2018)

272.40	1002.49	3.59	Asahi et al., (2016)
272.43	1002.57	3.62	Kender et al., (2018)
272.43	1002.57	3.67	Kender et al., (2018)
272.51	1002.81	3.58	Kender et al., (2018)
272.51	1002.81	3.72	Kender et al., (2018)
272.51	1002.81	4.00	Kender et al., (2018)
272.57	1002.99	3.78	Kender et al., (2018)
272.76	1003.53	3.82	Kender et al., (2018)
272.76	1003.53	4.18	Kender et al., (2018)
272.80	1003.65	3.35	Asahi et al., (2016)
272.86	1003.81	3.83	Kender et al., (2018)
272.86	1003.81	3.83	Kender et al., (2018)
272.94	1004.03	3.86	Kender et al., (2018)
272.94	1004.03	3.90	Kender et al., (2018)
273.01	1004.23	3.90	Kender et al., (2018)
273.08	1004.43	4.02	Kender et al., (2018)
273.08	1004.43	4.06	Kender et al., (2018)
273.27	1004.96	3.65	Kender et al., (2018)
273.27	1004.96	3.87	Kender et al., (2018)
273.36	1005.21	3.86	Kender et al., (2018)
273.50	1005.61	3.62	Kender et al., (2018)
273.50	1005.61	3.89	Kender et al., (2018)
273.63	1005.97	3.83	Kender et al., (2018)
273.63	1005.97	3.93	Kender et al., (2018)
273.70	1006.17	3.80	Kender et al., (2018)
273.70	1006.17	3.98	Kender et al., (2018)

273.82	1006.51	1.69	Kender et al., (2018)
273.88	1006.68	4.01	Kender et al., (2018)
273.99	1006.99	3.72	Kender et al., (2018)
273.99	1006.99	3.76	Kender et al., (2018)
273.99	1006.99	3.76	Kender et al., (2018)
274.01	1007.06	3.33	Asahi et al., (2016)
274.06	1007.19	3.38	Kender et al., (2018)
274.20	1007.58	3.69	Asahi et al., (2016)
274.26	1007.75	3.52	Kender et al., (2018)
274.26	1007.75	3.61	Kender et al., (2018)
274.26	1007.75	3.80	Kender et al., (2018)
274.30	1007.87	3.39	Asahi et al., (2016)
274.36	1008.03	3.76	Kender et al., (2018)
274.44	1008.26	3.56	Kender et al., (2018)
274.44	1008.26	3.68	Kender et al., (2018)
274.51	1008.45	4.03	Kender et al., (2018)
274.58	1008.65	3.59	Kender et al., (2018)
274.58	1008.65	3.76	Kender et al., (2018)
274.70	1008.99	3.44	Kender et al., (2018)
274.70	1008.99	3.68	Kender et al., (2018)
274.72	1009.06	2.89	Asahi et al., (2016)
274.77	1009.18	3.72	Kender et al., (2018)
274.77	1009.18	3.72	Kender et al., (2018)
274.86	1009.44	3.69	Kender et al., (2018)
274.86	1009.44	3.74	Kender et al., (2018)
274.92	1009.61	3.65	Kender et al., (2018)

274.92	1009.61	3.85	Kender et al., (2018)
275.05	1009.97	3.62	Kender et al., (2018)
275.05	1009.97	3.70	Kender et al., (2018)
275.13	1010.20	3.54	Kender et al., (2018)
275.20	1010.39	3.49	Kender et al., (2018)
275.26	1010.56	3.74	Kender et al., (2018)
275.32	1010.73	3.63	Kender et al., (2018)
275.38	1010.90	3.83	Kender et al., (2018)
275.49	1011.21	3.59	Kender et al., (2018)
275.49	1011.21	3.97	Kender et al., (2018)
275.51	1011.28	3.10	Asahi et al., (2016)
275.56	1011.41	3.69	Kender et al., (2018)
275.56	1011.41	3.71	Kender et al., (2018)
275.76	1011.97	3.68	Kender et al., (2018)
275.86	1012.25	3.54	Kender et al., (2018)
275.86	1012.25	3.68	Kender et al., (2018)
275.94	1012.48	3.60	Kender et al., (2018)
275.94	1012.48	3.63	Kender et al., (2018)
276.01	1012.67	3.37	Kender et al., (2018)
276.08	1012.87	3.69	Kender et al., (2018)
276.27	1013.41	3.42	Kender et al., (2018)
276.55	1014.19	3.61	Kender et al., (2018)
276.63	1014.42	3.73	Kender et al., (2018)
276.68	1014.56	3.71	Kender et al., (2018)
276.68	1014.56	3.79	Kender et al., (2018)
276.82	1014.96	3.61	Kender et al., (2018)

276.88	1015.12	3.74	Kender et al., (2018)
276.88	1015.12	3.75	Kender et al., (2018)
276.99	1015.43	3.65	Kender et al., (2018)
277.06	1015.63	3.80	Kender et al., (2018)
277.06	1015.63	3.88	Kender et al., (2018)
277.11	1015.77	3.51	Kender et al., (2018)
277.11	1015.77	3.79	Kender et al., (2018)
277.26	1016.19	4.12	Kender et al., (2018)
277.44	1016.70	3.74	Kender et al., (2018)
277.50	1016.87	3.59	Kender et al., (2018)
277.70	1017.43	3.73	Kender et al., (2018)
277.72	1017.50	2.23	Asahi et al., (2016)
277.77	1017.63	3.45	Kender et al., (2018)
277.77	1017.63	3.48	Kender et al., (2018)
277.86	1017.88	3.76	Kender et al., (2018)
277.92	1018.05	3.67	Kender et al., (2018)
277.92	1018.05	3.97	Kender et al., (2018)
278.00	1018.28	3.79	Kender et al., (2018)
278.05	1018.42	3.73	Kender et al., (2018)
278.13	1018.64	3.32	Kender et al., (2018)
278.26	1019.01	3.35	Kender et al., (2018)
278.32	1019.18	3.70	Kender et al., (2018)
278.36	1019.29	3.72	Kender et al., (2018)
278.65	1020.11	3.63	Kender et al., (2018)
278.69	1020.23	2.98	Asahi et al., (2016)
278.75	1020.39	3.60	Kender et al., (2018)

278.83	1020.61	3.38	Kender et al., (2018)
278.90	1020.81	3.28	Kender et al., (2018)
278.97	1021.01	3.52	Kender et al., (2018)
279.09	1021.35	3.33	Kender et al., (2018)
279.11	1021.42	3.10	Asahi et al., (2016)
279.25	1021.80	3.34	Kender et al., (2018)
279.25	1021.80	3.47	Kender et al., (2018)
279.31	1021.96	2.98	Kender et al., (2018)
279.44	1022.33	3.16	Kender et al., (2018)
279.93	1023.71	3.24	Kender et al., (2018)
280.03	1023.99	2.93	Kender et al., (2018)
280.03	1023.99	3.31	Kender et al., (2018)
280.11	1024.22	3.03	Kender et al., (2018)
280.18	1024.41	3.15	Kender et al., (2018)
280.44	1025.15	2.65	Kender et al., (2018)
280.44	1025.15	3.35	Kender et al., (2018)
280.67	1025.79	3.26	Kender et al., (2018)
280.67	1025.79	3.41	Kender et al., (2018)
280.80	1026.16	2.75	Kender et al., (2018)
280.80	1026.16	2.94	Kender et al., (2018)
280.82	1026.23	3.49	Asahi et al., (2016)
280.85	1026.30	2.80	Kender et al., (2018)
280.85	1026.30	3.10	Kender et al., (2018)
280.92	1026.51	2.60	Asahi et al., (2016)
280.93	1026.53	3.20	Kender et al., (2018)
280.93	1026.53	3.26	Kender et al., (2018)

280.99	1026.69	3.05	Kender et al., (2018)
280.99	1026.69	3.31	Kender et al., (2018)
281.01	1026.76	4.00	Asahi et al., (2016)
281.05	1026.86	3.12	Kender et al., (2018)
281.05	1026.86	3.14	Kender et al., (2018)
281.30	1027.57	2.72	Kender et al., (2018)
281.30	1027.57	3.07	Kender et al., (2018)
281.37	1027.76	3.21	Kender et al., (2018)
281.43	1027.93	3.18	Kender et al., (2018)
281.43	1027.93	3.35	Kender et al., (2018)
281.47	1028.06	3.27	Asahi et al., (2016)
281.75	1028.83	3.32	Kender et al., (2018)
281.89	1029.24	3.31	Asahi et al., (2016)
282.32	1030.45	3.07	Asahi et al., (2016)
282.50	1030.95	3.40	Chapter 3
282.68	1031.46	3.37	Asahi et al., (2016)
282.87	1031.92	3.56	Asahi et al., (2016)
282.97	1032.15	3.53	Asahi et al., (2016)
283.39	1033.10	3.78	Asahi et al., (2016)
283.82	1034.07	3.61	Asahi et al., (2016)
284.06	1034.61	3.65	Chapter 3
284.18	1034.89	3.96	Asahi et al., (2016)
284.28	1035.10	3.97	Asahi et al., (2016)
284.47	1035.55	3.78	Asahi et al., (2016)
284.62	1035.87	3.62	Chapter 3
284.89	1036.50	3.64	Asahi et al., (2016)
285.19	1037.17	3.71	Chapter 3
285.32	1037.47	3.77	Asahi et al., (2016)

285.66	1038.24	3.93	Asahi et al., (2016)
285.76	1038.46	3.77	Chapter 3
285.80	1038.56	3.66	Asahi et al., (2016)
285.97	1038.95	3.26	Asahi et al., (2016)
286.26	1039.59	3.71	Chapter 3
286.39	1039.90	3.75	Asahi et al., (2016)
286.82	1040.87	3.05	Asahi et al., (2016)
287.18	1041.69	3.92	Asahi et al., (2016)
287.33	1042.02	3.60	Asahi et al., (2016)
287.47	1042.34	3.60	Asahi et al., (2016)
287.89	1043.30	3.33	Asahi et al., (2016)
288.04	1043.63	3.62	Chapter 3
288.32	1044.27	3.40	Asahi et al., (2016)
288.68	1045.09	3.41	Asahi et al., (2016)
289.39	1046.70	3.18	Asahi et al., (2016)
289.47	1046.88	3.51	Asahi et al., (2016)
289.89	1047.83	3.57	Asahi et al., (2016)
290.56	1049.34	3.63	Chapter 3
290.68	1049.62	3.34	Asahi et al., (2016)
291.26	1050.92	3.69	Chapter 3
291.42	1051.30	3.55	Asahi et al., (2016)
291.82	1052.20	3.18	Asahi et al., (2016)
293.68	1056.42	3.47	Asahi et al., (2016)
293.97	1057.08	3.48	Asahi et al., (2016)
295.33	1060.16	3.56	Asahi et al., (2016)
295.47	1060.48	3.42	Asahi et al., (2016)
295.89	1061.43	3.36	Asahi et al., (2016)
296.32	1062.40	3.19	Asahi et al., (2016)

296.68	1063.28	3.31	Asahi et al., (2016)
296.86	1063.76	3.37	Asahi et al., (2016)
296.97	1064.09	3.36	Asahi et al., (2016)
297.04	1064.27	3.29	Chapter 3
297.39	1065.26	3.02	Asahi et al., (2016)
297.60	1065.83	3.12	Chapter 3
297.82	1066.46	2.99	Asahi et al., (2016)
298.18	1067.46	3.06	Asahi et al., (2016)
298.47	1068.27	2.63	Asahi et al., (2016)
298.76	1069.06	3.18	Chapter 3
298.89	1069.44	2.23	Asahi et al., (2016)
298.97	1069.66	3.36	Asahi et al., (2016)
299.19	1070.28	2.79	Asahi et al., (2016)
299.21	1070.33	2.78	Asahi et al., (2016)
299.61	1071.45	3.05	Asahi et al., (2016)
299.71	1071.73	2.97	Asahi et al., (2016)
299.85	1072.12	2.90	Asahi et al., (2016)
300.27	1073.29	3.29	Asahi et al., (2016)
302.60	1079.79	3.13	Asahi et al., (2016)
303.17	1081.38	3.32	Asahi et al., (2016)
303.60	1082.58	3.45	Asahi et al., (2016)
303.72	1082.90	3.24	Chapter 3
303.96	1083.58	3.61	Asahi et al., (2016)
304.22	1084.29	3.58	Chapter 3
304.25	1084.39	3.53	Asahi et al., (2016)
304.67	1085.56	3.33	Asahi et al., (2016)
305.10	1086.76	3.47	Asahi et al., (2016)
305.28	1087.25	2.72	Chapter 3
305.46	1087.77	3.67	Asahi et al., (2016)

305.82	1088.76	3.02	Chapter 3
306.17	1089.75	3.52	Asahi et al., (2016)
306.38	1090.32	3.61	Chapter 3
306.60	1090.95	3.55	Asahi et al., (2016)
307.20	1092.62	3.72	Asahi et al., (2016)
307.62	1093.79	3.70	Asahi et al., (2016)
307.96	1094.73	3.70	Chapter 3
308.08	1095.07	3.70	Asahi et al., (2016)
308.10	1095.13	3.48	Asahi et al., (2016)
308.47	1096.16	3.69	Asahi et al., (2016)
308.70	1096.78	3.62	Asahi et al., (2016)
308.76	1096.96	3.40	Chapter 3
309.10	1097.91	3.55	Chapter 3
309.12	1097.95	3.31	Asahi et al., (2016)
309.55	1099.15	3.48	Asahi et al., (2016)
310.76	1102.53	2.72	Chapter 3
311.13	1103.56	3.15	Asahi et al., (2016)
311.32	1104.10	2.93	Asahi et al., (2016)
311.42	1104.37	3.11	Asahi et al., (2016)
311.70	1105.16	3.45	Chapter 3
312.63	1107.74	3.24	Asahi et al., (2016)
312.92	1108.55	2.85	Asahi et al., (2016)
313.77	1110.92	3.39	Asahi et al., (2016)
313.88	1111.24	3.36	Chapter 3
314.13	1111.93	3.37	Asahi et al., (2016)
314.32	1112.46	3.31	Asahi et al., (2016)
314.42	1112.73	3.34	Asahi et al., (2016)
314.84	1113.91	3.48	Asahi et al., (2016)
315.27	1115.11	3.62	Asahi et al., (2016)
315.37	1115.41	3.23	Chapter 3

315.69	1116.28	3.89	Asahi et al., (2016)
316.02	1117.20	3.07	Chapter 3
316.02	1117.20	3.46	Chapter 3
316.76	1119.28	3.45	Chapter 3
316.90	1119.65	3.66	Asahi et al., (2016)
317.12	1120.27	3.37	Asahi et al., (2016)
317.53	1121.42	3.99	Asahi et al., (2016)
317.54	1121.44	3.60	Asahi et al., (2016)
317.68	1121.84	3.83	Chapter 3
317.97	1122.66	3.80	Asahi et al., (2016)
318.39	1123.83	3.31	Asahi et al., (2016)
318.54	1124.23	3.34	Chapter 3
318.54	1124.23	4.00	Chapter 3
318.82	1125.04	3.86	Asahi et al., (2016)
318.96	1125.53	3.81	Chapter 3
318.96	1125.53	3.97	Chapter 3
319.18	1126.34	3.96	Asahi et al., (2016)
319.36	1126.98	3.70	Chapter 3
319.39	1127.10	3.98	Asahi et al., (2016)
319.81	1128.62	3.96	Asahi et al., (2016)
320.24	1130.18	3.99	Asahi et al., (2016)
320.60	1131.48	3.46	Asahi et al., (2016)
320.71	1131.88	3.55	Asahi et al., (2016)
320.80	1132.20	3.30	Asahi et al., (2016)
321.09	1133.24	3.94	Chapter 3
321.22	1133.72	3.90	Asahi et al., (2016)
321.51	1134.76	3.63	Chapter 3
321.65	1135.28	3.78	Asahi et al., (2016)
321.89	1136.13	3.78	Chapter 3
322.01	1136.58	3.36	Asahi et al., (2016)
323.51	1142.01	3.08	Asahi et al., (2016)
323.66	1142.54	3.75	Chapter 3

323.69	1142.66	3.34	Asahi et al., (2016)
324.11	1144.18	3.18	Asahi et al., (2016)
324.54	1145.74	3.28	Asahi et al., (2016)
324.75	1146.46	3.48	Chapter 3
324.86	1146.88	3.41	Asahi et al., (2016)
325.19	1148.09	3.95	Asahi et al., (2016)
326.04	1151.17	2.95	Asahi et al., (2016)
326.22	1151.80	3.49	Chapter 3
326.39	1152.43	3.19	Asahi et al., (2016)
326.60	1153.19	3.24	Asahi et al., (2016)
326.97	1154.53	3.38	Asahi et al., (2016)
327.47	1156.31	3.37	Asahi et al., (2016)
327.57	1156.69	3.34	Chapter 3
328.07	1158.49	2.74	Asahi et al., (2016)
328.67	1160.66	3.14	Asahi et al., (2016)
329.23	1162.70	2.95	Chapter 3
329.23	1162.70	3.07	Chapter 3
329.57	1163.91	2.59	Asahi et al., (2016)
329.63	1164.15	3.58	Chapter 3
329.88	1165.03	3.10	Asahi et al., (2016)
330.17	1166.08	3.13	Asahi et al., (2016)
330.75	1168.19	2.84	Chapter 3
331.07	1169.34	3.25	Asahi et al., (2016)
331.97	1172.60	2.96	Asahi et al., (2016)
332.57	1174.77	2.66	Asahi et al., (2016)
332.88	1175.89	3.23	Asahi et al., (2016)
333.07	1176.58	3.09	Asahi et al., (2016)
333.47	1178.02	3.53	Asahi et al., (2016)
334.07	1180.20	3.18	Asahi et al., (2016)

334.38	1181.32	2.95	Asahi et al., (2016)
334.67	1182.37	3.18	Asahi et al., (2016)
334.97	1183.45	3.82	Asahi et al., (2016)
335.27	1184.54	3.19	Asahi et al., (2016)
335.57	1185.62	2.88	Asahi et al., (2016)
336.15	1187.72	3.51	Asahi et al., (2016)
336.45	1188.81	3.43	Asahi et al., (2016)
336.75	1189.89	3.85	Asahi et al., (2016)
336.90	1190.46	3.23	Chapter 3
336.90	1190.46	3.32	Chapter 3
336.95	1190.64	4.06	Asahi et al., (2016)
337.38	1192.19	3.18	Chapter 3
338.32	1195.60	3.34	Chapter 3
339.67	1200.47	3.55	Asahi et al., (2016)
340.64	1203.99	2.95	Unpublished
341.54	1207.25	3.65	Unpublished
342.09	1209.24	3.70	Unpublished
342.52	1210.79	3.71	Unpublished
342.67	1211.32	3.05	Asahi et al., (2016)
343.46	1214.19	2.51	Unpublished
344.16	1216.73	4.08	Unpublished
344.75	1218.84	3.75	Unpublished
345.90	1223.00	3.64	Unpublished
346.14	1223.90	4.95	Unpublished
346.50	1225.17	3.08	Unpublished
346.50	1225.17	3.99	Unpublished

Table 8.3 New bulk sedimentary $\delta^{15}N$ presented in this thesis (Chapter 2-3)

Sample ID	Depth (m CCSF-A)	Age (kyr)	$\delta^{15}N$ (‰)
U1343C_1-1_19-21cm	0.20	7.43	5.42
U1343C_1-1_120-122cm	1.21	11.03	6.95
U1343C-1H-2 W, 79.5--81.5 cm	2.31	14.93	8.25
U1343C-1H-3 W, 89.0--91.0 cm	3.90	20.61	5.83
U1343C-1H-4 W, 22.0--24.0 cm	4.73	23.56	6.48
U1343C-1H-4 W, 90.0--92.0 cm	5.41	25.98	6.05
U1343C-1H-5 W, 10.0--12.0 cm	6.11	28.47	5.66
U1343E-1H-3 W, 59.0--61.0 cm	7.08	31.93	6.32
U1343E_1-4_19-21cm	8.18	35.84	6.46
U1343E-1H-4 W, 88.0--90.0 cm	8.87	38.30	7.35
U1343E-1H-5 W, 38.5--40.5 cm	9.87	41.88	6.84
U1343C-2H-3 W, 77.0--79.0 cm	10.94	45.65	6.28
U1343C_2-4_10-12cm	11.77	48.61	6.89
U1343C_2-4_98-100cm	12.65	51.74	6.72
U1343C-2H-5 W, 36.0--38.0 cm	13.53	54.87	6.23
U1343C_2-5_120-122cm	14.37	57.75	4.91
U1343E_2-3_71-73cm	15.64	62.03	5.16
U1343E_2-4_8-10cm	16.51	64.90	4.60
U1343E-2H-4 W, 90.0--92.0 cm	17.33	67.60	5.00
U1343E-2H-5 W, 98.0--100.0 cm	18.91	72.80	5.26
U1343A-3H-4 W, 109.0--111.0 cm	20.44	77.82	4.50
U1343A-3H-5 W, 72.0--74.0 cm	21.57	81.54	4.90
U1343E_3-1_109-111cm	22.62	84.99	6.46
U1343E-3H-2 W, 120.0--122.0 cm	24.23	90.29	5.75
U1343E_3-3_76-78cm	25.29	93.78	5.41
U1343E_3-4_88-90cm	26.91	99.11	5.93
U1343A_4-3_9-11cm	28.06	102.90	5.59
U1343A_4-3_118.5-120.5cm	29.15	106.51	4.83
U1343A_4-4_119-121cm	30.66	111.46	5.17
U1343A_4-5_76-78cm	31.73	114.98	4.23
U1343A-4H-6 W, 31.0--33.0 cm	32.78	118.44	4.74
U1343E-4H-1 W, 129.0--131.0 cm	33.74	121.60	5.20
U1343E_4-2_38-40cm	34.33	123.54	4.93
U1343E_4-2_96-98cm	34.91	125.45	4.55
U1343E_4-3_8-10cm	35.53	127.49	5.07
U1343E_4-3_37-39cm	35.82	128.45	6.06
U1343E-4H-3 W, 71.0--73.0 cm	36.16	129.57	4.92
U1343E_4-3_107-109cm	36.52	130.78	6.04

U1343E-4H-3 W, 132.0--134.0 cm	36.77	131.63	6.72
U1343E-4H-4 W, 26.0--28.0 cm (2)	37.21	133.58	7.10
U1343E-4H-4 W, 76.0--78.0 cm	37.71	135.79	7.25
U1343E-4H-4 W, 109.0--111.0 cm	38.04	137.25	7.09
U1343E-4H-5 W, 10.0--12.0 cm	38.55	139.51	6.49
U1343E-4H-5 W, 52.0--54.0 cm	38.97	141.36	5.87
U1343E-4H-5 W, 102.0--104.0 cm	39.47	143.58	5.72
U1343E_4-6_9-11cm	40.04	146.10	5.51
U1343C-5H-3 W, 52.0--54.0 cm	40.94	150.10	6.47
U1343C_5-3_119-121cm	41.61	153.06	5.29
U1343C-5H-4 W, 66.0--68.0 cm	42.58	157.35	7.11
U1343C-5H-4 W, 129.0--131.0 cm	43.21	160.14	7.25
U1343C-5H-5 W, 76.0--78.0 cm	44.12	164.17	5.88
U1343E-5H-3 W, 8.0--10.0 cm	45.16	168.79	6.51
U1343E-5H-3 W, 109.0--111.0 cm	46.17	173.26	5.38
U1343A-6H-1 W, 99.0--101.0 cm	47.76	180.26	5.46
U1343A-6H-2 W, 137.5--139.5 cm	49.35	185.71	5.60
U1343A_6-3_99-101cm	50.47	189.29	5.53
U1343A_6-4_51.5-53.5cm	51.49	192.59	4.40
U1343A_6-5_10-12cm	52.58	196.07	5.12
U1343A_6-5_119.5-121.5cm	53.67	199.59	5.11
U1343A_6-6_126-128cm	55.24	204.62	3.63
U1343E_6-2_38-40cm	56.51	208.71	6.62
U1343E_6-2_108-110cm	57.21	210.96	6.20
U1343E-6H-3 W, 130.0--132.0 cm	58.93	216.48	5.49
U1343E_6-4_32-34cm	59.45	218.16	5.35
U1343E-6H-4 W, 109.0--111.0 cm	60.22	220.34	4.63
U1343E-6H-5 W, 76.0--78.0 cm	61.22	222.96	5.20
U1343C_7-3_22-24cm	62.28	225.73	4.35
U1343C_7-3_136.5-138.5cm	63.43	228.73	3.86
U1343C_7-4_109-111cm	64.59	231.78	4.56
U1343E_7-2_0-2cm	66.03	235.53	5.35
U1343E_7-3_19-21cm	67.63	239.72	5.77
U1343E_7-4_36-38cm	69.30	244.58	8.89
U1343A_8-3_79.5-81.5cm	70.89	250.08	6.49
U1343A-8H-4 W, 76.0--78.0 cm	72.35	255.15	5.42
U1343A-8H-5 W, 10.0--12.0 cm	73.19	258.06	5.58
U1343A-8H-5 W, 96.0--98.0 cm	74.05	261.04	5.63
U1343A-8H-6 W, 36.0--38.0 cm	74.90	263.98	5.76
U1343E-8H-1 W, 46.0--48.0 cm	75.54	266.19	5.20
U1343E_8-2_58-60cm	76.18	268.41	5.51
U1343E_8-2_130-132cm	76.90	270.91	6.21
U1343E_8-3_46-48cm	77.56	273.19	5.25
U1343E_8-3_86-88cm	77.96	274.57	5.99

U1343E_8-4_72-74cm	79.23	278.94	6.06
U1343E-8H-5 W, 8.0--10.0 cm	80.09	281.85	6.14
U1343E_8-5_90-92cm	80.91	284.56	6.28
U1343E-8H-6 W, 31.0--33.0 cm	81.82	287.56	6.40
U1343A-9H-3 W, 119.0--121.0 cm	82.48	289.73	5.55
U1343A-9H-4 W, 40.0--42.0 cm	83.19	292.07	5.44
U1343A-9H-4 W, 108.0--110.0 cm	83.87	294.31	5.49
U1343A-9H-5 W, 66.0--68.0 cm	84.90	297.71	4.80
U1343C-10H-2 W, 38.0--40.0 cm	85.54	299.81	5.52
U1343C-10H-2 W, 107.0--109.0 cm	86.23	302.08	5.70
U1343C_10-3_26-28cm	86.92	304.36	5.48
U1343C-10H-3 W, 96.0--98.0 cm	87.62	306.67	5.84
U1343C-10H-4 W, 19.0--21.0 cm	88.35	309.08	5.37
U1343C_10-4_109-111cm	89.25	312.05	5.07
U1343C_10-5_46-48cm	90.12	314.92	5.62
U1343C_10-5_131-133cm	90.97	317.73	6.11
U1343C_10-6_67-69cm	91.83	320.56	5.23
U1343C_10-7_26-28cm	92.72	323.50	5.65
U1343A_10-4_28-30cm	93.63	326.50	4.80
U1343A_10-4_112-114cm	94.47	329.27	5.36
U1343A_10-5_72-74cm	95.57	332.90	4.66
U1343A-10H-5 W, 140.0--142.0 cm	96.25	335.14	5.24
U1343A-10H-6 W, 68.5--70.5 cm	97.03	337.76	5.67
U1343C-11H-2 W, 112.0--114.0 cm	97.56	339.53	6.49
U1343C_11-3_30-32cm	98.24	341.79	5.46
U1343C_11-3_102-104cm	98.96	344.19	4.30
U1343C_11-4_28.5-30.5cm	99.73	346.74	3.94
U1343C-11H-4 W, 88.0--90.0 cm	100.32	348.72	4.87
U1343C-11H-5 W, 8.0--10.0 cm	101.02	351.05	5.32
U1343C-11H-5 W, 96.5--98.5 cm	101.91	354.00	5.41
U1343C-11H-6 W, 36.5--38.5 cm	102.81	357.00	6.88
U1343C-11H-7 W, 30.0--32.0 cm	104.24	361.78	7.43
U1343A-11H-5 W, 80.0--82.0 cm	105.80	366.96	5.84
U1343A-11H-6 W, 69.5--71.5 cm	107.11	371.34	7.43
U1343C-12H-2 W, 28.0--30.0 cm	108.03	374.40	6.23
U1343C_12-2_131.5-133.5cm	109.06	377.84	6.10
U1343C_12-3_85-87cm	110.10	381.29	6.79
U1343C_12-4_54-56cm	111.19	384.92	5.55
U1343C_12-5_36-38cm	112.36	388.82	4.97
U1343A-12H-3 W, 80.0--82.0 cm	113.82	393.67	4.98
U1343A_12-4_38-40cm	114.90	398.12	6.35
U1343A_12-4_80-82cm	115.32	400.60	6.03
U1343A_12-5_20-23cm	116.22	405.94	3.90
U1343A-12H-5 W, 79.0--81.0 cm	116.81	409.38	4.96

U1343A_12-5_132.5-134.5cm	117.34	412.54	5.43
U1343A-12H-6 W, 20.0--23.0 cm	117.72	414.78	5.75
U1343A-12H-6 W, 54.0--56.0 cm	118.06	416.75	5.62
U1343A-12H-6 W, 88.0--90.0 cm	118.40	418.76	6.20
U1343A-12H-6 W, 108.5--110.5 cm	118.60	419.97	6.25
U1343C-13H-2 W, 119.0--121.0 cm	119.15	423.19	7.25
U1343C_13-3_36-38cm	119.74	426.46	4.84
U1343C_13-3_78-80cm	120.16	428.71	5.14
U1343C_13-3_143-145cm	120.81	432.20	3.97
U1343C_13-4_54-56cm	121.42	435.47	3.13
U1343C_13-4_116-118cm	122.04	438.79	4.57
U1343C-13H-5 W, 8.0--10.0 cm	122.46	441.04	6.72
U1343C-13H-5 W, 63.0--65.0 cm	123.01	443.99	5.10
U1343C-13H-5 W, 107.0--109.0 cm	123.45	446.35	5.80
U1343C_13-6_108-110cm	124.96	454.44	3.59
U1343A-13H-3 W, 87.5--89.5 cm	125.11	455.27	5.79
U1343A_13-3_119.5-121.5cm	125.43	456.99	4.33
U1343A-13H-4 W, 30.0--32.0 cm	126.04	460.23	4.78
U1343A_13-4_88-90cm	126.62	463.34	3.09
U1343A_13-5_7.5-9.5cm	127.31	467.07	5.85
U1343A-13H-5 W, 102.0--104.0 cm	128.26	472.13	5.27
U1343C_14-1_84-86cm	129.74	478.17	4.05
U1343C_14-2_36-38cm	130.76	482.00	4.48
U1343C_14-3_40-42cm	132.30	486.00	5.62
U1343C_14-4_68-71cm	133.91	489.38	6.04
U1343A_14-3_8-10cm	135.74	493.24	5.71
U1343A-14H-4 W, 30.0--32.0 cm	137.41	496.75	6.61
U1343A-14H-4 W, 145.0--147.0 cm	138.56	499.18	6.89
U1343A-14H-5 W, 109.0--111.0 cm	139.70	501.58	4.98
U1343A-14H-6 W, 80.0--82.0 cm	140.83	503.96	6.39
U1343C_15-2_108-110cm	141.75	505.90	4.97
U1343C_15-3_96-98cm	142.93	508.39	5.96
U1343C-15H-4 W, 53.0--55.0 cm	144.00	510.64	5.77
U1343C-15H-5 W, 6.0--8.0 cm	144.93	512.60	6.51
U1343C-15H-5 W, 88.0--90.0 cm	145.75	516.20	5.83
U1343C-15H-6 W, 23.0--25.0 cm	146.60	520.15	6.09
U1343C-15H-6 W, 88.0--90.0 cm	147.25	523.17	5.67
U1343C-15H-7 W, 31.0--33.0 cm	147.96	526.48	5.71
U1343A-15H-5 W, 36.0--38.0 cm	148.71	529.94	6.12
U1343A-15H-6, 0.0 cm	149.85	535.24	6.69
U1343A-15H-6, 62.0 cm	150.47	538.12	6.87
U1343A-15H-6, 102.0 cm	150.87	539.99	5.03
U1343A-15H-6, 112.0 cm	150.97	540.45	5.33
U1343A-15H-7, 68.0 cm	151.96	545.06	4.52

U1343E-17H-3, 68.0 cm	152.05	545.45	4.59
U1343E-17H-4, 68.0 cm	153.55	550.93	5.24
U1343E_17-5_30-32cm	154.67	555.03	5.59
U1343E-17H-5, 102.0 cm	155.39	557.66	6.98
U1343A-16H-2, 68.0 cm	156.23	560.75	5.01
U1343A-16H-3, 52.0 cm	157.57	565.65	6.17
U1343A_16-4_8-10cm	158.63	569.52	5.93
U1343A-16H-4, 118.0 cm	159.73	573.55	6.50
U1343A_16-5_72-74cm	160.77	577.35	4.75
U1343A-16H-6, 37.0 cm	161.69	580.70	7.07
U1343A-16H-6, 102.0 cm	162.34	582.96	6.13
U1343E_18-4_46-48cm	163.30	586.29	4.93
U1343E_18-5_87-89cm	165.04	592.34	5.27
U1343E-18H-6, 16.0 cm	165.83	595.08	4.81
U1343E_18-6_68-70cm	166.35	596.89	6.07
U1343A-17H-2, 52.0 cm	167.39	600.52	4.63
U1343E-18H-8, 26.0 cm	168.09	602.96	5.90
U1343A-17H-2, 134.0 cm	168.21	603.36	5.65
U1343A-17H-3, 52.0 cm	168.79	605.38	5.87
U1343A-17H-3, 102.0 cm	169.29	607.12	6.66
U1343A-17H-4, 16.0 cm	169.84	609.03	6.29
U1343A_17-4_62-64cm	170.30	610.63	7.48
U1343A-17H-4, 118.0 cm	170.86	612.58	6.42
U1343A_17-5_8-10cm	171.26	613.97	4.42
U1343A-17H-5, 37.0 cm	171.55	614.98	5.84
U1343A-17H-5, 68.0 cm	171.86	616.06	5.53
U1343A_17-5_109-111cm	172.27	617.48	3.42
U1343A_17-5_143-145cm	172.61	618.67	4.32
U1343C-18H-2, 54.0 cm	172.92	619.76	6.69
U1343A-17H-6, 62.0 cm	173.30	621.06	6.20
U1343A-17H-6, 77.0 cm	173.45	622.35	5.51
U1343C-18H-2, 126.0 cm	173.64	625.60	5.97
U1343A-17H-6, 122.0 cm	173.90	629.84	5.07
U1343C-18H-3, 8.0 cm	173.96	630.94	4.88
U1343C-18H-3, 46.0 cm	174.34	637.28	3.99
U1343C_18-3_96-98cm	174.84	642.74	4.85
U1343C-18H-3, 109.0 cm	174.97	643.54	4.77
U1343C_18-3_129-131cm	175.17	644.78	4.75
U1343C-18H-4, 16.0 cm	175.54	647.07	4.93
U1343C-18H-4, 62.0 cm	176.00	649.92	5.50
U1343C-18H-4, 118.0 cm	176.56	653.39	5.75
U1343C_18-5_46-48cm	177.34	658.22	5.49
U1343C-18H-5, 118.0 cm	178.06	662.68	4.68
U1343C-18H-6, 0.0 cm	178.38	664.67	4.59

U1343C_18-6_86-88cm	179.24	669.99	3.19
U1343C_18-6_115-117cm	179.53	671.79	3.85
U1343C-18H-6, 118.0 cm	179.56	671.98	5.04
U1343A-18H-4, 45.0 cm	180.32	676.69	6.08
U1343A-18H-4, 102.0 cm	180.89	680.22	6.03
U1343A_18-5_8-10cm	181.45	683.69	4.12
U1343A-18H-5, 68.0 cm	182.05	687.41	6.00
U1343E-20H-2, 52.0 cm	182.63	690.94	6.42
U1343E_20-2_109-111cm	183.20	694.47	4.94
U1343E_20-3_23-25cm	183.76	697.94	2.72
U1343E_20-3_77-79cm	184.30	701.28	4.36
U1343E-20H-4, 46.0 cm	185.24	707.09	6.62
U1343E_20-4_109-111cm	185.87	710.99	5.76
U1343E-20H-5, 0.0 cm	186.28	713.52	5.56
U1343E-20H-5, 77.0 cm	187.05	718.28	5.23
U1343E_20-6_10-12cm	187.88	723.41	5.89
U1343E_20-6_51-53cm	188.29	726.14	4.16
U1343C-19H-4, 77.0 cm	188.83	730.53	5.33
U1343C-19H-4, 126.0 cm	189.32	734.64	5.59
U1343C-19H-5, 30.0 cm	189.86	739.17	5.55
U1343C-19H-5, 86.0 cm	190.42	743.86	7.49
U1343C_19-5_114-116cm	190.70	746.21	5.98
U1343E-21H-2, 30.0 cm	191.54	753.24	4.53
U1343E_21-2_109-111cm	192.33	755.93	5.33
U1343E-21H-3, 45.0 cm	193.19	758.60	7.40
U1343E-21H-3, 109.0 cm	193.83	760.58	5.98
U1343E_21-4_30-32cm	194.54	762.78	7.67
U1343E_21-4_126-128cm	195.50	765.76	4.02
U1343C-20H-3, 52.0 cm	196.51	768.89	4.79
U1343C-20H-3, 126.0 cm	197.25	771.18	6.38
U1343C_20-4_66-68cm	198.05	773.66	5.81
U1343C-20H-5, 8.0 cm	198.97	776.51	5.12
U1343C-20H-5, 96.0 cm	199.85	779.24	6.66
U1343C-20H-6, 30.0 cm	200.69	781.84	5.92
U1343E_22-1_77-79cm	202.14	786.34	4.41
U1343E-22H-2, 102.0 cm	203.89	792.07	5.36
U1343E-22H-3, 118.0 cm	205.45	798.38	6.80
U1343E-22H-4, 86.0 cm	206.53	802.75	6.41
U1343A-21H-2, 18.0 cm	206.96	804.46	4.93
U1343A_21-2_62-64cm	207.40	806.24	4.94
U1343A-21H-3, 23.0 cm	208.43	810.41	5.38
U1343A-21H-3, 134.0 cm	209.54	814.32	5.41
U1343A-21H-4, 96.0 cm	210.56	817.27	5.56
U1343A-21H-5, 62.0 cm	211.62	820.33	5.11

U1343A-21H-6, 23.0 cm	212.68	823.40	5.30
U1343E_23-3_77-79cm	213.93	827.04	5.19
U1343E-23H-4, 37.0 cm	215.03	830.22	6.24
U1343E_23-6_10-12cm	216.86	835.51	5.35
U1343E_23-6_118-120cm	217.94	838.64	4.82
U1343A-22H-2, 50.0 cm	218.11	839.11	4.82
U1343A_22-2_104-106cm	218.65	840.68	5.25
U1343A-22H-3, 10.0 cm	219.21	842.30	5.27
U1343A_22-3_66-68cm	219.77	843.92	4.46
U1343A_22-3_107-109cm	220.18	845.10	4.64
U1343A-22H-4, 118.0 cm	221.80	849.79	5.26
U1343E-30H-2, 106.0 cm	282.50	1030.95	5.63
U1343E-30H-3, 60.0 cm	283.53	1032.73	4.59
U1343E-30H-4, 18.0 cm	284.62	1035.87	7.48
U1343E-30H-4, 132.0 cm	285.76	1038.46	6.62
U1343E-30H-6, 0.0 cm	287.43	1042.60	7.02
U1343E-30H-CC, 20.0 cm	289.84	1048.05	5.34
U1343E-31H-2, 32.0 cm	291.26	1050.92	7.03
U1343E-31H-3, 74.0 cm	293.17	1055.38	7.41
U1343E-31H-4, 112.0 cm	295.05	1059.51	0.39
U1343E-31H-6, 10.0 cm	297.04	1064.27	7.88
U1343E-31H-7, 32.0 cm	298.76	1069.06	5.72
U1343E-32H-3, 10.0 cm	299.91	1070.94	3.64
U1343E-32H-3, 123.0 cm	301.04	1073.86	3.78
U1343E-32H-5, 100.0 cm	303.72	1082.90	5.54
U1343E-32H-6, 106.0 cm	305.28	1087.25	6.71
U1343E-32H-7, 66.0 cm	306.38	1090.32	6.69
U1343E-32H-8, 25.0 cm	307.41	1090.67	4.62
U1343E-33H-1, 10.0 cm	308.76	1096.96	4.39
U1343E-33H-3, 25.0 cm	310.13	1097.83	7.13
U1343E-33H-4, 32.0 cm	311.70	1105.16	6.74
U1343E-33H-4, 134.0 cm	312.75	1104.74	6.35
U1343E-33H-5, 100.0 cm	313.88	1111.24	6.39
U1343E-33H-7, 36.0 cm	316.02	1117.20	6.97
U1343E-33H-7, 111.0 cm	316.76	1119.28	6.19
U1343E-33H-CC, 60.0 cm	317.68	1121.84	6.60
U1343E-34H-1, 102.0 cm	318.96	1125.53	6.83
U1343E-34H-3, 32.0 cm	321.09	1133.24	6.50
U1343E-34H-3, 112.0 cm	321.89	1136.13	6.47
U1343E-34H-5, 0.0 cm	323.66	1142.54	6.51
U1343E-34H-5, 108.0 cm	324.75	1146.46	6.31
U1343E-34H-6, 66.0 cm	325.81	1145.91	5.17
U1343E-34H-CC, 32.0 cm	326.67	1148.75	5.79
U1343E-35H-2, 44.0 cm	327.57	1156.69	6.58

U1343E-35H-2, 123.0 cm	328.36	1154.30	4.87
U1343E-35H-3, 60.0 cm	329.23	1162.70	8.62
U1343E-35H-3, 136.0 cm	330.00	1159.71	4.41
U1343E-35H-5, 32.0 cm	331.95	1165.07	7.41
U1343E-35H-6, 0.0 cm	333.13	1168.18	5.58
U1343E-35H-6, 110.0 cm	334.23	1171.12	5.12
U1343E-36H-1, 10.0 cm	336.53	1178.73	6.76
U1343E-36H-2, 18.0 cm	336.90	1190.46	7.43
U1343E-36H-2, 112.0 cm	337.83	1183.02	4.00
U1343E-36H-3, 100.0 cm	339.21	1187.57	4.76
U1343E-36H-4, 44.0 cm	340.15	1190.67	5.40

Table 8.4 Bulk sedimentary $\delta^{15}N$ data for Site U1343 from Kim et al. (2017), Kender et al. (2017) and newly presented data in this thesis (Chapter 2-3), which combine to create a high resolution record between 0 – 1.2 Ma.

Depth (m CCSF-A)	Age (kyr)	$\delta^{15}N$ (‰)	Reference
0.16	7.29	5.1175	Kim et al., (2017)
0.20	7.43	5.42	Chapter 2
1.16	10.85	6.6311	Kim et al., (2017)
1.21	11.03	6.95	Chapter 2
2.10	14.20	7.8734	Kim et al., (2017)
2.31	14.93	8.25	Chapter 2
3.90	20.61	5.83	Chapter 2
4.73	23.56	6.48	Chapter 2
5.41	25.98	6.05	Chapter 2
5.58	26.59	6.2381	Kim et al., (2017)
6.11	28.47	5.66	Chapter 2
6.40	29.51	6.292680147	Kim et al., (2017)
7.08	31.93	6.32	Chapter 2
7.08	31.93	6.3864	Kim et al., (2017)
8.18	35.84	6.46	Chapter 2
8.87	38.30	7.35	Chapter 2
9.40	40.19	6.738381636	Kim et al., (2017)
9.87	41.88	6.84	Chapter 2
10.94	45.65	6.28	Chapter 2
11.77	48.61	6.89	Chapter 2
12.26	50.37	6.7083	Kim et al., (2017)
12.65	51.74	6.72	Chapter 2
13.53	54.87	6.23	Chapter 2
14.37	57.75	4.91	Chapter 2
14.83	59.36	5.387039303	Kim et al., (2017)
15.08	60.18	4.4173	Kim et al., (2017)
15.64	62.03	5.16	Chapter 2
16.51	64.90	4.60	Chapter 2
16.58	65.12	5.0038	Kim et al., (2017)
17.33	67.60	5.00	Chapter 2
17.84	69.28	6.153651215	Kim et al., (2017)
18.91	72.80	5.26	Chapter 2
20.44	77.82	4.50	Chapter 2
21.57	81.54	4.90	Chapter 2
22.00	82.96	5.6172	Kim et al., (2017)
22.62	84.99	6.46	Chapter 2
24.23	90.29	5.75	Chapter 2

24.44	90.98	6.104991852	Kim et al., (2017)
25.29	93.78	5.41	Chapter 2
26.18	96.72	5.3289	Kim et al., (2017)
26.91	99.11	5.93	Chapter 2
27.44	100.86	5.901866322	Kim et al., (2017)
28.06	102.90	5.59	Chapter 2
28.12	103.11	5.9071	Kim et al., (2017)
29.15	106.51	4.83	Chapter 2
30.06	109.50	5.2787	Kim et al., (2017)
30.66	111.46	5.17	Chapter 2
31.73	114.98	4.23	Chapter 2
32.12	116.28	4.8387	Kim et al., (2017)
32.78	118.44	4.74	Chapter 2
33.06	119.37	4.5159	Kim et al., (2017)
33.74	121.60	5.20	Chapter 2
34.33	123.54	4.93	Chapter 2
34.91	125.45	4.55	Chapter 2
35.35	126.90	4.62129484	Kim et al., (2017)
35.53	127.49	5.07	Chapter 2
35.60	127.73	4.8205	Kim et al., (2017)
35.82	128.45	6.06	Chapter 2
36.16	129.57	4.92	Chapter 2
36.52	130.78	6.04	Chapter 2
36.77	131.63	6.72	Chapter 2
37.21	133.58	7.10	Chapter 2
37.71	135.79	7.25	Chapter 2
38.04	137.25	7.09	Chapter 2
38.35	138.62	6.965825892	Kim et al., (2017)
38.55	139.51	6.49	Chapter 2
38.97	141.36	5.87	Chapter 2
39.47	143.58	5.72	Chapter 2
39.60	144.17	6.0013	Kim et al., (2017)
40.04	146.10	5.51	Chapter 2
40.94	150.10	6.47	Chapter 2
41.61	153.06	5.29	Chapter 2
42.03	154.92	6.4185	Kim et al., (2017)
42.58	157.35	7.11	Chapter 2
43.21	160.14	7.25	Chapter 2
43.51	161.47	5.5977	Kim et al., (2017)
44.12	164.17	5.88	Chapter 2
44.99	168.04	7.277351008	Kim et al., (2017)
45.16	168.79	6.51	Chapter 2
45.23	169.08	5.9822	Kim et al., (2017)
46.17	173.26	5.38	Chapter 2

47.76	180.26	5.46	Chapter 2
48.57	183.20	4.5636	Kim et al., (2017)
49.35	185.71	5.60	Chapter 2
50.47	189.29	5.53	Chapter 2
51.49	192.59	4.40	Chapter 2
51.57	192.84	4.861	Kim et al., (2017)
52.58	196.07	5.12	Chapter 2
53.63	199.45	5.2641	Kim et al., (2017)
53.67	199.59	5.11	Chapter 2
55.24	204.62	3.63	Chapter 2
56.51	208.71	6.62	Chapter 2
57.21	210.96	6.20	Chapter 2
57.54	212.02	6.315433564	Kim et al., (2017)
57.78	212.79	5.0176	Kim et al., (2017)
58.93	216.48	5.49	Chapter 2
59.45	218.16	5.35	Chapter 2
60.19	220.26	5.656163985	Kim et al., (2017)
60.22	220.34	4.63	Chapter 2
60.61	221.35	4.512	Kim et al., (2017)
61.22	222.96	5.20	Chapter 2
62.28	225.73	4.35	Chapter 2
62.65	226.69	4.9109	Kim et al., (2017)
63.43	228.73	3.86	Chapter 2
64.59	231.78	4.56	Chapter 2
66.03	235.53	5.35	Chapter 2
66.62	237.08	5.3699	Kim et al., (2017)
67.35	238.99	5.869754834	Kim et al., (2017)
67.63	239.72	5.77	Chapter 2
69.30	244.58	8.89	Chapter 2
69.53	245.39	6.292	Kim et al., (2017)
70.29	248.01	6.879162052	Kim et al., (2017)
70.89	250.08	6.49	Chapter 2
72.18	254.56	6.0605	Kim et al., (2017)
72.35	255.15	5.42	Chapter 2
73.19	258.06	5.58	Chapter 2
74.05	261.04	5.63	Chapter 2
74.90	263.98	5.76	Chapter 2
75.54	266.19	5.20	Chapter 2
76.18	268.41	5.51	Chapter 2
76.19	268.44	4.9085	Kim et al., (2017)
76.90	270.91	6.21	Chapter 2
77.00	271.24	6.030510795	Kim et al., (2017)
77.56	273.19	5.25	Chapter 2
77.96	274.57	5.99	Chapter 2

79.23	278.94	6.06	Chapter 2
79.90	281.20	5.540275473	Kim et al., (2017)
80.09	281.85	6.14	Chapter 2
80.91	284.56	6.28	Chapter 2
81.66	287.02	5.7657	Kim et al., (2017)
81.82	287.56	6.40	Chapter 2
82.48	289.73	5.55	Chapter 2
83.19	292.07	5.44	Chapter 2
83.38	292.71	5.4318	Kim et al., (2017)
83.87	294.31	5.49	Chapter 2
84.90	297.71	4.80	Chapter 2
85.54	299.81	5.52	Chapter 2
86.23	302.08	5.70	Chapter 2
86.81	304.01	4.5645	Kim et al., (2017)
86.92	304.36	5.48	Chapter 2
87.62	306.67	5.84	Chapter 2
88.35	309.08	5.37	Chapter 2
88.75	310.41	5.2559	Kim et al., (2017)
89.25	312.05	5.07	Chapter 2
89.46	312.74	6.04496292	Kim et al., (2017)
90.12	314.92	5.62	Chapter 2
90.81	317.21	5.5083	Kim et al., (2017)
90.97	317.73	6.11	Chapter 2
91.83	320.56	5.23	Chapter 2
92.23	321.88	6.318926119	Kim et al., (2017)
92.72	323.50	5.65	Chapter 2
93.63	326.50	4.80	Chapter 2
94.47	329.27	5.36	Chapter 2
94.49	329.36	4.8147	Kim et al., (2017)
95.57	332.90	4.66	Chapter 2
96.25	335.14	5.24	Chapter 2
96.48	335.93	4.972	Kim et al., (2017)
97.03	337.76	5.67	Chapter 2
97.56	339.53	6.49	Chapter 2
97.80	340.33	5.6064	Kim et al., (2017)
98.24	341.79	5.46	Chapter 2
98.96	344.19	4.30	Chapter 2
99.73	346.74	3.94	Chapter 2
99.78	346.92	5.273679299	Kim et al., (2017)
100.04	347.77	5.0729	Kim et al., (2017)
100.32	348.72	4.87	Chapter 2
101.02	351.05	5.32	Chapter 2
101.91	354.00	5.41	Chapter 2
102.73	356.75	6.31212449	Kim et al., (2017)

102.81	357.00	6.88	Chapter 2
103.06	357.83	5.3028	Kim et al., (2017)
104.24	361.78	7.43	Chapter 2
105.14	364.77	5.7238	Kim et al., (2017)
105.80	366.96	5.84	Chapter 2
107.11	371.34	7.43	Chapter 2
107.89	373.94	5.2576	Kim et al., (2017)
108.03	374.40	6.23	Chapter 2
109.06	377.84	6.10	Chapter 2
109.84	380.44	5.7473	Kim et al., (2017)
110.10	381.29	6.79	Chapter 2
110.41	382.32	6.834719729	Kim et al., (2017)
111.19	384.92	5.55	Chapter 2
112.36	388.82	4.97	Chapter 2
112.59	389.60	4.8719	Kim et al., (2017)
113.41	392.31	6.25342037	Kim et al., (2017)
113.82	393.67	4.98	Chapter 2
114.17	395.05	4.5807	Kim et al., (2017)
114.90	398.12	6.35	Chapter 2
115.32	400.60	6.03	Chapter 2
115.67	402.69	4.9587	Kim et al., (2017)
116.22	405.94	3.90	Chapter 2
116.81	409.38	4.96	Chapter 2
117.34	412.54	5.43	Chapter 2
117.66	414.42	5.5015	Kim et al., (2017)
117.72	414.78	5.75	Chapter 2
118.06	416.75	5.62	Chapter 2
118.40	418.76	6.20	Chapter 2
118.60	419.97	6.25	Chapter 2
119.15	423.19	7.25	Chapter 2
119.16	423.26	6.5919	Kim et al., (2017)
119.49	425.11	5.827632696	Kim et al., (2017)
119.74	426.46	4.84	Chapter 2
120.16	428.71	5.14	Chapter 2
120.17	428.78	5.2633	Kim et al., (2017)
120.81	432.20	3.97	Chapter 2
121.42	435.47	3.13	Chapter 2
121.52	436.00	5.88235016	Kim et al., (2017)
122.04	438.79	4.57	Chapter 2
122.46	441.04	6.72	Chapter 2
123.01	443.99	5.10	Chapter 2
123.45	446.35	5.80	Chapter 2
123.53	446.79	5.0715	Kim et al., (2017)
124.96	454.44	3.59	Chapter 2

125.11	455.27	5.79	Chapter 2
125.43	456.99	4.33	Chapter 2
126.04	460.23	4.78	Chapter 2
126.33	461.80	4.3763	Kim et al., (2017)
126.62	463.34	3.09	Chapter 2
127.31	467.07	5.85	Chapter 2
127.86	469.99	5.685100796	Kim et al., (2017)
128.26	472.13	5.27	Chapter 2
129.04	475.52	3.651	Kim et al., (2017)
129.74	478.17	4.05	Chapter 2
130.43	480.74	6.118392286	Kim et al., (2017)
130.76	482.00	4.48	Chapter 2
130.99	482.85	5.3077	Kim et al., (2017)
132.30	486.00	5.62	Chapter 2
133.81	489.17	4.8953	Kim et al., (2017)
133.91	489.38	6.04	Chapter 2
135.31	492.33	4.9657	Kim et al., (2017)
135.32	492.36	6.323887385	Kim et al., (2017)
135.74	493.24	5.71	Chapter 2
135.87	493.51	4.9605	Kim et al., (2017)
137.41	496.75	6.61	Chapter 2
138.18	498.39	7.038329945	Kim et al., (2017)
138.56	499.18	6.89	Chapter 2
138.75	499.58	5.0221	Kim et al., (2017)
139.70	501.58	4.98	Chapter 2
139.76	501.71	5.5317	Kim et al., (2017)
140.83	503.96	6.39	Chapter 2
141.75	505.90	4.97	Chapter 2
142.11	506.65	5.7241	Kim et al., (2017)
142.93	508.39	5.96	Chapter 2
144.00	510.64	5.77	Chapter 2
144.06	510.76	5.7023	Kim et al., (2017)
144.93	512.60	6.51	Chapter 2
145.01	512.89	5.6344	Kim et al., (2017)
145.11	513.27	7.076122707	Kim et al., (2017)
145.75	516.20	5.83	Chapter 2
146.60	520.15	6.09	Chapter 2
147.25	523.17	5.67	Chapter 2
147.79	525.67	5.6913	Kim et al., (2017)
147.96	526.48	5.71	Chapter 2
148.71	529.94	6.12	Chapter 2
149.50	533.63	6.1307	Kim et al., (2017)
149.85	535.24	6.69	Chapter 2
150.47	538.12	6.87	Chapter 2

150.87	539.99	5.03	Chapter 2
150.97	540.45	5.33	Chapter 2
151.24	541.71	6.399734619	Kim et al., (2017)
151.96	545.06	4.52	Chapter 2
152.05	545.45	4.59	Chapter 2
152.43	546.85	5.0006	Kim et al., (2017)
153.55	550.93	5.24	Chapter 2
154.23	553.42	6.663962072	Kim et al., (2017)
154.67	555.03	5.59	Chapter 2
155.39	557.66	6.98	Chapter 2
156.14	560.42	5.9613	Kim et al., (2017)
156.23	560.75	5.01	Chapter 2
157.19	564.26	5.1354	Kim et al., (2017)
157.57	565.65	6.17	Chapter 2
158.63	569.52	5.93	Chapter 2
159.73	573.55	6.50	Chapter 2
160.77	577.35	4.75	Chapter 2
161.18	578.86	5.434161441	Kim et al., (2017)
161.69	580.70	7.07	Chapter 2
162.34	582.96	6.13	Chapter 2
163.30	586.29	4.93	Chapter 2
164.02	588.81	6.871163985	Kim et al., (2017)
165.04	592.34	5.27	Chapter 2
165.83	595.08	4.81	Chapter 2
166.35	596.89	6.07	Chapter 2
167.39	600.52	4.63	Chapter 2
168.09	602.96	5.90	Chapter 2
168.21	603.36	5.65	Chapter 2
168.79	605.38	5.87	Chapter 2
169.29	607.12	6.66	Chapter 2
169.84	609.03	6.29	Chapter 2
170.30	610.63	7.48	Chapter 2
170.86	612.58	6.42	Chapter 2
171.26	613.97	4.42	Chapter 2
171.55	614.98	5.84	Chapter 2
171.86	616.06	5.53	Chapter 2
172.27	617.48	3.42	Chapter 2
172.61	618.67	4.32	Chapter 2
172.92	619.76	6.69	Chapter 2
173.30	621.06	6.20	Chapter 2
173.45	622.35	5.51	Chapter 2
173.64	625.60	5.97	Chapter 2
173.90	629.84	5.07	Chapter 2
173.96	630.94	4.88	Chapter 2

174.34	637.28	3.99	Chapter 2
174.84	642.74	4.85	Chapter 2
174.97	643.54	4.77	Chapter 2
175.17	644.78	4.75	Chapter 2
175.54	647.07	4.93	Chapter 2
176.00	649.92	5.50	Chapter 2
176.56	653.39	5.75	Chapter 2
177.34	658.22	5.49	Chapter 2
178.06	662.68	4.68	Chapter 2
178.38	664.67	4.59	Chapter 2
179.24	669.99	3.19	Chapter 2
179.53	671.79	3.85	Chapter 2
179.56	671.98	5.04	Chapter 2
180.32	676.69	6.08	Chapter 2
180.89	680.22	6.03	Chapter 2
181.45	683.69	4.12	Chapter 2
182.05	687.41	6.00	Chapter 2
182.63	690.94	6.42	Chapter 2
183.20	694.47	4.94	Chapter 2
183.76	697.94	2.72	Chapter 2
184.30	701.28	4.36	Chapter 2
185.24	707.09	6.62	Chapter 2
185.87	710.99	5.76	Chapter 2
186.28	713.52	5.56	Chapter 2
187.05	718.28	5.23	Chapter 2
187.88	723.41	5.89	Chapter 2
188.29	726.14	4.16	Chapter 2
188.83	730.53	5.33	Chapter 2
189.32	734.64	5.59	Chapter 2
189.86	739.17	5.55	Chapter 2
190.42	743.86	7.49	Chapter 2
190.70	746.21	5.98	Chapter 2
191.54	753.24	4.53	Chapter 2
192.33	755.93	5.33	Chapter 2
193.19	758.60	7.40	Chapter 2
193.83	760.58	5.98	Chapter 2
194.54	762.78	7.67	Chapter 2
195.50	765.76	4.02	Chapter 2
196.51	768.89	4.79	Chapter 2
197.25	771.18	6.38	Chapter 2
198.05	773.66	5.81	Chapter 2
198.97	776.51	5.12	Chapter 2
199.85	779.24	6.66	Chapter 2
200.69	781.84	5.92	Chapter 2

202.14	786.34	4.41	Chapter 2
203.89	792.07	5.36	Chapter 2
205.45	798.38	6.80	Chapter 2
206.53	802.75	6.41	Chapter 2
206.96	804.46	4.93	Chapter 2
207.40	806.24	4.94	Chapter 2
208.43	810.41	5.38	Chapter 2
209.54	814.32	5.41	Chapter 2
210.56	817.27	5.56	Chapter 2
211.62	820.33	5.11	Chapter 2
212.68	823.40	5.30	Chapter 2
213.93	827.04	5.19	Chapter 2
215.03	830.22	6.24	Chapter 2
216.86	835.51	5.35	Chapter 2
217.94	838.64	4.82	Chapter 2
218.11	839.11	4.82	Chapter 2
218.65	840.68	5.25	Chapter 2
219.21	842.30	5.27	Chapter 2
219.77	843.92	4.46	Chapter 2
220.07	844.78	6.252647775	Kender et al., (2018)
220.18	845.10	4.64	Chapter 2
220.29	845.42	5.044347015	Kender et al., (2018)
220.61	846.35	6.424864237	Kender et al., (2018)
220.94	847.30	5.418483776	Kender et al., (2018)
221.23	848.14	5.188480415	Kender et al., (2018)
221.57	849.12	5.903086413	Kender et al., (2018)
221.80	849.79	5.26	Chapter 2
221.87	849.99	5.100560112	Kender et al., (2018)
222.24	851.06	6.078509242	Kender et al., (2018)
222.63	852.19	6.484168558	Kender et al., (2018)
222.78	852.62	5.743879539	Kender et al., (2018)
222.97	853.17	5.57371552	Kender et al., (2018)
223.35	854.27	5.115760084	Kender et al., (2018)
223.65	855.14	4.987839943	Kender et al., (2018)
224.04	856.27	5.258775138	Kender et al., (2018)
224.31	857.06	5.599726991	Kender et al., (2018)
224.69	858.16	6.04389784	Kender et al., (2018)
224.97	858.97	4.807549607	Kender et al., (2018)
225.27	859.84	6.552843468	Kender et al., (2018)
225.59	860.77	5.293658341	Kender et al., (2018)
225.97	861.87	5.170055802	Kender et al., (2018)
226.13	862.33	6.32734481	Kender et al., (2018)
226.53	863.49	5.599658965	Kender et al., (2018)
226.85	864.41	5.690596908	Kender et al., (2018)

227.17	865.34	5.634814499	Kender et al., (2018)
227.46	866.32	5.483911852	Kender et al., (2018)
227.69	867.40	5.608156201	Kender et al., (2018)
228.04	869.04	5.751477841	Kender et al., (2018)
228.40	870.72	5.831194983	Kender et al., (2018)
228.73	872.29	5.214956713	Kender et al., (2018)
228.98	873.46	5.665136964	Kender et al., (2018)
229.28	874.86	5.633032084	Kender et al., (2018)
229.60	876.36	5.331524936	Kender et al., (2018)
229.90	877.77	5.699362333	Kender et al., (2018)
230.22	879.28	6.492236385	Kender et al., (2018)
230.56	880.87	6.065565743	Kender et al., (2018)
230.86	882.28	5.806328626	Kender et al., (2018)
231.18	883.79	5.102596706	Kender et al., (2018)
231.47	885.15	5.695999599	Kender et al., (2018)
231.78	886.61	6.032455545	Kender et al., (2018)
232.12	888.21	5.552532472	Kender et al., (2018)
232.44	889.71	6.292868032	Kender et al., (2018)
232.76	891.22	5.160082929	Kender et al., (2018)
233.05	892.58	6.478149823	Kender et al., (2018)
233.37	894.08	6.508307437	Kender et al., (2018)
233.62	895.26	6.640183457	Kender et al., (2018)
233.92	896.67	6.704594893	Kender et al., (2018)
234.26	898.27	5.544194214	Kender et al., (2018)
234.56	899.68	6.298731849	Kender et al., (2018)
234.87	901.14	5.30401805	Kender et al., (2018)
235.28	903.06	5.50264298	Kender et al., (2018)
235.53	904.24	5.663183152	Kender et al., (2018)
235.83	905.65	6.388282484	Kender et al., (2018)
236.12	907.01	6.965905232	Kender et al., (2018)
236.46	908.61	5.128892276	Kender et al., (2018)
236.71	909.79	5.339960083	Kender et al., (2018)
237.03	911.29	5.442054167	Kender et al., (2018)
237.37	912.89	5.341424191	Kender et al., (2018)
237.67	914.30	5.213192778	Kender et al., (2018)
237.96	915.66	7.39605642	Kender et al., (2018)
238.30	917.26	5.332895234	Kender et al., (2018)
238.62	918.19	4.611398746	Kender et al., (2018)
238.94	919.03	5.146877453	Kender et al., (2018)
239.24	919.82	5.844501597	Kender et al., (2018)
239.56	920.66	4.490885447	Kender et al., (2018)
239.80	921.29	4.785586421	Kender et al., (2018)
240.12	922.13	5.314336484	Kender et al., (2018)
240.44	922.97	5.345728236	Kender et al., (2018)

240.67	923.58	4.792568673	Kender et al., (2018)
241.06	924.60	4.12919744	Kender et al., (2018)
241.72	926.33	5.949163188	Kender et al., (2018)
242.02	927.12	6.228924015	Kender et al., (2018)
242.34	927.96	6.065376621	Kender et al., (2018)
242.68	928.86	5.364540597	Kender et al., (2018)
242.98	929.64	5.095644235	Kender et al., (2018)
243.21	930.25	6.180368001	Kender et al., (2018)
243.58	931.22	6.131621779	Kender et al., (2018)
243.99	932.30	7.149656137	Kender et al., (2018)
244.46	933.53	6.944848774	Kender et al., (2018)
244.93	934.77	6.724762281	Kender et al., (2018)
245.15	935.35	7.3171246	Kender et al., (2018)
245.59	936.50	7.700880692	Kender et al., (2018)
245.72	936.84	7.965503928	Kender et al., (2018)
246.21	938.13	7.492949231	Kender et al., (2018)
246.29	938.34	7.864294312	Kender et al., (2018)
246.59	939.13	8.475405576	Kender et al., (2018)
246.99	940.18	6.187709844	Kender et al., (2018)
247.31	941.02	8.439795986	Kender et al., (2018)
247.71	942.07	8.44993943	Kender et al., (2018)
247.90	942.57	9.137048709	Kender et al., (2018)
248.19	943.33	7.928525088	Kender et al., (2018)
248.59	944.38	7.418291734	Kender et al., (2018)
248.84	945.04	6.740999156	Kender et al., (2018)
249.16	945.88	5.716469835	Kender et al., (2018)
249.48	946.72	5.322789099	Kender et al., (2018)
249.78	947.51	5.713636731	Kender et al., (2018)
250.18	948.56	6.359607498	Kender et al., (2018)
250.51	949.43	6.545870657	Kender et al., (2018)
250.82	950.24	5.679023675	Kender et al., (2018)
251.10	950.98	5.16500316	Kender et al., (2018)
251.32	951.56	6.968490685	Kender et al., (2018)
251.64	952.40	6.373472228	Kender et al., (2018)
251.98	953.29	5.823596262	Kender et al., (2018)
252.28	954.08	6.277724649	Kender et al., (2018)
252.52	954.71	5.624362333	Kender et al., (2018)
252.84	955.55	6.498008301	Kender et al., (2018)
253.20	956.49	6.343857322	Kender et al., (2018)
253.48	957.23	4.507953226	Kender et al., (2018)
253.78	958.02	5.752766334	Kender et al., (2018)
254.02	958.65	5.457433648	Kender et al., (2018)
254.40	959.51	5.46145393	Kender et al., (2018)
254.70	960.12	4.673766806	Kender et al., (2018)

255.04	960.82	3.809692667	Kender et al., (2018)
255.36	961.47	4.240283585	Kender et al., (2018)
255.68	962.12	5.641875621	Kender et al., (2018)
255.98	962.74	5.684212261	Kender et al., (2018)
256.29	963.37	5.937512845	Kender et al., (2018)
256.61	964.02	6.215694395	Kender et al., (2018)
257.02	964.86	6.089822337	Kender et al., (2018)
257.25	965.33	5.723329025	Kender et al., (2018)
257.54	965.93	5.184719736	Kender et al., (2018)
257.87	966.60	6.245384342	Kender et al., (2018)
258.19	967.25	7.392556996	Kender et al., (2018)
258.48	967.85	5.390594104	Kender et al., (2018)
258.77	968.44	7.184430928	Kender et al., (2018)
259.11	969.14	4.627851777	Kender et al., (2018)
259.34	969.61	7.95646192	Kender et al., (2018)
259.68	970.30	5.352047627	Kender et al., (2018)
259.98	970.91	7.940825172	Kender et al., (2018)
260.05	971.06	8.223827062	Kender et al., (2018)
260.27	971.51	7.011500879	Kender et al., (2018)
260.52	972.02	7.843129144	Kender et al., (2018)
260.81	972.61	7.930913565	Kender et al., (2018)
261.01	973.02	7.608268232	Kender et al., (2018)
261.33	973.67	7.76381906	Kender et al., (2018)
261.55	974.12	6.057699251	Kender et al., (2018)
261.77	974.57	6.573690478	Kender et al., (2018)
262.02	975.08	5.621203809	Kender et al., (2018)
263.23	977.56	7.311522789	Kender et al., (2018)
263.45	978.01	6.931698457	Kender et al., (2018)
263.87	978.87	5.193172214	Kender et al., (2018)
264.05	979.23	4.973450896	Kender et al., (2018)
264.25	979.64	4.322588827	Kender et al., (2018)
264.73	980.62	5.379964149	Kender et al., (2018)
264.95	981.07	5.211007512	Kender et al., (2018)
265.23	981.65	4.364889992	Kender et al., (2018)
265.42	982.03	5.035804909	Kender et al., (2018)
265.69	982.59	5.517807382	Kender et al., (2018)
265.93	983.08	5.676208037	Kender et al., (2018)
266.31	984.03	5.428879153	Kender et al., (2018)
266.57	984.81	5.715355504	Kender et al., (2018)
266.79	985.48	6.757456153	Kender et al., (2018)
267.00	986.12	5.738279536	Kender et al., (2018)
267.19	986.69	5.719074382	Kender et al., (2018)
267.43	987.42	7.557541966	Kender et al., (2018)
267.81	988.57	6.049952205	Kender et al., (2018)

268.07	989.36	6.87756292	Kender et al., (2018)
268.29	990.02	6.892329959	Kender et al., (2018)
268.50	990.66	7.914605548	Kender et al., (2018)
268.69	991.24	7.320982126	Kender et al., (2018)
269.23	992.87	5.898396584	Kender et al., (2018)
269.45	993.54	6.42497437	Kender et al., (2018)
269.73	994.39	7.093103848	Kender et al., (2018)
270.43	996.51	4.589613576	Kender et al., (2018)
270.68	997.26	6.758372724	Kender et al., (2018)
270.94	998.05	5.603037478	Kender et al., (2018)
271.17	998.75	6.215687813	Kender et al., (2018)
271.35	999.29	3.878551577	Kender et al., (2018)
271.61	1000.08	5.14890365	Kender et al., (2018)
271.83	1000.75	4.934201627	Kender et al., (2018)
272.17	1001.78	5.725768857	Kender et al., (2018)
272.38	1002.42	4.478342475	Kender et al., (2018)
272.57	1002.99	4.717677381	Kender et al., (2018)
272.94	1004.03	5.750404585	Kender et al., (2018)
273.27	1004.96	6.453826236	Kender et al., (2018)
273.55	1005.75	5.700443603	Kender et al., (2018)
273.82	1006.51	5.676680278	Kender et al., (2018)
274.06	1007.19	4.38941013	Kender et al., (2018)
274.44	1008.26	5.142862469	Kender et al., (2018)
274.70	1008.99	4.948181117	Kender et al., (2018)
274.92	1009.61	4.918514908	Kender et al., (2018)
275.20	1010.39	6.086168628	Kender et al., (2018)
275.38	1010.90	5.389281788	Kender et al., (2018)
275.76	1011.97	6.227487479	Kender et al., (2018)
276.01	1012.67	5.096685248	Kender et al., (2018)
276.27	1013.41	8.075211833	Kender et al., (2018)
276.50	1014.05	7.775102744	Kender et al., (2018)
276.68	1014.56	7.921971722	Kender et al., (2018)
276.88	1015.12	6.094098879	Kender et al., (2018)
277.11	1015.77	6.648647718	Kender et al., (2018)
277.44	1016.70	7.411687301	Kender et al., (2018)
277.70	1017.43	6.463879011	Kender et al., (2018)
277.92	1018.05	6.471913004	Kender et al., (2018)
278.13	1018.64	6.125853292	Kender et al., (2018)
278.32	1019.18	5.729403622	Kender et al., (2018)
278.75	1020.39	6.496395494	Kender et al., (2018)
278.97	1021.01	5.765424771	Kender et al., (2018)
279.25	1021.80	6.639206749	Kender et al., (2018)
279.44	1022.33	8.213763084	Kender et al., (2018)
279.65	1022.92	8.285914425	Kender et al., (2018)

279.88	1023.57	8.966425485	Kender et al., (2018)
280.09	1024.16	8.255778318	Kender et al., (2018)
280.11	1024.22	7.878938424	Kender et al., (2018)
280.33	1024.84	8.82517939	Kender et al., (2018)
280.37	1024.95	8.09734222	Kender et al., (2018)
280.55	1025.46	7.903528771	Kender et al., (2018)
280.62	1025.65	9.582142096	Kender et al., (2018)
280.80	1026.16	8.038551466	Kender et al., (2018)
280.88	1026.38	9.084866422	Kender et al., (2018)
280.99	1026.69	7.71381974	Kender et al., (2018)
281.13	1027.09	8.127063686	Kender et al., (2018)
281.23	1027.37	8.135845997	Kender et al., (2018)
281.43	1027.93	7.687782416	Kender et al., (2018)
281.68	1028.64	8.383922099	Kender et al., (2018)
282.50	1030.95	5.63	Chapter 3
283.53	1032.73	4.59	Chapter 3
284.62	1035.87	7.48	Chapter 3
285.76	1038.46	6.62	Chapter 3
287.43	1042.60	7.02	Chapter 3
289.84	1048.05	5.34	Chapter 3
291.26	1050.92	7.03	Chapter 3
293.17	1055.38	7.41	Chapter 3
295.05	1059.51	0.39	Chapter 3
297.04	1064.27	7.88	Chapter 3
298.76	1069.06	5.72	Chapter 3
299.91	1070.94	3.64	Chapter 3
301.04	1073.86	3.78	Chapter 3
303.72	1082.90	5.54	Chapter 3
305.28	1087.25	6.71	Chapter 3
306.38	1090.32	6.69	Chapter 3
307.41	1090.67	4.62	Chapter 3
308.76	1096.96	4.39	Chapter 3
310.13	1097.83	7.13	Chapter 3
311.70	1105.16	6.74	Chapter 3
312.75	1104.74	6.35	Chapter 3
313.88	1111.24	6.39	Chapter 3
316.02	1117.20	6.97	Chapter 3
316.76	1119.28	6.19	Chapter 3
317.68	1121.84	6.60	Chapter 3
318.96	1125.53	6.83	Chapter 3
321.09	1133.24	6.50	Chapter 3
321.89	1136.13	6.47	Chapter 3
323.66	1142.54	6.51	Chapter 3
324.75	1146.46	6.31	Chapter 3

325.81	1145.91	5.17	Chapter 3
326.67	1148.75	5.79	Chapter 3
327.57	1156.69	6.58	Chapter 3
328.36	1154.30	4.87	Chapter 3
329.23	1162.70	8.62	Chapter 3
330.00	1159.71	4.41	Chapter 3
331.95	1165.07	7.41	Chapter 3
333.13	1168.18	5.58	Chapter 3
334.23	1171.12	5.12	Chapter 3
336.53	1178.73	6.76	Chapter 3
336.90	1190.46	7.43	Chapter 3
337.83	1183.02	4.00	Chapter 3
339.21	1187.57	4.76	Chapter 3
340.15	1190.67	5.40	Chapter 3

Table 8.5 Upwelling index result calculated using bulk sedimentary $\delta^{15}N$ (Table 8.3) and opal MAR (Kim et al., 2014), presented in Chapter 2-3.

Age (kyr)	Upwelling index	Age (kyr)	Upwelling index	Age (kyr)	Upwelling index	Age (kyr)	Upwelling index
8	0.12	**36**	-0.39	**148**	-0.35	**176**	-0.29
10	-0.03	**38**	-0.47	**150**	-0.37	**178**	-0.35
12	-0.32	**40**	-0.32	**152**	-0.28	**180**	-0.37
14	-0.24	**42**	-0.30	**154**	-0.36	**182**	-0.19
16	-0.57	**44**	-0.26	**156**	-0.51	**184**	-0.33
18	-0.70	**46**	-0.27	**158**	-0.52	**186**	-0.32
20	-0.52	**48**	-0.24	**160**	-0.52	**188**	-0.26
22	-0.52	**50**	-0.20	**162**	-0.29	**190**	-0.17
24	-0.40	**52**	-0.29	**164**	-0.42	**192**	0.11
26	-0.33	**54**	-0.22	**166**	-0.44	**194**	0.09
28	-0.25	**56**	-0.39	**168**	-0.48	**196**	-0.03
30	-0.29	**58**	-0.32	**170**	-0.40	**198**	-0.19
32	-0.26	**60**	-0.35	**172**	-0.33	**200**	0.02
34	-0.34	**62**	-0.47	**174**	-0.31	**202**	0.04

204	0.04	**236**	-0.01	**364**	-0.34	**396**	-0.02
206	-0.01	**238**	0.26	**366**	-0.31	**398**	-0.35
208	-0.08	**240**	0.21	**368**	-0.32	**400**	-0.25
210	-0.09	**242**	-0.12	**370**	-0.39	**402**	-0.01
212	0.00	**244**	-0.49	**372**	-0.44	**404**	0.05
214	0.22	**246**	-0.39	**374**	-0.24	**406**	0.01
216	0.09	**248**	-0.30	**376**	-0.35	**408**	-0.10
218	-0.14	**250**	-0.30	**378**	-0.22	**410**	-0.11
220	-0.36	**252**	-0.38	**380**	-0.05	**412**	-0.11
222	-0.10	**254**	-0.21	**382**	-0.10	**414**	0.09
224	-0.21	**256**	-0.12	**384**	-0.32	**416**	-0.10
226	-0.04	**258**	-0.11	**386**	-0.05	**418**	-0.01
228	-0.08	**260**	-0.22	**388**	-0.10	**420**	-0.06
230	0.04	**262**	-0.27	**390**	-0.12	**422**	-0.26
232	-0.06	**264**	-0.31	**392**	-0.24	**424**	-0.28
234	0.00	**266**	-0.33	**394**	0.10	**426**	-0.30
428	-0.33	**460**	-0.32	**588**	-0.28	**620**	-0.34

430	-0.32	**462**	-0.34	**590**	-0.30	**622**	-0.37
432	-0.24	**464**	-0.22	**592**	-0.18	**624**	-0.40
434	-0.19	**466**	-0.37	**594**	-0.18	**626**	-0.65
436	-0.55	**468**	-0.42	**596**	-0.38	**628**	-0.58
438	-0.48	**470**	-0.50	**598**	-0.44	**630**	-0.58
440	-0.51	**472**	-0.53	**600**	-0.26	**632**	-0.59
442	-0.61	**474**	-0.29	**602**	-0.28	**634**	-0.55
444	-0.47	**476**	-0.14	**604**	-0.16	**636**	-0.50
446	-0.56	**478**	-0.22	**606**	-0.11	**638**	-0.49
448	-0.45	**480**	-0.43	**608**	-0.18	**640**	-0.52
450	-0.44	**482**	0.03	**610**	-0.06	**642**	-0.60
452	-0.18	**484**	0.11	**612**	-0.08	**644**	-0.50
454	-0.18	**486**	-0.17	**614**	0.18	**646**	-0.39
456	-0.45	**488**	0.20	**616**	0.03	**648**	-0.41
458	-0.32	**490**	0.31	**618**	0.17	**650**	-0.44
652	-0.42	**684**	-0.11	**812**	-0.48	**844**	-0.08
654	-0.41	**686**	-0.25	**814**	-0.37	**846**	-0.22

656	-0.37	**688**	-0.38	**816**	-0.29	**848**	0.04
658	-0.36	**690**	-0.35	**818**	-0.23	**850**	0.02
660	-0.32	**692**	-0.17	**820**	-0.15	**852**	-0.62
662	-0.29	**694**	-0.10	**822**	0.08	**854**	-0.29
664	-0.33	**696**	-0.19	**824**	-0.07	**856**	0.01
666	-0.31	**698**	0.15	**826**	-0.07	**858**	0.12
668	-0.20	**700**	0.03	**828**	-0.41	**860**	0.06
670	-0.11	**702**	-0.13	**830**	-0.51	**862**	-0.10
672	-0.21	**704**	-0.21	**832**	-0.30	**864**	-0.21
674	-0.43	**706**	-0.29	**834**	-0.23	**866**	-0.33
676	-0.49	**708**	-0.35	**836**	-0.24	**868**	-0.37
678	-0.45	**710**	-0.27	**838**	-0.35	**870**	-0.52
680	-0.45	**712**	-0.38	**840**	-0.23	**872**	-0.53
682	-0.28	**714**	-0.41	**842**	0.11	**874**	-0.69
876	-0.59	**908**	-0.65	**940**	-0.33	**1068**	0.05
878	-0.66	**910**	-0.45	**942**	-0.24	**1070**	0.41
880	-0.68	**912**	-0.37	**944**	-0.12	**1072**	0.52

882	-0.59	**914**	-0.36	**946**	-0.15	**1074**	0.47
884	-0.47	**916**	-0.65	**948**	0.24	**1076**	0.39
886	-0.51	**918**	-0.35	**950**	0.08	**1078**	0.28
888	-0.50	**920**	-0.57	**952**	-0.03	**1080**	0.17
890	-0.52	**922**	-0.58	**954**	-0.12	**1082**	0.07
892	-0.45	**924**	-0.58	**956**	-0.27	**1084**	-0.13
894	-0.59	**926**	-0.15	**958**	-0.53	**1086**	-0.19
896	-0.60	**928**	-0.55	**960**	-0.28	**1088**	-0.35
898	-0.59	**930**	-0.50	**962**	-0.24	**1090**	-0.39
900	-0.68	**932**	-0.76	**964**	-0.34	**1092**	-0.03
902	-0.47	**934**	-0.47	**966**	-0.16	**1094**	-0.09
904	-0.50	**936**	-0.65	**968**	-0.34	**1096**	-0.09
906	-0.61	**938**	-0.52	**970**	0.04	**1098**	-0.40
1100	-0.44	**1132**	-0.49	**1164**	-0.07		
1102	-0.42	**1134**	-0.37	**1166**	-0.08		
1104	-0.15	**1136**	-0.46	**1168**	0.13		
1106	-0.26	**1138**	-0.49	**1170**	0.18		

1108	-0.19	**1140**	-0.39	**1172**	0.09
1110	-0.27	**1142**	-0.22	**1174**	-0.07
1112	-0.18	**1144**	-0.22	**1176**	-0.18
1114	-0.20	**1146**	-0.11	**1178**	-0.32
1116	-0.30	**1148**	-0.34	**1180**	-0.21
1118	-0.51	**1150**	-0.38	**1182**	-0.09
1120	-0.40	**1152**	-0.29	**1184**	0.07
1122	-0.57	**1154**	0.11	**1186**	0.08
1124	-0.56	**1156**	-0.24	**1188**	0.04
1126	-0.75	**1158**	0.02	**1190**	-0.42
1128	-0.67	**1160**	0.23		
1130	-0.59	**1162**	-0.17		

Table 8.6 Diatom assemblage results, classified here by ecological groupings (Stroynowski et al., 2017). For detailed results (e.g. species data) please contact the authors.

Sample code	Depth (m CCSF-A)	Age (kyr)	PACK (%)	ICE (%)	MARG (%)	Eastern shelf species (%)	Freshwater (%)	Mat-forming (%)	Pelagic (%)	Benthic (%)	Other (%)	*Chaetoceros* RVS (%)
U1343E-18H-6, 16.0 cm	165.83	595.08	35.93	16.27	12.54	5.08	2.03	10.51	11.53	0.68	5.42	39.80
U1343A-17H-2, 52.0 cm	167.38	600.48	53.75	9.06	4.38	8.13	1.88	6.25	12.50	0.63	3.13	41.60
U1343E-18H-8, 26-28.0 cm	168.11	603.01	46.83	9.97	10.88	5.74	0.60	4.83	16.31	3.63	0.91	17.18
U1343A-17H-3, 52.0 cm	168.79	605.38	26.06	13.88	13.03	4.53	0.00	7.93	31.16	1.98	1.13	15.99
U1343A-17H-4, 16.0 cm	169.84	609.03	15.82	9.25	5.07	13.43	0.30	14.33	35.82	2.69	3.28	15.73
U1343A-17H-4, 118.0 cm	170.86	612.58	31.85	8.62	8.09	6.79	0.52	14.10	26.63	2.61	0.78	22.99
U1343A-17H-5, 37.0 cm	171.55	614.98	22.37	11.18	6.25	7.89	0.00	4.61	45.72	1.32	0.66	16.58
U1343A-17H-5, 109.0 cm	172.27	617.48	43.46	2.29	8.17	16.99	0.33	1.96	24.51	0.98	0.98	16.67
U1343C-18H-2, 54.0 cm	172.92	619.76	41.65	11.07	9.86	3.62	0.60	1.01	25.75	8.25	1.41	6.28
U1343C-18H-2, 126.0 cm	173.64	625.60	37.29	9.69	4.84	15.98	0.00	8.72	13.08	9.20	2.66	15.87
U1343C-18H-3, 46.0 cm	174.34	637.28	18.96	8.35	4.97	14.00	8.13	7.67	21.67	23.48	3.61	9.94

U1343C-18H-3, 96.0 cm	174.84	642.74	33.66	6.27	3.63	14.85	0.00	8.58	18.15	17.49	3.63	13.35
U1343C-18H-4, 16.0 cm	175.54	647.07	41.53	7.99	3.51	8.95	0.96	9.90	22.04	4.47	1.92	22.43
U1343C-18H-4, 118.0 cm	176.56	653.39	41.53	7.67	4.79	8.31	0.64	11.18	22.68	1.60	1.92	10.64
U1343C-18H-5, 68.0 cm	177.56	659.59	63.87	2.90	2.90	3.87	0.00	6.77	16.77	1.61	1.29	4.66
U1343C-18H-6, 30.0 cm	178.68	666.53	45.32	6.95	3.63	2.72	0.30	6.34	32.93	0.30	1.51	6.36
U1343C-18H-6, 86.0 cm	179.24	669.99	58.06	3.87	2.58	4.52	2.58	10.97	10.97	1.94	4.84	10.70
U1343A-18H-4, 16.0 cm	180.03	674.89	60.11	2.13	3.19	2.93	0.53	14.89	14.10	0.53	1.86	32.63
U1343A-18H-4, 134.0 cm	181.21	682.20	38.46	5.69	6.35	4.01	4.68	18.39	13.04	4.35	5.02	16.97
U1343E-20H-2, 23.0 cm	182.34	689.15	35.48	11.05	11.57	2.83	0.00	17.22	17.74	1.80	3.08	4.81
U1343A-18H-6, 62.0 cm	183.49	696.33	41.10	7.06	5.52	7.06	0.00	2.76	32.52	5.52	0.92	16.23
U1343E-20H-3, 77.0 cm	184.30	701.28	20.18	10.09	6.23	23.74	0.59	2.67	34.12	2.08	0.59	7.36
U1343E-20H-4, 16.0 cm	184.94	705.24	33.66	5.85	8.78	15.85	0.98	4.88	27.80	1.22	1.22	15.93
U1343E-20H-4, 109.0 cm	185.86	710.93	49.67	2.29	5.88	5.23	2.29	8.50	13.07	15.03	4.25	10.25
U1343E-20H-5, 23.0 cm	186.51	714.95	40.19	7.79	5.61	11.84	0.00	16.51	12.46	3.43	2.18	25.06

U1343E-20H-5, 77.0 cm	187.05	718.28	52.44	8.47	4.23	3.26	0.98	4.89	14.98	11.73	3.58	20.66
U1343E-20H-6, 51.0 cm	188.29	726.14	40.81	6.22	4.86	10.27	1.62	7.03	20.81	11.89	1.35	23.61
U1343C-19H-4, 126.0 cm	189.32	734.64	24.87	7.33	6.02	14.66	3.66	10.99	23.82	12.30	1.31	10.33
U1343C-19H-5, 86.0 cm	190.42	743.86	25.54	8.15	1.63	33.15	2.72	2.72	17.12	12.77	2.17	17.84
U1343E-21H-2, 30.0 cm	191.54	753.24	48.71	2.26	2.90	14.52	4.19	9.35	15.81	1.61	0.65	17.97
U1343E-21H-2, 109.0 cm	192.28	755.78	50.00	1.27	2.85	11.08	0.32	17.72	13.92	0.63	2.22	32.86
U1343E-21H-3, 45.0 cm	193.19	758.60	48.68	6.58	3.29	7.24	0.99	6.25	25.66	0.33	0.99	15.43
U1343E-21H-4, 30.0 cm	194.54	762.78	32.24	8.22	5.59	7.24	0.33	19.74	22.37	3.29	1.64	15.13
U1343E-21H-4, 126.0 cm	195.50	765.76	36.77	1.94	3.23	8.39	8.39	18.71	18.71	3.23	0.65	33.90
U1343C-20H-3, 52.0 cm	196.51	768.89	21.84	30.00	6.05	7.37	2.37	3.95	19.21	7.11	5.00	11.00
U1343C-20H-4, 66.0 cm	198.05	773.66	30.29	10.00	5.14	7.71	3.14	14.57	23.71	2.86	2.86	18.89
U1343C-20H-5, 96.0 cm	199.85	779.24	34.54	15.13	4.61	12.83	2.30	5.59	19.41	3.95	1.97	19.69
U1343C-20H-6, 77.0 cm	201.16	783.30	12.11	17.39	11.80	15.22	1.55	4.97	32.92	0.31	2.80	13.33
U1343E-22H-1, 77.0 cm	202.14	786.34	30.77	5.13	4.17	19.87	0.64	3.53	31.41	1.92	0.64	29.65

U1343E-22H-2, 102.0 cm	203.89	792.07	55.66	12.94	2.59	10.68	0.97	2.91	6.47	9.06	0.97	44.89
U1343E-22H-3, 118.0 cm	205.45	798.38	50.00	17.20	2.55	6.69	0.00	4.78	10.19	10.19	1.59	103.90
U1343E-22H-4, 86.0 cm	206.53	802.75	49.22	7.84	3.45	11.29	1.88	8.78	14.11	2.82	0.94	67.42
U1343A-21H-2, 96.0 cm	207.74	807.62	37.99	6.69	2.13	15.20	1.22	8.21	22.80	3.04	2.74	65.41
U1343A-21H-3, 23.0cm	208.43	810.41	34.88	6.98	2.33	16.28	0.33	12.96	22.92	1.00	2.33	36.76
U1343A-21H-3, 52.0 cm	208.72	811.58	59.78	5.16	2.17	8.70	0.00	5.71	16.58	1.09	1.36	21.29
U1343A-21H-3, 96.0 cm	209.16	813.21	22.38	11.90	1.98	13.31	0.57	20.40	22.95	2.83	3.68	38.15
U1343A-21H-4, 68.0cm	210.27	816.43	45.34	13.98	4.35	9.63	0.93	5.28	16.46	1.55	1.86	21.41
U1343A-21H-5, 8.0 cm	211.08	818.77	42.19	13.29	4.20	7.46	1.63	7.93	20.75	1.86	1.17	35.41
U1343A-21H-5, 96.0 cm	211.95	821.29	41.32	7.57	13.56	5.99	1.89	4.73	21.77	0.63	2.52	30.54
U1343A-21H-6, 23.0 cm	212.68	823.40	32.78	16.30	6.85	11.48	0.00	6.48	20.93	1.85	3.89	11.87
U1343E-23H-3, 77.0 cm	213.93	827.04	58.92	4.14	2.23	15.29	0.00	6.69	11.78	0.64	0.32	24.85
U1343E-23H-4, 37.0 cm	215.03	830.22	69.67	3.33	3.67	7.67	0.00	3.00	10.00	2.00	0.67	38.48
U1343E-23H-6, 10.0 cm	216.84	835.45	8.38	20.52	11.85	15.03	0.58	3.76	33.24	2.60	5.20	18.79

U1343E-23H-6, 118.0 cm	217.94	838.64	13.45	13.45	8.48	14.91	2.05	11.70	26.90	4.39	5.26	14.67
U1343A-22H-3, 8.0 cm	219.19	842.24	20.43	11.59	13.11	12.80	0.61	12.50	26.83	0.30	1.83	17.14
U1343A-22H-3 W, 86.0--88.0 cm	219.96	844.46	21.18	7.77	6.43	10.46	2.41	5.09	41.02	1.88	3.75	28.09
U1343A-22H-4 W, 23.0--25.0 cm	220.83	846.98	55.64	8.66	4.72	5.51	0.52	6.04	14.96	1.05	2.89	10.98
U1343A-22H-4, 118.0 cm	221.79	849.76	45.74	5.68	8.20	11.04	0.32	4.42	22.08	0.95	1.89	39.73
U1343A-22H-5 W, 37.0--39.0 cm	222.38	851.47	24.53	11.80	7.76	14.29	1.24	2.80	33.54	1.86	2.17	6.81
U1343A-22H-5 W, 96.0 cm	222.97	853.17	51.49	8.91	2.97	9.90	1.98	4.95	15.18	1.32	3.30	40.27
U1343A-22H-6 W, 16.0--18.0 cm	223.57	854.91	41.98	11.85	7.90	8.40	0.00	4.94	19.26	0.49	5.19	6.95
U1343A-22H-6 W, 62.0--64.0 cm	224.03	856.24	29.80	20.41	12.04	10.00	0.61	2.86	20.61	2.04	2.24	33.70
U1343A-22H-6 W, 102.0 cm	224.44	857.43	22.27	11.14	9.61	11.14	0.66	3.06	39.08	2.62	1.53	5.33
U1343C-23H-3 W, 96.0--98.0 cm	224.96	858.94	9.88	13.09	2.47	5.68	1.23	3.70	60.25	1.23	2.72	24.79

U1343C-23H-4 W, 0.0--2.0 cm	225.50	860.51	20.18	4.59	5.50	5.96	0.46	2.29	57.11	3.90	1.61	22.20
U1343C-23H-4 W, 46.0--48.0 cm	225.96	861.84	40.59	4.84	2.42	8.06	2.15	1.88	37.90	0.27	1.88	14.08
U1343C-23H-4 W, 86.0--88.0 cm	226.36	862.99	13.69	9.78	3.67	29.83	3.91	4.16	26.41	7.58	1.22	9.07
U1343C-23H-4 W, 134.0--136.0 cm	226.85	864.41	55.63	5.00	4.06	7.19	0.94	3.13	14.69	12.81	1.56	58.76
U1343C-23H-5 W, 16.0--18.0 cm	227.16	865.31	72.19	2.66	2.37	3.55	0.59	1.48	8.88	10.06	2.37	26.63
U1343C-23H-5 W, 45.0--47.0 cm	227.45	866.27	64.07	3.89	3.89	5.09	0.60	4.19	10.78	9.28	0.90	51.53
U1343C-23H-5 W, 77.0--79.0 cm	227.77	867.78	48.85	9.51	4.59	4.59	0.66	4.59	19.67	9.18	1.97	18.26
U1343E-25H-2 W, 30.0--32.0 cm	228.39	870.67	38.44	3.18	3.47	2.89	0.58	5.78	38.73	6.94	1.45	13.78
U1343C-23H-6 W, 77.0--79.0 cm	228.72	872.24	61.74	4.69	4.46	3.05	1.17	3.29	13.62	12.21	0.70	32.55
U1343E-25H-2 W, 94.0--96.0 cm	229.03	873.68	58.10	3.81	5.40	6.03	0.00	5.08	17.46	5.71	0.63	7.30

U1343E-25H-2W, 126.0--128.0 cm	229.35	875.18	51.99	10.23	5.11	3.98	0.57	7.95	13.07	6.82	1.70	46.88
U1343E-25H-3W, 16.0--18.0 cm	229.75	877.07	45.81	4.19	5.16	7.74	0.00	13.23	14.19	14.52	0.65	17.93
U1343E-25H-3W, 52.0--54.0 cm	230.11	878.76	56.34	3.24	3.54	3.83	0.29	10.32	14.45	9.44	1.77	13.00
U1343E-25H-3W, 86.0--88.0 cm	230.45	880.36	51.68	1.34	5.70	9.40	0.00	20.13	6.38	8.05	0.67	30.57
U1343E-25H-3W, 126.0--128.0 cm	230.85	882.24	48.43	6.84	3.70	7.41	1.42	8.55	12.82	14.81	2.28	13.38
U1343E-25H-4W, 16.0--18.0 cm	231.25	884.12	55.62	3.65	1.82	8.21	1.52	10.64	12.77	6.69	1.52	6.14
U1343E-25H-4W, 52.0--54.0 cm	231.61	885.81	61.03	7.16	2.01	2.58	1.15	4.01	13.47	8.88	2.87	16.95
U1343E-25H-4W, 96.0--98.0 cm	232.05	887.88	41.91	29.05	5.54	2.22	1.77	2.66	14.41	2.88	0.44	30.43
U1343E-25H-4W, 134.0--136.0 cm	232.43	889.67	52.43	14.80	5.07	2.75	0.21	2.33	19.45	1.06	1.48	5.19

U1343E-25H-5 W, 30.0--32.0 cm	232.89	891.83	25.06	17.83	3.61	4.10	2.41	3.61	35.42	7.95	2.89	10.53
U1343E-25H-5 W, 68.0--70.0 cm	233.27	893.61	39.07	15.57	2.73	8.74	0.27	3.83	20.22	4.37	6.28	13.08
U1343E-25H-5 W, 102.0 cm	233.62	895.26	32.79	12.65	8.67	7.49	0.23	3.75	30.91	2.58	1.64	20.85
U1343E-25H-6 W, 8.0--10.0 cm	234.17	897.85	37.62	6.58	5.33	9.40	0.00	6.90	29.47	4.08	2.51	17.21
U1343E-25H-6 W, 54.0--56.0 cm	234.63	900.01	26.42	14.15	7.55	6.60	0.31	5.66	34.28	2.20	2.52	24.26
U1343E-25H-6 W, 102.0--104.0 cm	235.11	902.27	60.77	5.57	7.26	3.87	0.97	2.91	17.19	0.48	0.97	7.36
U1343E-25H-7 W, 0.0--2.0 cm	235.59	904.52	30.84	16.71	8.07	2.88	1.15	2.88	32.28	2.88	2.59	25.99
U1343E-25H-7 W, 62.0--64.0 cm	236.21	907.44	33.42	10.72	6.48	9.48	0.00	5.99	28.18	2.49	3.99	15.65
U1343C-24H-4 W, 86.0--87.0 cm	236.79	910.16	31.30	9.16	5.09	8.91	0.51	5.60	33.33	2.54	4.33	22.42
U1343C-24H-5 W, 8.0--10.0 cm	237.51	913.55	46.45	16.13	7.10	13.55	0.00	5.81	7.10	0.65	2.58	18.11
U1343C-24H-5 W, 86.0--88.0 cm	238.29	917.22	41.24	12.03	8.25	13.40	1.03	7.22	10.65	2.06	4.12	45.10

U1343C-24H-6 W, 8.0--9.0 cm	239.01	919.21	38.34	10.86	3.19	9.27	1.92	5.75	25.56	2.88	1.92	22.79
U1343C-24H-6 W, 86.0--88.0 cm	239.79	921.26	49.20	9.27	5.43	1.60	0.32	3.83	26.52	1.28	2.24	41.81
U1343C-24H-7 W, 16.0--18.0 cm	240.59	923.36	33.03	14.98	10.09	7.95	0.31	7.34	16.21	1.53	8.26	3.32
U1343E-26H-2 W, 96.0--97.0 cm	241.37	925.41	32.27	8.31	3.83	1.92	0.32	5.11	45.37	1.92	1.28	24.73
U1343E-26H-3 W, 52.0--54.0 cm	242.23	927.67	9.60	4.52	3.39	1.41	0.00	5.37	72.60	0.28	2.82	39.74
U1343E-26H-4 W, 0.0--2.0 cm	243.12	930.01	26.49	4.64	3.64	5.30	4.64	30.46	18.54	2.98	3.31	4.37
U1343E-26H-4 W, 86.0--87.0 cm	243.98	932.27	19.01	10.82	8.48	8.19	1.46	26.32	17.25	6.73	2.92	6.24
U1343E-26H-5 W, 30.0--32.0 cm	244.92	934.74	11.04	0.63	14.83	5.05	0.32	13.88	53.31	0.95	0.32	14.33
U1343E-26H-5 W, 126.0--128.0 cm	245.88	937.26	19.13	13.62	11.59	8.99	5.22	12.75	18.84	4.93	3.77	15.73
U1343E-26H-6 W, 68.0--69.0 cm	246.80	939.68	18.91	8.31	12.32	3.15	0.57	11.17	42.41	2.01	1.72	25.06

U1343E-26H-7 W, 10-11 cm	247.70	942.04	39.37	12.34	17.59	4.46	0.26	4.46	15.75	5.51	2.36	32.48
U1343C-25H-5 W, 86.0--88.0 cm	248.67	944.59	10.13	17.33	30.40	4.80	1.60	3.20	28.53	0.80	3.20	17.18
U1343C-25H-6 W, 31.0--32.0 cm	249.62	947.09	9.05	9.86	21.93	6.04	1.41	5.84	41.25	1.81	3.62	28.30
U1343C-25H-6 W, 119.0--121.0 cm	250.50	949.40	5.71	6.31	12.01	6.91	1.80	13.51	49.25	1.50	3.00	7.16
U1343C-25H-7 W, 77.0--79.0 cm	251.50	952.03	6.30	9.32	10.33	4.53	2.52	7.05	55.67	1.76	3.02	16.87
U1343E-27H-1 W, 143.0--144.0 cm	252.44	954.50	11.22	6.63	14.03	4.08	2.04	5.36	52.04	3.32	2.55	6.35
U1343E-27H-2 W, 86.0--88.0 cm	253.37	956.94	25.37	2.44	3.41	22.44	3.90	4.88	31.71	6.34	1.46	20.80
U1343E-27H-3 W, 30.0--32.0 cm	254.31	959.32	49.52	3.22	1.29	18.65	0.32	3.22	18.33	5.47	1.61	57.80
U1343E-27H-3 W, 126.0--127.0 cm	255.27	961.29	54.67	4.00	1.67	9.67	2.00	7.00	19.00	2.67	0.33	42.12
U1343E-27H-4 W, 77.0--79.0 cm	256.28	963.35	39.38	5.63	5.63	15.00	0.94	3.44	25.94	4.38	1.56	33.65

U1343E-27H-5 W, 16.0--18.0 cm	257.17	965.17	30.60	9.95	3.98	11.19	0.75	9.95	28.86	5.72	1.74	24.90
U1343E-27H-5 W, 108.0--109.0 cm	258.09	967.05	26.65	6.27	5.96	10.03	0.63	8.78	36.36	4.70	2.19	24.15
U1343C-26H-5 W, 77.0--79.0 cm	259.01	968.93	22.62	13.11	7.54	8.20	0.33	10.49	31.80	0.66	4.92	55.81
U1343C-26H-6 W, 16.0--18.0 cm	259.90	970.75	48.00	11.14	2.57	9.71	0.86	7.14	16.29	1.43	3.14	25.79
U1343C-26H-06 W, 106.0--108.0 cm	260.80	972.59	39.94	8.31	12.46	5.11	0.64	4.47	21.73	5.75	4.15	27.91
U1343C-26H-07 W, 46.0--48.0 cm	261.70	974.43	40.70	5.23	7.27	7.56	0.87	4.07	29.94	4.94	0.87	11.19
U1343E-28H-02 W, 0.0--2.0 cm	263.12	977.33	47.19	6.60	11.55	10.89	0.66	3.30	14.52	5.94	1.32	19.53
U1343E-28H-02 W, 92.0--94.0 cm	264.04	979.21	39.28	5.01	8.91	5.29	0.00	3.90	33.15	3.62	1.11	124.57
U1343E-28H-03 W, 32.0--34.0 cm	264.94	981.05	27.38	8.65	8.93	0.86	0.58	4.61	44.96	1.44	2.59	23.23

U1343E-28H-03 W, 112.0--114.0 cm	265.74	982.69	12.92	10.46	11.69	6.15	0.62	13.54	40.31	1.85	3.08	15.80
U1343E-28H-04 W, 51.0--53.0 cm	266.63	984.99	9.80	5.74	9.12	2.03	1.01	13.51	51.01	1.35	6.42	19.57
U1343E-28H-04 W, 130.0--132.00 cm	267.42	987.39	20.59	5.23	6.21	1.63	1.96	14.38	42.81	2.29	4.58	14.76
U1343E-28H-05 W, 60.0--62.0 cm	268.22	989.81	9.92	2.09	20.10	3.13	0.00	11.23	44.91	3.92	6.53	6.59
U1343E-28H-06 W, 0.0--2.0 cm	269.12	992.54	16.49	7.57	7.84	0.81	0.81	5.41	54.32	2.70	4.05	10.41
U1343E-28H-06 W, 74.0--76.0 cm	269.86	994.78	23.77	5.26	5.63	1.45	0.18	5.99	53.90	2.00	2.18	14.57
U1343E-29H-01 W, 18.0--20.0 cm	270.60	997.02	43.73	7.40	5.47	4.82	0.64	4.82	28.94	1.61	2.25	12.15
U1343E-29H-01 W, 92.0--94.0 cm	271.34	999.26	15.62	14.25	7.95	6.58	0.00	3.56	46.03	3.56	2.47	21.67
U1343E-29H-02 W, 51.0--53.0 cm	272.01	1001.29	33.54	10.44	5.38	1.58	0.00	3.48	43.35	1.90	0.63	19.59

U1343E-29H-02 W, 106.0--108.0 cm	272.56	1002.96	35.65	6.95	12.69	3.93	0.60	6.95	28.70	2.42	2.42	20.81
U1343E-29H-03 W, 51.0--53.0 cm	273.26	1004.93	18.98	3.74	22.73	0.53	1.07	6.68	39.04	1.60	5.61	12.82
U1343E-29H-04 W, 25.0--27.0 cm	274.50	1008.42	17.57	11.08	10.27	2.70	0.27	8.11	47.30	0.81	2.16	18.14
U1343E-29H-05 W, 0.0--2.0 cm	275.75	1011.94	15.00	2.33	2.33	8.00	0.33	6.67	57.67	0.33	7.33	8.54
U1343E-29H-05 W, 123.0--125.0 cm	276.98	1015.41	21.54	9.23	17.85	0.92	0.92	6.46	40.62	0.31	2.15	11.44
U1343E-29H-06 W, 110.0--112.0 cm	278.35	1019.26	23.51	11.63	14.47	9.30	0.00	4.39	32.56	1.03	2.84	19.88
U1343E-29H-07 W, 123.0--125.0 cm	279.87	1023.54	32.92	4.00	9.23	6.77	0.31	6.15	35.69	3.38	2.46	19.55
U1343E-30H-02 W, 0.0--2.0 cm (2)	281.42	1027.90	45.98	8.29	6.53	7.04	0.75	2.26	18.09	12.81	3.02	16.39
U1343E-30H-3, 10.0 cm	283.03	1032.27	26.61	11.31	8.87	11.93	1.22	2.75	30.58	7.34	2.14	27.01
U1343E-30H-4, 18.0 cm	284.61	1035.85	19.93	15.36	12.09	18.30	0.33	6.86	19.93	1.96	5.56	15.70

U1343E-30H-5, 32.0 cm	286.25	1039.57	15.31	4.07	2.63	37.56	0.72	2.87	32.06	3.83	1.91	8.73
U1343E-30H-6, 0.0 cm	287.43	1042.25	9.27	6.71	10.86	10.54	0.00	12.46	45.05	0.96	4.47	9.54
U1343E-30H-CC, 20.0 cm	289.84	1047.72	16.32	13.21	12.95	4.40	1.55	10.10	36.79	1.55	2.33	15.72
U1343E-31H-2, 32.0 cm (2)	291.25	1050.90	29.77	7.69	5.02	2.68	0.33	6.69	41.47	3.01	3.68	7.43
U1343E-31H-3, 10.0 cm	292.53	1053.80	14.12	7.34	5.37	0.56	0.85	4.80	59.89	1.69	5.37	20.63
U1343E-31H-4, 51.0 cm	294.44	1058.13	14.58	7.19	7.60	1.23	0.00	5.13	62.63	0.62	0.82	7.59
U1343E-31H-5, 32.0 cm (2)	295.75	1061.10	17.84	6.22	15.14	2.70	0.54	13.24	42.70	1.89	0.27	9.76
U1343E-31H-6, 10.0 cm	297.03	1064.24	6.72	12.16	10.34	2.90	0.54	9.98	52.81	3.63	2.72	14.17
U1343E-31H-7, 32.0 cm	298.75	1069.04	6.99	8.22	7.69	6.12	0.35	12.76	53.15	3.32	2.45	13.07
U1343E-32H-3, 66.0 cm (2)	300.47	1073.83	30.51	3.87	7.26	11.14	1.94	6.54	36.32	1.94	0.97	21.48
U1343E-32H-4, 25.0 cm	301.56	1076.89	10.56	9.57	6.60	6.60	1.65	12.54	48.84	1.65	2.64	32.96
U1343E-32H-5, 100.0 cm	303.71	1082.87	9.13	13.38	11.04	4.46	0.00	9.34	47.98	4.46	1.91	23.41
U1343E-32H-6, 106.0 cm (2)	305.27	1087.22	24.80	15.09	11.59	1.89	0.54	5.39	35.58	3.77	2.43	22.71
U1343E-32H-7, 120.0 cm	306.91	1091.81	45.51	8.38	3.89	3.59	0.00	3.89	31.74	2.69	0.60	14.36

U1343E-33H-1, 10.0 cm	308.75	1096.93	17.78	6.12	7.29	20.12	1.17	2.92	38.19	3.79	3.21	21.51
U1343E-33H-3, 25.0 cm (2)	310.12	1100.76	18.36	4.59	5.57	34.75	0.98	8.85	22.62	1.31	2.95	13.60
U1343E-33H-4, 32.0 cm	311.69	1105.13	22.68	10.72	12.16	5.36	0.62	6.80	38.35	2.89	1.44	42.54
U1343E-33H-5, 44.0 cm	313.31	1109.65	40.68	6.50	3.67	8.19	0.56	3.11	30.79	4.52	3.11	21.51
U1343E-33H-6, 100.0 cm (2)	315.36	1115.38	26.13	3.90	5.11	11.71	3.00	5.71	31.23	18.02	1.80	24.49
U1343E-33H-7, 111.0 cm	316.75	1119.25	30.85	5.85	6.12	20.48	1.33	6.12	22.34	8.78	2.13	16.63
U1343E-34H-1, 60.0 cm	318.53	1124.21	30.11	3.59	6.08	8.29	0.55	3.04	42.82	8.01	1.38	12.56
U1343E-34H-2, 0.0 cm (2)	319.35	1126.94	42.95	5.57	6.23	11.80	2.95	10.16	14.10	4.59	1.64	4.69
U1343E-34H-3, 32.0 cm	321.08	1133.20	34.87	9.51	6.63	2.59	0.00	4.61	38.90	2.31	0.86	7.96
U1343E-34H-4, 10.0 cm	322.36	1137.83	41.04	11.07	8.47	3.26	0.33	5.86	21.82	2.61	5.86	29.43
U1343E-34H-5, 0.0 cm	323.65	1142.50	31.10	3.68	27.09	3.01	0.00	4.35	27.76	2.34	1.67	6.27
U1343E-34H-5, 100.0 cm (2)	324.65	1146.14	18.15	3.96	5.61	4.29	0.33	8.91	56.44	2.31	0.33	34.70
U1343E-34H-6, 66.0 cm	325.81	1150.33	19.87	7.28	13.91	2.32	1.32	9.27	34.44	17.22	1.99	22.56
U1343E-35H-2, 44.0 cm	327.56	1156.66	27.13	4.65	13.70	3.62	0.26	5.94	40.05	4.13	1.81	11.85

U1343E-35H-3, 18.0 cm	328.80	1161.15	27.59	10.97	18.18	1.88	1.25	6.58	29.47	5.96	0.63	20.25
U1343E-35H-3, 136.0 cm	329.99	1165.43	10.74	2.81	6.14	10.23	1.53	3.84	61.13	4.35	1.28	16.99
U1343E-35H-5, 32.0 cm	331.95	1172.52	14.86	4.73	6.08	10.59	0.23	2.48	55.18	3.83	3.15	26.49
U1343E-35H-6, 60.0 cm	333.73	1178.97	27.67	6.51	6.28	16.74	2.33	3.72	29.53	8.14	2.79	29.28
U1343E-35H-6, 110.0 cm	334.23	1180.77	25.58	10.59	7.24	16.28	1.03	1.55	30.23	9.04	2.84	26.15
U1343E-35H-8, 18.0 cm	336.29	1188.23	18.88	3.54	6.19	27.73	1.18	5.31	33.04	3.24	1.77	28.33
U1343E-36H-2, 66.0 cm	337.37	1192.16	17.43	3.49	8.28	5.23	3.05	6.10	50.76	8.06	1.31	31.59
U1343E-36H-3, 51.0 cm	338.72	1197.04	18.26	5.48	8.68	9.59	0.68	4.57	42.92	14.84	1.37	34.04
U1343E-36H-4, 44.0 cm	340.15	1202.22	14.58	2.78	5.79	26.39	0.69	3.01	37.50	12.73	1.85	15.29
U1343E-36H-5, 44.0 cm	341.65	1207.65	48.60	4.75	2.79	26.54	1.12	2.79	11.17	2.23	0.56	10.05
U1343E-36H-6, 25.0 cm	342.96	1212.39	23.22	3.72	7.74	34.37	0.62	2.79	19.81	7.74	3.10	11.75
U1343E-36H-7, 49.0 cm	344.74	1218.80	20.38	7.32	11.46	17.52	1.27	5.10	27.71	13.69	1.91	13.74
U1343E-36H-CC, 18.0 cm	346.49	1225.13	10.49	0.98	4.92	22.30	1.64	5.57	52.79	0.33	0.98	2.56

Table 8.7 $\delta^{30}Si_{diatom}$ data measured on a cleaned sample, sieved at >38 µm ($\delta^{30}Si_{large}$). The rate of silicic acid utilisation ($Utilisation_{large}$) and supply ($Supply_{large}$) are discussed and presented in Chapter 5

Sample code	Age (kyr)	Fraction	$\delta^{30}Si_{large}$	$Utilisation_{large}$ (ε = -1.1, $\delta^{30}Si(OH)_4$ = 1.63)	$Supply_{large}$ (relative to 0.605 Ma)
U1343A-17H-3, 52.0 cm	605.38	>38 µm	1.18	58.86	0.00
U1343E-20H-03, 77.0cm	701.28	>38 µm	0.69	14.09	100.35
U1343E-21H-2, 109.0 cm	755.82	>38 µm	1.26	66.59	-46.11
U1343C-20H-5, 134.0 cm	780.41	>38 µm	1.32	71.95	7.80
U1343A-21H-3, 96.0 cm	813.21	>38 µm	1.73	109.32	-53.97
U1343E-23H-4, 37.0 cm	830.22	>38 µm	1.36	75.68	-39.62
U1343A-22H-3, 8.0 cm	842.30	>38 µm	1.23	63.73	42.68
U1343A-22H-4, 118.0 cm	849.79	>38 µm	0.72	16.95	192.49
U1343C-23H-3, 96.0 cm	858.97	>38 µm	1.23	63.45	48.25
U1343E-25H-7, 0.0 cm	904.57	>38 µm	0.58	4.77	415.96
U1343E-26H-3, 52.0cm	927.70	>38 µm	1.46	84.50	-56.31
U1343E-26H-5, 30.0 cm	934.77	>38 µm	1.45	83.95	-20.49
U1343E-26H-7, 10.0 cm	942.07	>38 µm	1.41	79.68	16.59
U1343C-25H-6, 119.0cm	949.43	>38 µm	1.47	85.86	29.90
U1343C-26H-5, 77.0 cm	968.95	>38 µm	1.50	88.14	-48.14
U1343E-28H-06, 0.0cm	992.57	>38 µm	1.38	77.05	-36.05
U1343E-29H-05, 123.0 cm	1015.43	>38 µm	1.50	88.14	-23.27
U1343E-30H-5, 32.0 cm	1039.59	>38 µm	1.21	62.05	13.95
U1343E-31H-5, 32.0 cm	1061.05	>38 µm	1.52	89.86	19.64
U1343E-32H-3, 66.0	1072.36	>38 µm	1.09	50.50	25.99
U1343E-32H-6, 106.0 cm	1087.25	>38 µm	1.36	75.73	-15.18

U1343E-33H-3, 32.0 cm	1100.895	>38 µm	1.23	63.23	-31.04
U1343E-33H-4, 32.0 cm	1105.16	>38 µm	1.13	54.32	53.43
U1343E-34H-5, 0.0 cm	1142.54	>38 µm	1.26	66.45	17.07
U1343E-35H-2, 44.0 cm	1156.69	>38 µm	1.39	78.18	-34.98
U1343E-35H-6, 60.0 cm	1169.77	>38 µm	1.17	58.18	31.39
U1343E-36H-4, 44.0 cm	1190.67	>38 µm	0.81	25.00	62.66

Table 8.8 $\delta^{30}Si_{diatom}$ data measured on a cleaned sample, sieved at 20-38 µm ($\delta^{30}Si_{small}$). The rate of silicic acid utilisation ($Utilisation_{small}$) and supply ($Supply_{small}$) are discussed and presented in Chapter 5

Sample code	Age (kyr)	Fraction	$\delta^{30}Si_{small}$	$Utilisation_{small}$ (ε = -1.1, $\delta^{30}Si(OH)_4$ = 1.63)	$Supply_{small}$ (relative to 0.605 Ma)
U1343A-17H-3, 52.0 cm	605.38	20-38 µm	1.40	79.41	0.00
U1343E-20H-03, 77.0cm	701.28	20-38 µm	1.17	57.91	-37.55
U1343E-21H-2, 109.0 cm	755.82	20-38 µm	1.32	71.95	-32.50
U1343C-20H-5, 134.0 cm	780.41	20-38 µm	1.35	74.86	40.32
U1343A-21H-3, 96.0 cm	813.21	20-38 µm	1.70	106.68	-36.07
U1343E-23H-4, 37.0 cm	830.22	20-38 µm	1.49	87.09	-29.03
U1343A-22H-3, 8.0 cm	842.30	20-38 µm	1.25	65.36	88.43
U1343A-22H-4, 118.0 cm	849.79	20-38 µm	1.24	64.50	-0.42
U1343C-23H-3, 96.0 cm	858.97	20-38 µm	1.28	68.00	87.26
U1343E-25H-5, 30.0cm	891.87	20-38 µm	1.14	55.77	-24.88
U1343E-25H-7, 0.0 cm	904.57	20-38 µm	1.13	54.14	-50.36
U1343E-26H-3, 52.0cm	927.70	20-38 µm	1.51	88.77	-43.68
U1343E-26H-5, 30.0 cm	934.77	20-38 µm	1.55	92.77	-2.61
U1343E-26H-7, 10.0 cm	942.07	20-38 µm	1.31	70.59	78.63
U1343C-25H-6, 119.0cm	949.43	20-38 µm	1.56	93.32	61.81
U1343C-26H-5, 77.0 cm	968.95	20-38 µm	1.48	85.95	-27.93
U1343E-28H-06, 0.0cm	992.57	20-38 µm	1.42	80.68	-17.30
U1343E-29H-03, 51.0cm	1004.96	20-38 µm	1.48	86.55	-59.82
U1343E-29H-05, 123.0 cm	1015.43	20-38 µm	1.45	83.77	9.46
U1343E-30H-5, 32.0 cm	1039.59	20-38 µm	1.22	62.59	53.04
U1343E-31H-5, 32.0 cm	1061.05	20-38 µm	1.40	78.95	84.80

U1343E-32H-3, 66.0	1072.36	20-38 µm	1.33	72.41	18.34
U1343E-32H-6, 106.0 cm	1087.25	20-38 µm	1.44	82.45	5.45
U1343E-33H-3, 32.0 cm	1100.895	20-38 µm	1.32	71.41	-17.41
U1343E-33H-4, 32.0 cm	1105.16	20-38 µm	1.12	53.32	111.88
U1343E-34H-5, 0.0 cm	1142.54	20-38 µm	1.24	64.64	63.17
U1343E-35H-2, 44.0 cm	1156.69	20-38 µm	1.39	78.36	-12.09
U1343E-35H-6, 60.0 cm	1169.77	20-38 µm	1.35	74.36	38.77
U1343E-36H-4, 44.0 cm	1190.67	20-38 µm	1.32	71.36	-24.82